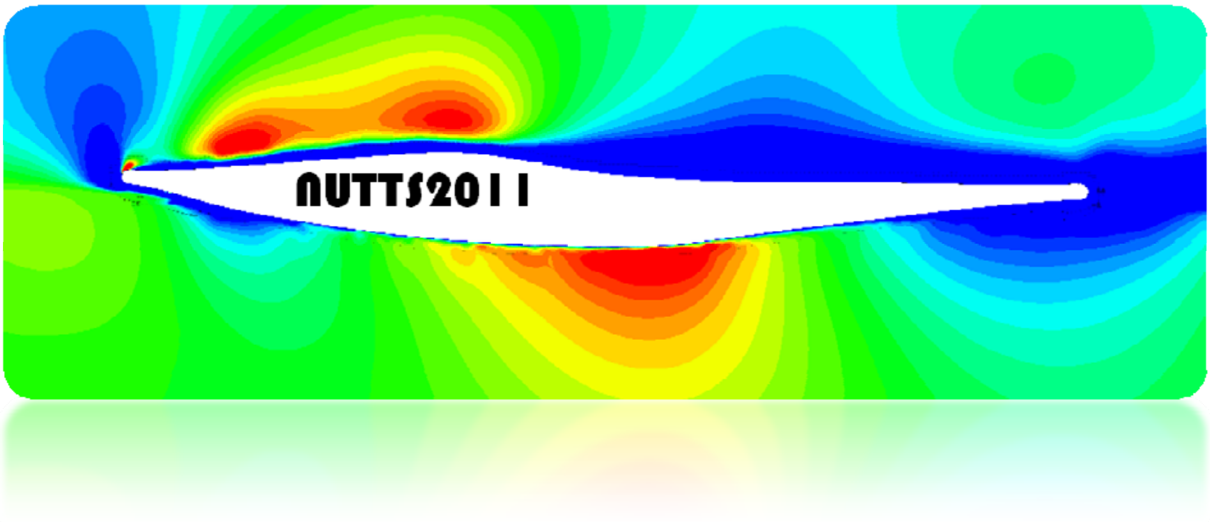

Proceedings of the 14th Numerical Towing Tank Symposium

22nd-24th October 2011

RNLI Training College, West Quay Road Poole, Dorset BH15 1HZ England.

Edited by Turnock, S.R., Bertram, V., Hudson, D.A.

Local Organising Committee

S.R.Turnock, D.A.Hudson, P.A.Wilson, A.B.Phillips
Faculty of Engineering and the Environment,
University of Southampton

Grateful acknowledgement for support is made to the following organisations

Lloyd's Register of Shipping , GL Group, Royal National Lifeboat Institution
Marine Technology Educational Consortium, University of Southampton,
Wolfson Unit for Marine Technology and Industrial Aerodynamics

Lloyd's Register
LIFE MATTERS

UNIVERSITY OF
Southampton

Table of Contents

Provisional Programme
List of Papers (alphabetical by presenters surname)
Papers
Call for Papers for 15th NUTTS in 2012

CALL FOR PAPERS NuTTS'11
14th Numerical Towing Tank Symposium
Poole, England, 22-24th Oct. 2011

UNIVERSITY OF Southampton
School of Engineering Sciences

You are invited to participate in the above event. The objective of the event is to provide a forum for informal discussions among experts in the field and to disseminate latest results. Younger workers and Ph.D. students are especially encouraged to participate. The event will be held at The Lifeboat College, Royal National Lifeboat Institution in Poole, Dorset. All participants stay and have meals together to maximize interaction and discussion.

The extended abstracts of the proposed talk will be directly reproduced in pdf proceedings. Work in progress, encountered problems, etc. should be discussed in an open, informal atmosphere (no ties!) among colleagues. The first page of the extended abstract should be headed with the title and authors' names, affiliation and email address in a compact form to economize on space. Academic titles and page numbers shall be omitted. The extended abstract shall neither contain an abstract of the abstract, nor keywords, nor further headers. Font size shall not be less than 10pt Times New Roman. Extended abstracts should be limited to 6 pages in A4 format with 2.5 cm margin. An early reply will help us in organizing the event better. For the early feedback, a tentative title or topic will suffice.

Following the tradition of previous NuTTS events, the fees will be kept low to allow a maximum number of scientists to attend. The fees including accommodation (2 nights) and all meals during the symposium.

Contact : Prof. Stephen Turnock,
School of Engineering Sciences
University of Southampton
s.r.turnock@soton.ac.uk

Topics:
- Nonlinear flows around marine structures (LES, RANSE, Euler with or w/o free surface)
- Free-surface flows around marine structures (3-d ship seakeeping, free-surface viscous flows)
- Related topics (validation experiments, numerical techniques, grid generation, etc)

Deadlines:	Early feedback (optional):	30 April 2011
	Extended Abstracts rec'vd:	30 July 2011
	Payment received:	30 Aug 2011

Fees:
300 Euro PhD candidates and students,
400 Euro authors
450 Euro other participants

1

Alphabetical List of Papers by Presenter

Stephan Berger, Markus Druckenbrod, Martin Greve, Lars Greitsch, M. Abdel-Maksoud (TUHH)
An Efficient Method for the Investigation of Propeller Hull Interaction

Stefan Harries (Friendship Systems), Volker Bertram (FutureShip), Pat Couser (FDS), Fabian Tillig (SSPA)
Numerical Hull Series using CFD and Response Surfaces

Andreas Brehm, Volker Bertram, Ould El Moctar (FutureShip)
CFD Guided Improvement of a Cavitation-Prone Rudder

Benjamin Bouscasse, Claudio Lugni, Riccardo Broglia (CNR-INSEAN)
Violent seakeeping tests of a fast catamaran

Guiseppina Colicchio, Sara Modini, Claudio Lugni, Giorgio Graziani (INSEAN)
Description of a 3D vortical flow by a Lattice Boltzmann Method

Pierre-Luc Delafin, François Deniset, Jacques-André Astolfi (Ecole Navale)
Influence of Transition on Hydrofoil Fluctuating Forces Prediction

Paweł Dymarski (CTO), Jan Szantyr (TU Gdansk), Marek Kraskowski (CTO)
Numerical analysis of cavitation, unsteady shaft forces and pressure pulses generated on the hull with and without vortex generators

Arash Eslamdoost, Lars Larsson, Rickard Bensow (Chalmers Technical University)
Pressure Jump Approach for Modeling Waterjet/Hull Interaction

Andreas Feymark, Alper Cesur (Chalmers Technical University)
Fluid-Structure Interaction using Open Source Software

Max Haase (University of Tasmania), Nikolai Kornev, Robert Bronsart),Christian Kruger (Rostock University
Validation of Viscous Free-Surface Flows around NPL Catamarans in Oblique Motion at Moderate Froude Number

Satu Hänninen, Tommi Mikkola, Jerzy Matusiak (TKK)
Comparing computed and measured ship wave load distributions

Joe Banks, Alex Phillips, Stephen Turnock, Dominic Hudson
Performing self propelled simulations of a kayak, using a Body-force paddle model

Jan Kaufmann, Volker Bertram (FutureShip)
Comparison of Multi-Reference Frame and Sliding-Interface Propeller Models for RANSE Computations of Ship-Propeller Interaction

Paula Kellett, Osman Turan, Atilla Incecik, Mahdi Khorasanchi (University of Strathclyde), Bernhard Godderidge (Shell Shipping)
A Comparison of Propeller Representation Methods for Numerical Underwater Noise Prediction

Olof Klerebrant Klasson, Tobias Huuva, Magnus Pettersson (Berg Propulsion)
Automation of Propeller Calculations and Application to the Potsdam Propeller Test Case - PPTC

Marek Kraskowski (CTO)
Analysis of the Floating Structures using Sliding Meshes

Surasak Phoemsapthawee, Marc Le Boulluec (IFREMER), Jean-Marc Laurens (ENSTA-Bretagne), François Deniset (Ecole Navale)
A Potential Flow based Underwater Glider Flight Simulator

Jens Ley, Jan Oberhagemann, Ould el Moctar (University Duisburg-Essen), Miguel Onorato (Univ Torino)
Simulation of Ships in Severe and Extreme Sea Conditions

Thomas P. Lloyd, Stephen R. Turnock and Victor F. Humphrey (University of Southampton)
Unsteady CFD of a Marine Current Turbine using OpenFOAM with Generalised Grid Interface

Ulf Barkmann, Hans-Jürgen Heinke, Lars Lübke (SVA Potsdam)
Potsdam Propeller Test Case (PPTC)

Greg Melling, Justin Dix, Stephen Turnock, University of Southampton, Richard Whitehouse, HR Wallingford
CFD-based methods for numerical modelling of scour

Philipp Mucha, Ould el Moctar (University of Duisburg-Essen)
Numerical Analysis of Propeller Loads for a Drifting Container Vessel using RANSE

Henry Piehl, Jens Höpken, Ould el Moctar (University of Duisburg)
Influence of Shape Variation on Hydrodynamic Damping of Rigid Body Motion

Nobuaki Sakamoto (NMRI)
Investigations for wake field of single-screw and twin-skeg container ships in model and full-scale by unstructured grid based RANS solver

Abolfazl Shiri (Chalmers Technical University)
The numerical and experimental study of the hydrodynamics of an Air Cavity Ship

Nikolai Kornev, Andrey Taranov, E. Shchukin, Johann Turnow (Rostock University)
Development of Hybrid URANS-LES Methods for Flow Simulation in the Ship Stern Area

Florian Vesting, Rickard Bensow (Chalmers Technical University)
Propeller Blade Optimisation applying Response Surface Methodology

Erik Vroegrijk (Lloyd’s Register)
Case Study – Coupling CFD+DEM with FEM

Patrick Queutey, Ganbo Deng, Jeroen Wackers (Ecole Centrale de Nantes)
Coupled Sliding Grids and Adaptive Grid Refinement for RANS Simulation of Ship-Propeller Interaction

Wei Zhang (Chalmers Technical University)
Numerical Simulation of high-Reynolds number flow around Flettner rotors

Lu Zou, Lars Larsson (Chalmers Technical University)
A Verification and Validation Study Based on Resistance Submissions to the Gothenburg 2010 Workshop on Numerical Ship Hydrodynamics

Final Schedule

Event	Paper	Time	Location/Title
Registration		11:30-13:00	RNLI Training College Reception
Lunch		13:00-14:00	
Session 1		14:00-14:05	Welcome Chair Stephen Turnock
Resistance	1	14:05-14:30	Lu Zou, Lars Larsson (Chalmers Technical University) *A Verification and Validation Study Based on Resistance Submissions to the Gothenburg 2010 Workshop on Numerical Ship Hydrodynamics*
	2	14:30-14:55	Abolfazl Shiri (Chalmers Technical University) *The numerical and experimental study of the hydrodynamics of an Air Cavity Ship*
	3	14:55-15:20	Joe Banks, Alex Phillips, Stephen Turnock, Dominic Hudson *Performing self propelled simulations of a kayak, using a Body-force paddle model*
	4	15:20-15:45	Nobuaki Sakamoto (NMRI) *Investigations for wake field of single-screw and twin-skeg container ships in model and full-scale by unstructured grid based RANS solver*
Teabreak		15:45-16:15	
Session 2			Chair: François Deniset
Propeller-hull	5	16:15-16:40	Stephan Berger, Markus Druckenbrod, Martin Greve, Lars Greitsch, M. Abdel-Maksoud (TUHH) *An Efficient Method for the Investigation of Propeller Hull Interaction*
	6	16:40-17:05	Arash Eslamdoost, Lars Larsson, Rickard Bensow (Chalmers Technical University) *Pressure Jump Approach for Modeling Waterjet/Hull Interaction*

	7	17:05-17:30	Jan Kaufmann, Volker Bertram (FutureShip) *Comparison of Multi-Reference Frame and Sliding-Interface Propeller Models for RANSE Computations of Ship-Propeller Interaction*
	8	17:30-17:55	Patrick Queutey, Ganbo Deng, Jeroen Wackers (Ecole Centrale de Nantes) *Coupled Sliding Grids and Adaptive Grid Refinement for RANS Simulation of Ship-Propeller Interaction*
Landrini Award		17:55-18:10	
Evening Meal		19:00-20:00	
Sunday 23rd			
Breakfast		07:00-09:00	
Session 3			Chair: Guiseppina Colicchio
Seakeeping I	9	09:00-09:25	Benjamin Bouscasse, Claudio Lugni, Riccardo Broglia (CNR-INSEAN) *Violent seakeeping tests of a fast catamaran*
	10	09:25-09:50	Satu Hänninen, Tommi Mikkola, Jerzy Matusiak (TKK) *Comparing computed and measured ship wave load distributions*
	11	09:50-10:15	Marek Kraskowski (CTO) *Analysis of the Floating Structures using Sliding Meshes*
Coffeebreak		10:15-10:45	
Session4			Chair: Dominic Hudson
Seakeeping II	12	10:45-11:10	Jens Ley, Jan Oberhagemann, Ould el Moctar (University Duisburg-Essen), Miguel Onorato (Univ Torino) *Simulation of Ships in Severe and Extreme Sea Conditions*
	13	11:10-11:35	Henry Piehl, Jens Höpken, Ould el Moctar (University of Duisburg) *Influence of Shape Variation on Hydrodynamic Damping of*

			Rigid Body Motion
	14	11:35-12:00	Max Haase (University of Tasmania), Nikolai Kornev, Robert Bronsart, Christian Kruger (Rostock University) *Validation of Viscous Free-Surface Flows around NPL Catamarans in Oblique Motion at Moderate Froude Number*
	15	12:00-12:25	Stefan Harries (Friendship Systems), Volker Bertram (FutureShip), Pat Couser (FDS), Fabian Tillig (SSPA) *Numerical Hull Series using CFD and Response Surfaces*
Lunch		12:25-14:00	
Symposium Photo		13:45-14:00	
Session 5			Chair: Volker Bertram
Maritime Fluids I	16	14:00-14:25	Guiseppina Colicchio, Sara Modini, Claudio Lugni, Giorgio Graziani (INSEAN) *Description of a 3D vortical flow by a Lattice Boltzmann Method*
	17	14:25-14:50	Pierre-Luc Delafin, François Deniset, Jacques-André Astolfi (Ecole Navale) *Influence of Transition on Hydrofoil Fluctuating Forces Prediction*
	18	14:50-15:15	Nikolai Kornev, Andrey Taranov, E. Shchukin, Johann Turnow (Rostock University) *Development of Hybrid URANS-LES Methods for Flow Simulation in the Ship Stern Area*
	19	15:15-15:40	Greg Melling, Justin Dix, Stephen Turnock, University of Southampton, Richard Whitehouse, HR Wallingford *CFD-based methods for numerical modelling of scour*
Teabreak		15:40-16:10	
Session 6			Chair Jeroen Wackers
Maritime Fluids II	20	16:10-16:35	Surasak Phoemsapthawee, Marc Le Boulluec (IFREMER), Jean-

			Marc Laurens (ENSTA-Bretagne), François Deniset (Ecole Navale) *A Potential Flow based Underwater Glider Flight Simulator*
	21	16:35-17:00	Erik Vroegrijk (Lloyd's Register) *Case Study – Coupling CFD+DEM with FEM*
	22	17:00-17:25	Thomas P. Lloyd, Stephen R. Turnock and Victor F. Humphrey (University of Southampton) Unsteady CFD of a Marine Current Turbine using OpenFOAM with Generalised Grid Interface
	23	17:25-17:50	Wei Zhang (Chalmers Technical University) *Numerical Simulation of high-Reynolds number flow around Flettner rotors*
Evening Meal		19:30-21:00	
Monday 24th			
Breakfast		07:00-08:30	
Session 7			Chair Jean-Marc Laurens
Propellers I	24	08:30-08:55	Ulf Barkmann, Hans-Jürgen Heinke, Lars Lübke (SVA Potsdam) *Potsdam Propeller Test Case (PPTC)*
	25	08:55-09:20	Paweł Dymarski (CTO), Jan Szantyr (TU Gdansk), Marek Kraskowski (CTO) *Numerical analysis of cavitation, unsteady shaft forces and pressure pulses generated on the hull with and without vortex generators*
	26	09:20-09:45	Olof Klerebrant Klasson, Tobias Huuva, Magnus Pettersson (Berg Propulsion) *Automation of Propeller Calculations and Application to*

			the Potsdam Propeller Test Case - PPTC
	27	09:45-10:10	Paula Kellett, Osman Turan, Atilla Incecik, Mahdi Khorasanchi (University of Strathclyde), Bernhard Godderidge (Shell Shipping) *A Comparison of Propeller Representation Methods for Numerical Underwater Noise Prediction*
Coffeebreak	28	10:10-10:40	
Session 8			Chair: Stephen Turnock
Propellers II	29	10:40-11:05	Florian Vesting, Rickard Bensow (Chalmers Technical University) *Propeller Blade Optimisation applying Response Surface Methodology*
	30	11:05-11:20	Reddy Devalpalli (Lloyd's Register) *Possible areas of further research in CFD applications from LR's perspective*
	31	11:20-11:45	Andreas Brehm, Volker Bertram, Ould El Moctar (FutureShip) *CFD Guided Improvement of a Cavitation-Prone Rudder*
	32	11:45-12:10	Philipp Mucha, Ould el Moctar (University of Duisburg-Essen) *Numerical Analysis of Propeller Loads for a Drifting Container Vessel using RANSE*
	33	12:10-12:35	Andreas Feymark, A. Cesur (Chalmers Technical University) *Fluid-Structure Interaction using Open Source Software*

List of Attendees

Surname	First name	Organisation
Ahmed	Tauseef	UoS
Badoe	Charles	UoS
Berger	Stephan	TU Hamburg
Bertram	Volker	GL
bouscassa	Benjamin	INSEAN
Cesur	Alper	Lund
Colicchio	Giuseppina	INSEAN
Delafin	Pierre-Luc	Ecole-navale
Deniset	Francois	Ecole-navale
Devalapalli	Reddy	LR
Dymarski	Pawel	CTO
Eslamdoost	Arash	Chalmers
Feymark	Andreas	Chalmers
Greitsch	Lars	
Hanninen	Satu	Aalto
Hoepken	Jens	Potsdam
Hudson	Dominic	UoS
Kaufmann	Jan	GL-group
Kellett	Paula	Strathclyde
Klasson	Olof	Berg
Kraskowski	Marek	CTO
Krueger	Christian	Rostock
Laurens	Jean-Marc	ENSTA
Lewis	Simon	CJR
Ley	Jens	Duisburg
Lloyd	Tom	UoS
Luebke	Lars	Potsdam
Malas	Bertrand	BMT Defence Services
Melling	Greg	UoS
Mucha	Philipp	Duisburg
Pattenden	Richard	Qinetiq
Piehl	Henry	Dusiburg
Sakamoto	Nobuaki	NMRI
Shiri	Abolfazl	Chalmers
Spenkuch	Thomas	UoS
Trimarchi	Daniele	UoS
Turnock	Stephen	UoS
Turnow	Johann	Rostock
Vesting	Florian	Chalmers
Vroegrijk	Erik	LR
Wackers	Jereon	ECN
Watson	Stephen	QinetiQ
Winden	Bjorn	UoS

Zegos	Constantinos	LR
Zhang	Wei	Chalmers
Zou	Lu	Chalmers

An Efficient Method for the Investigation of Propeller Hull Interaction

Stephan Berger, Markus Druckenbrod,
Martin Greve, Moustafa Abdel-Maksoud
TUHH Hamburg University of Technology
Hamburg, Germany
stephan.berger@tu-harburg.de | *www.tu-harburg.de/fds*

Lars Greitsch
MMG Mecklenburger Metallguss GmbH
Waren (Müritz), Germany

1. Introduction

Propeller-induced pressure fluctuations may be a crucial factor in the entire ship design process of certain ship types. Thus, it is important to develop methods which are able to reliably and quickly predict the flow around ship propeller configurations.

The flow in this region can be divided into two interacting parts: The wake field of the ship, which is strongly influenced by viscous effects; and the flow around the propeller, which basically has the character of an unsteady potential flow. Viscous methods, such as RANS methods, are able to cover all these effects.

Nowadays high-efficient processors allow for the investigation of the flow around a whole ship with RANS methods including the propeller and the rudder, but this is far away from practice with respect to the integration of such computations in the ship design process.

For the computation of flows around complex geometry shapes of propellers a high grid resolution is needed. In this paper an approach is presented in which the propeller itself is not geometrically considered in the fluid domain but its influence on the flow is modelled by a propeller model.

This model is based on a body force approach, i.e. the impact of the propeller on the flow is simulated by adding certain forces to the source terms of the Navier-Stokes equations. This approach has already been used successfully in [1], [2], [3] and [4], for example.

In contrast to similar works, neither the forces are averaged circumferentially nor is the blade thickness neglected. The distribution of the forces is calculated by a boundary element code using the ship's wake field as input. Both solvers, the RANS solver and the boundary element code, run in parallel. Thus, the unsteady interaction of propeller and hull is covered as well.

In this work the viscous flow solver ANSYS CFX is coupled with *pan*MARE (*www.panmare.de*), the in-house panel code of the Hamburg University of Technology.

After having introduced the applied methods, the principle of the coupling algorithm and its implementation are explained. A numerical study is carried out for the KCS test case geometry, and the calculated pressure fluctuations of the developed propeller model are compared with the results of the RANS computation using the resolved propeller geometry.

2. Underlying Methods

2.1. Viscous Method

The behaviour of viscous flows can be described by the Navier-Stokes equations (1) and the continuity equation (2). In this work the Reynolds-averaged form is used (indicated by the bars above velocity $\mathbf{u}$ and pressure p) in order to simulate turbulent effects:

$$\rho\left(\frac{\partial}{\partial t}+\mathrm{J}\overline{\mathbf{u}}\right)\cdot\overline{\mathbf{u}} = -\mathrm{grad}\,\overline{p} + \mathrm{div}\,\left(\overline{\boldsymbol{\tau}}+\boldsymbol{\tau}_T\right)+\mathbf{f} \qquad (1)$$

and

$$\mathrm{div}\,\overline{\mathbf{u}} = 0 \qquad (2)$$

In (1), $\overline{\boldsymbol{\tau}}$ denotes the Reynolds-averaged molecular stress tensor and $\boldsymbol{\tau}_T$ the Reynolds stress tensor due to the Reynolds-averaging, whose components are approximated by appropriate turbulence models. $\mathrm{J}\overline{\mathbf{u}}$ is the Jacobian matrix of the velocity field.

The ANSYS CFX code [5] is applied to solve the system of equations mentioned above. ANSYS CFX is a finite-volume-based method which can consider structured and unstructured numerical grids with control volumes of four to eight corners. In ANSYS CFX the control volumes are constructed around the vertices of the grid. Variables, such as velocity and pressure, are stored in these vertices.

ANSYS CFX offers a powerful FORTRAN-like user coding which gives access to the calculated data and allows the manipulation of these data. By these means an interface to the boundary element method *pan*MARE can be implemented.

2.2. Boundary Element Method

*pan*MARE is a tool which has been developed to simulate flows based on potential theory. It is mainly used for propeller flow analysis [6].

The fluid is considered to be incompressible and the velocity field irrotational. Consequently, no viscous effects can be captured by this theory. These assumptions lead to the Laplace equation $\triangle\Phi = 0$ for the velocity potential Φ. Since this differential equation is a linear one, the linear combination of simple solutions is a solution as well. Boundary element methods utilize this principle: The boundary S_B of the submerged body is divided into N_B panels, the thin body of the wake layer S_W in N_W panels, respectively (ref. Figure 1).

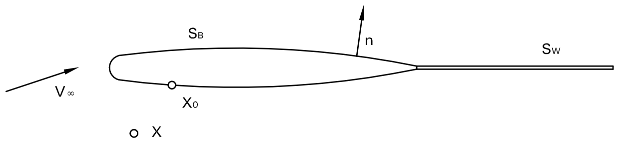

Figure 1. Boundaries of Submerged Body and Wake Layer.

The velocity potential $\Phi(\mathbf{x})$ at the location $\mathbf{x}$ can be expressed as a combination of N_B potential sources σ_k on the submerged body S_B and $N_B + N_W$ potential dipoles μ_k on the body S_B and the wake layer S_W:

$$\begin{aligned}\Phi(\mathbf{x}) &= \frac{1}{4\pi}\sum_{k=1}^{N_B+N_W}\mu_k\int_{A_k}\mathbf{n}_k\nabla\frac{1}{r_k(\mathbf{x})}dS \\ &\quad -\frac{1}{4\pi}\sum_{k=1}^{N_B}\sigma_k\int_{A_k}\frac{1}{r_k(\mathbf{x})}dS + \Phi_\infty(\mathbf{x}) \qquad (3)\end{aligned}$$

Note that the distance $r_k = ||\mathbf{x} - \mathbf{x}_k||$ between the location $\mathbf{x}$ and the collocation point (in this case the midpoint) $\mathbf{x}_k$ of the panel k with the area A_k and the surface normal $\mathbf{n}_k$ are geometrically determined. The potential of the inflow Φ_∞ with $\mathbf{V}_\infty = \nabla\Phi_\infty$ is given. The remaining unknowns can be found by employing the impermeability boundary condition,

$$\mathbf{V}\cdot\mathbf{n} = 0 \qquad \text{on } S_B \qquad (4)$$

which claims that the normal component of the total velocity $\mathbf{V}$ vanishes on the boundary S_B. The Kutta condition forces the pressure difference at the trailing edge of S_B to be zero.

*pan*MARE can be applied for both homogeneous and inhomogeneous inflows $\mathbf{V}_\infty$ making it particularly suitable for the purpose of the present numerical study.

3. Outline of the Coupling Algorithm

3.1. The Two Steps of the Algorithm

The coupling algorithm can be decomposed in two main steps (ref. Figure 2).

Step 1 The first step is reading the velocity distribution in a circular plane located between 0.1 and $0.2D$ upstream the propeller. The plane is composed of a number of points (typically 300 to 400) distributed radially and circumferentially. For each of these points the nearest grid vertex is determined and the velocity is mapped from there to the respective point.

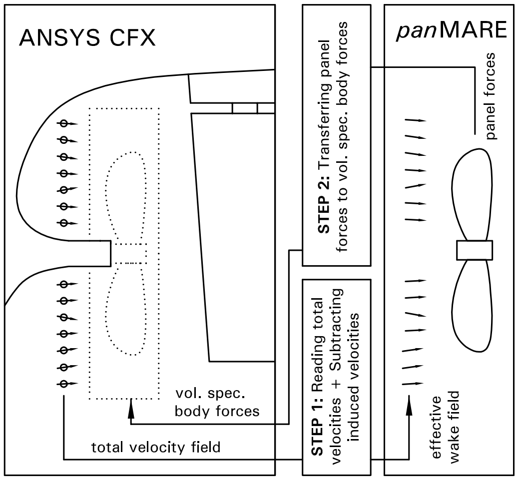

Figure 2. Principle of the Coupling Algorithm.

*pan*MARE interprets a given inflow as an effective wake field. In fact, the velocity distribution extracted in Step 1 is already affected by the induced velocities of the propeller. In order to obtain the effective wake field, the induced velocities have to be subtracted from the read velocity distribution, see Figure 2. This is performed by an internal routine of *pan*MARE.

Step 2 In the second step the distribution of the forces calculated by *pan*MARE is transferred to the viscous fluid domain in ANSYS CFX. *pan*MARE provides one resulting force $\mathrm{d}\mathbf{F}_k$ for each panel k acting on the midpoint of this panel. This force contains both a part due to pressure and an empirically estimated part due to friction. Let $N_{panel} = N_B$ (ref. Section 2.2) be the number of panels and N_{CV} the number of control volumina in the viscous fluid domain. $\mathbf{x}_k$ is the current position of the force application point on the kth panel, and $\mathbf{x}_m$ is the position of the vertex which the mth control volume dV_m is constructed around. The task is to convert the distribution of N_{panel} panel acting forces into a distribution of volume-specific forces.

For each force application point k, a routine looks for the control volumes situated in the vicinity of the point k. For this purpose it is checked whether the grid vertex m lies in an imaginarily drawn sphere with the radius r_{smt} around the point k. Respectively, the factor $a_{k,m}$ is defined as follows:

$$a_{k,m} = \begin{cases} 1 & \text{if } ||\mathbf{x}_m - \mathbf{x}_k|| \leq r_{smt} \\ 0 & \text{if } ||\mathbf{x}_m - \mathbf{x}_k|| > r_{smt} \end{cases} \qquad (5)$$

Finally, the mth control volume is charged with the volume specific force $\mathbf{f}_m$ (ref. Equation 1):

$$\mathbf{f}_m = \sum_{k=1}^{N_{panel}} a_{k,m}\frac{\mathrm{d}\mathbf{F}_k}{V_k} \qquad (6)$$

with

$$V_k = \sum_{m=1}^{N_{CV}} a_{k,m} dV_m \tag{7}$$

being the sum of all control volumes within the sphere of the radius r_{smt} around $\mathbf{x}_k$.

Figure 3 demonstrates the procedure with the help of a 2D grid. Note the effect of the radius r_{smt}: The bigger it is the more control volumes of the viscous flow domain get involved in the panel force distribution. The shape of the virtual propeller gets blurrier but the calculations are more stable.

The procedure described above allows the separate consideration of the forces on the pressure and the suction side of the blade. By this means it is possible to capture the geometrical characteristics of the propeller blades, such as contour shape or thickness distribution.

All the necessary routines have been implemented with ANSYS CFX user coding.

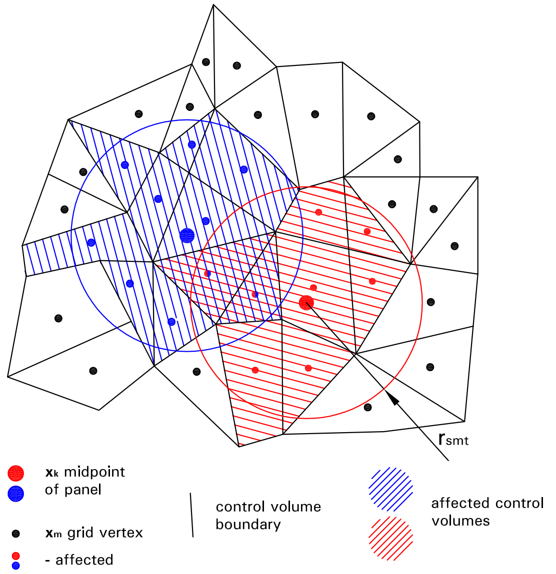

Figure 3. 2D Example for the Force Transfer Process.

3.2. Flow of the Coupling Algorithm

Two different coupling modes have been implemented: The implicit (or strong) and the explicit (or weak) coupling mode. Figure 4 shows the basic flow of the algorithm.

Implicit Coupling Mode At the beginning of a new time step the first coupling step is performed as described in Section 3.1: The velocity distribution is extracted and the induced velocities are subtracted. With these data as input, *pan*MARE computes the potential flow around the propeller. Afterwards, the calculated panel forces are transferred to the viscous fluid domain in ANSYS CFX (Step 2, ref. Section 3.1). Taking these forces into account, ANSYS CFX carries out one iteration of the viscous flow problem. Unless a certain convergence criterion is reached, the iteration loop is repeated. The velocities are read again and *pan*MARE computes new panel forces without changing the angular position of the propeller. If the convergence criterion is satisfied, the algorithm starts the calculation of the next timestep, which means that the geometry of the propeller is rotated according to the size of the timestep and the angular speed of the propeller.

Although this description implies that the solvers run serially, only a few minor modifications concerning the data exchange make sure that the solvers run in parallel.

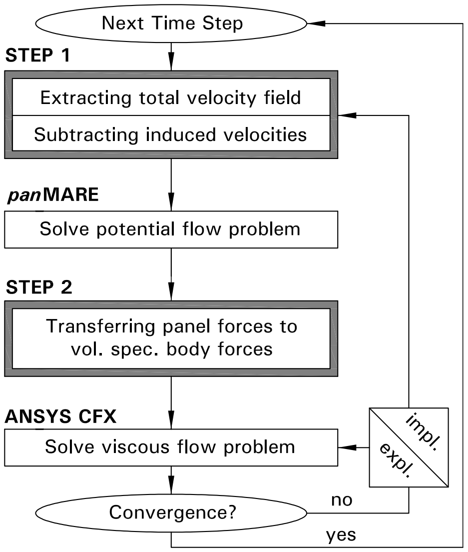

Figure 4. Flow Chart of the Algorithm.

Explicit Coupling Mode In contrast to the implicit coupling mode, data exchange is done only once per time step in the explicit mode. ANSYS CFX performs the coefficient loops of a time step with the same body force distribution which has been calculated by *pan*MARE at the beginning of the current time step. Evidently, the computational effort can be reduced slightly in comparison to the implicit mode. This coupling mode might be more applicable to rather uniform inflow conditions. For simulations with a typical wake field the implicit mode is the better choice.

4. Applications of the Coupling Algorithm

In this section the results of the numerical investigation of the KCS test case (KRISO Container Ship) are presented. To evaluate the performance of the developed propeller model, the results of the propeller model are compared with those of a fully RANS computation [7]. The dimensions of the model hull and the model propeller P 1356 are shown in Table 1.

Dimension		Unit	
KCS Hull			
L_{PP}	Length between pp.	[m]	7.278
S	Wetted surface w/o rudder	[m^2]	9.438
c_B	Block Coefficient	[-]	0.651
v_s	Speed	[$^m/_s$]	2.196
Fn	Froude Number	[-]	0.260
Propeller P 1356			
D	Diameter	[m]	0.250
z	Number of blades	[-]	5
$^{P_{0.7}}/_D$	Pitch ratio	[-]	0.997
$^{A_e}/_{A_0}$	Area ratio	[-]	0.800
θ_{eff}	Skew	[°]	31.830
$^{s_f}/_D$	Relative minimum distance blade tip - hull	[-]	0.266
	Sense of rotation (looking from behind)		clockw.
n	Number of revolutions	[s^{-1}]	9.5

Table 1. Main Dimensions of the KCS Model Hull and the Propeller.

The following settings have been used for the RANS computation:

- Starting from the aft perpendicular the fluid domain extends 4.2 ship lengths backward and 3.2 forward. The breadth is 4.5 ship lengths and the ground lies one ship length under the keel. The shape of the free water surface is computed by employing a VOF method. The calculations are carried out without accounting for the rudder.
- The mesh has 11.6 mil. cells, thereof 1.7 mil. belong to the propeller grid. Turbulence is modelled by employing the SST turbulence model.
- The propeller is turned 3° per time step in order to capture unsteady effects accurately.

For the calculations with propeller model the real propeller geometry is replaced by a cylindrical "empty" grid, which only includes the propeller hub (ref. Figure 5). This grid has only 70,000 cells. Thus, the complete grid shrinks to 10.0 mil. cells.

The propeller model and *pan*MARE have been configured as follows:

- The velocity extraction plane is located $0.2D$ upstream the propeller and counts 320 reading points distributed over 8 radii. The innermost radius is $0.2D$, the outermost $1.15D$.
- The radius $r_{smt} = 0.023D$ (ref. Section 3.1) turned out to be a good compromise between numeric stability and sufficient resolution of the propeller shape.
- The implicit coupling mode is used.
- For the computation of the potential flow problem in *pan*MARE the propeller is discretized by $N_B = 3.060$ panels, i.e. 17 radial panels and 18 panels in chord direction per blade. The hub is not modelled in *pan*MARE. The shape of the free vortex panels shedded from the propeller blades is kept fixed during the iterations. This simplification is acceptable for small thrust loading coefficients and helps to stabilize the computation.

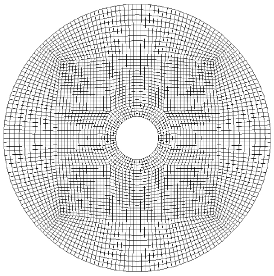

Figure 5. Grid for the Propeller Model.

4.1. Prediction of Thrust and Suction Effects

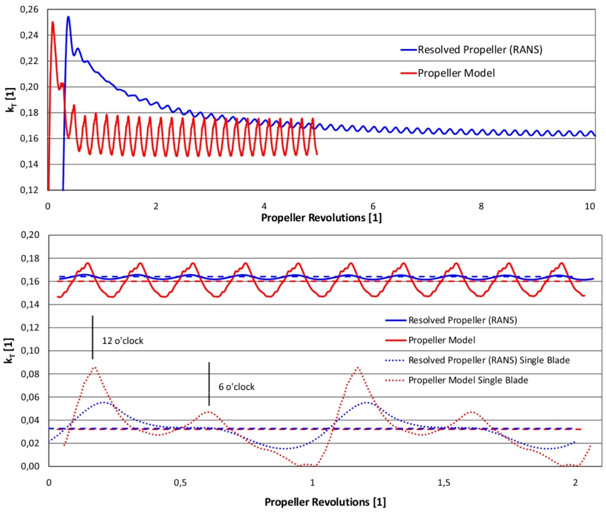

Figure 6. Convergence Behaviour of Calculated Thrust Coefficient.

Thrust In Figure 6 the convergence behaviour of the thrust is compared between propeller model and fully RANS computation. Two observations can be made: The RANS solution needs nearly ten revolutions to reach a steady average thrust, whereas the propeller model already tends to a steady average thrust after less than two revolutions. This is due to the fact that the system of wake vortices is existent in *pan*MARE from the beginning. However, the wake vortices have to be developed in the RANS computation which takes more time. The predicted thrust of the propeller model differs 2% from the RANS solution. Seeing the immense reduction of computing time, this difference may be acceptable.

The second observation is that the thrust oscillations calculated by the propeller model are much higher. Figure 6 illustrates in detail the thrust over two revolutions for the whole propeller and for a single blade. The frequency of the oscillations is the blade frequency. The lower curves in Figure 6 show the reason for the oscillations: Whenever a blade passes the 12 o'clock position it is exposed to high effective angles of attack and consequently the thrust increases. The thrust curve calculated by the propeller model even shows a similar but less strong behaviour in the 6 o'clock position. The difference between both methods is the intensity with which this effect occurs.

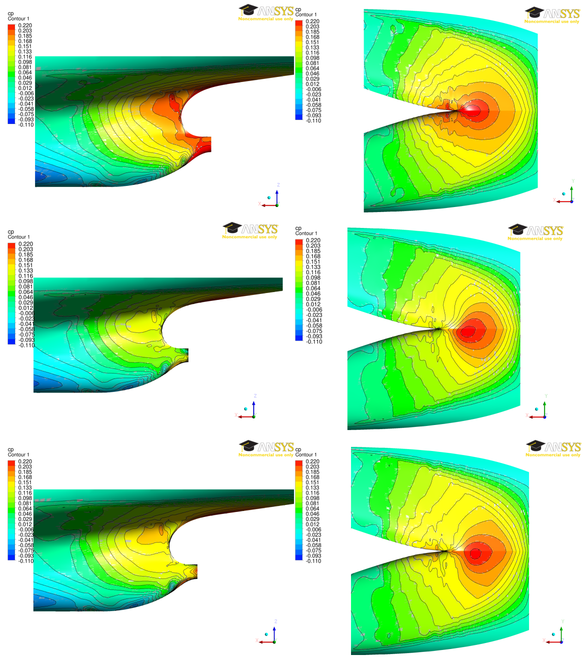

Figure 7. Pressure Distribution in the Propeller Region. Above: without propeller, middle: with geometrically resolved propeller, bottom: with propeller model.

One reason for the different intensities could be that the RANS solution is affected by viscous and numerical damping, the other could be that the inflow of the propeller is not absolutely the same in both cases: The geometrically resolved propeller is located in a rotating grid which is connected with the surrounding grid by an interface. This interface possibly filters out the wake peaks and smoothes the inflow artificially. The velocity extraction plane of the propeller model lies *upstream* the interface.

Suction Effects Figure 7 shows the distribution of the dynamic pressure in the propeller region. The first two graphics represent the pressure distribution without propeller; the following graphics show the propeller influence for nearly the same blade position calculated by both methods. In the right column the hull bottom is shown. It can be observed that the working propeller reduces the high pressures in the stern region. Since the propeller model does not take the hub into account, the pressure fields close to the stern bulbus are not comparable. Apart from this, the contours show a widely coincident behaviour.

4.2. Prediction of Propeller-Induced Pressure Fluctuations

Propeller-induced pressure fluctuations often cause vibrations of the ship structure with severe consequences. Thus, it is of great interest to investigate a ship propeller configuration with regard to this problem.

Three effects contribute to propeller-induced pressure fluctuations [8]:

- *Pressure fluctuations due to blade displacement.* This effect is important for regions in the direct vicinity of the propeller. It decays quickly with increasing distance to the propeller.
- *Pressure fluctuations due to varying blade lift.* The maximum of this effect can be observed approximately $0.1...0.2D$ downstream the propeller, since the varying velocity field needs a while to be built up by the system of wake vortices. A propeller working in an unsteady inflow is much more affected by this effect than by the first one.
- *Pressure fluctuations due to cavitation.* If cavitation occurs, this effect causes much higher pressure fluctuations than the other effects. Because the propeller model is not able to predict cavitation phenomena, the effect is not considered in this paper.

Five monitoring points have been placed on the hull in the propeller region. The positions are shown in Figure 8. Points 2, 3, and 4 are placed directly above the propeller; Point 1 $0.2D$ upstream, and Point 2 $0.2D$ downstream.

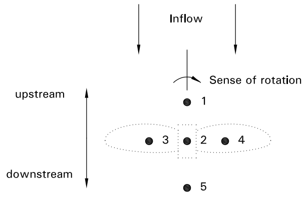

Figure 8. Position of the Monitoring Points.

The results have been transformed from the time domain to the frequency domain by a Fourier transformation. The results calculated by the propeller model show a good overall agreement with the results from the RANS computation.

As expected, the main component of the calculated fluctuations appears with blade frequency.

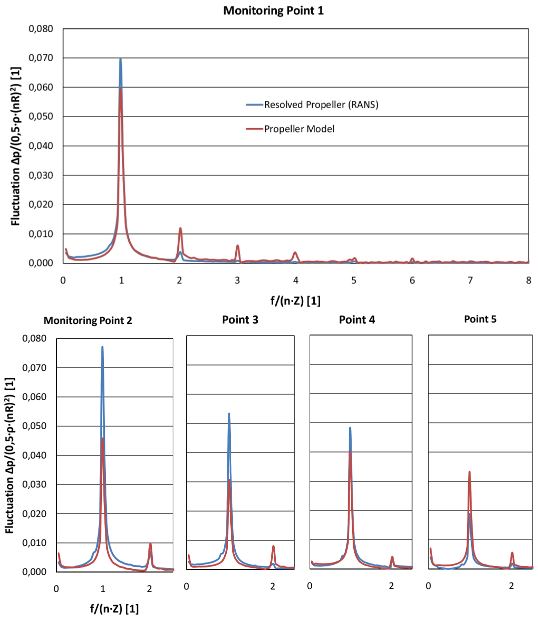

Figure 9. Pressure Fluctuations in Frequency Domain.

Different reasons may have direct influence on the calculated pressure fluctuations: In Section 4.1 it has been reported that the propeller model predicts higher thrust fluctuations. Accordingly, the blade lift variations are predicted to be higher as well. For every monitoring point, the values for the higher harmonics calculated by the model are a little bit higher than calculated by the variant with resolved propeller. This indicates that the blade lift effect dominates the propeller model predictions.[1]

The used sphere radius r_{smt} of $0.023D$ (ref. Section 3.1) resolves the over-all geometry sufficiently, but may be oversized for the blade tips. This artificially smoothes the pressure peaks on the blade tips and apparently reduces the pressure fluctuations on the hull. To avoid this problem and assure numeric stability simultaneously, a variable sphere radius considering the local blade thickness could be an option.

Keeping this in mind, the differences of the curves in Figure 9 can be explained: Monitoring Points 2, 3 and 4 are placed directly above the propeller. A good resolution of the blade tips is important here. The pressure fluctuations predicted by the fully RANS computation may be more reliable in this case. The upward component of the inflow causes a higher blade lift in the position of Point 4 than in the position of Point 3. For this reason the propeller model calculates a much higher fluctuation in position 4. In Monitoring Point 5 the displacement effect becomes less important, whereas the blade lift effect already has reached its maximum. Since the propeller model tends to overemphasize the blade lift effect, a greater fluctuation is predicted by the propeller model.

5. Conclusions

By employing the propeller model, the number of grid cells for the propeller could be reduced from 1.3 mil. to 70,000, and the propeller grid shrinks to 5% of its previous size. The computation time decreased drastically. Especially the thrust prediction can be performed very quickly. Although in this study a fixed operation point was imposed on the propeller, a numerical propulsion test is theoretically possible.

The estimation of pressure fluctuations of non-cavitating propellers is an important application. The results presented in Section 4.2 are not completely satisfactory but encourage further development of the algorithm.

References

[1] F. Stern, H. T. Kim, V. C. Patel, H. C. Chen: *A Viscous Flow Approach to the Computation of Propeller-Hull Interaction*, Journal of Ship Research, Vol. 32, No. 4, pp. 246-262, 1988

[2] I. Zawadzki, D. Fuhs, J. Gorski: *Integration of a Viscous Flow RANS Solver with an Unsteady Propulsor Force Code*, Caderock Division, Naval Surface Warfare Center, Maryland, 1997

[3] S. B. Müller, M. Steden, J. Neugebauer, M. F. El-Haddad, M. Abdel-Maksoud: *Comparing a Propeller Model with a Rotating Propeller in a CFD Simulation of the Viscous Flow around a Ship*, 9th Numerical Towing Tank Symposium, Le Croisic, 2006

[4] K. Wöckner, M. Greve, M. Scharf, T. Rung, M. Abdel-Maksoud: *Unsteady Viscous/ Inviscid Coupling Approaches for Propeller Flow Simulations*, 2nd International Symposium on Marine Propulsors, Hamburg, 2011

[5] NN: *ANSYS CFX 12.0 Documentation*, ANSYS, Canonsburg, 2009

[6] M. Abdel-Maksoud, M. Steden, J. Hundemer: *Design of a Multi-Component Propulsor*, 28th Symposium on Naval Hydrodynamics, Pasadena, 2010

[7] M. Greve, M. Abdel-Maksoud, S. Eder, J. de Causmaecker: *Unsteady Viscous Flow Calculation around the KCS-Model with and without Propeller under the Consideration of the Free Surface*, Gothenburg 2010. A Workshop on CFD in Ship Hydrodynamics, Göteborg, 2010

[8] W. S. Vorus, V. R. Paulling (ed.): *Vibration*, The Principle of Naval Architecture Series, SNAME, Jersey City, 2010

---

[1] The displacement effect has a strong influence on the first harmonic whereas the blade lift effect also contributes to the higher harmonics significantly.

Violent seakeeping tests of a fast catamaran.

Benjamin Bouscasse, Claudio Lugni, Riccardo Broglia
CNR-INSEAN, Rome/Italy, b.bouscasse@insean.it

With the main goal of increasing the cruise speed of the ships, designers have proposed a wide variety of arrangements. In the most of them, the weight of the vessel can be supported by submerged hulls, hydrofoils, air cushion effects, or combinations of them. Two different geometries, the mono-hulls and catamarans are the commonly used. A mono-hull with the same displacement of a catamaran is characterized by a lower wave induced vertical acceleration since its larger length is beneficial from this point of view. The beam-to-draught ratio B/D of high-speed mono-hulls, typically around 5, can also exceed 7 in some cases; large B/D values limit the accelerations in heave and pitch motions, Faltinsen (2005). However the roll motions of mono-hulls need special attention and may matter for ship stability. Among multi-hull ships, Small Waterplane Area Twin Hull (SWATH) has higher heave and pitch natural periods and generally lower vertical excitation loads than a similarly sized catamaran. On the other hand, if control surfaces are not introduced, the SWATH is dynamically unstable in the vertical plane, beyond a threshold Froude number. When operating in head-sea conditions, its seakeeping behaviour is better than the one of a corresponding catamaran. However, if the sea state, speed and heading cause resonant vertical motions, the SWATH may not have a good seakeeping behaviour. Surface Effect Ships (SES) use an air cushion mechanism to obtain the desired cruise velocity and performances. The excess pressure in the air cushion between the two SES hulls lifts the vessel and carries about 80% of its weight. On the other hand, it reduces the metacentric height and causes wave generation and additional wave resistance. As a consequence, it can suffer more speed loss in waves than for instance a catamaran. Still, the total calm water resistance is smaller than the one of a catamaran of similar dimensions.

In the past, several researcher performed theoretical Doctors (2003), numerical and experimental Molland *et al.* (1995) studies of fast vessel in calm water condition, while few works for the dynamic behaviour Lugni *et al.* (2004) in waves exists, in particular for extreme sea conditions. In this case the role of the nonlinear effects becomes important, motivating the present research work. More in detail, after a descritption of the experimental set-up used, we report the results of a dedicated experimental investigation of the global motion in waves of a catamaran at high speed vessel. This work is part of a cooperative project bwtween IIHR (University of Iowa) and CNR-INSEAN for the study of the performances of a fast catamaran in calm water and in waves as well as for the construction of a certified database for CFD validation.

Experimental Set-up A dedicated and comprehensive experimental investigation has been performed to analyze the unsteady behaviour of a semi-displacement catamaran in waves. A geosym model of the DELFT-372 has been built in fiberglass at the INSEAN workshop (INSEAN model 2554); the main geometric and hydrostatic properties are given in the table 1. The experimental activity has been carried out at the INSEAN basin No. 2: 220 m long, 9 m large and 3.6 m deep. The model is towed through a kinematic system suitably designed for the seakeeping test of catamarans. It is composed of a twin-gimble (one for each demihull) rigidly connected with a transversal beam, ensuring free pitch motion around the CG axis, and a vertical beam sliding in a linear bearing in order to keep free the heave motion. Surge, sway, roll and yaw, are completely restrained. To increase the rigidity of the catamaran model, the two demihulls are furtherly connected with two transversal aluminium beams ahead and behind the center of gravity and with a third aluminium beam at the fore perpendicular (see figure **??**).

This configuration ensures a sufficient rigidity of the catamaran without using the deck in the

Length between perpendicular	L_{pp}	3·00 m
Beam Overall	B	0·94 m
Beam demihull	b	0·24 m
Distance between centre of hulls	H	0·70 m
Draught	D	0·15 m
Displacement	Δ	87·07 kg
Vertical centre of gravity	KG	0·34 m
Longitudinal centre of gravity	LCG	1·41 m
Pitch radius of gyration	k_{yy}	0·782 m

Table 1: Main dimensions and hydrostatic properties of the INSEAN model 2554

fore part of the model. As a consequence no deck-slamming phenomena can occur during the tests.

Krypton optical system, consisting of 3 CCD cameras that detect the position of a reference system fixed to the body (identified through three infrared LEDs) is used to measure the motions of the model. This instrument ensures a high spatial resolution, less than 1 mm for the linear displacements and less than 0.05 deg for the angular degrees of freedom. The incident waves are measured using two different transducers fixed to the carriage: a finger (Kenek) and a Keyence ultrasound wave probe. The Kenek is a non-intrusive instrumentation with an accuracy of 0.1 mm and a maximum range of measurement of 150 mm. Because of the dynamic limitations of the mechanical part, for the larger values of the wave steepness and for the highest Fr, the finger probe is unable to measure in accurate way. In this case, the ultrasound probe still gives a reliable measurement. The wave elevation recorded 3m ahead the model is the measure of the undisturbed incident wave. A second wave measurement, given by an identical set of two probes approximately 3m aside the hull and at the LCG position, provides the wave elevation partially affected, only for the lower Fr, by the hull. For a direct measurement of the total resistance in waves, two HYDRONICS load cells (maximum range of 100 lb and accuracy around 0.1% of the maximum load) are placed between the gimble and the ship model, one for each gimble. The added resistance in the ship reference frame results from the subtraction of the calm water resistance to the mean value of the total resistance in waves. Finally, an acquisition system with sample rate of 300Hz records all the physical quantities.

Discussion of the results The present study aims to the construction of a certified experimental database for the physical understanding of the seakeeping performances of a fast catamaran and to the validation of CFD codes. To this purpose, the following strategy has been adopted:

a- taking advantage of its high accuracy and efficiency, a linear transient test technique (Clauss (2008), Lugni *et al.* (2004)) is used to determine the response amplitude operator (RAO) of the catamaran, as well as the Froude of maximum response, i.e. the Froude number for which the maximum value of the vertical motion RAO is measured. Fr numbers in the range [0.6,0.8] (with step 0.05) have been investigated;

b- once the Froude of maximum response has been identified, an ad-hoc experimental campaign in regular wave is carried out at this Fr, varying the wavelength and the steepness of the incident wave train. In particular, using the RAO determined in a-,7 different steepnesses (from $H/\lambda = 1/100$ up to 1/15) and 6 different wavelengths of the incident wave system have been explored to investigate the role of the nonlinearities in the ship motions. Because of the excessive severity of the input conditions, some runs in regular waves have been omitted to preserve the integrity of model;

c- an experimental campaign in mild sea state has been finally performed.

Because the study looks at the building of a certified experimental database, a proper uncertainty analysis, limited to the repeatability error, has been performed. In the specific, all the Fr scheduled in a- have been repeated 10 times, while, for the regular wave tests planned in b-, two conditions (two wavelengths and 1 steepness) have been identified for the repeatability analysis. The latter, is an ongoing activity and the results will be presented at the conference.

Before discussing the physical meaning of the measured results, figure 1 shows the comparison between the heave and pitch experimental RAOs measured at INSEAN (both with transient test and in regular wave) and the equivalent results measured at the Delft Univ. Veer (1998) at $Fr = 0.75$. Because the aim of this comparison is the verification of the experimental set-up, exactly the same regular wave system used in Veer (1998) have been reproduced at INSEAN. The transient test results are plotted along with the standard deviation, calculated on the repeated runs. Generally a satisfactory agreement is observed between INSEAN and Delft data, confirming the reliability of the experimental set-up used.

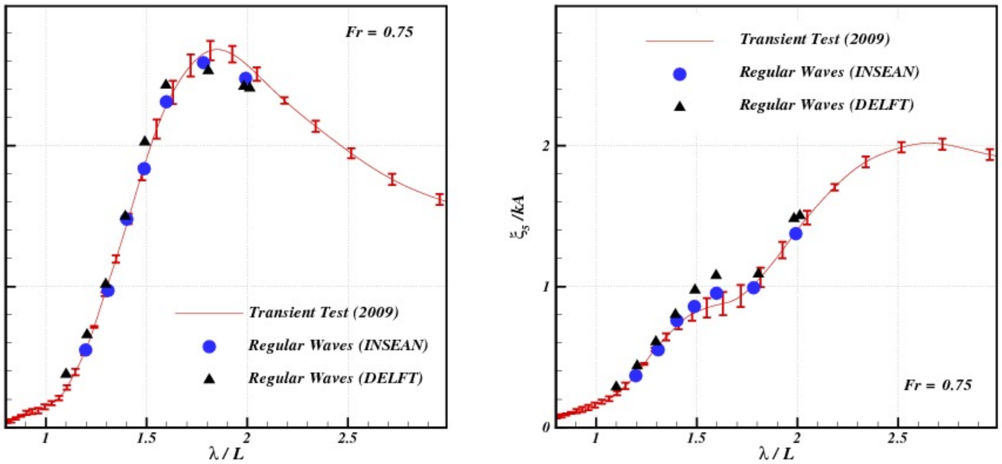

Figure 1: Heave (left) and Pitch (right) Response Amplitude Operator of the catamaran INSEAN-2554 at $Fn = 0.75$.

Linear Transient tests Figure 2 shows the RAO (both magnitude and phase) of the catamaran varying the Fr number within the interval $0.6 - 0.8$. A Froude number, for which the heave response is maximum, is singled out, i.e. $Fr = 0.7$. The same is not possible for the pitch motion as a continuous increasing trend is observed.

Regular wave tests The knowledge of the RAO allows also the identification of the resonance area, around which larger effects of the nonlinearities are expected. Then 6 different wavelengths, i.e. three of them around the resonance, two for lower wavelength and the one for higher wavelength, are chosen. Figure 3 shows the role of the nonlinearities on the heave and pitch RAOs, for 7 several steepness, varying from the linear case ($H/\lambda = 1/100$) up to an extremely severe wave train ($H/\lambda = 1/15$). As expected, relatively to the heave motion, the nonlinear contribute due to the viscous and potential hydrodynamic damping, strongly reduces the response of the ship, specifically in the resonance area, where the motions are the largest. In contrast, in the region far away from the resonance region, the effect of the nonlinearities is

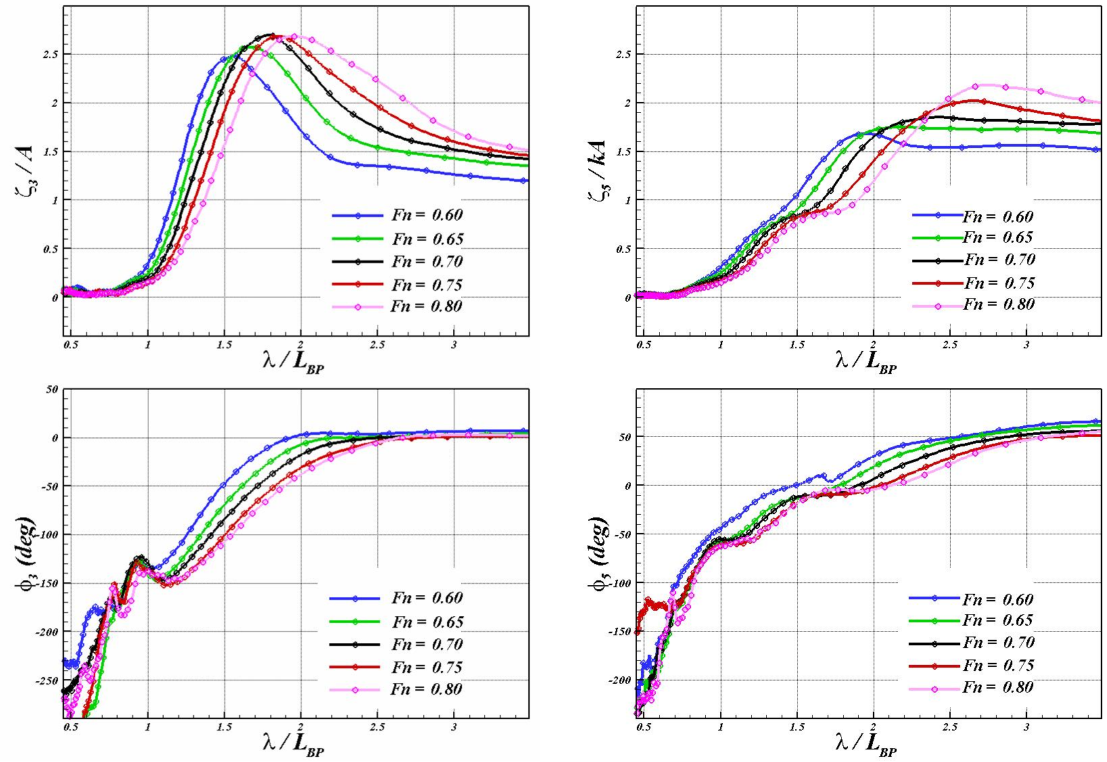

Figure 2: Heave (left) and Pitch (right) Response Amplitude Operator varying the Froude number. Both magnitude (top) and phase (bottom) functions are reported.

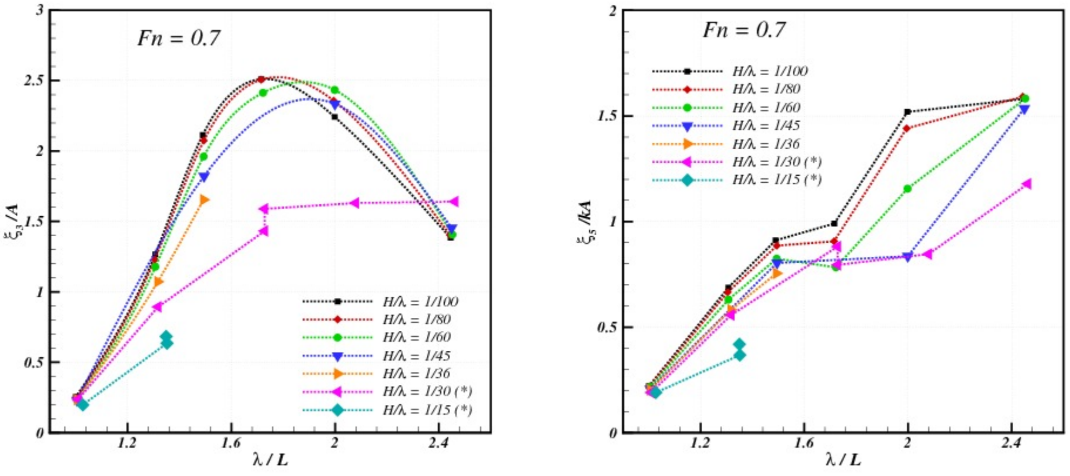

Figure 3: Heave and Pitch Response Amplitude Operator

less evident, and the measurement recover the linear trend. Similarly, pitch motion confirms the growth of the nonlinear damping with the steepness in the resonance area. But in this case, the resonance region occurs at larger wavelength and the data available does not allow the recovering of the linear trend. The experimental investigation in regular wave allows the measurement of the added resistance as function of the wavelength and for the several steepness investigated. In particular, the right panel of figure 4 shows the added resistance operator. From the theoretical point of view, it is well known that the added resistance is a second order loads (Faltinsen

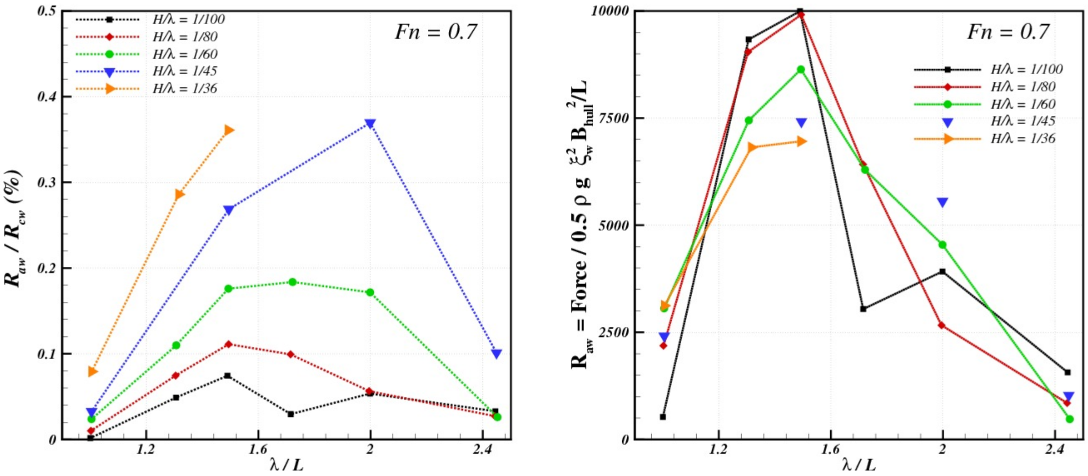

Figure 4: $Fr = 0.7$. Left panel: added resistance value as percentage of the calm water resistance; right panel: added resistance operator.

(1990)). As a consequence, an almost unchanged operator is expected by varying the steepness of the wave. In contrast, right panel of figure 4 seems to contradict the expectation, at least for stepness larger than 1/80. A possible cause can be identified in the higher order nonlinear effects, that matter when the steepness increases. Still, further investigations are needed, for example investigating the influence of the repeatability error. To give an estimation of the influence of the increasing steepness on the added resistance value, left panel of figure 4 shows the percentage variation of the resistance in waves, with respect to the resistance in calm water. A maximum value around 40% of the corresponding value in still water condition is reached for wavelength included between 1.5 and 2 times the ship length.

Irregular wave tests To state the effects of nonlinearities in operative conditions, the RAO for irregular waves is calculated. Assuming that the length of the real ship is $L = 60m$, that is a scale factor of $/lambda = 20$, $Fn = 0.7$ represents a speed of 33 kn. The model is tested at this speed for sea state 2 and 3 (Pierson Moskovitz spectrum). In figure 5, the orange and blue lines shows that the motion of the "real" ship are still in a linear range.

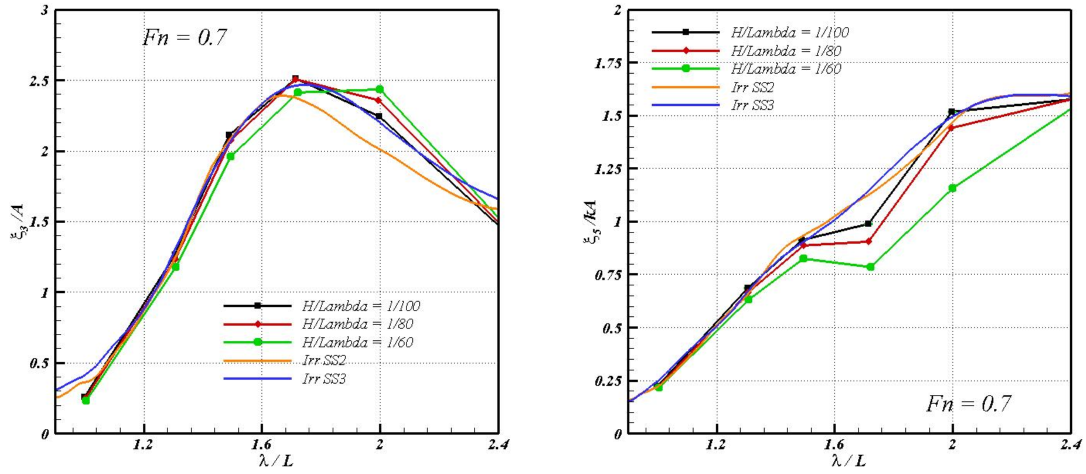

Figure 5: $Fr = 0.7$. Heave and Pitch Response Amplitude Operator

CONCLUSIONS A comprehensive experimental campaign to study the seakeeping performances of a catamaran has been performed at INSEAN. Preliminarly transient tests at several speeds have been carried out to identify the Froude number for which the maximum response occurs. Then, regular wave tests at the identified Fr have been realized varying the wavelength and the steepness of the incident wave train. The last experiments allow the investigation of the role of the nolinearities in the vertical ship motion of the catamaran, confirming a strong influence of the nonlinear damping in the resonance region. All the tests have been certified through repeatability analysis. The results, still under investigation, will be discussed at the symposium.

ACKNOWLEDGEMENTS The work has been done in the framework of the NICOP project *"Complementary EFD and CFD Analysis of Calm Water Hydrodynamics and Large Amplitude Motion for High-Speed Catamarans"* financially supported by the U.S. Office of Naval research, through Dr. L. Patrick Purtell (Grant N00014-08-1-1037).

References

Clauss, G. The Taming of the Shrew: Tailoring Freak Wave Sequences for Seakeeping Tests. J. of Ship Research 52(3), 2008.

Doctors, L. Hydrodynamics of the flow behind a transom stern. Proceedings of 29th Israel Conference on Mechanical Engineering, pp. 1–11. Haifa, Israel, 2003.

Faltinsen, O. M. Sea loads on ships and offshore structures. Cambridge, England: Cambridge University Press, 1990.

Faltinsen, O. M. Hydrodynamics of High Speed Marine Vehicles. Cambridge, 2005.

Lugni, C., A. Colagrossi, M.Landrini, and O. Faltinsen. Experimental and Numerical Study of Semi-displacement Mono-hull and Catamaran in calm water and incident waves. 25th Symposium on Naval Hydrodynamics. Canada, 2004.

Molland, A., J. Wellicome, and P. Couser. Resistance experiments on a systematic sense of high speed displcement hull forms: Variation of length-displacement ratio and breadth-draught ratio. The Royal Institution of Naval Architects, 1995.

Veer, R. V. Experimental results of motions and structural loads on the 372 catamaran model in head and oblique waves. Technical Report 1130, TU Delft Report, 1998.

CFD Guided Improvement of a Cavitation-Prone Rudder

Andreas Brehm, Volker Bertram, Ould El Moctar,
FutureShip, Hamburg/Germany, andreas.brehm@GL-group.com

As a response to increasingly observed rudder damages on large container vessels, Germanischer Lloyd (GL) initiated a research project, together with SVA Potsdam, focussed on the hydrodynamics of semi-balanced rudders. The main findings of this research project are presented here. See Brehm et al. (2011) for more details. The project's aims were to investigate the hydrodynamics and structural loads on a large semi-balanced rudder, and investigate the cavitation risks and how moderate modifications may reduce cavitation occurrence. The test case was a typical 8.500 TEU container vessel, *Brehm et al. (2011)*. Initial studies investigated the influence of boundary conditions and computational control parameters on results for our test case and our RANSE method. We used the commercial RANSE solver Comet for our work.

Steady RANSE simulations for the propeller in uniform flow compared reasonably well to model tests, Fig. 1. Lift and drag for the rudder in uniform flow (for angles 0° and 35° in steps of 5°) were compared to model tests of SVA Potsdam and HSVA (Hamburg Ship Model Basin) and CFD results of SVA Potsdam (CFX), Figs. 2 and 3. The measured values differ between the two basins despite using the same model. The RANSE results lie mostly between the two measurements. Fig. 2 shows results from steady and unsteady RANSE simulations. Fig. 3 shows the transient RANSE results for the lift on the rudder blade alone and on rudder blade and rudder horn. The forces on the rudder horn cannot be measured in model tests. Therefore all other figures compare only the forces on the rudder blade.

We discuss here only the measurement of the velocity field behind hull-propeller and rudder in greater detail. SVA Potsdam employed particle image velocimetry (PIV). For the model test campaign, the PIV system was enhanced by a stereoscopic camera allowing measurements of all three velocity components in one plane. The velocity field was measured near the rudder while the ship model was towed with freely rotating propeller at drift angles of 0° and 10° and various rudder angles. There were two measurement campaigns. Initially, four cross-section planes were investigated, Fig. 4. In a second campaign, a total of 28 planes were investigated. Figs. 5 and 6 compare exemplarily RANSE simulations and PIV measurements for the measuring plane E1. The velocity component u (in longitudinal direction) was normalised with ship speed u_a. The agreement between simulations and model tests was generally good.

For full-scale simulations, the RANSE grid covered hull, rudder and propeller. The conditions were taken as recorded during the maiden voyage of the vessel. The model was detailed enough to include all attachments to the rudder, such as baffle plates and wedges. The torsion and bending stresses at ship's rudder stock and horn were recorded by stress-strain gauges. The hydrodynamic loads for the finite element analysis (FEA) were determined in RANSE simulations. The simulations neglected ship motions, cavitation, free-surface deformation and the change in propeller rpm. The rudder was kept fixed at a given rudder angle, varying between 0° and 35° in 5° steps. The periodical loads at steps of 10° propeller turn were mapped to the FEA model to compute the resulting stresses in the rudder at the positions of the stress-strain gauges. The computed stresses agreed satisfactorily with the full-scale measured stresses, Fig. 7. Fig. 8 shows the time history of the rudder stock moment and the rudder angle during a 35°/35° zig-zag sea trial. The rudder was moved with the same rate of turn as observed in the sea trial. The time histories of the rudder stock moment are similar between sea trial and simulation, as long as the ship has not started to turn. Then the moment histories start to diverge. The most important factor for this divergence should lie in the neglected ship motions. Further detailed studies to quantify the effects of the assorted simplifications are planned for late 2011.

Another goal of the project was the design of a rudder with significantly lower cavitation. A constraint for the new design was that only small modifications of the original rudder design were permitted, excluding specifically a change of rudder type (full-spade instead of semi-spade rudder), twisted rudder, a shift of the horizontal gap between horn and blade, a change of the rudder area or shift of the rudder stock. The remaining design freedom was limited to changes in the profile shape and addition of small appendages. The design was guided by 2D and 3D RANSE simulations. In a first step, the original rudder was cut in three horizontals planes, Fig. 9. The original full profile section in the cut A-A was improved using the potential flow code XFOIL, http://web.mit.edu/drela/Public/web/xfoil/. The section was compared with assorted NACA profiles and hybrid profile shapes. Then we designed our own profile shape aiming at a small low-pressure peak and a rather balanced pressure distribution over the chord of the profile, Fig. 10, while not making lift and drag coefficients worse. The partition between horn and rudder for cuts B-B and C-C leads to flow phenomena that cannot be captured by XFOIL. Therefore, 2D RANSE simulations had to be employed for these cuts. 28 gap variants were investigated. Rudder angles were varied between ±8° and angles of attack between 6° and 28° in steps of 2°. In total, more than 3000 RANSE simulations were performed. Based on the best 2D profile sections, a 3D model (including hull and propeller) was investigated. The RANSE simulations included hull and propeller in the model. Only such comprehensive models can capture appropriately the 3D flow effects, which are vital for the correct assessment of forces and moments at the rudder. Details of the rudder sole have a significant impact on the rudder forces. The first design (variant A) had a significantly curved forward part. This reduced the cavitation on the rudder blade noticeably. The low pressure gradient with smooth transition between pressure and suction side unfortunately also leads to lower lift forces on the profile and made variant A therefore not acceptable. Two further variants of the rudder sole were investigated: Variant B had a curved forward part with much smaller radius, variant C was fitted with an end plate instead of rounding the forward part.

Rudder sole cavitation is induced by low-pressure regions stemming from the fluid's attempt to balance the pressure difference between suction and pressure side by flowing rapidly from one side to the other over the sole. The broad end plate in variant C forces the major part of the flow around the leading edge which was designed to be particularly smooth to reduce cavitation. The end plate also moderates the pressure regions from the rudder surface to the outer edges of the plate on both sides. The pressure difference is then balanced at the edges with lower risk of cavitation, Fig. 11. Figs. 12 and 13 show the computed cavitation extent for rudder angle 5° and 10° for original rudder and our new design. The cavitation extent is significantly lower at blade and vertical gaps in our new design. Cavitation is not completely avoidable, due to the high velocities involved. For our new design, significant cavitation appears for rudder angles above 8°. However, most of the time, rudder angles do not exceed 5° in real ship operations. For the new design, one constraint was that the lift forces should not be lower than in the original design. This condition was met. The new design was also better in terms of rudder stock moments, with maximum stock moment determines the size of the rudder engine; this improvement has significant impact in practice.

BREHM, A.; BERTRAM, V.; EL MOCTAR, O.M. (2011), *Loads acting on a semi-spade rudder*, 2nd Int. Symp. Marine Propulsors (smp), Hamburg

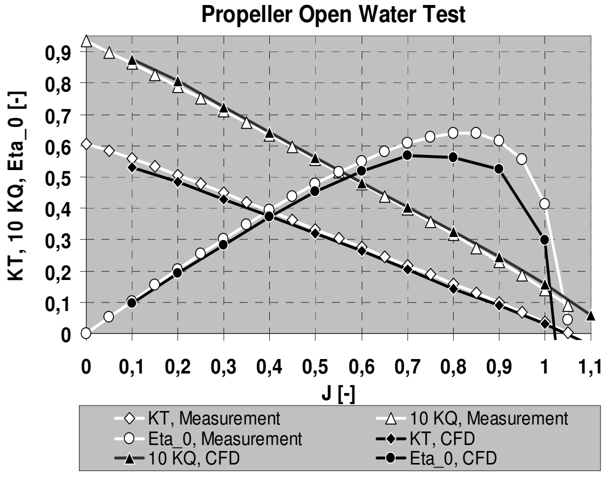

Fig. 1: Calculated and measured open-water Diagram

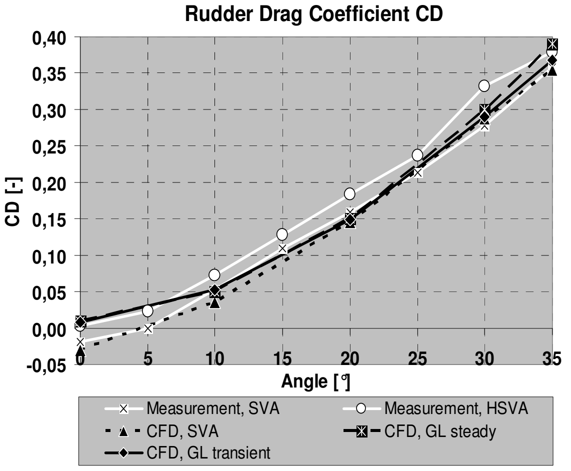

Fig. 2: Calculated and measured rudder drag

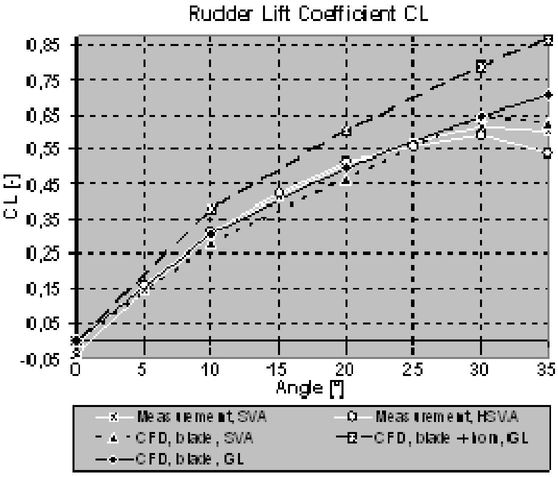

Fig. 3: Calculated and measured rudder lift

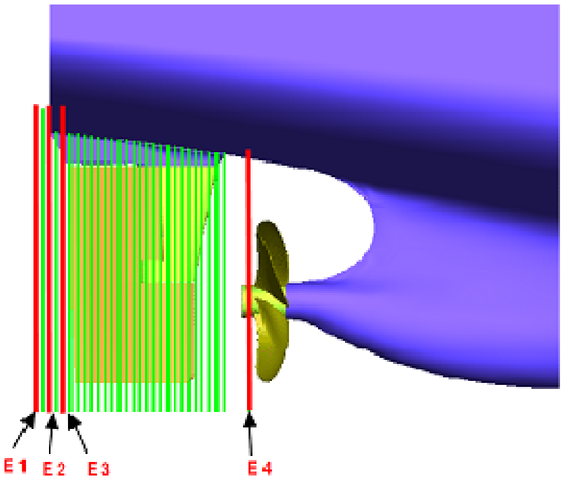

Fig. 4: Locations of cross-sectional planes

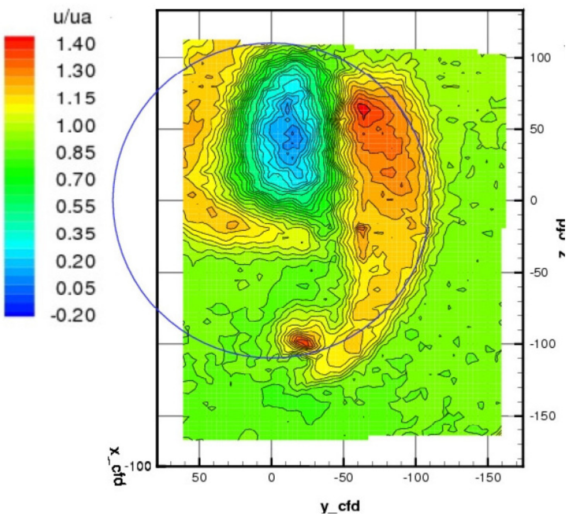

Fig. 5: Measured velocities in ship's longitudinal direction in plane E1; rudder angle= +20°

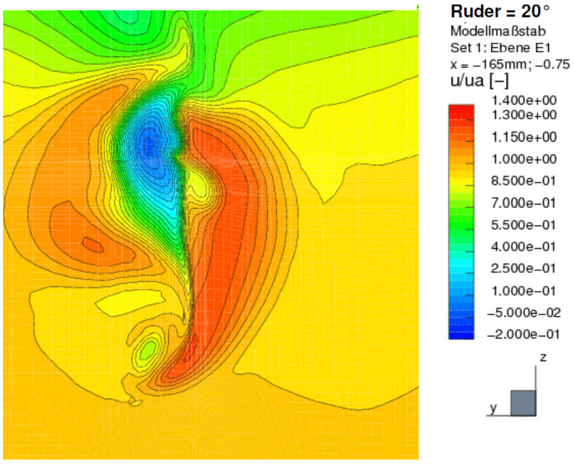

Fig. 6: As Figure 5, but computed

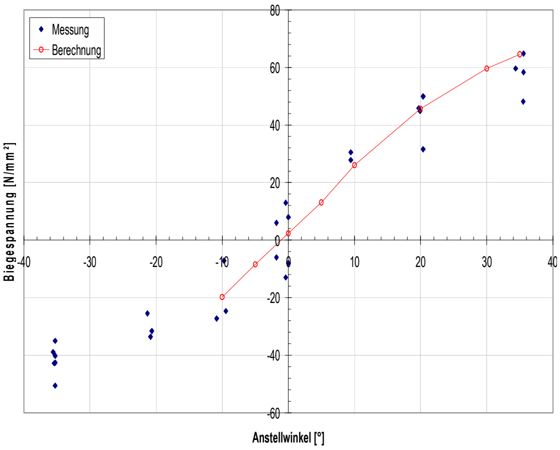

Fig. 7: Computed (red line) and measured (blue dots) max. bending stress of rudder stock

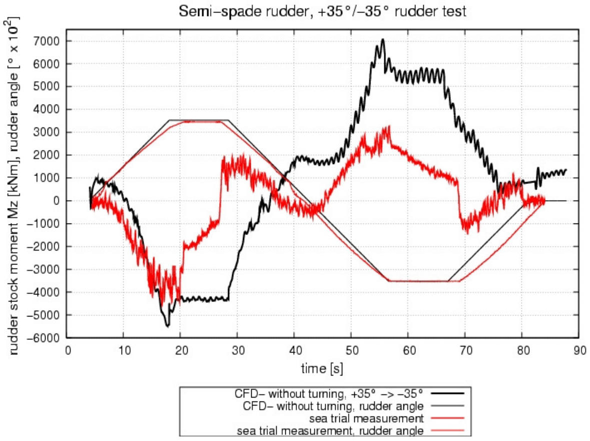

Fig. 8: Full-scale measured (red) and computed (black) rudder stock moments

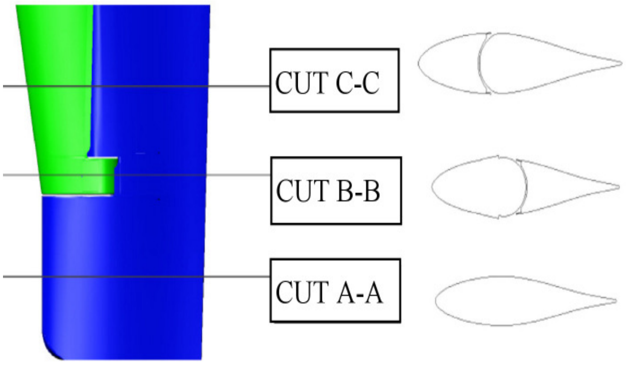

Fig.9: 2D- investigated horizontal cuts

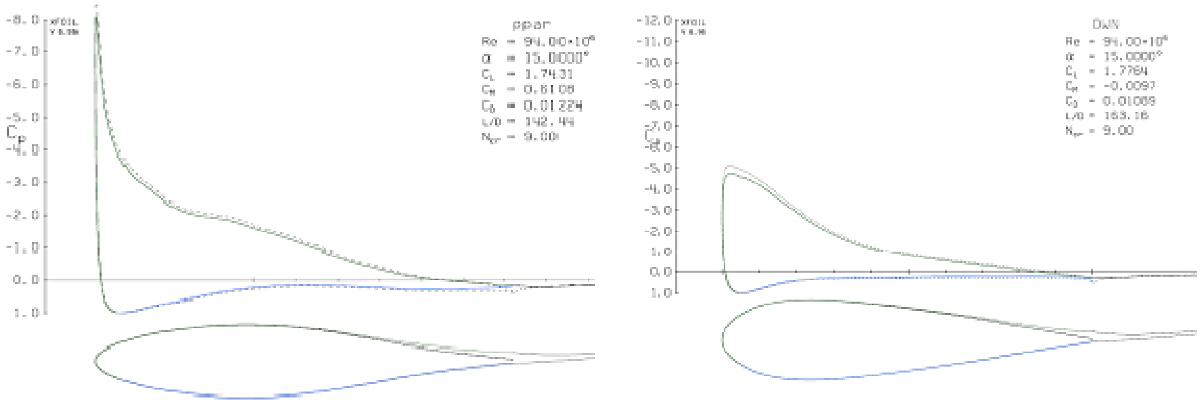

Fig. 10: 2d results with XFOIL: Pressure distribution over original profile (left) and modified profile (right)

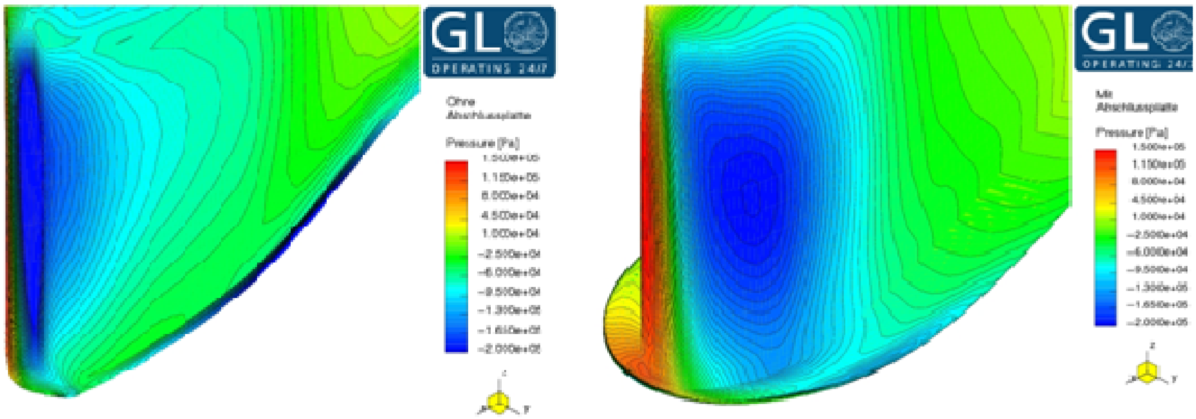

Fig. 11: Pressure distribution around rudder sole; original rudder (left) and new design (right)

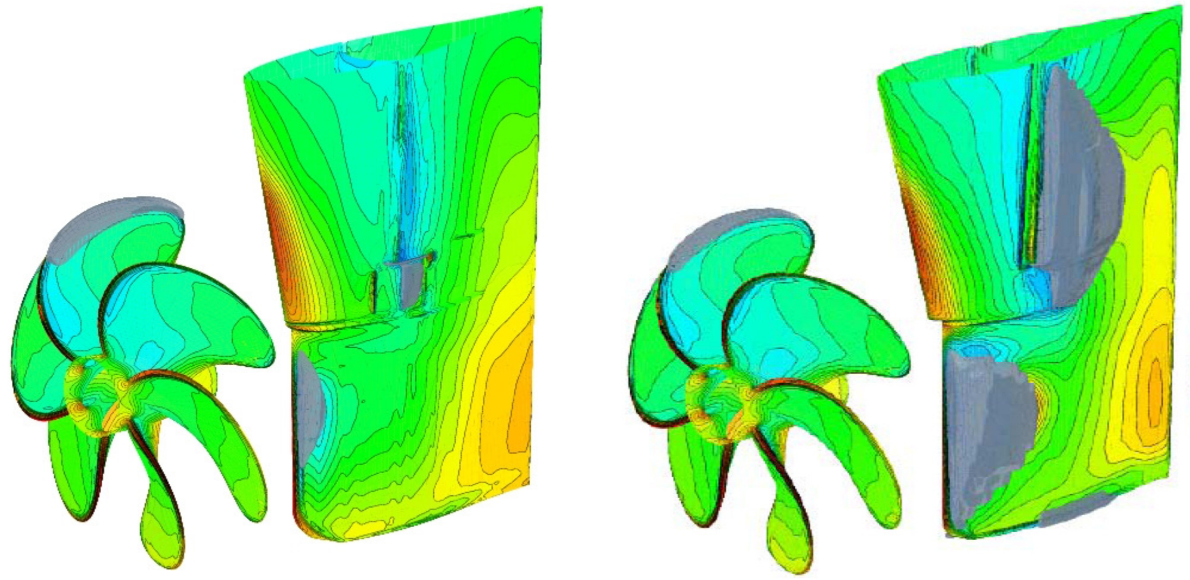

Fig. 12: Pressure and cavitation (gray: iso-surface of a VoF cav-concentration of 0.01) distribution for original rudder design at 5° (left) and 10° (right) rudder angle

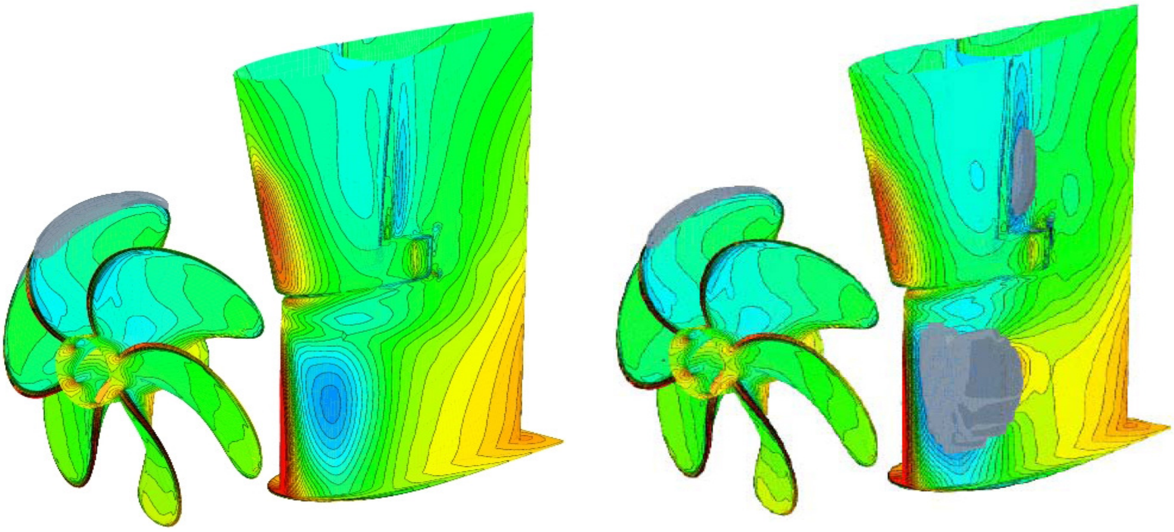

Fig. 13: As Fig. 12, but for new design with end plate

Description of a 3D vortical flow by a Lattice Boltzmann method

Giuseppina Colicchio[1], **Sara Modini**[1], **Claudio Lugni**[1],**Giorgio Graziani**[2]
[1]CNR-INSEAN, Italy g.colicchio@insean.it, s.modini@insean.it, c.lugni@insean.it
[2]Dept. of Mechanical and Aerospace Engineering, University of Roma ”La Sapienza”, Italy
g.graziani@uniroma1.it

Introduction

The Lattice Boltzmann Method (LBM) has been introduced about 20 years ago (see [1] and [2]), but only the recent development of a multiple-relaxation-time (MRT) collision model [3] has allowed its application to a wide range of Reynolds numbers. The comparison of its results with those obtained with a DNS incompressible-flow spectral element solver has also shown that it can correctly capture the details of the fluid turbulence [4], preserving its basic features of simplicity, flexibility and intrinsic parallelism.

For these last features and for its enhanced suitability to deal with viscous flows, the LBM starts to be appealing to deal with high vorticity generated in water and its interaction with the both the solid and deformable boundaries as the air-water interface. For moving vehicles, e.g. submarines and airplanes, vorticity generation and its interaction with the downstream body part can cause boundary layer separation and transition to turbulence with a dramatic effect on the unsteady forces [5].

Here, we present the application of the MRT Lattice Boltzman model to a variety of fluid-body interaction dealing with vorticity generation and dissipation. The vorticity is either generated in 2D or 3D lid driven cavity. The computed flow features are widely compared with data available in literature. In particular, the velocity, vorticity and pressure evolution are analyzed versus the same quantities obtained with Navier-Stokes solutions or in the experiments. The results show convergence and accuracy of the LBM solver. Finally, the 3D problem of a vortex ring impacting on a flat wall is analyzed. The effects of the interaction with the solid boundary are highlighted: dissipation at low Reynolds (Re) numbers, instabilities at high Re.

The model

The model used in the following is derived by d'Humires *et al.* [3]. It is a classical Lattice Boltzmann model, represented on a cubic lattice. Differently from the classical lattice Bhatnagar-Gross-Krook (BGK) equation [6], the single relaxation time is substituted with a collision matrix $\mathbf{S}$, whose eigenvalues are chosen so that the relaxation times of the non-conserved quantities are faster than the hydrodynamic time scale. Practically, this has allowed a larger stability of this scheme with respect to the classical BGK models. For more details refer to [3].

In the following, two kinds of boundary conditions shall be used: no-slip boundaries and constant pressure. The former is represented with the classical bounce back technique; for the latter, the moments are set equal to the equilibrium quantities.

Validation of the code, convergence studies and comparison with other results

The validation of the code has been carried out using classical test cases dealing with vorticity and its interaction with solid boundaries.

The first test case is quite commonly used. It is a 2D lid driven flow in a square cavity. A Reynolds number equal to 1000 has been chosen to analyze the steady state conditions. The 3D model has been adapted to describe a 2D problem by imposing periodic boundary conditions in the third direction, in particular three meshes with sizes, 60x60, 120x120 and 240x240, have

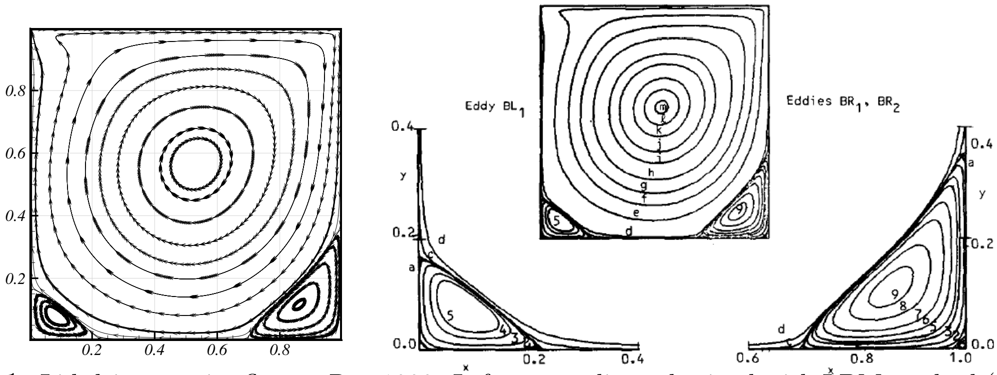

Figure 1: Lid-driven cavity flow at Re=1000. Left: streamlines obtained with LBM method (240x240x5 mesh); right: comparison streamlines by [7].

been used for the following results (in the third direction periodic boundary conditions are applied). The mass conservation has been the first check performed in this case with a closed domain. Whatever the mesh discretization, the mass conservation is perfect; the error is of the order of the machine error, as expected from the used equations, where mass is explicitely preserved.

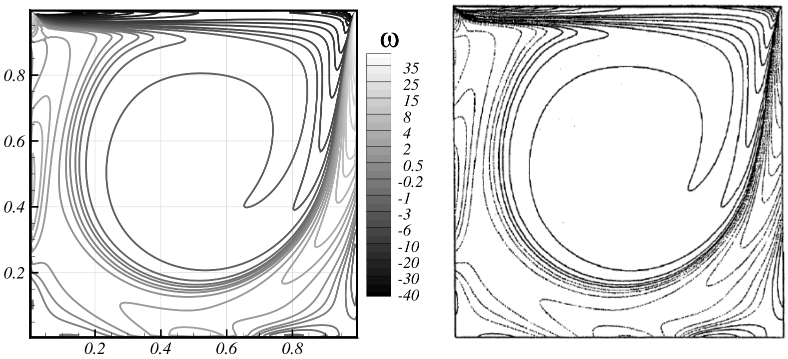

Figure 2: Same case as in Fig. 1. Left: iso-vorticity lines from LBM (240x240 mesh); right: comparison iso-line by [8].

Figure 1 shows the vorticity generated in the cavity along with the main vortex and the two secondary ones as well as the comparison with the classical results by Ghia *et al.* [7]. The shape of the streamlines and the position of the secondary vortices are correctly captured by the present LBM.

The comparison in Figure 2 is more significant, the vorticity iso-contours are compared with those calculated in Bruneau *et al.* [8]. Those results are obtained on a much finer mesh (1024x1024) with respect to the 240x240 used in the LBM solution, nonetheless the details of the developed vorticity are well captured.

The convergence of the numerical algorithm has been tested both for pressure and velocity along the mid-horizontal and vertical sections (Fig. 3). Two kinds of convergence studies have been carried out: the first is obtained simply by using LBM results and the order of convergence has been calculated as

$$O_{num}(q) = \log_\alpha \left(\frac{abs(\int_0^1 q(\Delta x_2)dx_i - \int_0^1 q(\Delta x_1)dx_i)}{abs(\int_0^1 q(\Delta x_3)dx_i - \int_0^1 q(\Delta x_2)dx_i)} \right), \tag{1}$$

where Δx_i, for $i = 1..3$, are the discretization from the coarsest to the finest, α is the ratio among the three discretizationes, q is either the pressure or the velocity component, dx_i is the direction along which the integration is performed.

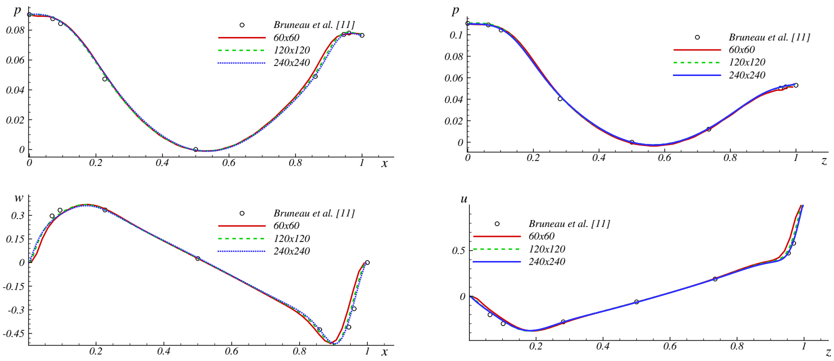

Figure 3: Same case as in Fig. 1. Left: Pressure and vertical velocity in the horizontal midsection; right: pressure and horizontal velocity in the vertical midsection.

The second technique uses the results in [8] as reference data, *i.e.*

$$O_{ref}(q) = \log_\alpha \left(\frac{abs(\sum_{k=1}^{n_{samples}} q_k(\Delta x_2) - \sum_{k=1}^{n_{samples}} q_k(ref))}{abs(\sum_{k=1}^{n_{samples}} q_k(\Delta x_3) - \sum_{k=1}^{n_{samples}} q_k(ref))} \right), \qquad (2)$$

with $q(ref)$ the reference value. The obtained convergence rates are shown in the table below.

	O_{num}	O_{ref}
p along x	1.2	0.98
w along x	1.95	1.83
p along y	1.23	1
u along y	1.72	1.65

The lowest convergence rates, around 1, are for the pressure. Actually, the pressure is defined but for a constant and the constant value affects the convergence rate. To make the data comparable with the experiments, a zero value has been chosen at the center of the domain ($x = 0.5, z = 0.5$). Higher order of convergence can be found choosing a different point for the reference pressure.

The other variables u and w, that are not affected by this problem, show a convergence rate close to 2, that is what we would have expected. In each case the O_{ref} is always lower than the O_{num}; the former being obtained as the sum of nine discrete values (according to those provided in [8]), mostly localized close to the boundaries where the uniform LBM mesh can suffer lack of accuracy.

To make a proper use of the 3D code, the same lid-driven problem has been studied in 3D. The longitudinal section of the cavity BxD is always a square and the cavity is long $L = 2B$. The experiments by [9] have shown how 3D effects develop in the lid driven cavity even at low Reynolds number as $Re = \frac{U_{bc}B}{\nu} = 1000$. Here, as in the experiments, the flow is started instantaneously and the vorticity evolution is followed.

Because of the no-slip condition at the extreme section two longitudinal streams develop from the side faces and move the fluid towards the mid section. This is highlighted in Figure 4, where the comparison between experimental and numerical smoke-lines is shown. The smoke lines are

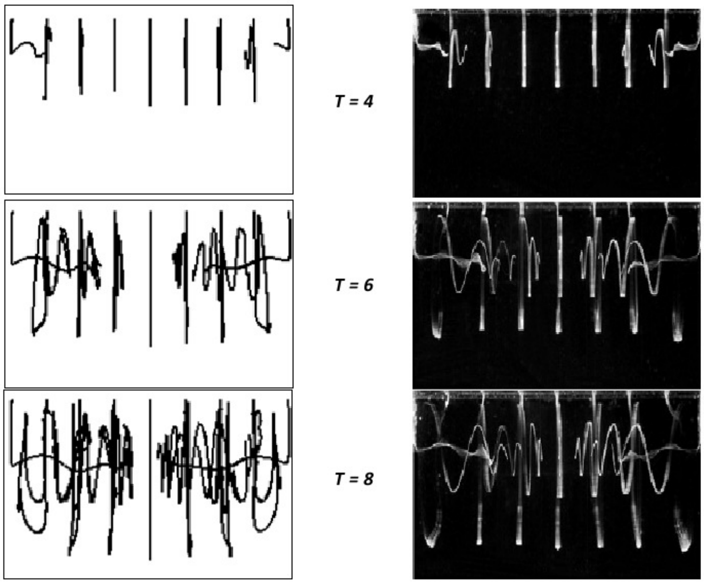

Figure 4: Evolution of smoke lines inside the square cavity (left: numerical results, right: experiments by [9]).

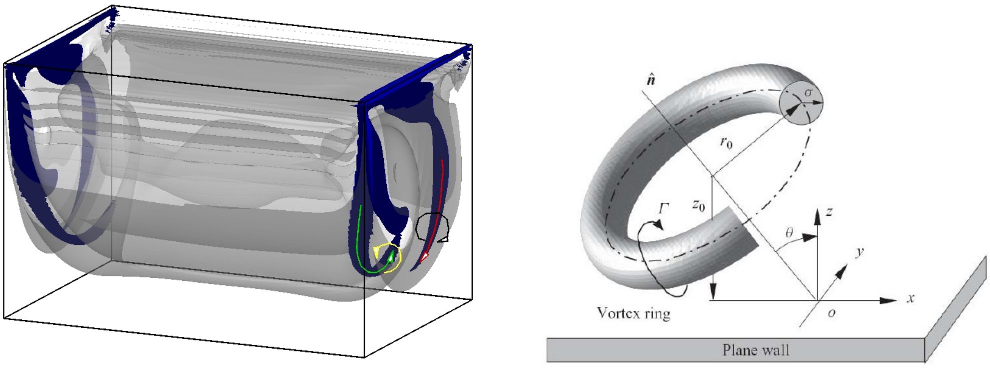

Figure 5: Left: iso-surface of vorticity, $T = 11$. The grey iso-surface corresponds to $\omega = 2.28$, the blue ones the iso surface at $\omega - \omega_{mid-section} = 1.42$. Right: Vortex ring: sketch of the problem.

generated by the injection of dye by nine orifices uniformly spread along the cavity. The times in Figure 4 are $T = \frac{tU_{bc}}{B} = 4, 6, 8$. Since $T = 4$, the flow three dimensionalities have already developed. As time goes on, they become more intense and create a kind of conical shape along the longitudinal direction. The only smoke-line that does not present any three-dimensionality is the central one. The good agreement between the two data set testifies the accuracy of the LBM method not only in space but also in time.

The centrifugal forces interaction with the end plates causes the generation of counter rotating vortices, commonly named TGL (Taylor-Gortler-like) vortices. Their presence has been guessed experimentally trying to reconstruct the 3D from the horizontal planes obtained using a thin laser sheet to illuminate the tiny particles dispersed in the fluid. The numerical calculation is, instead, able to visualize properly this vorticity as shown in the right of Figure 5. In particular the side walls are characterized by a vorticity, counteracting the flow generated in the middle of the cavity by the lid motion. The red arrow in the plot shows the velocity of the flow close to the end walls with respect to the mid section. This flow is also characterized by a rotation around the red arrow, shown in black in the figure. The interaction of such rotational flow with the main one causes a counter-rotating vorticity (green line in the right panel of Figure 5) rolling around a faster rotating section (yellow arrow). The two excess-vorticity, with respect to the mid section, are shown in Figure 5 with a blue iso surface of $\omega - \omega_{mid-section} = 1.42$ where $\omega = \frac{\nabla \text{x} \boldsymbol{u} B}{U_{bc}}$.

Vortex ring against a flat wall

Once the LBM has proved its ability to model correctly both in time and space the interaction of the vorticity with solid boundaries, the numerical code has been applied to the case of an inclined vortex ring interacting with a flat wall as studied in [10]. A vortex ring of radius r_o, initial height z_o and circulation Γ impacts on flat wall with an angle θ from the vertical, see right panel of Figure 5. The initial velocity field is defined by $u_o = \frac{\Gamma}{2\pi\sigma}[1 - e^{-(\frac{\sigma}{\sigma_o})}]$, where σ is the radial distance from the center of the core and σ_o is the initial core radius $\sigma_o = 0.21 r_o$, the initial translation speed of the ring can be estimated as $u_s = \frac{\Gamma}{2\pi r_o}(\ln \frac{8 r_o}{\sigma_o} - \frac{1}{4})$ so that the Reynolds number is $Re = \frac{2 u_s r_o}{\nu}$.

Figure 6 shows the effect of Reynolds number (Re=100, 500, 1000) on the dynamics of the vortex ring. When the ring comes close to the flat surface, it creates a counter rotating vorticity along the wall (later named as wall vorticity) that starts to interact with the main one when the distance becomes very short. For small Re (left of Figure 6), the dissipation of both main and wall vorticity is the principal feature, the vortices are dissipated so quickly that they do not interact with each other. Increasing Re to 500 (center of Figure 6), the main ring interacts with the wall shear layer creating a secondary vortex that rolls around the main one, above all where it is more distant from the wall. Nonetheless the vorticity is well organized and only small instabilities appear along the annular direction. As the Reynolds number becomes higher (right of the same figure), the annular instabilities develop and wrap around the main vorticity in a complicated pattern.

Figure 7 shows the effect of the angle of impact on the evolution of the flow at intermediate Re. For a zero angle of attack, the vortex enlarges as soon as it interacts with the wall, until the wrapping of secondary vorticity and the azimuthal instabilities smooth this effect. As soon as the angle of attack increases, the local wrapping of the secondary vorticity quickly stops the expanding action of the flat wall. Meanwhile the annular instabilities develops even though it is less intense than in the flat case. At even larger angles, the three-dimensionality of the flow overcomes the azimuthal instability. The secondary vorticity wrapping around the main one causes a squeezing of the ring in the impact side and the growth of a helicoidal structure in the other direction.

Conclusions

The application of the LBM to problems of the vorticity development and interaction with solid walls have been analyzed, checked and validated against numerical and experimental results. The algorithm has shown good qualities in convergence and mass conservation besides a good agreement with reference data. The solver has proved its ability to follow the processes of vorticity dissipation and break down in smaller scale instabilities.

References

[1] Higuera, F. and Jimenez, J. “Boltzmann approach to lattice gas simulationsi,” in *Europhys. Lett.*, **9**, 663 (1989).

[2] Higuera, F. and Succi, S. and Benzi, R. “Lattice gas dynamics with enhanced collisions,” in *Europhys. Lett.*, **9**, 345 (1989).

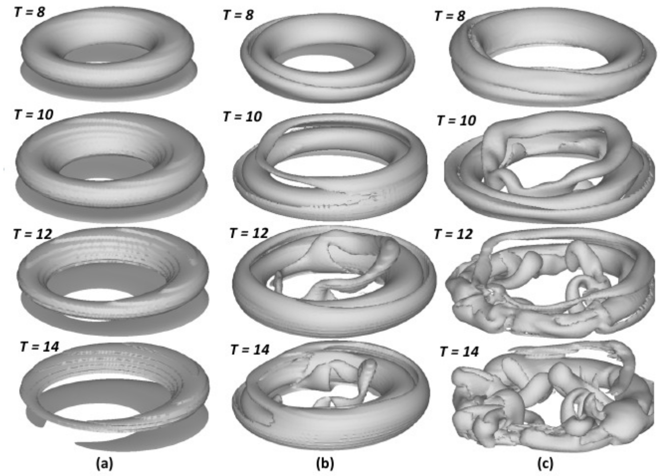

Figure 6: Iso-surfaces of vorticity for $\theta = 10^o$, at a) Re=100, b) Re=500, c) Re=1000.

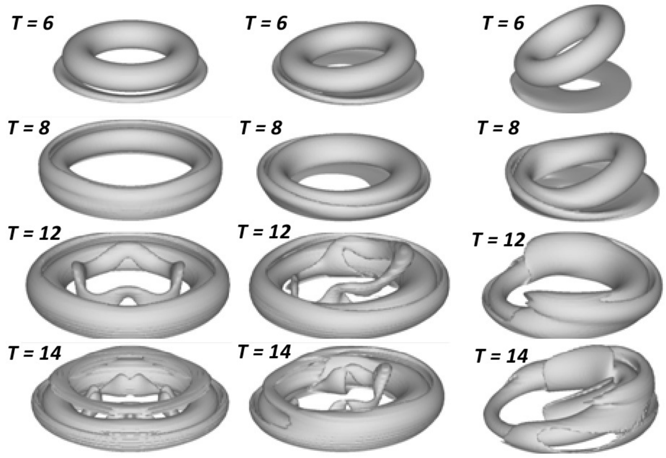

Figure 7: Iso-surfaces of vorticity for Re=500, at a) $\theta = 0^o$, b) $\theta = 10^o$, c) $\theta = 30^o$.

[3] d'Humières, D., Ginzburg, I., Krafczyk, M., Lallemand, P. and Luo, L.S., "Multiple-relaxation-time lattice Boltzmann models in three dimensions, " in *Phil. Trans. R. Soc. Lond. A*, **360**, 437-451 (2002).

[4] Chikatamarla, S.S., Frouzakis, C.E., Karlin, I.V., Tomboulides, A.G. and Boulouchos, K.B., " Lattice Boltzmann method for direct numerical simulation of turbulent flows, " in *J. Fluid Mech.*, **656**, 298-308 (2010).

[5] Doligalski, T.L., Smith, C.R., Walker, J.D.A., "Vortex interactions with walls", *Annual Review of Fluid Mechanics*, **26** (1), 573-616 (1994).

[6] Qiam, Y, d'Humières, D., Lallemand, P., " Lattice BGK models for Navier-Stokes equations, " in *Europhys. Lett.*, **17**, 479-484 (1992).

[7] Ghia, U., Ghia, K. N. C., Shin, T., "High-Re Solutions for Incompressible Flow Using the Navier-Stokes Equations and a Multigrid Method", in *J. of Comput. Physics*, **48**, 387-411 (1982).

[8] Bruneau, C.H., Saad, M., "The 2D Lid-Driven Cavity Problem Revisited ", in *Computers & Fluids*, **35**, 326-348 (2006).

[9] Migeon, C., Pineau, G., Texier A., "Three-dimensionality development inside standard parallelepipedic lid-driven cavities at Re=1000", in*J. of Fluids and Struct.*, **17**, 717-738 (2003).

[10] Cheng, M., Lou, J., Luo, L.S., "Numerical study of a vortex ring impacting a flat wall", in*J. of Fluid Mech.*, **660**, 430-455 (2010).

Influence of transition on hydrofoil fluctuating forces prediction

Pierre-Luc Delafin, François Deniset, Jacques-André Astolfi
IRENav, Ecole navale, Lanveoc, CC-600, 29240 Brest cedex9, France

pierre-luc.delafin@ecole-navale.fr

1 Introduction

Naval applications and current interest in marine energy extraction systems require increasing precision in computational fluid dynamics (CFD) so as to predict more accurately the performances of lifting bodies and then of the whole devices. These devices may be rudders, propellers or tidal stream turbines. For moderate Reynolds applications such as small scale tidal stream turbines or Autonomous Underwater Vehicles, managing an accurate simulation of the laminar to turbulent transition represents an important increase in this accuracy.

Transition simulation has been available in RANS computations for only a few years thanks to transition models based on empirical correlations. Many works focusing on foils in unsteady regimes dedicated to different domains like unsteady propulsion, renewable energies or biomimetism deal with influence of turbulence model and boundary layer behavior. The importance of stall phenomenon is often used to categorize the different regimes [1]. Laminar to turbulent transition has been recently considered in CFD RANS codes [2, 3]. The purpose of this study is then to evaluate the interest of a $\gamma - Re_\theta$ two equations model for moderate Reynolds number hydrofoil applications (Re = 7.5 10^5). The main goal is to show the importance of considering laminar to turbulent transition in predicting instantaneous hydrodynamic forces. The work focuses on the characteristics of the boundary layer, in particular, time and spatial progressions of the points of separation, transition, reattachment and relaminarization and stall events. The calculations accuracy improvement due to the consideration of transition effect is highlighted on the basis of validations with measurements.

After a brief description of the model and the numerical methods, results concerning a fixed foil at three different incidences and a quasi-static pitching hydrofoil will be discussed.

2 Model and numerical methods

2.1 Geometry and mesh

The Naca 66312 hydrofoil considered is mounted horizontally in the IRENav hydrodynamic tunnel. The 2D computational domain has the dimensions of the test section (Fig. 1). The test section is 1 m long and has a 0.192m square section. The O-4H grid is created and smoothed with ICEM CFD software. The foil is discretized by 742 nodes (Fig. 2) and the domain contains 160,000 quadrilateral elements. The mesh is voluntarily dense to capture accurately transition and detachment. Max y^+ is kept of the order of 1 during the simulations and the expansion ratios never exceed 1.2 in the region of the mesh close to the foil (and rarely in the outer region of the mesh). The solver requires a 3D mesh that we obtain by extruding the 2D one with one cell along the span direction.

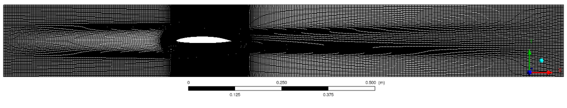

Figure 1: Mesh of the computational domain

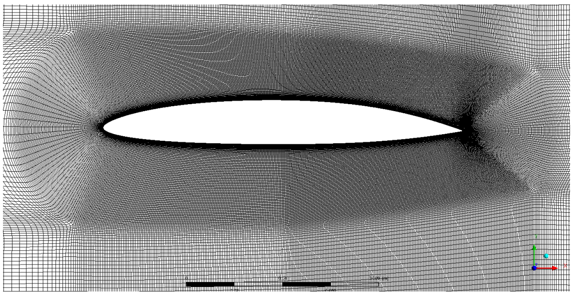

Figure 2: High-density mesh close to the hydrofoil

2.2 Model

The physical model is based on the mass and momentum conservation equations. The fluid is considered viscous and incompressible. The $k - \omega\ SST$ closure turbulence model used is known to predict better boundary layers submitted to adverse pressure gradients than other RANS turbulence models [4, 5]. The turbulence model is coupled with a two transport equations ($\gamma - Re_\theta$) transition model based on experimental correlations [6]. One equation is dedicated to intermittency (γ) which is used to turn on the production term of the turbulent kinetic energy downstream of the transition point.

$$\frac{\partial(\rho\gamma)}{\partial t}+\frac{\partial(\rho U_j\gamma)}{\partial x_j}=P_\gamma-E_\gamma+\frac{\partial}{\partial x_j}[(\mu+\frac{\mu_t}{\sigma_f})\frac{\partial\gamma}{\partial x_j}] \tag{1}$$

The second transport equation is for transition momentum thickness Reynolds number ($Re_{\theta t}$). This equation transforms non local empirical correlations into local quantities and allows the calculation of the transition length and the critical Reynolds number that are useful for the intermittency calculation.

$$\frac{\partial(\rho\overline{Re_{\theta t}})}{\partial t}+\frac{\partial(\rho U_j\overline{Re_{\theta t}})}{\partial x_j}=P_{\theta t}+\frac{\partial}{\partial x_j}[\sigma_{\theta t}(\mu+\mu_t)\frac{\partial\overline{Re_{\theta t}}}{\partial x_j}] \tag{2}$$

In the paper, calculations carried out with the fully turbulent $k-\omega\ SST$ model only will be referred as SST while those carried out with the $k-\omega\ SST$ model and the $\gamma-Re_\theta$ transition model will be referred as SST-TM.

2.3 Boundary conditions

Calculations are carried out in water (density $\rho = 997\ kg.m^{-3}$, kinematic viscosity $\nu = 0.89\ 10^{-6}\ m^2.s^{-1}$). The velocity inlet is set to $5\ m.s^{-1}$ so that the chord based Reynolds number equals 7.5 10^5 (c = 0.15 m). Inlet turbulence intensity is set to 2.95 % which is the experimental value. A *pressure outlet* condition with a 0 Pa static pressure is imposed on the outlet boundary. Lower and upper faces are set as *symmetry* since the hydrodynamic tunnel corresponding walls are slightly divergent to avoid a confinement effect due to the boundary layers development on these faces. Front and back faces are also set as *symmetry*. At last, a *wall* condition is imposed on the foil.

For pitching motion, the law defining the angular position of the foil is based on the characteristics of the electrical engine used in the corresponding experiments. The foil executes one pitching oscillation between $\alpha = 0$ and $\alpha = 15°$ around an axis located at the quarter of its chord. The angular variation is linear except in the acceleration and deceleration stages that each last 0.08 s. Mesh deformation is performed so that small cells (i.e. near foil cells) are not distorted.

2.4 Numerical method

The problem is solved by the finite volumes method [7], using the CFD RANS based code CFX [8]. The conservation equations are resolved in an arbitrary referential with the ALE (Arbitrary Lagrangian Eulerian) formulation [9, 10].

2.5 Experimental setup

The calculations presented in this paper are validated by experiments carried out in the IRENav hydrodynamic tunnel. The dimensions of the test section are $1m * 0.192m * 0.192m$. Velocity can vary from 3 to 15 $m.s^{-1}$ and pressure from 30 mbar to 3 bars. The 0.15 m chord NACA 66312 hydrofoil is mounted horizontally, halfway up the test section and its pitch variation is controlled by an electrical engine. Ten pressure transducers are aligned on the suction side along the chord, starting at the leading edge (x/c = 0.05) and finishing near the trailing edge (x/c = 0.9), [11].

3 Foil at constant incidence

First, the NACA 66312 hydrofoil at a constant incidence of 6° is studied. Convergence of Cl shows oscillations with transition model that we do not observe without the model. Steady fully turbulent calculations without consideration of transition lead to constant Cl = 0,845 and constant Cd = 0,0179. Unsteady calculations are then adopted with transition model. Time step convergence is reached for a time step dt = 2.5 10^{-4} s. In this case, lift and drag coefficients oscillate with a constant period of 0.21 s (Fig. 3). This periodic oscillation is associated with the oscillation of the transition location.

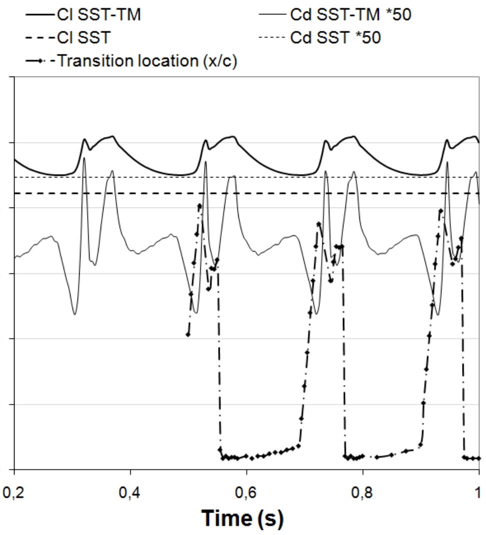

Figure 3: Unsteady lift and drag coefficients with and without transition model and transition location. $\alpha = 6°, Re = 7.5\ 10^5$

Similar variations are observed for Cl and transition location curves : one sudden peak is soon followed by a peak of larger width. For both lift coefficient peaks, the maximum value of Cl is observed just after the peak of transition location near the trailing edge. Maximum Cd does not correspond to the first time when transition

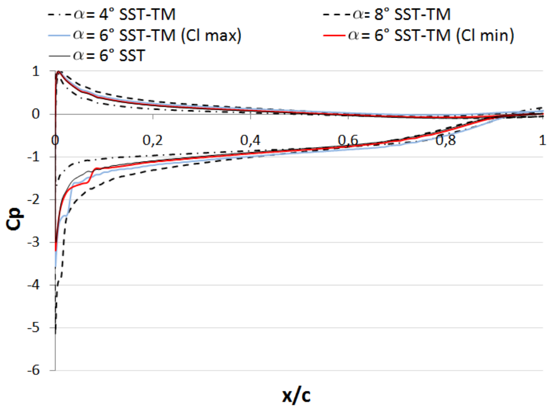

Figure 4: Pressure coefficient distribution with and without transition model, $\alpha = 4,\ 6$ and $8°, Re = 7.5\ 10^5$

reaches the leading edge since during four time steps, a relaminarization of the boundary layer can be observed before a new transition close to the trailing edge. The suction side is quite fully turbulent after these 4 time steps and the maximum Cd of the second peak is then reached.

Considering the curves obtained at 6°, Fig. 4 shows the effect of transition location on the pressure coefficients (Cp) distribution. It can be seen that the fully turbulent simulation (SST) leads to the lower inner curve area and appears to be the inner limit of transition model curves. This explains that the simulation with transition model creates higher Cl. Small oscillations can be observed on the pressure and suction sides curves near the leading edge and near the trailing edge of the suction side. The authors believe that oscillations are due to numerical instability caused by the very fine discretization of the foil.

Friction coefficient (Fig. 5) is highly influenced by the transition model. Levels of Cf on the pressure side are much lower with the transition model than with the fully turbulent model since the boundary layer remains partially laminar with the first model whereas it is fully turbulent with the second one. The suction side presents a laminar part of variable length with the transition model which leads to an oscillation of the viscous drag coefficient in the range of $2.6\ 10^{-3}$ to $7\ 10^{-3}$, to compare to the fully turbulent value of $9.6\ 10^{-3}$. This means that the transition model leads to an oscillation of the viscous drag coefficient in the range of 28 to 73 % of the fully turbulent value.

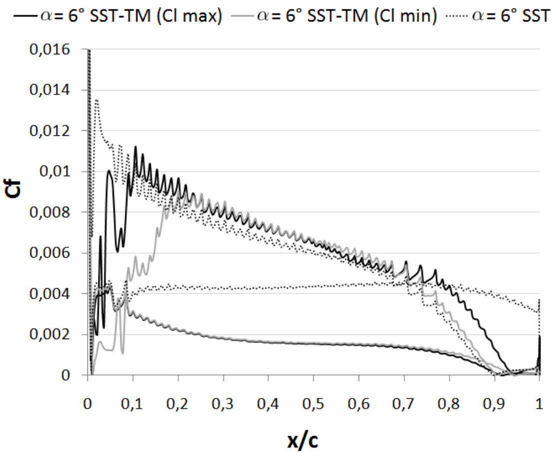

Figure 5: Friction coefficient distribution with and without transition model, $\alpha = 6°, Re = 7.5\ 10^5$

Calculations at 6° have shown the interest of the transition model to get the fluctuations of the global coefficients at an incidence close to the one where the transition location moves suddenly from the trailing edge to the leading edge. Let us call this incidence α_t. Two other unsteady calculations at 4 and 8° show no oscillation of the global coefficients (Fig. 6 and Fig. 7). A comparison between the SST-TM and the SST calculations shows that at an incidence of 4°, $Cl_{SST} = 79$ % of Cl_{SST-TM} whereas at an incidence of 8°, $Cl_{SST} = 101$ % of Cl_{SST-TM}. The very slight difference observed at 8° between Cl_{SST} and Cl_{SST-TM} is due to the fact that the transition location predicted by the transition model is really close to the leading edge (x/c = 0.02). The suction side is then quite fully turbulent and there is no major interest in using the transition model. At 4° however, there is a noticeable difference between both Cl since the transition occurs at x/c = 0.77. A major part of the suction side is then laminar whereas the fully turbulent model considers it as fully turbulent. The same differences can be observed on the Cd : at 4° $Cd_{SST} = 210$ % of Cd_{SST-TM} whereas at 8°, $Cd_{SST} = 103$ % of Cd_{SST-TM}.

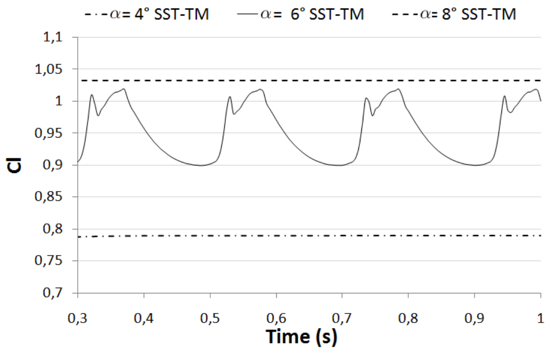

Figure 6: Unsteady lift coefficients of fixed foils. $\alpha = 4,\ 6$ and $8°, Re = 7.5\ 10^5$

Pressure coefficient curves (Fig. 4) show that there is no great difference on the pressure side while the main differences come from the suction side. Each one of the 4 curves that uses the transition model show a different transition location on the suction side. Transition location is located at the trailing edge for the inci-

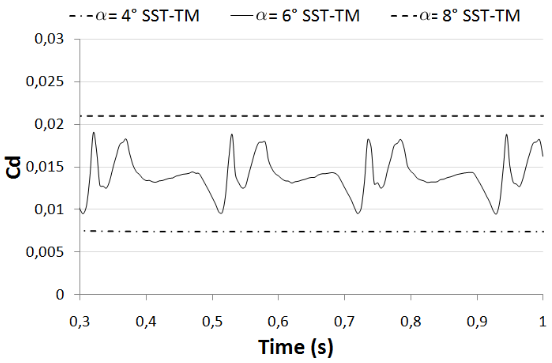

Figure 7: Unsteady drag coefficients of fixed foils. $\alpha = 4,\ 6$ and $8°, Re = 7.5\ 10^5$

dence 4° while it is located near the leading edge for the incidence 8°. Near α_t, the transition location varies along the chord as can be observed at 6°. The transition model then seems to be relevant at moderate Reynolds numbers and for incidences lower than α_t.

4 Quasi-static pitching motion

NACA 66312 is now studied with a quasi-static pitching motion at 6 $°/s$ which corresponds to a reduced frequency of $\dot{\alpha}^* = 0.18$ ($\dot{\alpha}^* = \frac{\dot{\alpha}*c}{U_\infty}$ and $\dot{\alpha} = \frac{2.\alpha_{max}}{t_f}$ with α_{max} the maximum incidence of the foil and t_f the duration of one oscillation). Calculations are initialized by a steady simulation of the flow around the foil at 0° of incidence. Time-step convergence is obtained for dt = 0.001s.

4.1 Numerical-experimental comparison

In this section, both SST and SST-TM models have been employed. The numerical results are compared with experimental data obtained in the IRENav hydrodynamic tunnel. To validate the calculations and determine the relevance of each model, pressure coefficients of two sensors are plotted. These sensors are located near the quarter chord (x/c = 0.3, Fig. 8) and near the trailing edge (x/c = 0.8, Fig. 9).

At x/c = 0.3, SST-TM results are in good agreement with experimental data : laminar flow is well predicted from 0 to 5°, transition is a little delayed from 5 to 6° and the vortex shedding zone is pretty well estimated even if the numerical signal does not perfectly fit with the experimental one due to the RANS model. Fully turbulent simulation however does not take into account the laminar part, as expected, but also do not predict the vortex generation and shedding. A lot of information is lost when using the SST model rather than the SST-TM model. Fig. 8 also shows that both SST and SST-TM models predict the same Cp from 6 to about 10°, i.e. when the boundary layer flow on the suction side is almost fully turbulent and the laminar separation bubble (LSB) remains small. Similar observations can be done for the downstroke since the quasi-static pitching induces very little hysteresis.

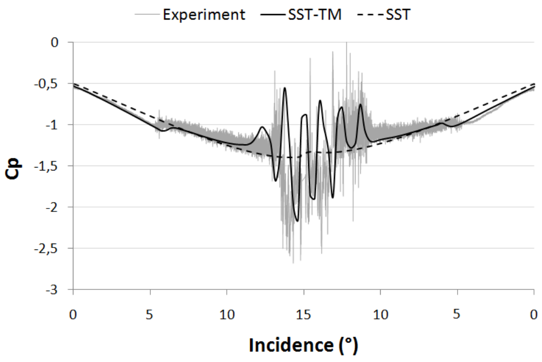

Figure 8: Numerical results superimposed on Cp signal of pressure transducer located at x/c = 0.3. $Re = 7.5\ 10^5,\ \dot{\alpha}^* = 0.18$

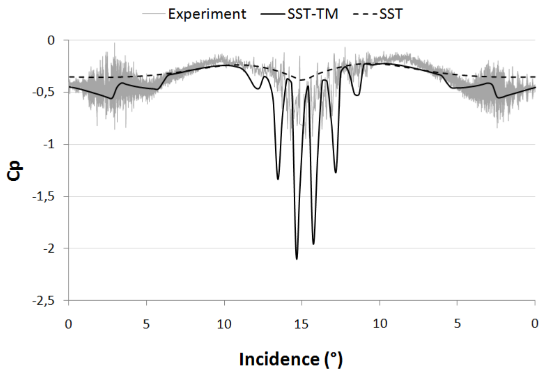

Figure 9: Numerical results superimposed on Cp signal of pressure transducer located at x/c = 0.8. $Re = 7.5\ 10^5,\ \dot{\alpha}^* = 0.18$

At x/c = 0.8, SST-TM results correctly fit with experimental data. The first sudden increase of Cp at 3° corresponds to the moment when transition is located at x/c = 0.8. The second increase in Cp corresponds to the incidence (6°) where transition moves from the trailing edge to the leading edge (Fig. 10). Between 6 and 10°, the turbulent boundary layer is fully developed and both SST-TM and SST models predict the same Cp, as for the previous sensor. The vortex shedding zone is well predicted but the signal amplitude is over estimated.

These two comparisons performed for two different sensors show good agreement between experimental and numerical Cp values and validate the SST-TM used in the calculations.

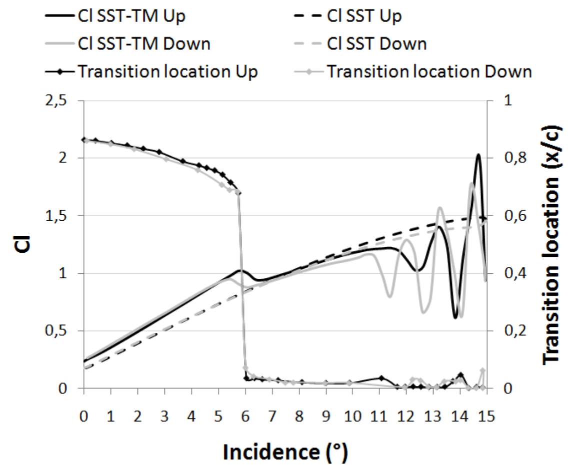

Figure 10: Lift Coefficient of SST and SST-TM models with transition locations against incidence. Up = Upstroke, Down = Downstroke. $Re = 7.5\ 10^5,\ \dot{\alpha}^* = 0.18$

4.2 Discussion

The effect of transition on Cp directly impacts Cl and Cd. Cl evolution with SST-TM model (Fig. 10) first takes into account the large part of laminar flow over its suction side from 0 to 6° (here 6° = α_t). This leads to $Cl_{SST} = 76$ % of Cl_{SST-TM} at 0° and $Cl_{SST} = 80$ % of Cl_{SST-TM} at α_t. From α_t to 10°, predictions of the SST-TM model are very close to those of the SST model for the same reason as Cp at x/c = 0.3 : the boundary layer flow on the suction side is quite fully turbulent and the LSB remains small. At α = 10°, the SST-TM Cl prediction starts to diverge from the SST one since the LSB starts to grow. The growth accelerates at stall (11.4°) and leads to the generation of a first large leading edge vortex that induces a first oscillation of the Cl. The vortex is then shed in the wake and others are generated from the leading edge creating other oscillations of high amplitude. Maximum amplitude reaches ΔCl = 1.4 which represents 115 % of the maximum Cl before stall. Cl oscillations stop at 10.5° in the downstroke, i.e. 1° lower than in the upstroke. This little hysteresis is kept during the downstroke, as can be seen for α_t that is about 0.5° lower than in the upstroke. SST simulation show no oscillation and a very little hysteresis around the maximum incidence. The hydrofoil reaches Cl = 1.48 right before stall at 14.9°, i.e. 121 % of the SST-TM value obtained right before stall and nearly 4° after the SST-TM stall prediction.
Cd results with SST-TM model (Fig. 11) present similar evolutions to Cl. From 0 to 6°, the large laminar part of the suction side leads to $Cd_{SST} = 210\%$ of Cd_{SST-TM} at 0° and $Cd_{SST} = 171\%$ of Cd_{SST-TM} at 5.68°. From 7 to 11°, after the transition location moved to the leading edge, SST and SST-TM models predictions are close to each other and $Cd_{SST} = 101\%$ of Cd_{SST-TM} at 8°. From 11 to 15°, SST-TM model shows oscillations and higher Cd than SST model. Highest amplitude oscillations are close to the maximum incidence and reach $\Delta Cd = 0.4$, i.e. about 8.7 times the value before oscillations. Maximum Cd predicted by SST-TM model is much higher than the one predicted by SST model : $Cd_{SST\ max} = 13\%$ of $Cd_{SST-TM\ max}$.

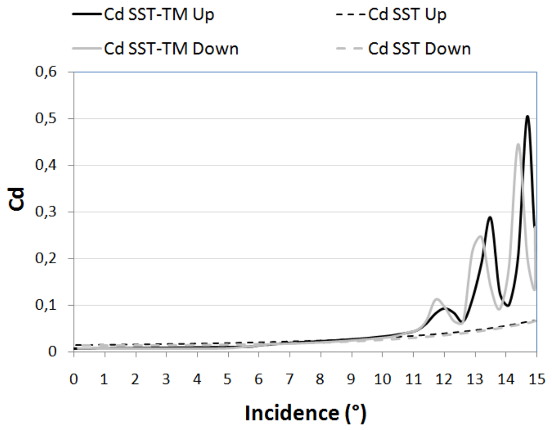

Figure 11: Drag Coefficient of SST and SST-TM models against incidence. Up = Upstroke, Down = Downstroke. $Re = 7.5\ 10^5,\ \dot{\alpha}^* = 0.18$

5 Conclusion

CFD calculations on a NACA 66312 at $Re = 7.5\ 10^5$ have been carried out with a fully turbulent $k - \omega\ SST$ model coupled or not with a two transport equations ($\gamma - Re_\theta$) transition model (TM). Simulations at fixed incidences 4, 6 and 8° have shown different behaviors of both models. A quasi-static pitching motion ($\dot{\alpha}^* = 0.18$) of the hydrofoil has then been calculated to quantify the incidence ranges where the transition model is relevant. These ranges can be summed up as follows :

- From 0° to α_t, SST-TM predicts a higher Cl (+ 25%) and a lower Cd (-50%)

- When calculating the flow around a fixed hydrofoil near α_t, SST-TM model predicts oscillations of all the coefficients due to an oscillation of the transition location.

- Between α_t and 10°, SST-TM model makes the same predictions as SST model since the suction side is nearly fully turbulent and the LSB stays small.

- From 10 to 15°, the LSB grows and generates a vortex shedding that induces oscillations of global coefficients Cl and Cd for SST-TM model whereas the SST model predicts no oscillation of global coefficients.

SST-TM is then interesting for computations at moderate Reynolds numbers and at most incidences. Efforts fluctuations seem to be better predicted but their amplitude may be over estimated as it has been shown in the Cp study. Further studies will focus on the relevance of the transition model for dynamic pitching effects (higher $\dot{\alpha}^*$ values).

6 References

1. Barakos, G., Drikakis, D., 1997, Simulation of unsteady aerodynamic flows using low-Re wall-distance-free turbulence models. ASME Fluids Engineering Division Summer Meeting, FEDSM97-3651

2. Smith, M.J., Wong, T.C., Potsdam, M., Baeder, J., Phanse, S., Evaluation of CFD to determine two-dimensional airfoil characteristics for rotorcraft applications, in: American Helicopter Society 60th Annual Forum, Baltimore, MD, June 7-10, 2004.

3. Shelton, A., Abras, J., Hathaway, B., Sanchez-Rocha, M., Smith, M.J., Menon, S., An investigation of the numerical prediction of static and dynamic stall, Proceedings of the 61 American Helicopter Society Annual Forum, Grapevine 10 (10) (2005) 6.

4. Menter, F.R., Kuntz, M. and Langtry, R., 2003, Ten years of industrial experience with the SST turbulence model. Proc. Turbulence, Heat and Mass Transfer 4, eds.: Hanjalic, K., Nagano, Y and Tummers, M.

5. Wang S., Ingham D.B., Ma L., Pourkashanian M., and Tao Z., 2010, Numerical investigations on dynamic stall of low Reynolds number flow around oscillating airfoils. Computers & Fluids, 39, 1529-1541.

6. Menter, F.R., Langtry, R.B., Volker, 2006, Transition modelling for general purpose CFD codes. Flow Turbulence Combust 77, 277-303.

7. Ferziger, J., and Peric, M., 2002. Computational methods for fluid dynamics. Springer New York.

8. Ansys, Ansys CFX Solver Modeling Guide, Software Release, vol. 12, 2009.

9. Maman, N., and Farhat, C., 1995. Matching fluid and structure meshes for aeroelastic computations: A parallel approach. Computers and Structures, 54(4), pp. 779–785.

10. Farhat, C., Lesoinne, M., and Le Tallec, P., 1998. Load and motion transfer algorithms for fluid/structure interaction problems with non-matching discrete interfaces: Momentum and energy conservation, optimal discretization and application to aeroelasticity. Computer Methods in Applied Mechanics and Engineering, 157(1-2), pp. 95–114.

11. Ducoin, A., Astolfi, J.-A., Deniset, F., Sigrist, J.-F., 2009, Computational and experimental investigation of flow over a transient pitching hydrofoil, European Journal of Mechanics / B Fluids 28, December 2009, pp 728-743.

Numerical analysis of cavitation, unsteady shaft forces and pressure pulses generated on the hull with and without vortex generators

Paweł Dymarski* (padym@wp.pl); Jan Szantyr** (jas@pg.gda.pl); Marek Kraskowski*
(marek.kraskowski@cto.gda.pl)

* Ship Design and Research Centre - CTO S.A,

** Gdansk University Of Technology, Faculty of Mechanical Engineering.

Keywords: vortex generators, wake, shaft forces, pressure pulses, cavitation

1 INTRODUCTION

The basic idea of using the vortex generators for improving the wake flow of large ships consists in introducing the vortices to the boundary layer in the flow around the aft part of the hull, realized by small fins fitted to the hull shell plating at some angle of attack relative to the streamlines. The vortices show the tendency to stick to the hull, which allows preventing the flow separation; moreover, the presence of vortices in the boundary layer causes equalizing the axial velocity distribution, by mixing the low velocity region and high velocity region of the boundary layer.

Equalizing the axial velocity distribution may results in reduced propeller vibration and cavitation, it can also possibly improve the overall propulsion efficiency by reducing the suction coefficient, and allowing for using the propeller of higher efficiency. The possible profits would be achieved at the cost of additional resistance induced on the vortex generators, which makes it especially difficult to achieve a positive balance of profits and losses.
Potential efficiency of the vortex generators depends on the type of vessel; it is expected that the profit of using them will be possible to achieve for vessels characterized by blunt, complex stern shapes and highly non-uniform wake flows.

The work presented here includes the numerical analysis, carried out in order to predict amplitudes of propeller shaft forces, amplitudes of pressure pulses at specified points in the aft part of the ship hull, as well as to predict volume of sheet cavity on propeller blade.
The article also presents the results of propulsion tests and wake measurements which were performed in order to prepare data for numerical analysis of propeller.
Model tests have been carried out for three cases: bare hull and for hull with two different configurations of VG's. For numerical computations of propeller additional three cases were taken into consideration (modified propeller pitch and skewback) in order to capture the influence of propeller geometry modification on shaft forces, pressure pulses and cavitation.

2 GEOMETRY OF THE ANALYZED OBJECTS

2.1 Geometry of the hull

In this chapter, main characteristics of the vessel used as test case are presented, as well as the configuration of the vortex generators and details of the generator's geometry.
The vessel considered in the analysis is a bulk carrier. Geometry of the hull is presented in Figure 1. Main parameters of the ship are listed in Table 1.
For the analysed vessel, a typical configuration of vortex generators consisted of an array of three fins fitted to the vessel’s skeg. In both cases, their angle of attack relative to the streamlines (derived for bare hull flow) was such that they were deflecting the streamlines upwards. An example of “typical” configuration with three vortex generators is presented in Figure 2

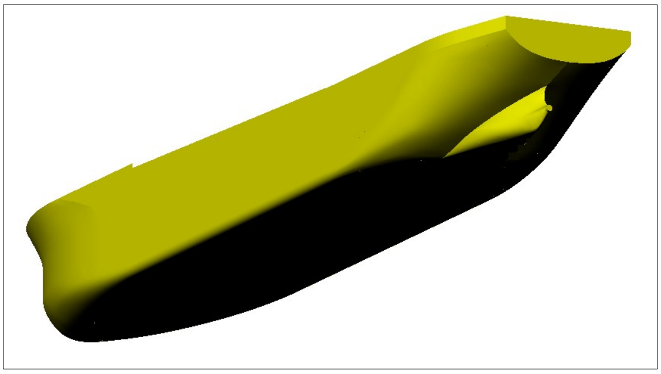

Fig. 1 Hull geometry

Table 1 Main parameters of the analyzed vessels

Vessel type	Bulk carrier
Length b.p. [m]	250.80
Breadth [m]	44.40
Draught [m]	13.00
Block coefficient [-]	0.836
Speed [kn]	15.0
Froude number [-]	0.156
Model scale factor [-]	38

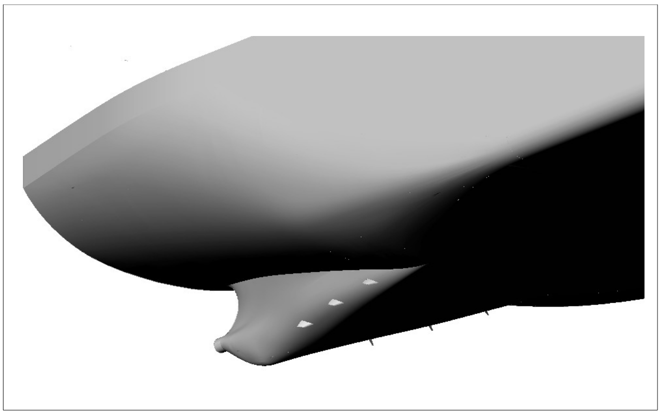

Fig. 2 Location of the vortex generators on the hull

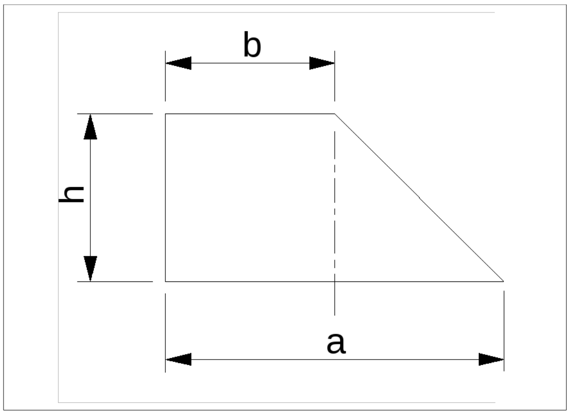

Fig. 3 Geometry of the vortex generator

2.2 Geometry of vortex generators

In each of analyzed cases, vortex generators are trapezoidal fins, presented in Figure 3. The fin profile is NACA 0010-35. Proportions of the fin dimensions are constant and equal to: $a/h=2$, $b/h=1$. The fin base length a is used as a characteristic dimension; in the presented study, three sizes of the fins were used: $a=20$ mm, $a=30$ mm, and $a=40$ mm at model scale.

2.3 Geometry of the propeller

Sketch of the propeller is shown in Fig. 4, while the main parameters of the propeller geometry are listed in Table 2

Table 2 Propeller parameters

Type:	Fixed pitch
Diameter D [m]:	7.600
No of blades z:	4
Pitch ratio at 0.70 radius $P_{0.7}/D$:	0.6419
Exp. area ratio A_E/A_0:	0.5359
Hub ratio d/D:	0.182
Blade width at 0.70 radius $c_{0.7}$ [m]	2.234
Blade thick. at 0.70 radius $t_{0.7}$ [m]	0.1208
Blade profile	NACA 16 A=8

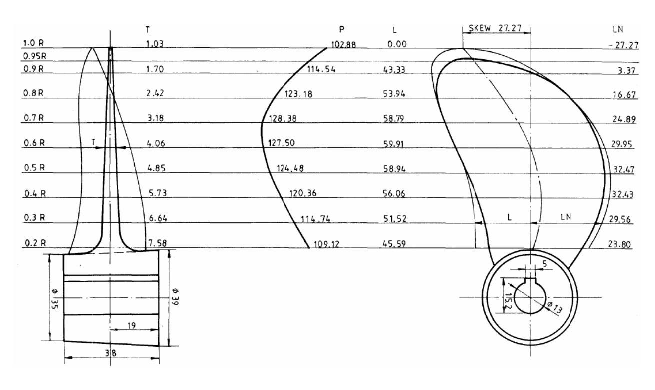

Fig. 4 Sketch of the propeller model

3 MODEL TESTS RESULTS

Within the project model tests of resistance and wake measurements have been performed for bare hull and for the model with six different configurations of vortex generators.

Based on the resistance and wake results, two configurations of VG's, referred to as “4th” and the “5th”, have been selected for further studies. For these two configurations (and for the bare hull) propulsion test was performed to determine the overall propulsion efficiency, as well as to obtain data for numerical analysis of propeller.

Results of propulsion tests (delivered power) for the two selected configurations and for the bare-hull are presented in Figure 5.

Figure 6 shows wakes behind the hull with and without VG's

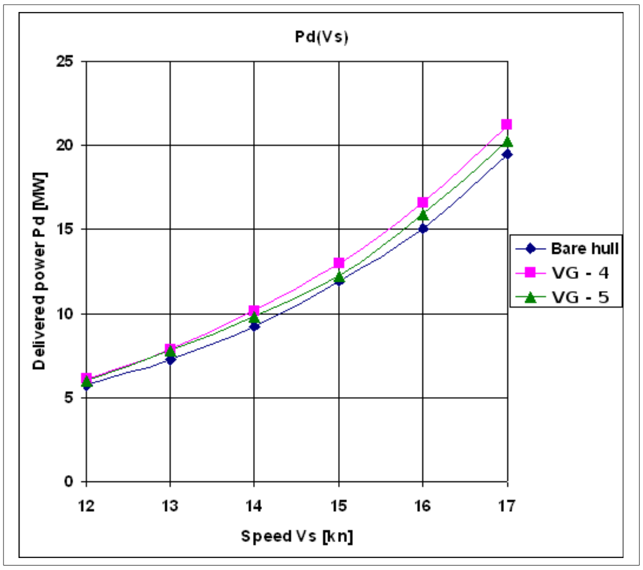

Fig. 5 Power prediction for the hull with and without VG

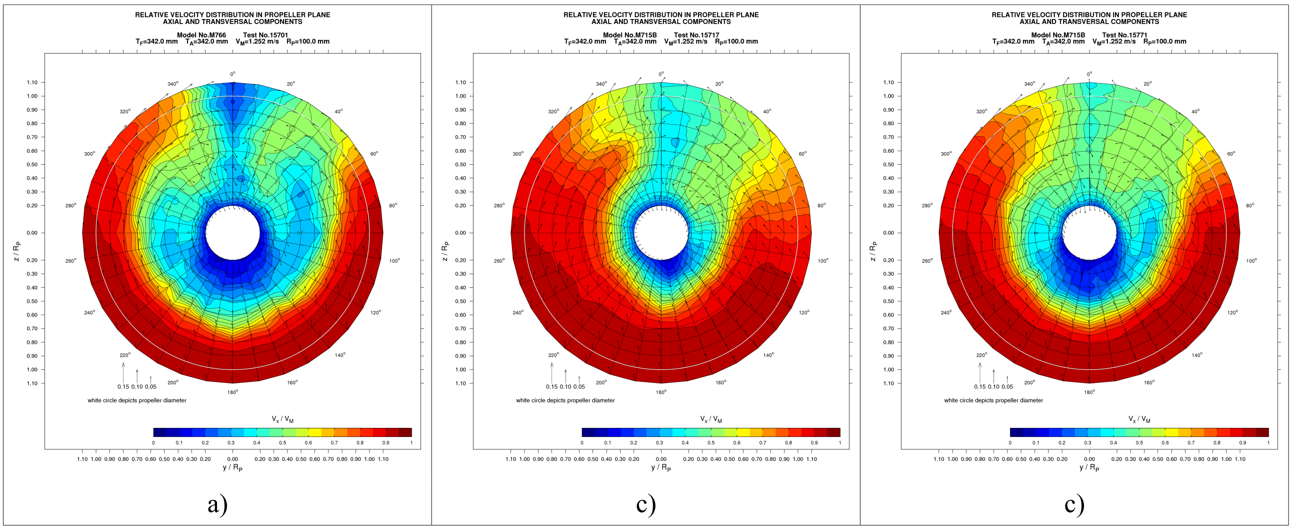

a) c) c)

Fig. 6 Nominal wake of a) bare hull; b) configuration 4; c) configuration 5

4 NUMERICAL ANALYSIS OF CAVITATION, UNSTEADY SHAFT FORCES AND PRESSURE PULSES

The analysis described in this section has been performed using the unsteady lifting surface program, the algorithm of which is described in [3]. The analysis covered six cases;

- **case 0** – the original propeller, operating in the bare hull wake field,
- **case 4** – the original propeller, operating in wake 4 modified by the vortex generators,
- **case 5** – the original propeller, operating in wake 5 modified by the vortex generators,
- **case 4A** – the propeller with pitch multiplied by 1.057 operating in the propulsive condition of case 0,
- **case 4SK** – the propeller with radically increased skewback (multiplied by 2.0), operating in the propulsive condition of case 4,
- **case 5A** – the propeller with pitch multiplied by 1.033, operating in the propulsive condition of case 0.

The respective propulsive conditions of the above computation cases, as determined in self-propulsion model experiments, are listed in Table 3 below together with the analytically computed propeller efficiency (not propulsive efficiency).

Table 3 Propulsive conditions determined in model experiments

Case		**0**	**4**	**5**	**4A**	**4SK**	**5A**
Ship speed	knots	15.0	15.0	15.0	15.0	15.0	15.0
Rpm	1/min	104.9	109.3	107.4	104.9	109.3	104.9
Thrust	kN	1383	1355	1299	1383	1355	1383
Torque	kNm	1084	1132	1088	1084	1132	1084
Computed efficiency		0.562	0.571	0.575	0.575	0.572	0.575

The results of calculation of the unsteady hydrodynamic shaft forces are presented in Table 4 in the form of the blade frequency harmonic amplitudes of three force components FX, FY, FZ and three moment components MX, MY, MZ. FX corresponds to propeller thrust, while MX corresponds to propeller torque.

Table 4 Harmonic amplitudes of the blade frequency unsteady shaft forces

Component	**FX** [kN]	**FY** [kN]	**FZ** [kN]	**MX** [kNm]	**MY** [kNm]	**MZ** [kNm]
0	127.3	19.8	13.8	96.3	157.9	143.1
4	107.5	22.0	9.1	84.2	194.2	126.5
5	68.2	11.8	11.8	55.2	111.7	130.8
4A	103.3	23.9	10.9	86.7	204.5	128.5
4SK	97.3	26.9	9.3	77.1	252.3	143.3
5A	66.4	12.3	13.4	54.6	111.3	134.6

The graphical presentation of the calculated blade frequency harmonic amplitudes of the unsteady shaft forces is shown Fig. 7.

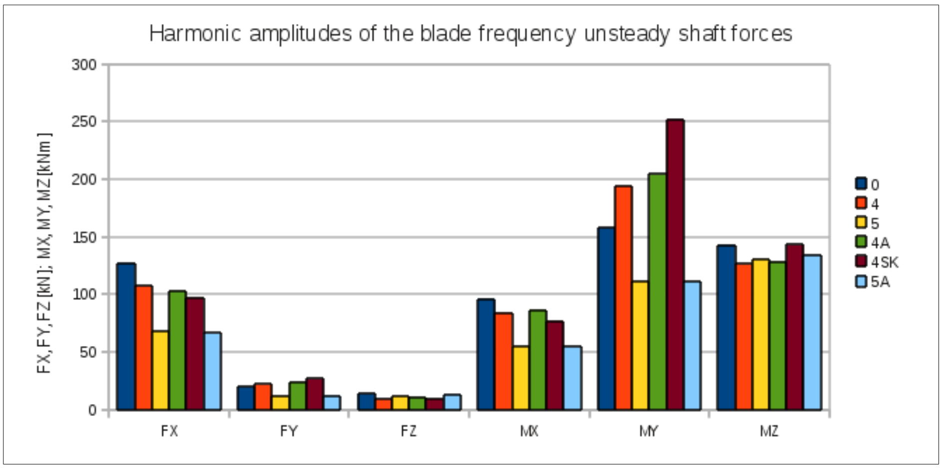

Fig. 7 Blade frequency harmonic amplitudes of the unsteady shaft forces

The calculation of the pressure pulses generated on the hull by the propeller in the above six cases is performed for seven selected points on the hull, the locations of which are shown in Fig. 8. The calculated pressure pulses are generated first of all by the unsteady cavitation on the blades, but they also include the effects of varying hydrodynamic blade loading and thickness of the rotating propeller blades.

The results of calculations of pressure pulses are included in Table 5 in the form of blade frequency harmonic amplitudes for the above seven points. The graphical presentation of these amplitudes is shown in Fig. 9.

The pressure pulses depend strongly on the unsteady cavitation phenomena developing on the propeller blades. Therefore it is interesting to analyze Fig. 10, which shows the computed volume of unsteady sheet cavity for the above six cases. A direct correlation between Fig. 9 and Fig. 10 may be noticed, in particular very high maximum cavity volume for cases 4 and 4A corresponding to high pressure pulses amplitudes.

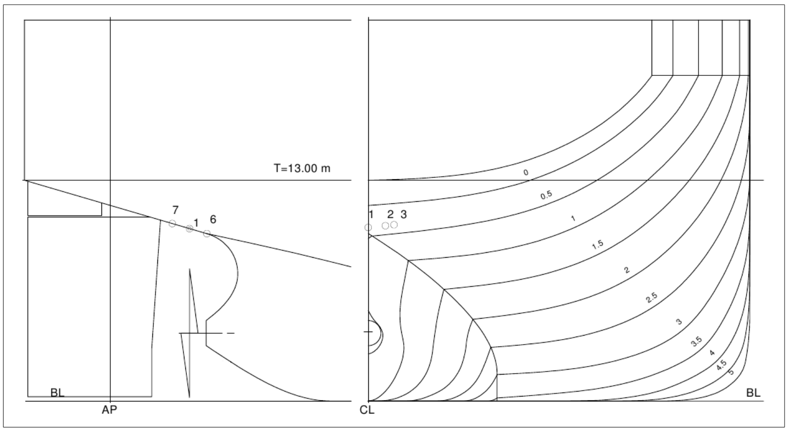

Fig. 8 Location of points on the hull for calculation of pressure pulses (points 4 and 5 are symmetrical to points 2 and 3 respectively)

Table 5 Harmonic amplitudes of the blade frequency harmonics of pressure pulses in [kPa]

Point	**1**	**2**	**3**	**4**	**5**	**6**	**7**
0	5.46	5.07	4.81	5.26	5.05	5.36	4.85
4	11.05	10.81	10.44	10.07	9.49	11.05	9.86
5	3.89	3.56	3.43	3.91	3.80	3.95	3.59
4A	10.63	10.38	10.02	9.72	9.16	10.62	9.49
4SK	9.61	9.14	8.75	8.92	8.42	9.56	8.59
5A	3.36	3.05	2.92	3.41	3.33	3.39	3.09

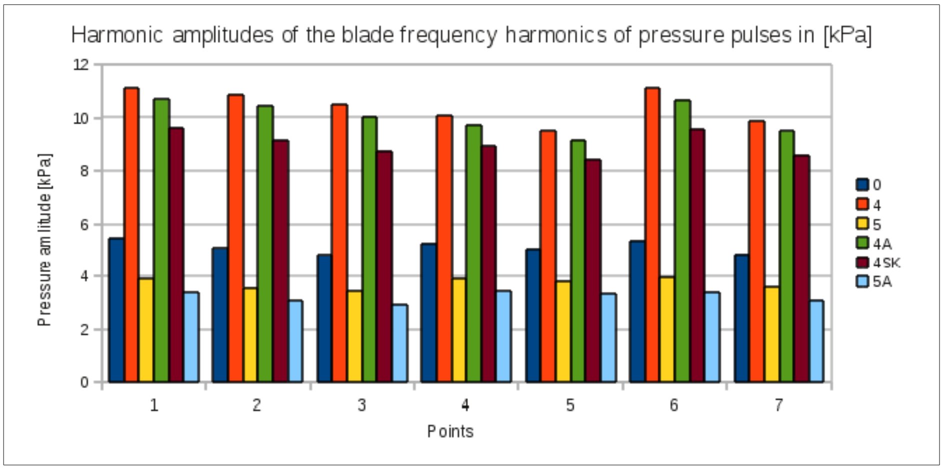

Fig. 9 Harmonic amplitudes of the blade frequency harmonics of pressure pulses

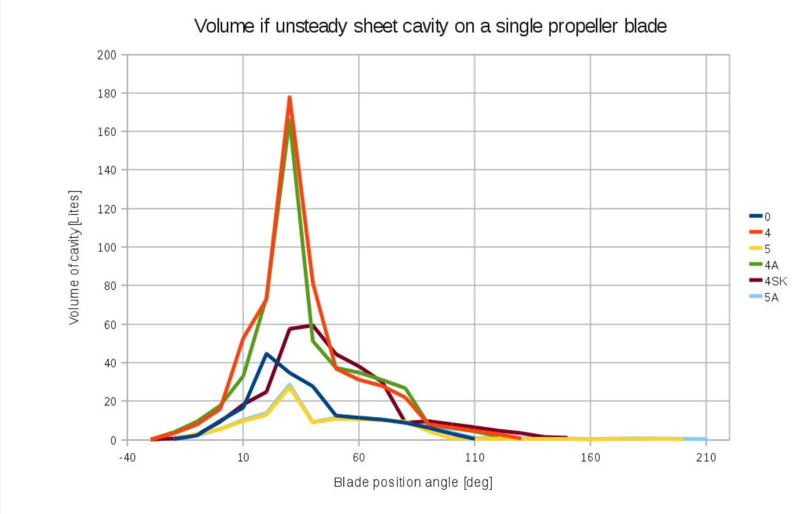

Fig. 10 Volume if unsteady sheet cavity on a single propeller blade in [litres]

5 CONCLUSION

The above computational analysis leads to the following observations:

- the propeller efficiency in all six cases is very similar, consequently it is the hull efficiency which decides about the resulting propulsive efficiency in respective cases,
- the original wake velocity field is not extremely unfavorable – it produces acceptable level of pressure pulses (below 8 kPa); however the fluctuations of propeller thrust are on the verge of acceptability (slightly above 8 per cent of mean thrust) and the bending moments on the shaft are high,
- modified wake 4 makes the situation even worse – the pressure pulses are now unacceptably high, the thrust fluctuation is slightly reduced but the MY bending moment components increases,
- modification of pitch and moving the propulsive condition to 4A does not change this situation significantly – the bending moment MY increases further while the pressure pulses decrease only slightly,
- application of high skewback in case 4SK reduces the pressure pulses, but they are still above the acceptable level; fluctuations of thrust and torque are visibly reduced to an acceptable level but the bending moments MY and MZ increase to dangerous levels,
- the main problem with modified wake 4 is that the iso-wake lines reproduce the outline of the propeller blade leading edge, what leads to high amplitudes of hydrodynamic forces and a violent growth of sheet cavity volume,
- modified wake 5 seems to be very good – it leads to very low pressure pulses and low fluctuations of all components of the shaft forces; modification of pitch and moving propulsive condition to 5A reduces these low values still further.

It may be concluded that the visual assessment of the ship wake velocity field modified by the vortex generators does not guarantee positive result of the modification. It is necessary to perform the detailed analysis of propeller performance, concerning unsteady cavitation, fluctuating shaft forces and pressure pulses, similar to that presented above, in order to be convinced about the positive effect of the vortex generators.

ACKNOWLEDGEMENT

The research presented in this paper has been financially supported by The Polish National Centre for Research and Development (NCBiR), Grant No. N R10 0040 06/2009. The authors would like to express their gratitude for this support.

REFERENCES

[1] Dymarski P., Kraskowski M. (2011): *Numerical and experimental investigation of the possibility of forming the wake flow of large ships by using the vortex generators,* Proceedings of The 2nd International Symposium on Marine Propulsors – SMP'11, Hamburg – Germany, 15-17 of June, 2011

[2] Schmöde D. (2008): *RANS computations for wake improving vortex generators*, Proceedings of 11th Numerical Towing Tank Symposium (NuTTS), Brest, France

[3] Szantyr J.A. (1994): *A Method for Analysis of Cavitating Marine Propellers in Non-uniform Flow*, Intern. Shipbuilding Progress, Vol. 41, No.427

Pressure Jump Approach for Modeling Waterjet/Hull Interaction

Arash Eslamdoost, Lars Larsson, Rickard Bensow

Department of Shipping and Marine Technology,
Chalmers University of Technology, 412 96 Gothenburg, Sweden
arash.eslamdoost@chalmers.se

Introduction

Nowadays waterjet propulsion systems are frequently being used as one of the major propulsion systems on high-speed vehicles operating in the range of 30-35 Knots or even further. Moreover, due to the high maneuverability achievable by means of waterjet systems, these propulsion units are being installed on craft, which require high maneuverability. The key point in operation of waterjet systems is the momentum increment of the water drawn through a ducting channel by the action of an internal pump. The difference between the low energy flow at the system intake and high-energy flow expelled out of the nozzle generates the required thrust force for propelling the craft. Based on the required thrust force different numbers and sizes of these units can be applied on the vehicle. A comprehensive discussion on various types of waterjet systems, their operating curves and flow pattern inside these systems are presented in [1]. General appearance and placement of an axial flow waterjet propulsion system is depicted in Fig. (1).

The momentum flux method is applied in [2] and [3] to analyse waterjet propulsion systems. There are some discrepancies in conclusion of these researches on the possibility of applying the momentum flux method for waterjet system's power prediction. The main reason of this discrepancy is the pressure distribution estimation on the part of the control volume streamtube below the hull, and it is worthwhile investigating whether it is possible to neglect this force or not. In the following sections, first the conventional momentum flux method will be discussed and then another approach, which is independent of the intake streamtube properties, will be introduced. This method is called pressure jump approach.

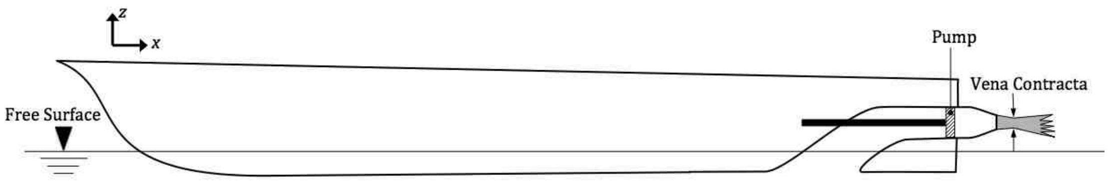

Fig. (1) General appearance of the waterjet propulsion system

General Definitions

In this section general definitions, which are frequently used in waterjet system analysis, will be introduced. Fig. (2) shows the cross section of a waterjet propulsion unit and the control volume ABCDEA, which is normally applied for the system analysis.

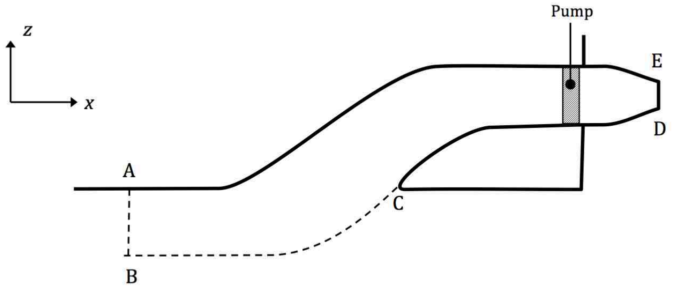

Fig. (2) Section cut through the waterjet ducting system

Surface BC in Fig. (2) shows the dividing streamtube. This streamtube is an imaginary surface, which separates the flow drawn into the ducting system from the rest of the flow field. According to the definition of streamtube no flow crosses this surface. Surface CD and EA are waterjet system internal material boundaries and surface DE represents the nozzle opening area.

Water enters the ducting system through area AB. This area is called capture area of the intake. Sometimes it becomes cumbersome to obtain the exact shape of the capture area and therefore there are some assumptions for simplifying the shape. Two of the most conventional assumptions for the shape of the capture area are a rectangular shape or half-elliptical shape which, according to the ITTC waterjet specialist committee is suggested to be placed one impeller diameter ahead of the intake tangency point [4], [5]. Experimentally it has been observed that in the range of intermediate to high Froude number the width of the capture area is almost constant; hence, in order to reduce the number of variants, the width of the capture area, w_{capt}, is considered to be constant value which is a function of intake geometry width, w. Empirical widths of the rectangular and half-elliptical capture areas are shown in Fig. (3). Height of the capture area, h, is varying based on the flow rate through the system and it is a bit higher in half-elliptical intake geometry comparing to the rectangular one.

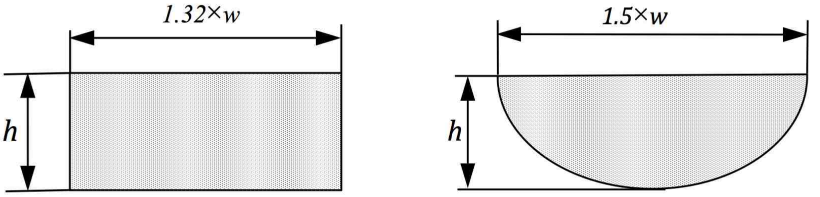

Fig. (3) Two different assumptions for the capture area geometry[4]

The Momentum Flux Approach

The waterjet propulsion concept is based on the momentum flux change through the system. This is the actual source of thrust production in these systems. Low speed velocity enters the system through the capture area. Inside the ducting channel the pump adds momentum to the entrained water and thereafter high-speed jet is spewed out through the nozzle. Writing the momentum flux balance for the control volume ABCDEA, Fig. (2), gives the resultant force acting on this control volume. Momentum flux vector, M, in i direction is defined as **Eq. (1)**;

$$\bar{M}_i = \iint_A \rho u_i (u_k n_k) dA \qquad \text{Eq. (1)}$$

where ρ is the fluid density, u is the velocity vector and n shows the normal vector normal to the surface A.

Calculating the momentum flux for the inlet and outlet surfaces of the control volume ABCDEA, Fig. (2), one can obtain the gross thrust, Tg, of the system, which is identical to the momentum flux change between the inlet and outlet. The gross thrust is equal to the resistance of the whole system including losses inside the ducting system[2]. This is expressed mathematically in **Eq. (2)**;

$$T_{g,i} = |\bar{M}_{jet,i}| - |\bar{M}_{capt,i}| = F_{surface,i} + F_{body,i} + F_{Pump,i} \qquad \text{Eq. (2)}$$

where $\bar{M}_{jet,i}$ and $\bar{M}_{capt,i}$ are the momentum flux vectors at the nozzle outlet section and the capture area, respectively. $F_{surface,i}$ represents the forces exerted on all the surfaces of the control volume including all material boundaries and imaginary ones. $F_{body,i}$ and $F_{Pump,i}$ represent the body force (gravity) acting on the mass contained control volume and the pump force acting on the fluid, respectively. The index i takes the values 1,2,3 and represents the three coordinate directions.

The major issue when applying this method is the fact that obtaining the force on the imaginary surface, BC, is not straight forward; especially, by means of experimental methods. Numerically, it is possible to capture the surface of the streamtube and extract the forces exerted on surface BC. This has been done in [3] and [6].

The Pressure Jump Approach

To start with, it is required to write the force balance for the waterjet-hull system. The contribution of different part of the system on the total resistance is depicted in Fig. (4). In this figure, R_H is the hull resistance, R_D is the ducting channel drag and R_N is the drag force of the nozzle chamber. F_p is the force exerted by the impeller.

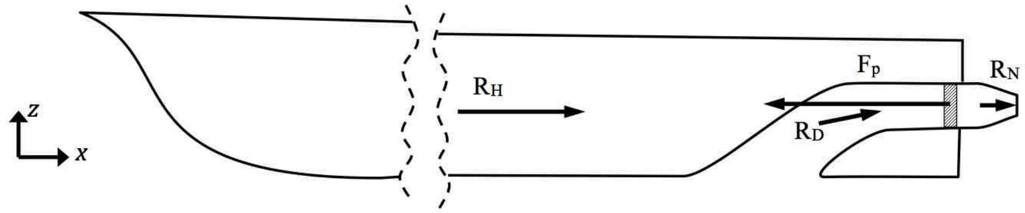

Fig. (4) Force balance of the waterjet-hull system

Writing the force balance in the *x*-direction for the shown system, Fig. (4), results in **Eq. (3)**.

$$F_{P,x} = R_H + R_{D,x} + R_{N,x} \quad \text{Eq. (3)}$$

Because of the action of the pump there is a difference in pressure between the sides of the impeller. In fact, this pressure jump at the impeller section is the main source of the created thrust force of the waterjet system. A simplified sketch of the nozzle geometry is shown in Fig. (5). Assuming a constant pressure on each side of the impeller disk and a nozzle opening perpendicular to the *x*-direction, one can write **Eq. (4)** for balancing the force in the *x*-direction.

$$F_{P,x} = (P_{after} - P_{front})A_{impeller} \quad \text{Eq. (4)}$$

where P_{after} and P_{front} are the pressures just after and before the impeller disc, respectively. $A_{impeller}$ is the projected area in the *x*-direction of the impeller disk.

Moreover, it is possible to write the nozzle resistance, $R_{N,x}$, in the following integral form;

$$R_{N,x} = \iint_{S_{nozzle}} \sigma . n_x dA \quad \text{Eq. (5)}$$

where σ is the mean stress, S_{Nozzle} is the internal surface of the nozzle chamber and n_x is the normal unit vector in *x*-direction.

One can split the stress tensor shown in **Eq. (5)** into the pressure, *p*, and shear stress, τ, components.

$$\iint_{S_{nozzle}} \sigma . n_x dA = \iint_{S_{nozzle}} p . n_x dA + \iint_{S_{nozzle}} \tau . n_x dA \quad \text{Eq. (6)}$$

Moreover, separating the static pressure, *p*, after the impeller disk into the static pressure inside the nozzle in the absence of the pump system, p_{WOP}, plus a constant pressure jump, Δp, which occurs due to the action of the pump, it is possible to split the first term on the right hand side of **Eq. (6)** into two separate terms as in **Eq. (7)**.

$$\iint_{S_{nozzle}} p \cdot n_x dA = \iint_{S_{nozzle}} p_{WOP} \cdot n_x dA + \iint_{S_{nozzle}} \Delta p \cdot n_x dA \quad \text{Eq. (7)}$$

It should be noted that τ will be the same with and without the pressure jump in the nozzle chamber, since a constant pressure increase does not change the flow.

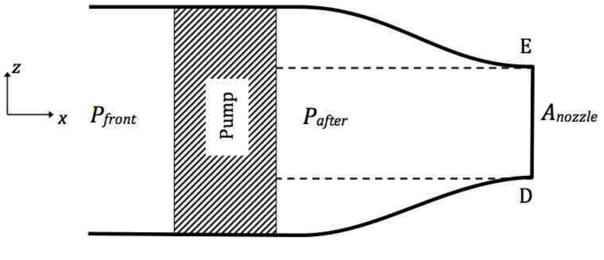

Fig. (5) Schematic presentation of the nozzle section

Since the impeller disk $A_{impeller}$ and nozzle opening surface A_{nozzle} can be assumed perpendicular to the *x*-direction, one may simplify the second integral in the right hand side of **Eq. (7)** as follows:

$$\iint_{S_{nozzle}} \Delta p \cdot n_x dA = \Delta p(A_{Impeller} - A_{nozzle}) \quad \text{Eq. (8)}$$

Manipulation of **Eq. (4)** to **Eq. (8)** and replacing the expanded form of $R_{N,x}$ into **Eq. (3)** gives **Eq. (9)**.

$$\Delta p \cdot A_{impeller} = R_H + R_{D,x} + \left[\Delta p\left(A_{impeller} - A_{nozzle}\right) + \iint\limits_{S_{nozzle}} p_{WOP} \cdot n_x dA + \iint\limits_{S_{nozzle}} \tau . n_x dA\right] \qquad \text{Eq. (9)}$$

Simplified form of **Eq. (9)** is shown in **Eq. (10)**.

$$\Delta p \cdot A_{nozzle} = R_H + R_{D,x} + \left[\iint\limits_{A_{nozzle}} p_{WOP} \cdot n_x dA + \iint\limits_{A_{nozzle}} \tau . n_x dA\right] \qquad \text{Eq. (10)}$$

The right hand side of **Eq. (10)** is equal to the total resistance of the whole system without pressure jump and is named R_{TWOP}.

$$R_{TWOP} = R_H + R_{D,x} + \left[\iint\limits_{A_{nozzle}} p_{WOP} \cdot n_x dA + \iint\limits_{A_{nozzle}} \tau . n_x dA\right] \qquad \text{Eq. (11)}$$

Hence from **Eq. (10)**,

$$\Delta p = \frac{R_{TWOP}}{A_{nozzle}}. \qquad \text{Eq. (12)}$$

Eq. (12) is a general formula for the required pressure jump to balance the total resistance of the system.

Potential Flow Assumption

In the following it is assumed that the flow from the capture area to the nozzle exit is inviscid and therefore there is no head loss inside the ducting channel. The total head at the section DE is then equal to the total head at section AB plus the constant pressure jump, Δp. This is expressed using Bernoulli's equation in **Eq. (13).** It has been assumed that the pressure at the nozzle outlet section is atmospheric. Subscripts applied in **Eq. (13)** are based on the notation presented in Fig. (2);

$$\left[P_{AB} + \rho g h_{AB} + \frac{1}{2}\rho U_{AB}^2\right] + \Delta P = P_{atm} + \rho g h_{DE} + \frac{1}{2}\rho U_{DE}^2 \qquad \text{Eq. (13)}$$

where ρ is the water density and g is the gravitational acceleration in z-direction. P_{AB} and P_{atm} are pressures at the capture area and atmospheric pressure, respectively. Heights of the streamlines at the capture area and nozzle outlet section are denoted h_{AB} and h_{DE}, respectively. U_{AB} and U_{DE} are the velocities at the sections AB and DE.

All terms in **Eq. (13)** are known except the term that contains the jet velocity, U_{DE}. So, re-arranging this equation for obtaining U_{DE} and dividing both hand sides by the undisturbed velocity, U_∞, results in **Eq. (14)**;

$$\frac{U_{DE}}{U_\infty} = \pm\sqrt{\frac{\left(P_{AB} - P_{atm}\right)}{\frac{1}{2}\rho U_\infty^2} + \frac{\Delta P}{\frac{1}{2}\rho U_\infty^2} + \frac{2g\left(h_{AB} - h_{DE}\right)}{U_\infty^2} + \frac{U_{AB}^2}{U_\infty^2}} \qquad \text{Eq. (14)}$$

or,

$$\frac{U_{DE}}{U_\infty} = \pm\sqrt{C_{p\,AB} + \Delta C_p + \frac{2}{Fn^2} \cdot \frac{\left(h_{AB} - h_{DE}\right)}{L_{pp}} + \left(\frac{U_{AB}}{U_\infty}\right)^2} \qquad \text{Eq. (15)}$$

where L_{pp} is the length between perpendiculars and Fn is the Froude number of the craft.

$$Fn = \frac{U_\infty}{\sqrt{g \cdot L_{pp}}} \qquad \text{Eq. (16)}$$

Numerical Simulation

The potential flow is computed using SHIPFLOW [7], a suite of computer codes based on in house research. The module XPAN is a potential flow panel method, using Rankine sources on the hull and part of the free surface. A Neumann boundary condition for the potential is applied on the hull (corresponding to zero normal velocity) and a combined kinematic and dynamic condition is applied on the free surface at its exact location. The latter is obtained iteratively.

In the present work the panels are extended into the duct all the way to the nozzle exit, where a velocity U_{DE} in the direction of the nozzle axis is specified. This is achieved by covering the exit plane with panels with the normal velocity U_{DE} at their control points. Fig. (6) shows the upper part of the computational domain, the water below the free surface and outside the hull plus the duct back to the exit. The outer domain boundary is assumed infinitely far away. A potential flow solution can thus be obtained not only around the hull, but also inside the duct, with the given exit velocity, U_{DE}. Note that the free jet is outside of the computational domain. In principle it has no effect on the solution, but in practice it makes it difficult for the free surface panels in the wake to satisfy the boundary condition, so if the exit is close instabilities may occur. So far, this has been resolved by moving the jet exit slightly forward.

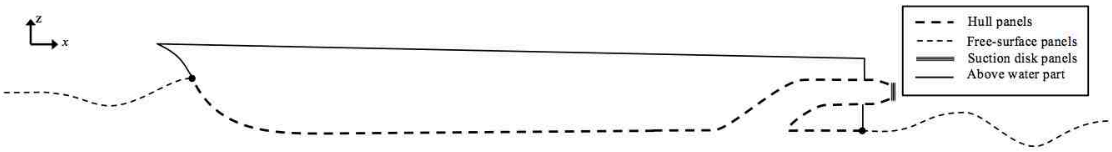

Fig. (6) The computational domain is located below the dashed line, representing panelized surfaces.

The potential flow solution contains the pressure distribution around the hull and in the duct for the given U_{DE}. This yields the wave resistance of the hull and an approximate pressure resistance of the duct. The latter is approximate, since SHIPFLOW assumes a constant total head in the whole computational domain, while in the duct the total head in reality is somewhat reduced, as discussed above. Since both the velocity (specified by U_{DE}) and the height of the nozzle are correct the pressure will be over predicted by a constant value in the duct. This will result in a very small error in the pressure resistance since the duct is essentially a closed volume.

The frictional resistance of the hull is computed by the boundary layer module XBOUND in SHIPFLOW, based on the computed pressure. There is no need to include the RANS module for hull like the ITTC proposed hull [4], with a wide submerged transom, where the boundary layer stays relatively thin over the whole hull. Inside the duct the friction coefficient is approximately computed by extrapolation form the hull. As long as the wetted surface is correct this is a small approximation.

Note that there is no pump force used in the SHIPFLOW solution. The key is to adjust the exit velocity U_{DE} such that **Eq. (12)** and **Eq. (15)** are satisfied simultaneously. This has to be done iteratively. After each iteration, all terms on the right hand side of **Eq. (11)** are known, which means that R_{TWOP} can be computed and inserted in **Eq. (12)** to obtain Δp. This is then inserted (non-dimensionalized) in **Eq. (15)**, where $C_{p\,AB}$ is obtained as the potential flow pressure on the hull at point A and U_{AB}^2 is taken as the average of the squared velocity at AB, considering the boundary layer velocity profile computed by XBOUND. A new U_{DE} can then be obtained and the process repeated. It is convenient to start the process by neglecting the resistance of the duct.

To account for the trimming moment due to the water jet the position (height) of the thrust force $\Delta p \cdot A_{nozzle}$ is specified at the center of the impeller disk. SHIPFLOW then automatically trims the hull to balance the moment created by the total resistance force and the thrust.

Preliminary Results

General appearance of the panelization and the pressure coefficient, C_p, contour inside the ducting channel is shown in Fig. (7).

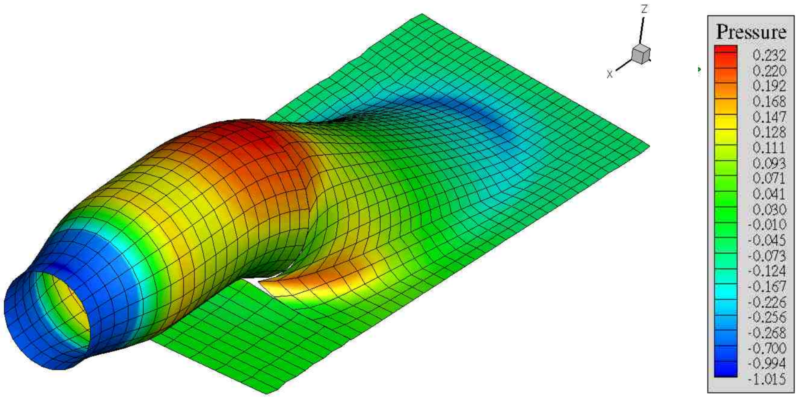

Fig. (7) General presentation of panels forming the intake geometry and the pressure coefficient distribution from SHIPFLOW (i.e. without the pressure jump at the impeller)

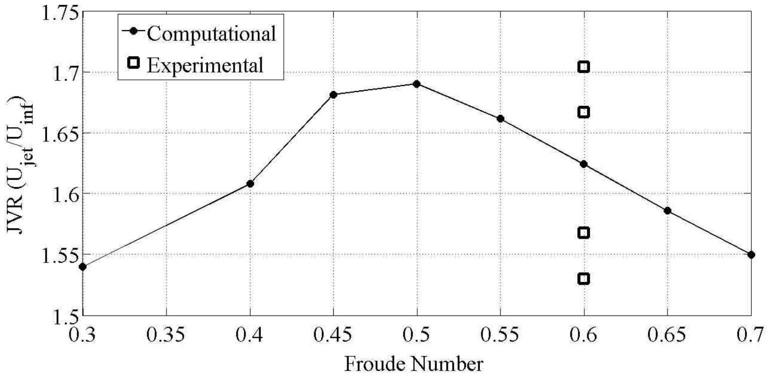

Fig. (8) Jet velocity ratio against Froude number variations

Fig. (8) demonstrates the variation of jet velocity ratio, JVR, against Froude number. The solid line is obtained using the pressure jump approach and the experimental data is extracted from [5]. Each square symbol is from a separate test. According to Fig. (8), the computed JVR value is within the range of data from the test. At low Froude numbers JVR is low comparing to its value at the intermediate Froude numbers. JVR starts to decrease after *Fn=0.5*. Fig. (9) depicts the variation of volumetric flow rate with Froude number. It is seen that the, volume flow rate through the system gradually increases with Froude number to generate the required momentum flux for propelling the craft.

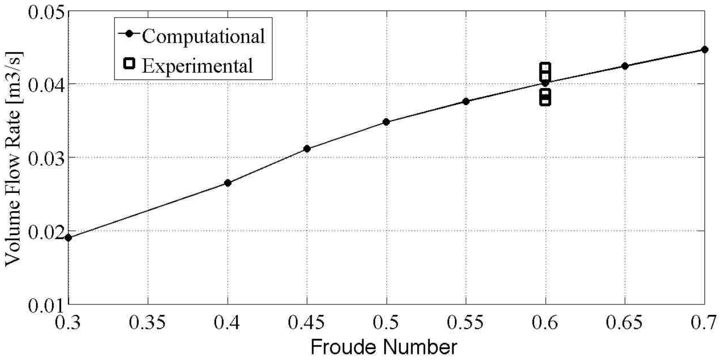

Fig. (9) Volume flow rate against Froude number variations

Conclusion

A different approach than the conventional momentum flux method for investigating the waterjet systems analysis is introduced. The advantage of the pressure jump approach in comparison with the momentum flux method is the fact that in this approach it is not required to consider the part of the control volume stream tube below the hull, which is one of the major complications when analysing the waterjet systems experimentally and also numerically. Agreement of the preliminary results with the test data is promising.

References:

[1] John Allison, Marine Waterjet Propulsion, SNAME Transaction, vol. 101, pp. 275-335, 1993.

[2] Tom van Terwisga; Waterjet-Hull Interaction; PhD thesis, Delft Technical University, ISBN90-75757-01-8, April, 1996.

[3] Norbert Willem Herman Bulten; Numerical Analysis of a Waterjet Propulsion System, PhD thesis, Eindhoven University of Technology, 2006.

[4] Tom van Terwisga, John George Hoyt III, Mehrdad Zangeneh, Gun-II Choi, Niclas Ollofson, Daniele Ranocchia, Dmitry Sadovinkov; The Specialist Committee on Validation of Waterjet Test Procedures: Final Report and Recommendations to the 23rd ITTC, Proceedings of 23rd ITTC, vol. 2, pp 387-415, 2002.

[5] Tom van Terwisga, John Georg Hoyt III, Daniele Ranocchia, Reima Aartojärvi, Ho Hwan Chun, Elena Semionycheva, Mehrdad Zanganeh, Alan Becnel; The Specialist Committee on Validation of Waterjet Test Procedures, Proceedings of the 24th ITTC, 2005.

[6] Ding Jiang-Ming, Wang Yong-sheng; Research on Flow Loss of Inlet Duct of Marine Waterjets; Journal of Shanghai Jiatong University (Since), vol. 15, issue 2, pp. 158-162, 2010.

[7] Flowtech International AB, SHIPFLOW Users Manual, 2007.

FLUID-STRUCTURE INTERACTION USING OPEN SOURCE SOFTWARE

A. Feymark† & A. Cesur‡
†Dept. of Shipping and Marine Technology,
Chalmers University of Technology, SE-412 96, Göteborg, Sweden
‡Division of Fluid Mechanics, Dept. Energy Sciences, LTH
Lund University, Box 118, SE-22100, Lund, Sweden

Introduction and Background

Since the first ships saw the light of day the influence of the sea on the ship has been apparent and naval architects have been forced to take the impact of the corresponding strains and stresses into consideration. Although a complete model of the dynamic behavior of a ship would be of great interest and importance, the field has been divided into distinct subject areas. However, as the computational models and resources keep evolving increasingly complex problems, covering several subject areas, may be considered. The term hydroelasticity was first introduced by Heller and Abramson, [1], as the naval counterpart to aeroelasticity and falls under Fluid-Structure Interaction (FSI), which is the dynamic state of a structure modified by fluid force acting on it and the structural response, in return, affecting the surrounding fluid. Hydroelasticity is a broad area and of great importance in the analysis and prediction of e.g., wave-induced vibrations, such as springing, whipping and slamming, propeller singing, flexible propeller blades, signature levels from submarines, structural fatigue, wave induced movements and loads of marine structures, properties and sea loads on rapidly moving vessels and human comfort and fatigue. Many of these problems are today, using a simple flow model based on potential flow theory, reasonably and satisfactorily treated. However, in some cases the complexity of these FSI problems puts greater demands on the modeling and resolution, needed to produce accurate and reliable predictions and we will here refer to these more demanding problems. The mathematical model for the fluid is based on the Navier-Stokes Equations (NSE), which in most practical cases cannot be solved analytically, and therefore Computational Fluid Dynamics (CFD), in which the equations are solved numerically, is most frequently used. Due to the wide range of scales in most turbulent flows full scale Direct Numerical Simulation (DNS) is too expensive and therefore other methods dealing with a reduced set of scales are required. The industrial standard today is Reynolds Averaged Navier-Stokes (RANS) and Unsteady Reynolds Averaged Navier-Stokes (URANS) in which the flow is divided into an averaged and a fluctuating part. In almost all cases the averaging is applied in the time domain making it a computationally cheap method but due to the large amount of modeling involved also less general. Moreover, the standard use of a time average assumes the mean flow to contain no (RANS) or only very slow variations with time (URANS), making it unreliable in other contexts. More viable methods includes Large Eddy Simulation (LES), Implicit Large Eddy Simulation (ILES) and Detached Eddy Simulation (DES), in which the large energy-containing scales are resolved on the grid, and only the influence of the small subgrid scales needs to be modeled. The suitable structural model on the other hand is dependent on both structural material and applied forces, and as new materials and more computational resources are developed new models keep appearing. In most applications involving large solid deformations nonlinear effects may not be omitted and a nonlinear model is required. However, if the deformations are small it might be possible to acquire accurate and reliable results using simply a linear model. The most common approach used to solve these equations is the Finite Element Method (FEM).

In the on going work we aim at developing a parallelized computational method, capable of producing accurate and reliable predictions in order to investigate FSI related problems within the area of Shipping and Marine Technology. This will be done creating an interface between two different open source codes OpenFOAM, [2], for fluid dynamics and OOFEM, [3], used for structural analysis.

Computational Models

Flow equations

The computational flow model consists of the incompressible Navier-Stokes equations, extended to handle moving grids, comprising the balance equations of mass and momentum for a linear viscous fluid, e.g. [4],

$$\partial_t(\mathbf{v})+\nabla\cdot(\mathbf{v}\otimes(\mathbf{v}-\mathbf{v_m}))=-\nabla \mathrm{p}+\nabla\cdot\mathbf{S},\quad \nabla\cdot\mathbf{v}=0, \tag{1}$$

where $\mathbf{v}$ is the velocity, $\mathbf{v}_\mathrm{m}$ the grid velocity, p the pressure, $\mathbf{S}=2\nu\mathbf{D}$ the viscous stress tensor, $\mathbf{D}=\frac{1}{2}(\nabla\mathbf{v}+\nabla\mathbf{v}^T)$ the rate-of-strain tensor and ν the viscosity.

Large Eddy Simulation (LES)

In LES, all scales larger than the grid spacing are resolved with a space-time accurate algorithm and only the effects of the small, unresolved eddy scales are modeled. The LES equations are derived from Eq. (1) by low-pass filtering, using a pre-defined filter kernel $G = G(\mathbf{x},\Delta)$, in which Δ is the filter width so that,

$$\partial_t(\bar{\mathbf{v}}) + \nabla\cdot(\bar{\mathbf{v}}\otimes(\bar{\mathbf{v}}-\mathbf{v}_{\mathbf{m}})) = -\nabla\bar{\mathrm{p}} + \nabla\cdot(\bar{\mathbf{S}}-\mathbf{B}) + \mathbf{m},\quad \nabla\cdot\bar{\mathbf{v}} = m, \tag{2}$$

where overbars denote the low-pass filtered dependent variables. The additional terms separating Eq. (2) from Eq. (1) are the subgrid stress tensor $\mathbf{B} = (\overline{\mathbf{v}\otimes\mathbf{v}} - \bar{\mathbf{v}}\otimes\bar{\mathbf{v}})$, representing the influence of the small, unresolved scales on the large, resolved scales and the commutation error terms, $\mathbf{m} = \nabla\cdot\overline{(\mathbf{v}\otimes\mathbf{v}+p\mathbf{I}-\mathbf{S})} - \overline{\nabla\cdot(\mathbf{v}\otimes\mathbf{v}+p\mathbf{I}-\mathbf{S})}$ and $m = \nabla\cdot\bar{\mathbf{v}} - \overline{\nabla\cdot\mathbf{v}}$, resulting from changing the order between differentiation and filtering. Although both types of terms contribute to the LES closure problem, we here neglect **m** and *m* and focus the modeling effort on **B**.

Modern explicit LES closures can broadly be classified as functional or structural models, [5]. Functional Models are designed to mimic the kinetic energy cascade from large to small-scales that is considered a 'universal' physical mechanism in fully developed turbulent flows. The main effect of the energy cascade is the energy drain at the resolved scales by the subgrid scales, $\varepsilon_{\mathrm{t}} = -\mathbf{B}\cdot\bar{\mathbf{D}}$. An empirical model for ε_{t} is the use of a subgrid viscosity, ν_{k}, the amplitude of which is calibrated to enforce the desired mean energy cascade rate. The resulting contribution in the LES equations, Eq. (2), then becomes $\mathbf{B} \approx -2\nu_{\mathrm{k}}\bar{\mathbf{D}}$. To close these models, the subgrid viscosity, ν_{k}, needs to be prescribed by a model of the form $\nu_{\mathrm{k}} \propto \ell_{\mathrm{k}}v'_{\mathrm{k}}$, where ℓ_{k} is the subgrid length scale and v'_{k} the subgrid velocity. A number of subgrid viscosity models are available, see [6] for a comprehensive review, including the Smagorinsky (SMG) model, [7], the Dynamic Smagorinsky model (DSMG), [8], the Structure Function (SF) model, [9], the One Equation Eddy Viscosity (OEEVM) model, [10] and the Localized Dynamic *k*-Equation Model (LDKM), [11]. In this work we utilize the OEEVM for which the subgrid viscosity is given by, $\nu_{\mathrm{k}} = c_{\mathrm{k}}\Delta k^{1/2}$, and the subgrid kinetic energy, *k*, is estimated by solving a separate modeled transport equation of the form,

$$\partial_{\mathrm{t}}(k) + \nabla\cdot(k(\bar{\mathbf{v}}-\mathbf{v}_{\mathrm{m}})) = 2\nu_{\mathrm{k}}\,\|\bar{\mathbf{D}}\|^2 + \nabla\cdot(\nu_{\mathrm{k}}\nabla k) - \varepsilon,\quad \varepsilon = c_{\varepsilon}k^{3/2}/\Delta \tag{3}$$

where c_{k} and c_{ε} are model coefficients. In OEEVM, c_{k} and c_{ε} are obtained from integrating the energy spectra assuming an infinitely long inertial sub-range, [4], resulting in that $c_{\mathrm{k}} \approx 0.07$ and $c_{\varepsilon} \approx 1.05$.

Wall Modeling for LES

If the computational grid is too coarse to resolve the flow in the wall boundary layer, which is likely to be the case in most engineering flows, a model must be used to account for the presence of the wall. Such models are usually based on statistical arguments together with the mean velocity profiles of the viscous sub-layer and the logarithmic region, [4]. The majority of these methods, need the mean wall shear stress, $\langle\tau_{\mathrm{w}}\rangle$, to be specified, which may not be uncomplicated. As suggested by Fureby *et al*, [12], more versatile methods, capable of seamlessly handling unstructured grids and complex geometries, can be developed from the filtered boundary layer equations. Through simplification of these by assuming zero streamwise pressure gradient and convective transport, they integrate analytically to the law-of-the-wall. This relation can be used to modify the subgrid model by adding a subgrid wall-viscosity, ν_{BC}, to all the control volumes adjacent to the wall, so that the effective viscosity, $\nu + \nu_{\mathrm{BC}}$, becomes $\nu + \nu_{\mathrm{BC}} = \tau_{\mathrm{w}}/(\partial v_{\mathrm{y}}/\partial y)_{\mathrm{P}} = u_{\tau}y_{\mathrm{y,P}}/v^{+}_{\mathrm{y,P}}$, where the subscript P denotes evaluation at the first grid point away from the wall. This wall-model can be combined with any (explicit or implicit) subgrid model.

Numerical Methods for LES

OpenFOAM, [2], is based on an unstructured collocated Finite Volume (FV) method in which the discretization uses Gauss theorem together with a multi-step time-integration method, [13]. The resulting discretized mass and momentum equations, respectively, takes the form,

$$\begin{cases} \sum_{\mathrm{f}}(\bar{\mathbf{v}}\cdot d\mathbf{A})^{\mathrm{n+1}}_{\mathrm{f}} = 0, \\ \sum_{\mathrm{i=0}}^{\mathrm{m}}(\alpha_{\mathrm{i}}(\bar{\mathbf{v}})^{\mathrm{n+1}}_{\mathrm{P}} + \frac{\beta_{\mathrm{i}}\Delta t}{V_{\mathrm{P}}}\Sigma_{\mathrm{f}}[((\bar{\mathbf{v}}_{\mathrm{f}}-\mathbf{v}_{\mathrm{m}})\cdot d\mathbf{A}_{\mathrm{f}})\bar{\mathbf{v}}_{\mathrm{f}}) - (\nu_{\mathrm{eff}})_{\mathrm{f}}(\nabla\bar{\mathbf{v}})_{\mathrm{f}}]^{\mathrm{n+i}}) = \Delta t\sum_{\mathrm{i=0}}^{\mathrm{m}}(\beta_{\mathrm{i}}(-(\nabla\bar{p})^{\mathrm{n+i}}_{\mathrm{P}})), \end{cases} \tag{6}$$

in which $\bar{\varphi}_\mathrm{P} = V_\mathrm{P}^{-1} \int_{\Omega_\mathrm{P}} (\varphi) dV$ defines the discrete representation of φ, with V_P being the volume of control volume P, $d\mathbf{A}_\mathrm{f}$ the area of cell face f of control volume P, Δt the time step and α_i and β_i being coefficients of the time integration scheme. Here, ν_eff denotes the effective viscosity being $\nu + \nu_\mathrm{k}$ for explicit closures. More specifically, the time integration is here performed by a semi-implicit 2nd order two-point backward differencing scheme, with m=2, $\alpha_0=0.5$, $\alpha_1=-2$, $\beta_0=\beta_1=0$ and $\beta_2=1.0$, whereas the convective fluxes, $\bar{\mathbf{v}}_\mathrm{f}$, are approximated by interpolation between adjacent control volumes. The velocity gradient, $(\nabla \bar{\mathbf{v}})_f$, is decomposed into orthogonal and non-orthogonal parts to minimize the non-orthogonality error. Central difference approximations are applied to the orthogonal part whilst face interpolation of the gradients of the dependent variables is used for the non-orthogonal parts. A Poisson equation is used to handle the pressure-velocity coupling and solved using the PISO (Pressure Implicit with Splitting of Operators) procedure with a modified Rhie & Chow interpolation for cell-centered data, [14]. The equations are solved sequentially, with iteration over the explicit source terms to obtain fast convergence.

When a moving or deforming computational grid is used, the temporal derivatives introduce a rate of change of the cell volume and a mesh motion flux, due to the mesh convection. The relationship between the temporal derivative and the change in cell volume must satisfy the space conservation law, $\partial_\mathrm{t} \int_\Omega (\mathbf{v}) dV = \int_\Gamma (\mathbf{v}_\mathrm{m} \cdot \mathbf{n}) dS$, [15], in order to conserve mass. The change in cell volume is calculated from the sum of the mesh motion fluxes, $\Sigma_\mathrm{f} (\mathbf{v}_\mathrm{m} \cdot \mathbf{n})_\mathrm{f}$, during the current time step rather than form the grid velocity, $\mathbf{v}_\mathrm{m}$, making it consistent with the cell volume calculation. Here the mesh points at the wall are given by the displacement of the solid and the resulting fluid mesh deformation is accounted for using a Laplace equation where a diffusion parameter, γ, controls the displacement of the internal grid points.

Nonlinear Finite Element Formulation

The nonlinear finite element formulation describing the structural governing equations is based on the principle of virtual work expression, [16]. The use of a hyperelastic material for constitutive behavior allows the following relationship for the virtual work expression for solid mechanics in the reference state, i.e. the balance between the time rate of change of momentum and the resultant force acting on the body

$$\int_v \rho \, \delta \mathbf{u}^T \ddot{\mathbf{u}} dv + \int_v \hat{\mathrm{E}}^T \mathrm{S} dv - \int_v \delta \mathrm{u}^T \mathrm{t} ds - \int_v \delta \mathrm{u}^T \mathrm{b} dv = 0, \tag{7}$$

which is based on the second Piola-Kirchhoff stress tensor and Green-Lagrange's strain tensor in order to allow for large deformations. The corresponding FE formulation, [17], is approximated as

$$\mathbf{c}^T (\int_v \rho \mathbf{N}^T \ddot{\mathbf{u}} dv + \int_v \mathbf{B}^T \mathrm{S} \, dv - \int_s \mathbf{N}^T \mathbf{t} \, ds - \int_v \rho \mathrm{N}^T \mathbf{b} \, dv) = 0, \tag{8}$$

where the displacement field, **u**, and the arbitrary virtual displacements, $\delta \mathbf{u}$, are approximated by the shape functions, **N**, as

$$\mathbf{u}(\mathbf{x},t) = \mathbf{N}(\mathbf{x}) \mathbf{a}(t), \quad \delta \mathbf{u}(\mathbf{x},t) = \mathbf{N}(\mathbf{x}) \mathbf{c}(t) \tag{9}$$

and **a** is the nodal displacement vector. Evidently, Eq. (7) describes the linear momentum of the system in a weighted sense for which the system of equations has to be solved for. Depending on the specific problem a suitable solution procedure has to be formulated. Restricting the physical problem to dynamic loading situations with a certain damping property the following set of equations can be formulated:

$$\mathbf{M} \ddot{\mathbf{a}} + \mathbf{C} \dot{\mathbf{a}} + \mathbf{F}_\mathrm{int} - \mathbf{F}_\mathrm{ext} = 0, \tag{10}$$

where **M** is the mass matrix, **C** the damping matrix, $\mathbf{F}_\mathrm{int}$ the internal load vector and $\mathbf{F}_\mathrm{ext}$ the external load vector.

Numerical Method for Structure

The structural parallel solver in OOFEM, *PNLDEIDynamic*, utilizes a parallel explicit nonlinear dynamic integration scheme, where the governing equilibrium equations, Eq. (10), are discretized using a central difference time-stepping algorithm. Written in incremental form, it reads

$$(\mathbf{M} \frac{1}{\Delta t^2} + \mathbf{C} \frac{1}{2\Delta t}) \Delta \mathbf{a}_t = \mathbf{F}_t^\mathrm{ext} - \mathbf{F}_t^\mathrm{int} + (\mathbf{M} \frac{1}{\Delta t^2} - \mathbf{C} \frac{1}{2\Delta t}) \Delta \mathbf{a}_{t-\Delta t} \tag{11}$$

where $\Delta\mathbf{a}_t = \mathbf{a}_{t+\Delta t} - \mathbf{a}_t$, $\mathbf{F}_{\mathrm{t}}^{\mathrm{ext}}$ is the external load vector, and $\mathbf{F}_{\mathrm{t}}^{\mathrm{int}}$ is the vector of internal forces at time *t*. The mass matrix is diagonalized and a damping matrix proportional to the mass matrix is assumed, $\mathbf{C} = \alpha\mathbf{M}$. The discretized governing equations, Eq. (11), are solved for incremental displacements, $\Delta\mathbf{a}_t$, using inversion of the diagonal mass matrix, [18]. From given displacement increment vectors $\Delta\mathbf{a}_t$ and $\Delta\mathbf{a}_{t-\Delta t}$, the corresponding velocity and acceleration vectors are computed using,

$$\dot{\mathbf{a}}_t = (\mathbf{a}_t + \mathbf{a}_{t-\Delta t})/(2\Delta t), \quad \ddot{\mathbf{a}}_t = (\mathbf{a}_t + \mathbf{a}_{t-\Delta t})/(\Delta t^2). \tag{12}$$

For parallel processing the *PNLDEIDynamic* solver is able to utilize both *nodecutmode* and *elementcutmode* partitioning schemes, [19].

The Coupling

Solvers used for FSI problems may be divided into two groups: monolithic and partitioned. In principle one may use either approach, however in this work the partitioned approach has been used in order to benefit from software already developed specifically for solving either the flow equations or the structural equations. Thus, the focus of the development lies on creating an interface connecting both solvers in a way that ensures stable and accurate simulations. To facilitate the procedure, the interface surface meshes on the fluid and solid side have been chosen to have the same topology that is the same number of nodes and faces. The major benefit is of course that no interpolation is needed in the transfer between the two solvers. The partitioned approach may be further subdivided into weak and strong coupling. In Figure 1a the week coupling is described as follows; the time loop starts with an update of the fluid mesh according to the displacement field, at the interface, acquired from the solid solver, subsequently the fluid equations are solved for. The traction vector field is, thereafter, computed and transferred from the fluid solver to the solid solver. Next the time is updated and if time, t, is less then the user defined simulation end time, T, the whole procedure is repeated. The weak coupling, in general, requires a smaller time step for numerical stability as compared to the strong coupling approach [20]. The strong coupling, on the other hand, may be preferred due to its often better stability characteristics. Nevertheless, under feasible conditions the weak coupling approach is also usable. The preferable choice is to be examined in future work.

The moving of the fluid mesh requires the solid displacement to be transferred to the fluid solver, something that is not trivial, especially not in parallel. The problem has here been addressed using the Portable, Extensible Toolkit for Scientific Computation (PETSc), [21]. The input needed by PETSc is the locally accessible data and an array with indices corresponding to global ghost points. The same procedure is used to transfer the fluid forces to the solid solver.

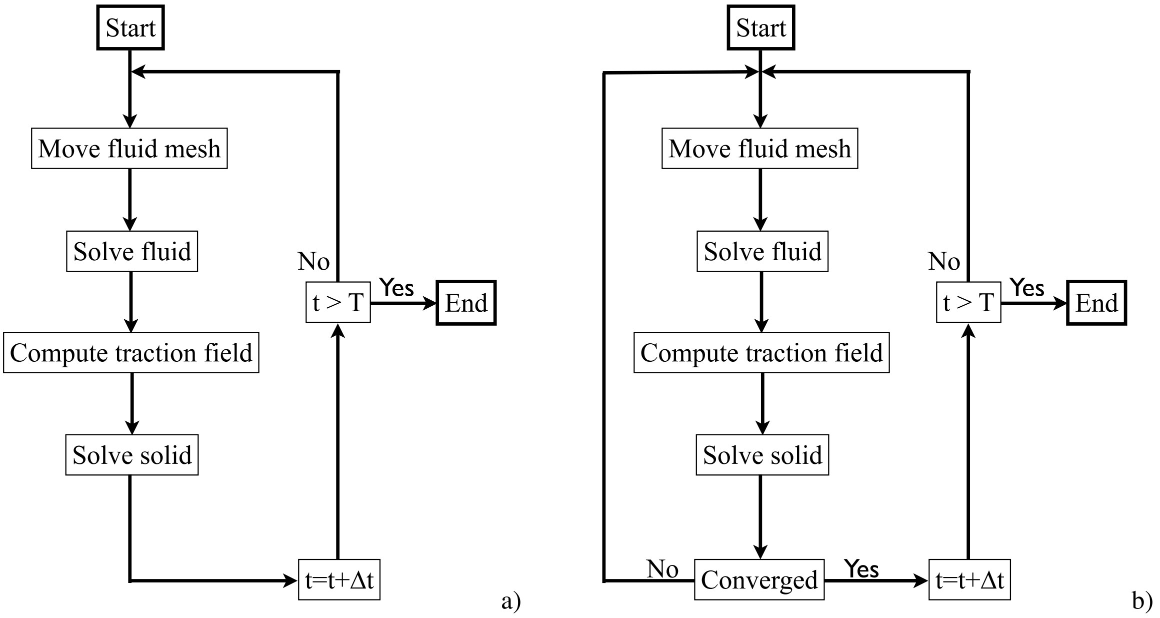

Figure 1. Schematic of weak coupling, a), and strong coupling, b).

Preliminary results and future work

Despite the current lack of verification of the code, and validation of the method, we will here present some early FSI predictions of a cantilever in a freestream, [22]. The cantilever, with thickness D = 0.2 m, is placed along the centerline, 5D from the inlet, in a domain measuring (5D, 6D, 12.5D). The case is characterized by the inlet velocity, $U = 1\ \text{m/s}$, the Reynolds number, $\mathrm{Re} = 400$, the fluid density, $\rho_f = 100\ \text{kg/m}^3$, the Poisson number, $\nu = 0.3$, the Young's modulus, $\nu = 20 \cdot 10^6\ \text{Pa}$, and the solid density, $\rho_s = 300\ \text{kg/m}^3$. Figure 2a shows the pressure distribution around the cantilever, with almost constant pressure on the upstream and downstream side. In figure 1b the magnitude of the nodal displacement of the fluid mesh is shown. In Lorentzon, [22], the maximum amplitude of the displacement for this case was computed to be $1.4 \cdot 10^{-2}\ \text{m}$. As seen in Figure 2b we attain a maximum displacement of $1.2 \cdot 10^{-2}\ \text{m}$, which at this first stage is reasonably close.

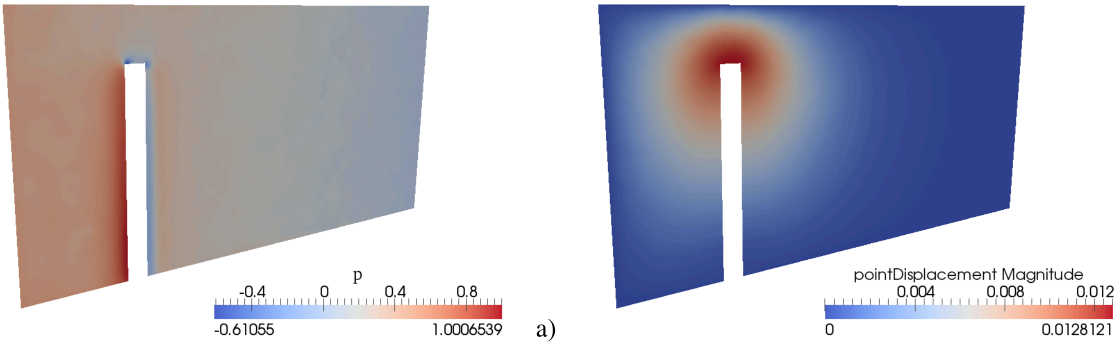

a) b)

Figure 2. The pressure distribution, a), and nodal displacement, b), in the fluid domain.

We thus consider the implementation correct enough to proceed with verification and validation, and assessing the way forward; which cases to use, in this process, are still to be decided. The main questions to look into, before turning to engineering problems, are, as mentioned in the previous sections, the matter of weak or strong coupling and whether replacing the currently used explicit structural solver with an implicit solver, with more flexible time stepping is beneficial.

References

[1] Heller, S. R., and Abramson, H. N., "Hydroelasticity: A New Naval Science," *Journal of the American Society for Naval Engineers*, Vol. 71, No. 2, 1959, pp. 205–209.
doi: 10.1111/j.1559-3584.1959.tb02326.x

[2] Weller, H. G., Tabor G., Jasak, H., and Fureby, C., "A Tensorial Approach to Computational Continuum Mechanics Using Object Oriented Techniques", *Computers in Physics*, Vol. 12, No. 6, 1998, pp. 620-631.
doi: 10.1063/1.168744

[3] B. Patzák and Z. Bittnar., "Design of Object Oriented Finite Element Code", *Advances in Engineering Software*, Vol. 32, No. 10-11, 2001, pp. 759-767.
doi: 10.1016/S0965-9978(01)00027-8

[4] Pope, S. B., *Turbulent Flows*, Cambridge University Press, Cambridge, England, UK, 2000.
doi: 10.2277/0521598869

[5] Sagaut, P., *Large Eddy Simulation for Incompressible Flows*, 3nd ed., Springer, Berlin, 2006.
doi: Sagaut, P., Large Eddy Simulation for Incompressible Flows, 3nd ed., Springer, Berlin, 2006.

[6] Grinstein, F. F., Margolin, L., and Rider, B. Implicit Large Eddy Simulation: Computing Turbulent Fluid Dynamics, 1st ed., Cambridge University Press, Cambridge, England, UK, 2007.
doi: 10.2277/052186982X

[7] Smagorinsky, J., "General Circulation Experiments With the Primitive Equations I. The Basic Experiment," *Monthly Weather Review*, Vol. 91, No. 3, 1963, pp 99-164.
doi: 10.1175/1520-0493(1963)091<0099:GCEWTP>2.3.CO;2

[8] Germano, M., Piomelli, U., Moin, P., Cabot, H. W., "A Dynamic Subgrid-Scale Eddy Viscosity Model," *Physics of Fluids*, Vol. 3, No. 7, 1991, pp. 1760-1765.
doi: 10.1063/1.857955

[9] Metais, O., and Lesieur, M., "Spectral Large Eddy Simulation of Isotropic and Stably Stratified Turbu-

lence," *Journal of Fluid Mechanics*, Vol. 239, 1992, pp. 157-194.
doi: 10.1017/S0022112092004361

[10] Menon, S., and Kim, W.-W., "High Reynolds Number Flow Simulations Using the Localized Dynamic Subgrid-Scale Model," *34th AIAA Aerospace Sciences Meeting and Exhibit,* Reno, Nevada, Jan. 15-18, AIAA-1996-425, 1996.

[11] Lilly, D. K., "A Proposed Modification of the Germano Subgrid-Scale Closure Method," *Physics of Fluids*, Vol. 4, No. 3, 1992, pp. 633-635.
doi: 10.1063/1.858280

[12] Fureby, C., "On LES and DES of Wall Bounded Flows," *Ercoftac Bulletin,* Bulletin 72, 2007.

[13] Lambert, J. D., *Computational Methods in Ordinary Differential Equations*, 1st ed., John Wiley & Sons Inc, New York, 1973.

[14] Rhie, C. M., and Chow, W. L., "Numerical Study of the Turbulent Flow Past an Airfoil with Trailing Edge Separation," *AIAA Journal*, Vol. 21, No. 11, 1983, pp. 1525-1532.
doi: 10.2514/3.8284

[15] Demirdzic, I., and Peric, M., "Space Conservation Law in Finite Volume Calculations of Fluid Flow," *International Journal for Numerical Methods in Fluids*, Vol. 8, No. 9, 1988, pp. 1037-1050.
doi: 10.1002/fld.16500809068

[16] Krenk, S., *Non-linear Modeling and Analysis of Solids and Structures,* Cambridge University Press, Cambridge, England, UK, 2009.

[17] Ristinmaa M., and Ljung, C., *An introduction to stability analysis,* Dept. Solid Mechanics, Lund University, Lund, Sweden.

[18] Patzák, B., Rypl, D., and Bittnar, Z., "Parallel Explicit Finite Element Dynamics with Nonlocal Constitutive Models," *Computers and Structures*, Vol. 79, No. 26-28, 2001, pp. 2287-2297.
doi: 10.1016/S0045-7949(01)00069-4

[19] Krysl, P., and Bittnar, Z., "Parallel Explicit Finite Element Solid Dynamics with Domain Decomposition and Message Passing: Dual Partitioning Scalability," *Computers and Structures*, Vol. 79, No. 3, 2001, pp. 345-360.
doi: 10.1016/S0045-7949(00)00130-9

[20] Matthies, H.G., and Steindorf, J., "Partitioned strong coupling algorithms for fluid-structure interaction, " *Computers and Structures*, Vol. 81, No. 8-11, 2003, pp. 805-812.
doi: 10.1016/S0045-7949(02)00409-1

[21] Balay, S., Brown, J., Buschelman, K., Gropp, W. D., Kaushik, D., Knepley, M. G., Curfman-McInnes, L., Smith, B. F., and Zhang, H., 2011, http://www.mcs.anl.gov/petsc

[22] Lorentzon, J., "Fluid-Structure Interaction (FSI) Case Study of a Cantilever using OpenFOAM and DEAL.II with application to VIV," *M.Sc. Dissertation*, Division of Fluid Mechanics, Department of Energy Sciences, LTH, Lund University, Lund, Sweden, 2009.

COMPARING COMPUTED AND MEASURED SHIP WAVE LOAD DISTRIBUTIONS

Satu K. Hänninen, Tommi Mikkola, Jerzy Matusiak
Aalto University, School of Engineering, Department of Applied Mechanics, Marine Technology[1]

1 INTRODUCTION

Applying interface-capturing methods to a ship advancing in waves has an encouraging history, e.g. [1-7]. However, examples with short and steep encountered waves are still few. Marine Technology unit of Aalto University became interested in applying an interface-capturing method for such wave conditions as a part of our project on springing excitation [8-13]. The motivation on using a method, that allows arbitrary free-surface behaviour, relates to our observations of wave breaking in cases of significant springing loads.

This abstract gives comparisons of computed and measured 1st-3rd harmonic wave load distributions on the bow areas of two ships that advance in short and steep head waves. The purpose of these comparisons is to have a preliminary idea of the reliability of the computed results. The presented discussion reflects the challenge of modelling severe deformation of encountered waves on a hull and the influence of this on the predicted wave loads.

2 FLOW CASES

This study considers two passenger ships with different bow forms (*Ship A* and *Ship B*), Fig 1. The ships have different overall lengths, Table 1, but it is not relevant to this study, as the focus is in the flow behaviour on the bow area. The encountered head waves are steep (wave height / wave length = 0.08) and short compared with the ship lengths ($L_{wave}/L_{ShipA} = 0.16$ and $L_{wave}/L_{ShipB} = 0.15$). The observation area of the wave loads is given in Fig 2.

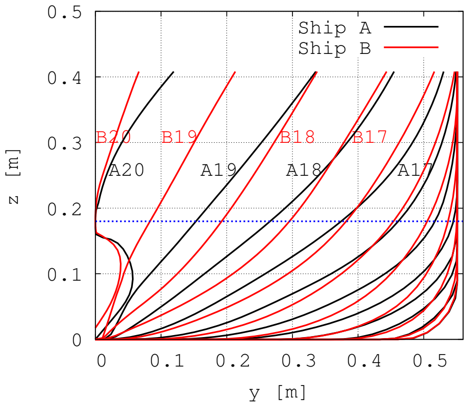

Figure 1: Frames 10-20

---

[1] P.O.Box 15300, FIN-00076 Aalto, Finland. E-mail: satu.hanninen@aalto.fi

Table 1: Ship parameters

Length, Ship A	6.69m
Length, Ship B	7.00m
Breadth B	1.10m
Draught T	0.18m
Speed V	1.47m/s

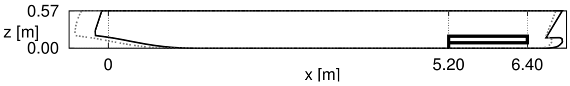

Figure 2: Observation area of wave loads (thick black line) with the two ship profiles.

3 COMPUTATIONS

The applied flow solver ISIS-CFD is an unstructured finite volume solver [14,15]. It uses a volume-of-fluid type interface-capturing method for the free-surface flows. In the present computations, the viscosity of the fluid is ignored and second-order discretisation schemes are applied (a backward scheme for the time derivatives, the GDS-scheme for the velocities, centered differencing with discontinuity modifications for pressure, the BICS-scheme for the volume fraction).

The unstructured hexahedral grids were generated according to the same principles for the two ships using only one half of a hull due to the symmetry of the flow cases. The cell sizes are chosen according to the encountered wave lengths (not ship lengths). The number of cells is 87.5 / wave length around the free-surface level. The grids have 6.09M and 6.59M cells in the case of *Ship A* and *Ship B*, respectively. The number of time steps is 368 / encounter period. The waves were generated on the inlet boundary with a numerical wave boundary condition. Further details on the computational setups are given in [13].

The vertical frame forces are calculated on 30 frames within the observation area. One frame is presented with the grid points located within a thin strip around a particular frame. There are 35-72 points within a strip depending on the local grid around the selected frame location. The frame forces are calculated with the trapezoidal rule using the pressure values in these grid points and the relative distances of these points (y-direction). The calculation of the frame forces is explained in detail in [13].

4 MEASUREMENTS

The measurements of the present two flow cases are a part of a large model-test campaign on ship-wave interaction in head waves [9]. They were done in the towing tank of Marine Technology unit of Aalto university in 2008. In the tests, the waves were generated with a plunger type wave maker that moves vertically in one end of the tank. On the other end of the tank, a sloping beach acted as a wave damper. The carriage of the tank towed a model with the chosen velocity.

The local pressures on the bow area were measured with pressure sensors on eight frames. Within the vertical observation area given in Fig 2, there were two sensors per frame. The sampling frequency of the sensors was 1057Hz.

5 RESULTS

5.1 Encountered waves on hull

Fig 3 gives an example of the instant wave behaviour on the ship bows. Both the computed and the measured results show that free-surface level deforms differently on the hull of these two bow shapes. The free-surface behaviour on *Ship A* includes clear deformation with water splash, while the wave deformation on *Ship B* is more moderate.

For *Ship A*, the computed propagation of the water splash along the bow area is shown at four ship cross-sections in Fig 4.

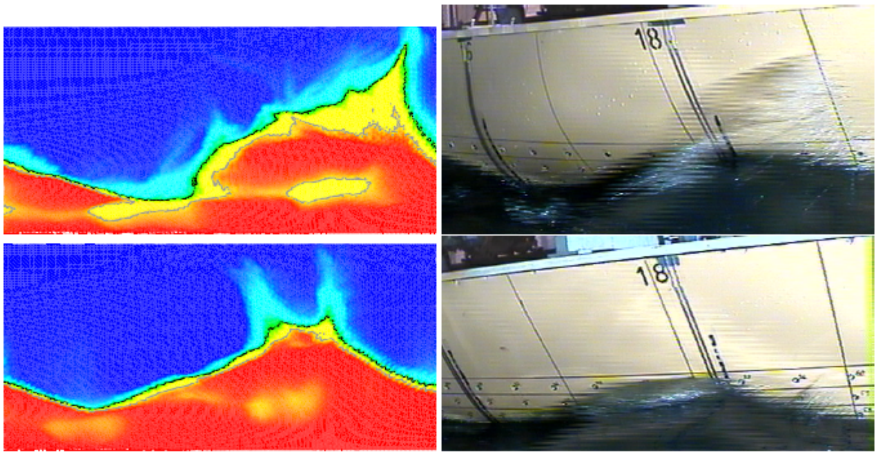

Figure 3: An instant free-surface level between x ≈5.2m and x ≈6.4m. Above: *Ship A*, below: *Ship B*, left: computed result (red indicates water and blue air), right: measured result.

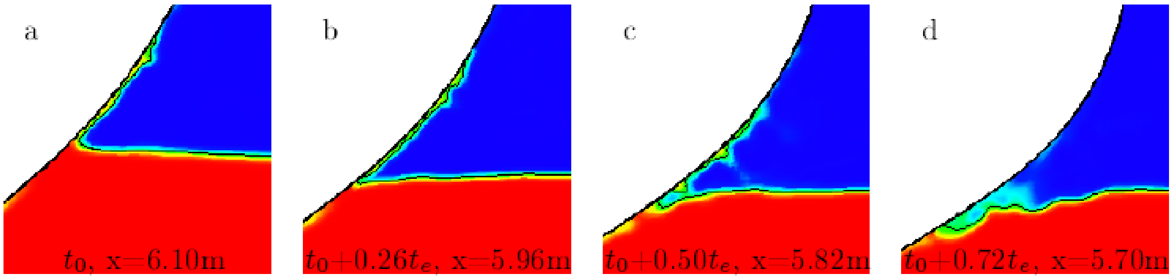

Figure 4: *Ship A*: propagation of the water splash at four ship cross-sections. These results are taken from [13].

5.2 Wave load distribution

Fig 5 compares the computed and the measured wave load distributions for *Ship A* and *Ship B*. In the case of *Ship A*, the computed and the measured 1$^{\text{st}}$ harmonic wave loads behave differently as a function of x, especially in the middle part of the observation area. In the case of *Ship B*, the 1$^{\text{st}}$ harmonic wave loads behave rather similarly as a function of x. As for the 2$^{\text{nd}}$ and 3$^{\text{rd}}$ harmonic results, the computed and the measured load distributions seem to be rather similar, even if they differ locally. E.g. in the case of *Ship B*, the measured 2$^{\text{nd}}$ harmonic distribution has two humps, which do not exist in the computed results.

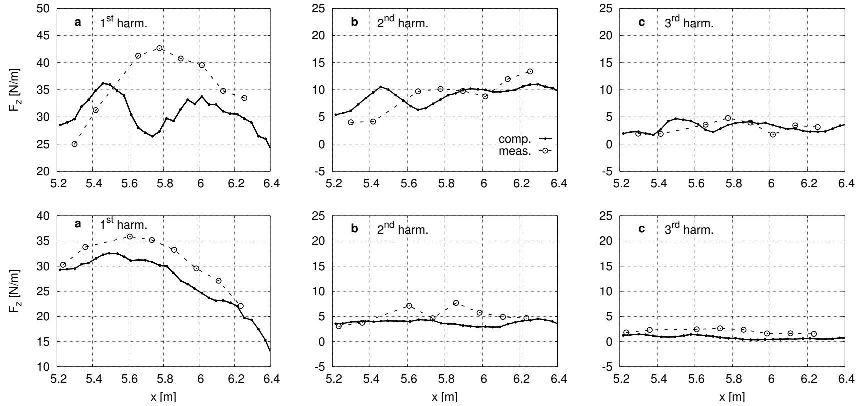

Figure 5: $1^{\text{st}} - 3^{\text{rd}}$ harmonic wave load distributions on the ship bow area. Above: *Ship A*, below: *Ship B*

6 DISCUSSION AND CONCLUSIONS

The present results indicate that the agreement of the computed and the measured results is different for the two bow forms. This is most clearly seen in the comparison of the computed and the measured 1^{st} harmonic wave load distributions: The computed and the measured distributions behave similarly as a function of x for slender *Ship B*, but the forms of the computed and measured distributions are clearly different for fuller *Ship A*.

The present results indicate that the flow case *Ship A* should be studied more carefully to understand why the computed and the measured 1^{st} harmonic distributions are different. Why the computation gives a local hollow in the middle part of the distribution, which is a consistent hump according to the measurement? There seems to be three possible reasons: an insufficient discretisation resolution in the computation, an insufficient numerical model and an insufficient accuracy in the measurements.

As for the effect of the discretisation resolution, the numerical accuracy of the present computation of *Ship A* has been studied in [13]. The computation was repeated with three discretisation resolutions, which showed that the hollow in the 1^{st} harmonic distribution becomes deeper with finer resolutions. Based on those three computations, it seems to be unlikely that refining the resolutions could remove the hollow. The study in [13] also showed that the deepening of the hollow with refining resolution relates to the modelling a water splash that travels along the hull. Around the location of the hollow in the 1^{st} harmonic wave load distribution, the remains of the splash (mixture of water and air) locate above the free-surface level at the same time when the wave elevation is in its lowest position, Fig 4d. The refining of the discretisation resolutions shows that the propagating splash becomes stronger with refinements, [13]. This applies also to the amount of the remains of the splash at the location of the hollow in the 1^{st} harmonic distribution. This means that the fluid density and also the local pressure increase above the free-surface level with refinements at an instant when the loading below the free-surface level is the smallest on the observed frame. As a consequence, the amplitude of the total frame force becomes smaller due to increased fluid density above the free-surface level. Thus, the hollow in the 1^{st} harmonic wave load distribution relates to the numerical modelling of a water splash that travels along the ship hull. Is the numerical model adequate for modelling such flow details?

As for the numerical model, the effect of fluid viscosity and surface tension were omitted in the present computations. Do they affect the behaviour of the water splash in the present flow case of *Ship A*? The modelling of the water splash includes two consecutive phases: the growth of the splash and its collapse. Due to the ship forward speed, the splash propagates on the hull during these phenomena. According to the computed results, the splash originates in the wave crest that encounters the ship near the ship fore perpendicular. When this wave crest travels somewhat further, some of the water mass is pushed higher and backwards (back towards the ship fore perpendicular) due to the ship hull form. After reaching its full height, the splash continues propagation towards the ship stern at the rear part of the propagating encountered wave and collapses simultaneously. It seems likely that the phase, where the viscous and the surface tension forces could have an effect on the splash, is the growth of the splash. They could perhaps restrain the spreading of the splash. As for the collapse of the splash, the behaviour of the interface capturing method (fluid becoming a mixture of water and air) may be more significant than the effect of these forces. It seems unlikely that the surface tension could act against the gravity force during splash falling.

In practice, the significance of different forces on a flow case can be evaluated using dimensionless parameters. The problem here is how to choose the essential characteristic measures from the point of view of the water splash. Normally, the main dimensions of the object should be used. The study [16] on water splash phenomena, for instance, has evaluated the importance of different forces using Froude, Weber and Ohnesorge numbers in the case of a two-dimensional wedge falling to water using the wedge width and the falling speed.

In the present case, if the viscous effect was included in the computational model, some practical trouble would appear. Could the viscous effect on a water splash propagating on a ship hull be modelled with e.g. a turbulence model that uses wall functions? What criteria should then be used when selecting e.g. y^+-value? If a test run showed that the numerical results are not affected by the viscous effect, would it be a reliable result or rather an indication that the modelling of viscous effect was not done correctly?

As for the next step of this study, the accuracy of the model-tests needs to be defined to find out the actual agreement of the computed and the measured results. This requires re-designing and repeating the model-tests, because the previous measurement does not allow uncertainty estimates. The task is challenging. Generating such steep waves means that their properties vary when they propagate in the towing tank. Small pressure amplitudes themselves are hard to measure. In addition to the estimation of the uncertainties of the frame forces, an important purpose is to observe the behaviour of the water splash in the case of *Ship A*.

7 ACKNOWLEDGEMENT

This work has been done with the fundings of Tekes (Finnish Funding Agency for Technology and Innovation), Aker Yards (now STX Europe), Academy of Finland and The Finnish Graduate School in Computational Fluid Dynamics. The financial support is gratefully acknowledged. The computational resources provided by CSC - the Finnish IT Center for Science is also gratefully acknowledged. The authors are thankful to Prof. Michel Visonneau and the CFD-team of ECN-CNRS for the discussions and the development of ISIS-CFD. Special thanks belong to Ragnar Linnas and Teemu Manderbacka for the model-tests.

REFERENCES

1. Sato Y, Miyata H, Sato T (1999) CFD simulation of 3-dimensional motion of a ship in waves: application to an advancing ship in regular heading waves. J Mar Sci Technol 4:108-116

2. Orihara H, Miyata H (2003) Evaluation of added resistance in regular incident waves by computational fluid dynamics motion simulation using an overlapping grid system. J Mar Sci Technol 8:47-60

3. CFDWS05 Tokyo (2005) Proceedings of CFD Workshop Tokyo 2005. Editor Takanori Hino, National Maritime Research Institute

4. Klemt M (2005) RANSE simulation of ship seakeeping using overlapping grids. Ship Technology Research 52:65-81

5. Carrica P, Wilson R, Stern F (2006) Unsteady RANS simulation of the ship forward speed diffraction problem. Comput Fluids 35:545-570

6. Carrica P, Wilson R, Noack R, Stern F (2007) Ship motions using single-phase level set with dynamic overset grids. Comput Fluids 36:1415-1433

7. Oberhagemann J, Holtmann M, el Moctar O, Schellin T, Kim D (2009) Stern slamming of LNG carrier. Journal of Offshore Mechanics and Arctic Engineering 131

8. Hänninen SK, Mikkola M (2008) Wave Excitation on a ship bow in short waves. 11th Numerical Towing Tank Symposium. 7.-9. Sept. 2008

9. Linnas R. (2008) Model tests of springing type wave loads on a bow of a cruise vessel. Master's thesis, Marine Technology, Department of Applied Mechanics, Helsinki University of Technology

10. Manderbacka, Tenovuo K, Matusiak J. (2008) Model Experiments of springing-type wave loads on a cruise vessel. 8th International Conference on Hydrodynamics. 30. Sept. -3. Oct. 2008

11. Mikkola M (2009) Simulation of forces on ship-like cross-sections in beam waves. TKK-AM-9, Marine Technology, Department of Applied Mechanics, Helsinki University of Technology

12. Kalske S (2010) Application of ray theory in prediction of wave excitation for cruise ships in short waves. AALTO-AM-19, Marine Technology, Department of Applied Mechanics, School of Engineering, Aalto University

13. Hänninen SK, Mikkola K, Matusiak M. On the numerical accuracy of the wave load distribution on a ship advancing in short and steep waves. Under review in J Mar Sci Technol

14. Queutey P, Visonneau M (2007) An interface capturing method for free-surface hydrodynamic flows. Comput Fluids 36: 1481-1510

15. Fine/Marine v2.0. Fine/Marine v2.0 (2007) Tutorial, Comprehensive description of the input data file for ISIS-CFD v2.0

16. Alam A, Kai H, Suzuki K (2007) Two-dimensional numerical simulation of water splash phenomena with and without surface tension. J Mar Sci Technol 12:59-71

Numerical Hull Series using CFD and Response Surfaces

Stefan Harries, Friendship Systems GmbH, Potsdam/Germany, stefan.harries@GL-group.com
Volker Bertram, FutureShip GmbH, Hamburg/Germany, volker.bertram@GL-group.com
Patrick Couser, Formation Design Systems Pty Ltd, Fremantle/Australia, patc@formsys.com
Fabian Tillig, SSPA Sweden AB, Göteborg/Sweden, fabian.tillig@sspa.se

Design knowledge can be gained in several ways. For example, an existing vessel may serve as a basis design from which a new vessel fitting the design requirements can be derived. Alternatively, designers have used "series" (based on systematic model tests). These are largely out of date, but the NPL series is still frequently used for fast boats. In essence, the same approach could be used based on "numerical basins" rather than model basins. The approach has been described in more detail in *Harries (2010), Couser et al. (2011).* We use here a megayacht as illustrative example, but the approach is generally applicable.

The design-space investigation comprises three main tasks:

1. Definition of a suitable parametric model to generate feasible design variants from a few key parameters
2. Numerical analysis of the vessel using simulation tools
3. Automation of vessel design variation, analysis, and post-processing

The FRIENDSHIP-Framework (FFW) was used for the parametric hull model, the automatic design variation and process control. The vessel's calm-water resistance was estimated using SHIPFLOW, whilst sea-keeping characteristics and hydrostatic stability using Seakeeper (linear strip theory method) and Hydromax. The rapid development of computer hardware and the advent of computer clusters and clouds mean that the hardware resources necessary for the type of numerical investigations described here are now accessible to even small design teams.

The general hull-form chosen for the example megayacht was a classical twin-screw design with bulbous bow and skeg. Appendages were not included at this initial phase of the design. The bulb was modelled in some detail, since it had a significant impact on the hull resistance. The bulb was blended into the main hull over a region of transition aft of the forward perpendicular. The main hull itself was split into fore- and aft-body regions joined at the section with maximum cross-sectional area. The model was parameterised using the parameters (free variables) given in Table I.

Table I: Parameters of parametric model with range of variation

	Min - Max		Min - Max
Length L_{PP}	68.00 – 72.00 m	*DWL* fullness coefficient	0.58 – 0.62
Beam [m]	14.00 – 14.25 m	Bulb area : midship area	0.092 – 0.098
C_M	0.82 – 0.89	Bulb fullness coefficient	0.75 – 0.85
Prismatic coeff. of forebody	0.60 – 0.63	Longitudinal position of section with max. cross-sectional area	44 – 48 % L_{PP}
DWL half angle of entrance	14° – 18°		

The flow simulations with SHIPFLOW were computed on a standard dual-core notebook and took 4 to 5 min per variant and speed. SHIPFLOW is essentially a nonlinear wave resistance method (panel method) with boundary layer theory calculation added. Fig.1 shows a typical panel arrangement and results. With a license for both cores, around 200 designs could be computed in one overnight job. For other applications with more focus on aftbody and appendages, full free-surface RANSE simulations would be required with an associated much higher computational effort. However, re-start options from similar solutions and larger computing power make full RANSE simulations absolutely feasible for industry purposes.

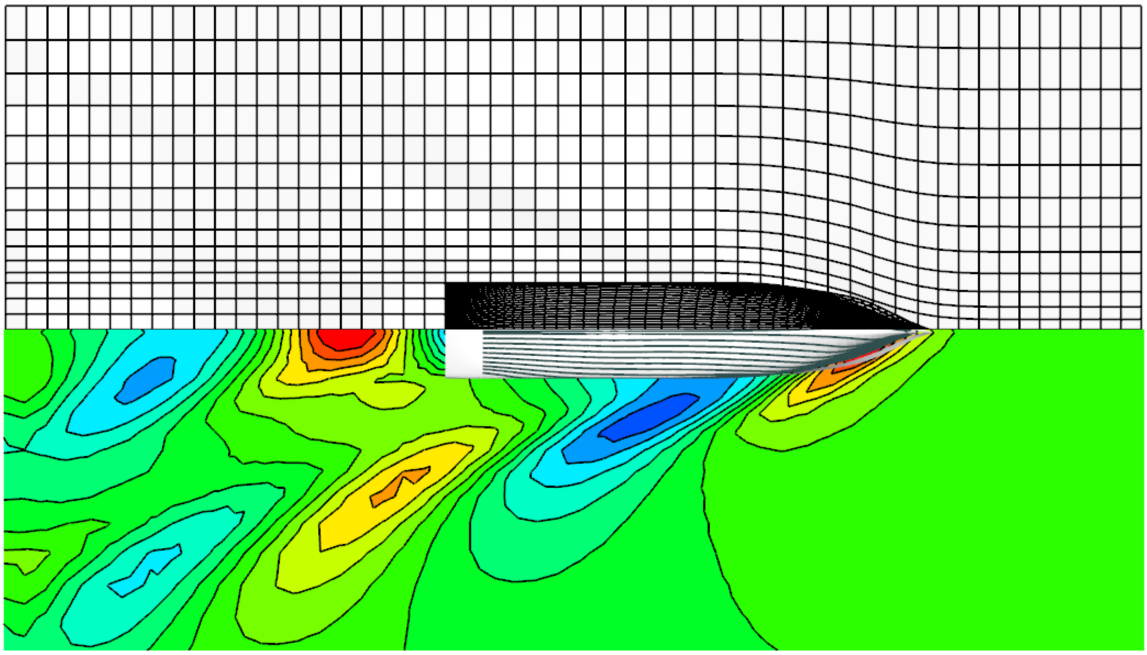

Fig. 1: Typical panel arrangement of free surface and hull with wave height contours and hull streamlines at $F_N = 0.393$

The vessel motions in waves were analysed for two scenarios, Table II. The motion sickness incidence (MSI) after 2 h exposure was computed at different longitudinal positions along the length of the vessel, following the standard O'Hanlon – McKauley approach. The performance measure extracted from the analysis was simply the minimum MSI along the length of the vessel for each of the two scenarios considered. The seakeeping model used 41 equally spaced sections through the hull. Conformal mapping was used to model the sections and compute the sectional added mass and damping in heave. The heave and pitch response amplitude operators (RAOs) were calculated at 200 frequencies and these were used to calculate the MSI. The calculations, for 200 variants, were computed on an average desktop computer in an overnight job controlled by the FFW.

Table II: Two scenarios considered for the sea-keeping calculations

	"Party"	"Cruise"
Vessel speed	0 kn	16 kn
Characteristic wave height	0.5 m	2.0 m
Modal period	2.0 s	7.1 s
Wave heading	Head seas	
Wave spectrum type	1-Parameter Bretschneider	

A small subset of intact-vessel stability criteria typically applied to megayachts was selected from the "Large Commercial Yacht Code", *NN (2007)*. These criteria are summarized in Table III. In order to obtain a meaningful performance measure of stability, the maximum vertical centre of gravity (*VCG*) at which all criteria were just passed was calculated for a range of displacements. The measure of performance used was the area under the maximum allowable *VCG* curve integrated over the displacement range of 1800t to 2600t. This measure was chosen because early in the design process, neither the *VCG* nor the displacement would be known with certainty; the measure gives some indication of the scope of *VCG* change that can be accommodated whist still passing the criteria. The analysis was performed in Hydromax using a range of heel angles at each displacement to calculate the *GZ* curve for a given *VCG*. The vessel was free-to-trim ensuring a longitudinal balance of *CG* and *CB* (the *LCG* being derived from the *LCB* of the upright vessel). The *VCG* was then systematically varied to determine the maximum value of *VCG* at which all the stability criteria were still passed. The calculations, for 200 variants, were computed in a matter of several hours.

Table III: Stability criteria considered

Section	Description	Required
11.2.1.1.1a	Area under *GZ* curve 0° to 30°	≥ 0.055 m·rad
11.2.1.1.1b	Area under *GZ* curve 0° to 40°	≥ 0.090 m·rad
11.2.1.1.2	Area under *GZ* curve 30° to 40°	≥ 0.030 m·rad
11.2.1.1.3	Maximum *GZ* at 30° or greater heel	≥ 0.2 m
11.2.1.1.4	Angle at which max. *GZ* occurs	≥ 25°
11.2.1.1.5	Initial metacentric height (GM_t)	≥ 0.15 m

The FFW and the simulation software come from different software vendors. In order to automate the task of generating design variants and analyzing their performance, it is essential that the software systems are able to communicate. The inter-process communication was implemented in Microsoft Windows Component Object Model (COM). COM allows access to suitably COM-enabled applications via a common interface from a variety of programming languages (C#, VBA, etc. and also the FFW's own macro language). Suitable macros were developed in FFW to export the hull geometry and then import this geometry and run the analyses in Hydromax and Seakeeper. The results of the analyses were then read back into the FFW for post-processing to calculate the final performance measures for each variant. Fig. 2 shows a screenshot of the FFW, Hydromax and Seakeeper in action.

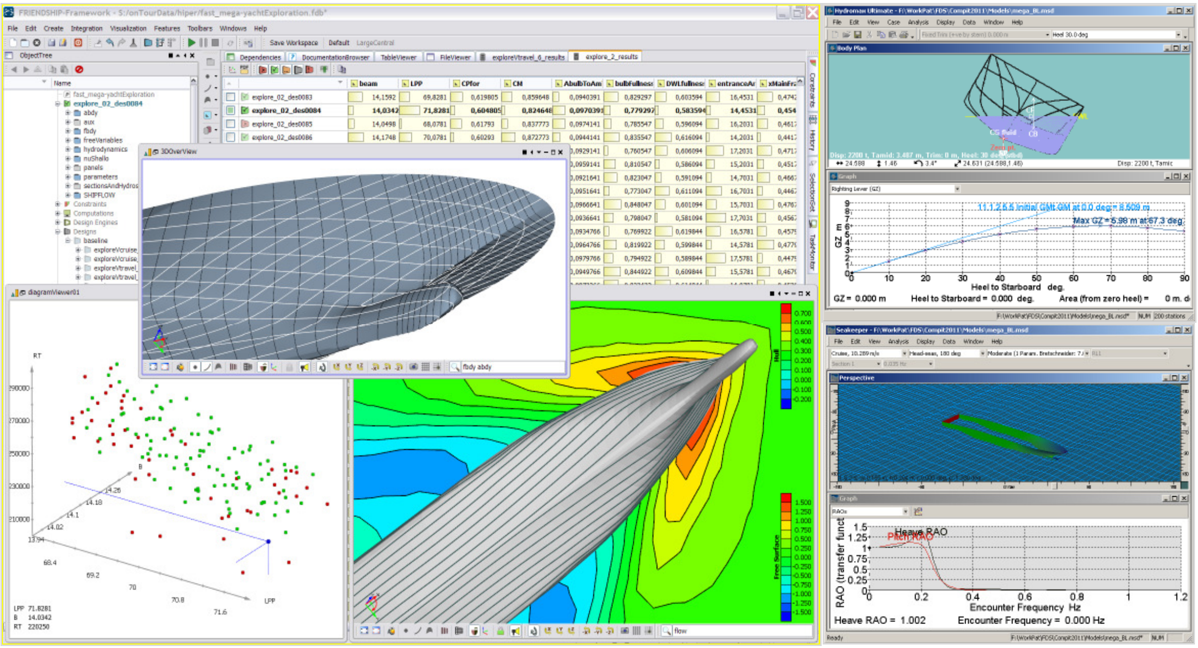

Fig. 2: Screenshot of FRIENDSHIP-Framework, Hydromax and Seakeeper in use

The design-space was investigated using a "Design of Experiments" approach to populate the domain with variants. A Sobol algorithm was used to give a quasi-random, yet uniform sampling of these variables over the desired range, Table I. The design-space exploration generates a large quantity of data and represents a significant computational effort (especially if simulation tools are used). There are several ways to build meta-models interpolating on the direct computations. These include: statistical regression, artificial neural networks and response surfaces. Following *Harries (2010)* a response surface method was used that fitted n-dimensional (where n is the number of parameters) response surfaces using a Kriging approach. Once response surfaces are generated, interpolation is de facto instantaneous. Care should be taken to ensure that the response surface is used for interpolation, and not extrapolation.

The results presented are only meaningful in the context of the chosen parametric model (the established design-space). They rely on the validity of the simulations. Even though these simulations are built on first principles, there are notable simplifications, for instance the wave resistance and seakeeping analyses used in this example ignore viscosity.

Results from the Sobol investigation of the design-space are often presented as correlation plots. These correlation plots highlight general trends in the data but the points represent discrete variants where all of the parameters have changed; thus these diagrams do not accurately represent the continuous variation of a single variable. The band-width of the scatter of points about the mean line gives an appreciation of the difference that can be achieved due to variation of all the other parameters. Even when there is reasonably strong correlation between performance and a parameter, there is often a significant range of performance (which thus depends on the other parameters). The range of performance can be taken as an initial indication of how much potential for optimisation is available.

Fig. 3 shows some sample correlation plots. A general trend towards higher displacement for longer vessels can be seen. Nevertheless, there are instances of vessels with higher and lower displacements (for fixed L_{PP}) that depend on the values of the remaining parameters. The longer the vessel, the lower the resistance; see *Harries (2010)* for further details. As the length increases, the motion sickness incidence decreases. However, the correlation between MSI and beam is not very strong, contrary to what might be expected. The inverse correlation between L_{PP} and stability is probably due to the fact that the displacement range for the stability calculations was fixed irrespective of vessel length. Shorter vessels would be broader and/or deeper in the water generally resulting in greater intact stability (up to the angles of heel investigated). Other parameters showed little or no influence on stability indicating that they can be varied to improve other performance measures without penalising the stability performance.

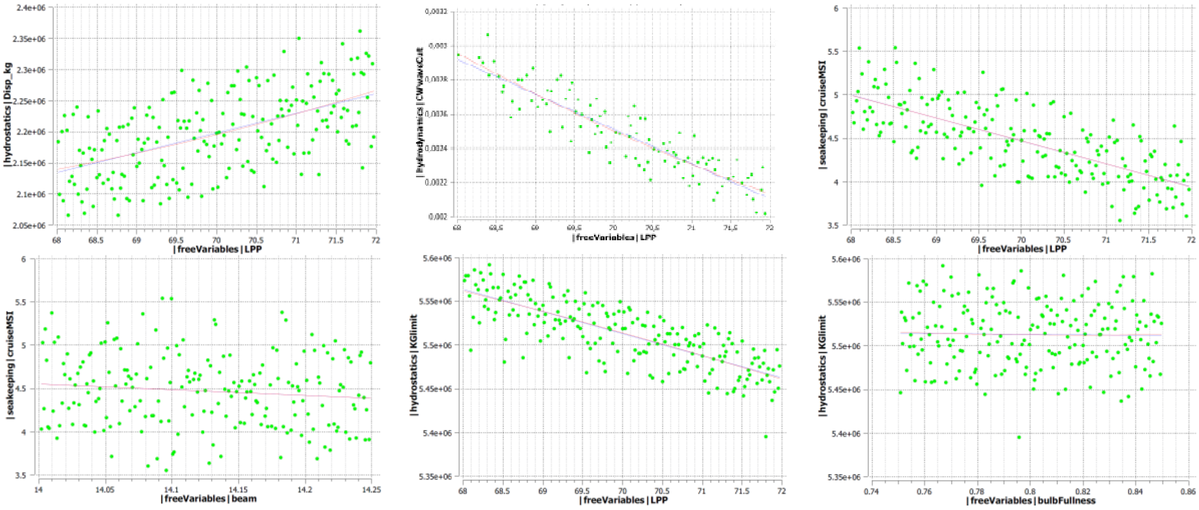

Fig. 3: Correlation plots for: Displacement vs length (top left); wave resistance coefficient vs. L_{PP} (top center); MSI vs. L_{PP} (top right); MSI vs. beam (bottom left); stability vs. L_{PP}. (bottom center); stability vs. bulb fullness (bottom right)

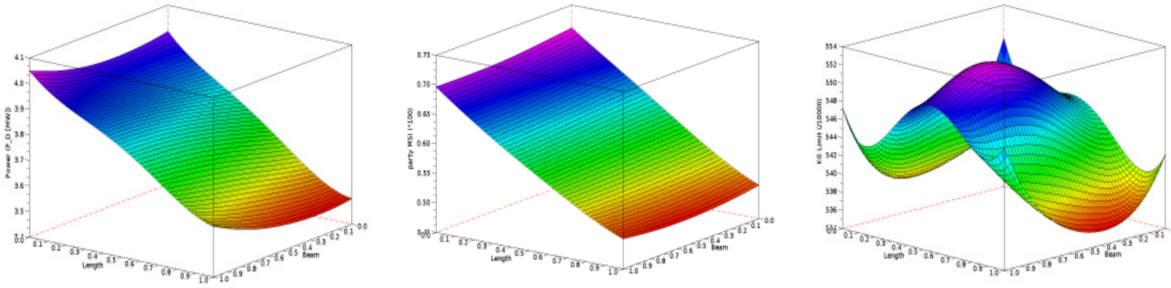

Fig. 4: Response surfaces for power (left), seakeeping (center), stability (right) vs. length and beam

N-dimensional response surfaces were fitted to the discrete data obtained from the design-space exploration. Fig. 4 shows iso-parametric surfaces for variation of two parameters. The range of each parameter was normalised to 1.0. In most cases the response surfaces follow what might be expected: the power requirement is reduced for longer and generally narrower vessels; MSI is reduced for longer vessels, with the optimum beam near the middle of the range. However, for the stability performance measure response surface, the effects of length and beam are more complex. The sharply raised corners indicate extrapolation with insufficient variants to adequately describe the response surface in these regions.

In this paper, we used relatively simple numerical simulation tools to investigate three aspects of the design process: calm-water resistance (using potential flow and boundary layer theory), seakeeping (using strip theory) and static stability. However, the same methodology could be applied to different problems using advanced CFD tools where appropriate. Using the resulting response surfaces to drive an optimisation search would be the logical next step of the design process; see *Harries (2010)* for an example).

COUSER, P.; HARRIES, S.; TILLIG, F. (2011), *Numerical hull series for calm water and sea-keeping,* 10th Int. Conf. Computer and IT Applications in the Maritime Industries (COMPIT), Berlin, pp.206-220
http://www.friendship-systems.com/applications/papers/papers2011/fsys_2011_couser.harries.tillig_numerical-hull-series-for-calm-water-and-sea-keeping_compit-2011.pdf

HARRIES, S. (2010), *Investigating multi-dimensional design spaces using first principle methods,* 7th Int. Conf. on High-Performance Marine Vehicles (HIPER), Melbourne, pp.179-194.
http://www.friendship-systems.com/applications/papers/papers2010/FSYS_2010_harries_designspace-investigation_HIPER.pdf

NN (2007), *The Large Commercial Yacht Code (LY2).* Maritime And Coastguard Agency
http://www.mcga.gov.uk/c4mca/msn_1792_edition_2.pdf

Performing self propelled simulations of a kayak, using a Body-force paddle model

J. Banks*, A.B. Phillips, S.R. Turnock, D.A. Hudson
*jb105@soton.ac.uk

1 Introduction

Understanding the interactions between a hull and a propeller is a common problem naval architects have to solve to provide efficient powering solutions. The world of elite sport is becoming increasingly scientific in a similar drive for increased performance. To allow a kayak's hull and paddle to be optimised, their interactions have to be considered to provide a realistic race scenario. It is therefore proposed that numerical techniques currently used by naval architects could be applied to the problem of a self propelled kayak.

The computational cost of fully resolving the flow around a rotating propeller and hull inhibits the use of numerical simulations for commercial use. However, several groups have implemented simplified body force propeller models, which accurately induce the accelerations produced by a propeller into the fluid (Phillips et al, 2010). A similar body force methodology is adopted to simulate the impact a paddle stroke has on the fluid around a moving kayak. This is done using the open source CFD package OpenFOAM (OpenFOAM, 2009).

2 Theoretical approach

A finite volume method is adopted, using a Volume of Fluid (VOF) approach for the free surface. This method is derived from the surface integration of the conservative form of Navier Stokes' equations over a control volume. The incompressible Reynolds averaged Navier-Stokes (RANS) equations, written in tensor form, are defined as

$$\frac{\partial(\rho U_i)}{\partial t}+\frac{\partial(\rho U_i U_j)}{\partial x_j}=-\frac{\partial P}{\partial x_i}+\frac{\partial}{\partial x_j}\left[\mu\left(\frac{\partial U_i}{\partial x_j}+\frac{\partial U_j}{\partial x_j}\right)\right] -\frac{\partial}{\partial x_j}\ \rho\overline{u'_i u'_j}\ +f_i \qquad \textbf{2-1}$$

and

$$\frac{\partial U_i}{\partial x_i}=0 \qquad \textbf{2-2,}$$

for momentum and mass continuity respectively. While the volume fraction transport equation is defined as

$$\frac{\partial c}{\partial t}+\frac{\partial(cU_j)}{\partial x_j}=0 \qquad \textbf{2-3,}$$

where c is the volume fraction defined as (V_{air}/V_{total}) (Peric and Ferziger, 2002).

The fluid density, ρ, and viscosity, μ, can then be calculated as

$$\rho=\rho_{air}c+\rho_{water}(1-c) \qquad \textbf{2-4}$$

and

$$\mu=\mu_{air}c+\mu_{water}(1-c) \qquad \textbf{2-5}$$

respectively.

External forces applied to the fluid are represented as f_i, which include buoyancy forces and momentum sources representing the influence of the paddle. The effect of turbulence is represented in equation 2-1 by the Reynolds stress tensor $\rho\overline{u'_i u'_j}$ and is modelled using the k-omaga SST turbulence model contained within OpenFOAM-1.6 (OpenFOAM, 2009).

The SST model blends a variant of the k-ω model in the inner boundary layer and a transformed version of the k-ε model in the outer boundary layer and the free stream (Menter, 1994). This has been shown to be better at replicating the flow around the stern of a ship, than simpler models such as k-ε, single and zero equation models (Larsson et al, 2000)(Hino, 2005).

3 Body force Paddle model

3.1 Simple mathematical force model

To start with the fluid forces generated by the paddle blade were calculated based on a simple mathematical model of a flat plate rotating around a point moving with an advance speed of U_0 (see Figure 3-1). The angle of rotation θ is measured from the horizontal, in the direction of movement (i.e. increases throughout the stroke).

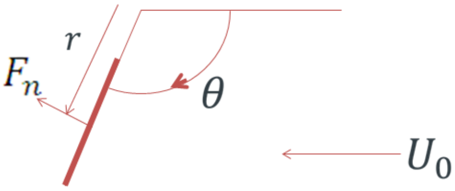

Figure 3-1 - free body diagram of paddle model.

The normal velocity encountered by the blade at a radius r is given by

$$V_n = (\dot{\theta} \times r - U_0) \cdot \hat{n} \tag{3-1,}$$

where n is the unit vector normal to the blade calculated as

$$n = \theta \times r \tag{3-2.}$$

It follows, therefore that the hydrodynamic force on a length of blade dr ,at a radius r is given by

$$F_n = \frac{1}{2}\rho(V_n)^2 C_D c.\, dr \cdot n \tag{3-3,}$$

where ρ is the density of water, C_D is the drag coefficient and c is the chord of the blade at r.

3.2 Calculating momentum source strengths from paddle force model

To represent the impact of the paddle on the fluid, the calculated paddle forces are applied to a propulsive domain located within the fluid. This domain represents the swept area of the paddle defined by the length (R) and the width (c). An inner radius can also be defined to account for the length of the paddle handle. The propulsive domain is then divided up into sectors of radius dR and angle dθ, this is demonstrated in Figure 3-2.

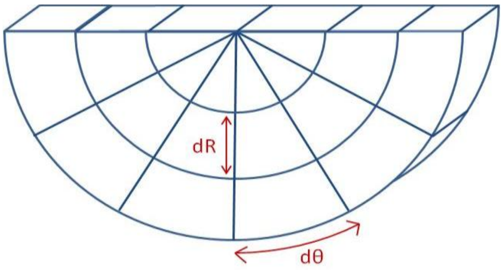

Figure 3-2 - Schematic of stroke propulsive domain divided into sectors.

When the paddle blade passes through a sector, the paddle force (F_n) is calculated for a section of blade, with length and chord equal to the sector dimensions, located at the centre of that sector. The momentum source term for that sector is then calculate as

$$\frac{F_n}{SectorVolume}.$$

Obviously as dr and dθ get smaller the propulsion model better represents a paddle moving smoothly through the water.

3.3 Applying source terms within OpenFOAM

The standard multiphase solver interFoam was modified to accommodate momentum source terms and renamed mom_interFoam. A new module within the solver was created ‘createBodyForce.H’ which is called every time step from within the top level solver program ‘mom_interFoam.C’.

The parameters that define the propulsive model are defined within a dictionary located within the case files.

The propulsion domain is defined by the paddle dimensions, centre of rotation and unit vectors providing the direction of forward motion and the roll angle. The polar coordinates of the centre of each cell within the mesh are then calculated relative to the paddle centre of rotation. These are then used to determine which cells are within a given sector of the propulsive domain providing an accurate sector volume.

The run time of the current time step is then used to calculate the position of the paddle within the propulsive domain, based on prescribed paddle angles throughout a single stroke cycle and a defined stroke rate. This is used to calculate the angular velocity of the paddle using the paddle position form the previous time step.

For each cell, within a sector containing the paddle, the momentum source term is calculated using the paddle force calculated for that sector divided by the sector volume. The source term for all other cells are set to zero. These source terms are stored within a volume vector field which is then added to the momentum equation (Ueqn.H within openFoam). The total paddle force is determined for each time step by multiplying each cell's source term with its cell volume and summating over the propulsive domain. The instantaneous thrust is then acquired by resolving this force into the direction of movement.

3.4 Experimental data

Experimental data for a rotating paddle was obtained as part of a student research project at the University of Southampton (Ellison, 2010). A kayak paddle was mounted on an instrumented pivot mechanism attached to a towing tank dynamometer (Figure 3-3). This allowed lift, drag and rotation angle to be recorded against time. A constant torque was applied to the paddle via a dropping weight allowing the dynamic forces generated by the blade to be measured against time. Various angles of attack were tested with a range of torques.

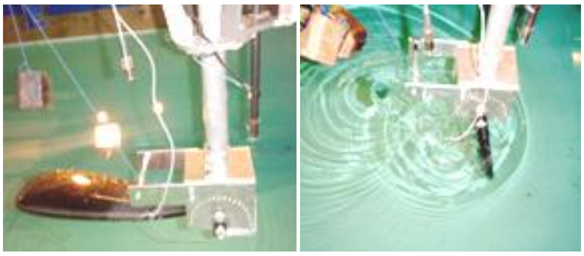

Figure 3-3 - Experimental setup for paddle test.

The experimental data for the blade at 90 degrees to the flow can be seen in Figure 3-4. Due to the blade starting out of the water, it accelerates quickly at first, entering the water at a high velocity resulting in a peak in the thrust at this point. A small blip in the angle data, at approximately 110 degrees from the horizontal, is thought to be due to the rotary potentiometer and not the flow physics. This error gets amplified when the angular velocity is calculated.

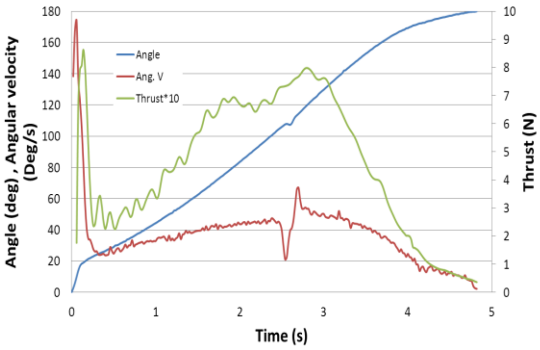

Figure 3-4 - Experimental data for a rotating paddle.

3.5 Validation against experimental data

The paddle that was used in the experiments was represented as a flat plated of the same length and chord (0.54 and 0.2m respectively). A flat plate drag coefficient of 1.2 was used as an initial approximation (Hoerner, 1965) whilst the propulsion domain was divided into 18 angular and 8 radial divisions, with an inner radius of 0.1m.

To start with the centre of rotation was placed on the surface of the water, so as to remove the complications of paddle entry. The angular velocity was maintained at a constant value throughout the stroke, determined as the average angular velocity from the experimental paddle stroke.

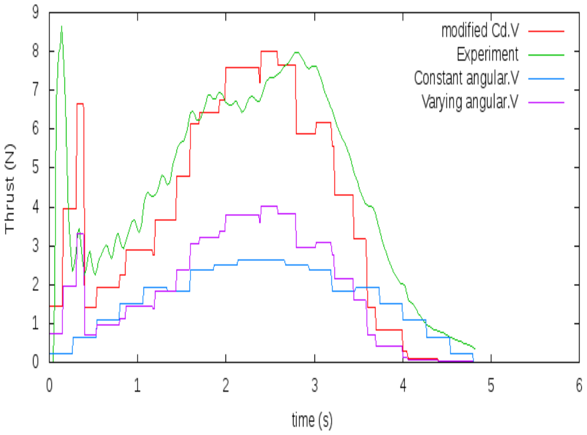

Figure 3-5 - Thrust generated by propulsive model compared with experimental data.

Out of a crude mesh of 40,000 cells, 740 were contained within the propulsive domain.

It can be seen in Figure 3-5 that the constant velocity propulsion model significantly underestimates the thrust measured in the experiment. However it is not just the magnitudes which do not match, the general shape of the curves differ significantly. To try and improve the paddle model the blade angle data that was recorded during the experiment was used to prescribe the paddle motion during the stroke. This modified thrust data can also be seen in Figure 3-5. Despite the magnitude of the thrust being approximately half that of the experimental data it can now be seen that the general trends aligns much more closely. This is easier to in the final thrust trace, where the drag coefficient has been doubled to 2.4.

There are many improvements that need to be made to the body-force model that could account for the discrepancies between the experimental data. Predominantly these would focus on including added mass terms to the mathematical model, so as to include unsteady flow features, and to remove the step-like variation in thrust through a smoother implementation of source terms within the fluid domain.

3.6 Applying two propulsion models within the same simulation

A second paddle model was easily added to the modified solver by having two identical modules that independently calculate momentum sources. The only difference is that the second paddle has a different centre of rotation and applies a phase shift to the prescribed paddle motion so that they are out of phase (typically 180 degrees).

4 Self propelled Simulation

4.1 Numerical model

The solver settings and simulation parameters can be found in Table 4-1.

Table 4-1 - Numerical settings

Property	**Mesh**
Type of mesh	Unstructured (Hexahedral)
No. of elements	Approximately 1.2M
y+ on the hull	10-15
Domain Physics	Homogeneous Water/Air multiphase, kOmegaSST turbulence model, Automatic wall function
Boundary physics:	
Inlet	Free stream velocity of 2m/s
Outlet	Zero gradient
Bottom/side wall	Wall with free stream velocity
Top	Opening
Hull	Wall with no slip condition
Solver settings:	
Transient scheme	1st order Euler
Grad (U) Scheme	Gauss linear
Div (U)	Gauss limitedLinearV 1
Pressure coupling	PISO
Convergence criteria	P 1e-7, U 1e-6, k 1e-8, omega 1e-8
Multiphase control	Volume fraction coupling
Timestep control	max Courant No = 0.4
Processing Parameters:	
Computing System	Iridis 3 Linux Cluster (University of Southampton)
Run type	Parallel (9 - 24 Partitions run on 5x8 core nodes each with 23 Gb RAM)

4.2 Meshing Technique

An unstructured hexahedral mesh around the kayak was created using the snappyHexMesh utility within OpenFOAM. Firstly a coarse block mesh of hexahedral cells is created, using the blockMesh utility, defining the size of the domain and the initial cell size in each direction. Specific areas within the domain are then specified for mesh refinement in progressive layers. For each layer of refinement conducted each cell within the specified region is split into 8 equal parts, doubling the mesh density in all directions. However uni-directional refinement was used across the free surface to provide good wave pattern resolution, whilst minimising computational cost. Boundary layer element are also grown out from the kayak surface mesh. This localised refinement process results in a general mesh structure that can be seen in **Error! Reference source not found.**. It should be noted that the images of the mesh are generated using Paraview which currently displays hexahedral cells as two tetrahedral cells. The mesh is actually fully hexahedral.

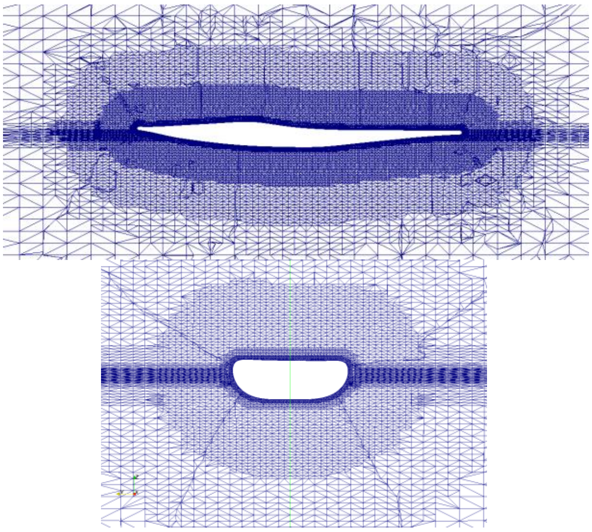

Figure 4-1 - Kayak mesh structure.

4.3 Naked hull resistance

The naked hull resistance of the kayak was determined to be 22.68 N. The resulting free surface deformation can be seen in Figure 4-2.

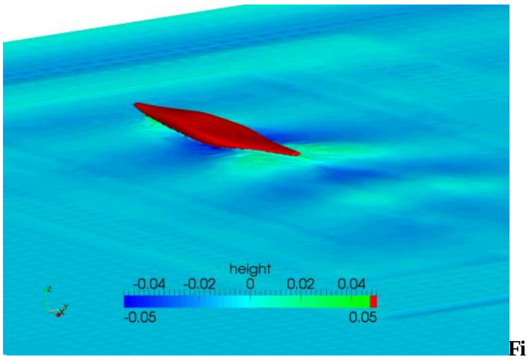

Figure 4-2 - Free surface deformation for naked hull kayak simulation

4.4 Determining the self propelled stoke rate

The naked hull resistance case files could then be used as an initial condition for the self propelled simulation. For this first attempt a self propelled kayak a fixed stroke rate was selected that would provide a thrust approximately equal to the naked hull resistance. In time this will become an iterative process varying stroke rate to match the self propelled resistance.

Without access to real stroke path data, the rate of angular velocity throughout the stroke was modelled as being sinusoidal, with zero angular velocity on paddle entry and exit. This provides a crude approximation of how an athlete might vary the velocity of the paddle to take account of the kayak's forward speed. The resulting force trace for a single paddle operating at a stroke rate of 40 can be seen in Figure 4-3. This happened to provided an average thrust of 11.3 N, so with two paddles operating out of phase with each other the average thrust would be 22.6 N. This was assumed to be close enough to the naked hull resistance of for the purposes of this study.

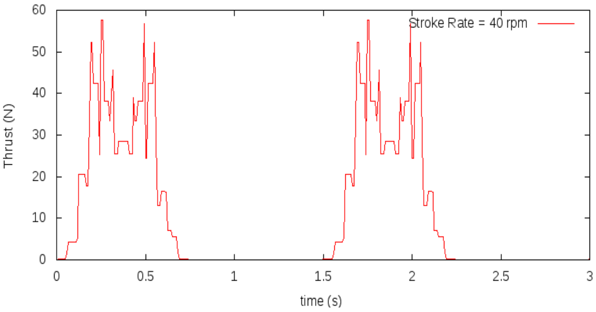

Figure 4-3 - thrust generated by a single paddle, with a sinusoidal angular velocity, against time

4.5 Paddle-hull interactions

The paddle induced velocities alongside the kayak can be seen in Figure 4-4, while their effect on the pressure field over the hull can be seen in Figure 4-5. Although this simulation far from replicates a realistic paddle stroke the interaction between the paddle and the hull an be clearly seen.

To see the impact this change in pressure field has on the kayak you have to look at the hydrodynamic forces and moments acting on the hull. In Figure 4-6 you can see how the side force varies throughout the stroke. As the paddle passes the right hand side of the hull, the pressure drops due to the increase in velocity, pulling the kayak to the right hand side (positive side force). The same phenomenon is observed on the left. Likewise the paddle hull interaction can clearly be seen in all three moments. Although only initial, un-validated self propulsion data is presented, the potential benefits of this type of analysis is clear.

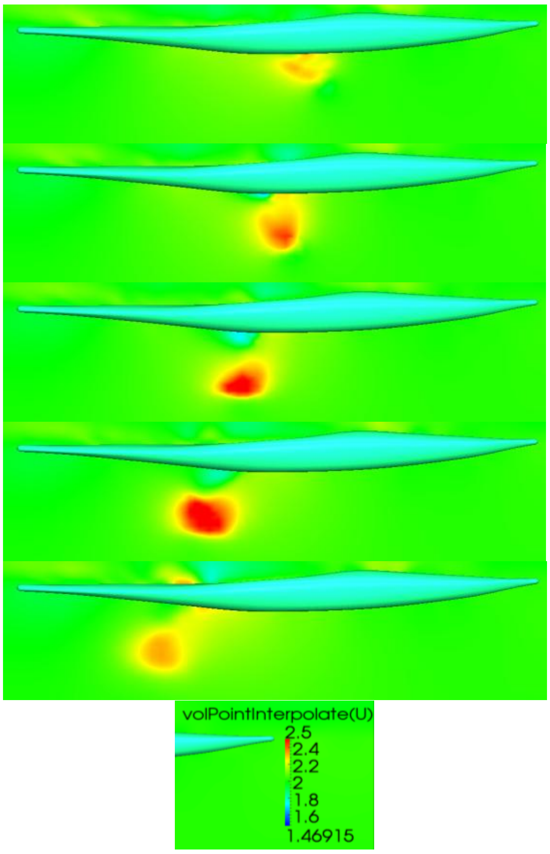

Figure 4-4 - Paddle induced velocities throughout a single paddle stroke, viewed on a plane placed through the centre of rotation of the paddle.

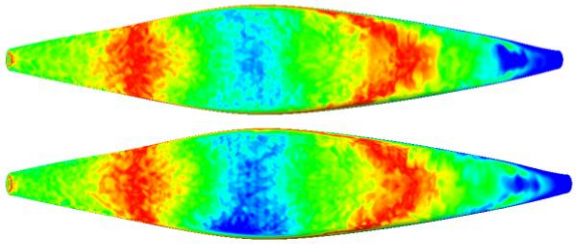

Figure 4-5 - hydrodynamic pressure field on the bottom of the kayak (naked hull above, as paddle blade passes below).

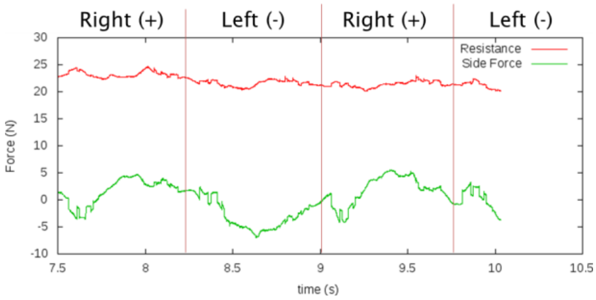

Figure 4-6 - Self propelled hydrodynamic forces acting on the kayak

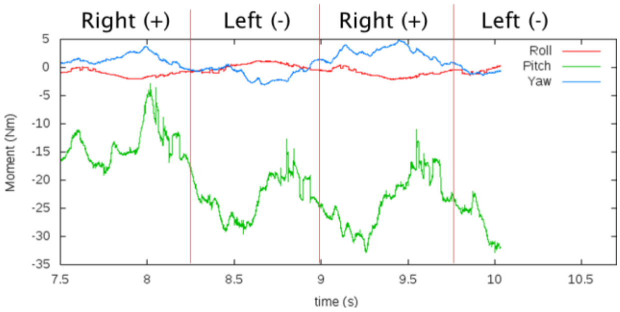

Figure 4-7 - Moments induced by the self propelled forces.

5 Conclusions

A simplified mathematical model of a paddle has been used to simulate a paddle stroke using a body force method. Experimental data has been used to validate the model and refine the drag coefficients used until improvements to the mathematical model can be included.

An initial self propelled kayak simulation has been performed using the developed methodology, which highlights the significant impact the paddle stroke has on the kayak's fluid dynamic forces.

6 References

Ellison, W., Turnock, S.R., (2010) Investigation into the effect of the kayak paddle stroke on elite kayak performance, Ship Science Individual Project, School of Engineering Sciences, University of Southampton, UK.

Hino T. (2005) CFD Workshop Tokyo 2005. In: The Proceedings of CFD Workshop Tokyo.

Hoerner, S.F., (1965) Fluid-Dynamic Drag. 3-16. Published by the author, Midland Park, NJ

Larsson L, Stern F, Bertram V. (2003) Benchmarking of Computational Fluid Dynamics for Ship Flows: The Gothenburg 2000 Workshop. Journal of Ship Research 2003;47:63–81(19).

Menter, F.R., (1994) Two-equation eddy-viscosity turbulence models for engineering applications. AIAA Journal 32(8):1598 –605.

OpenFOAM®, (2009) OpenFOAM – The Open Source CFD Toolbox- User Gide, Version 1.6.

Peric, M., Ferziger, J.H., (2002) Computational Methods for Fluid Dynamics, Springer, 3rd edition.

Phillips, A.B., Turnock, S.R. and Furlong, M.E. (2010) Accurate capture of rudder-propeller interaction using a coupled blade element momentum-RANS approach. *Ship Technology Research (Schiffstechnik)*, 57, (2), 128-139.

Comparison of Multi-Reference Frame and Sliding-Interface Propeller Models for RANSE Computations of Ship-Propeller Interaction

Jan Kaufmann, Volker Bertram, FutureShip, Hamburg/Germany, jan.kaufmann@GL-group.com

Ship motions in regular and irregular seaways and the resulting loads depend strongly on the forward ship speed. The frequent assumption of constant speed (suppressed surge motion) is in many applications questionable. In reality, the ship speed varies with time, especially in severe sea states. There are various approaches (differing in required effort and achieved realism) to capture surge motions and propeller action. As a first approximation, one could apply a constant propulsion force and leave the surge motion free. But the speed variation due to surge changes not only the resistance of the ship (with averaged contributions to added resistance in wave), it also introduces varying propeller loads, hence varying propeller efficiency. Capturing this effect requires more sophisticated numerical models. The following describes variations on RANSE models capturing propeller and free motions in waves, all in principle capturing the complex interaction. The focus lies then on how the alternative numerical techniques differ in required effort and quality of results.

For all computations, the CFD Code OpenFOAM 1.6-ext was used. OpenFOAM is a free, open-source software package. It provides the General Grid Interface (GGI) for interpolation at the interfaces between rotating and static domains. The meshes were generated with OpenFOAM's automatic meshing software snappyHexMesh 2.0.0. The convection terms in the momentum equations are approximated using a TVD-limited linear second-order scheme. In the chosen solvers from the OpenFOAM libraries, the pressure and velocity are coupled by a variant of the SIMPLE algorithm. All equations except the pressure correction equations are under-relaxed using a relaxation factor of 0.7, while the pressure-correction equation is under-relaxed with a factor between 0.2 and 0.4, finding in each case a suitable compromise between stability and convergence speed. In all computations the k-ω SST turbulence model was used. The two-fluid system is modelled following a two-phase formulation of the governing equations. In order to avoid numerical smearing of the interface, OpenFOAM employs the explicit MULES scheme.

The computational model simulated motions of ships in seaways with a geometrically modelled propeller. To account for the propeller rotation, two alternative methods were compared:

- Multiple Reference Frame (MRF) method.
  In the MRF approach, the mesh in the propeller region is not moving. Instead, a source term is applied to the momentum equations to account for the additional Coriolis forces due to the rotating propeller. Details of the formulations are found e.g. in *Petit et al. (2009).*
- Sliding Interface (SI) Method.
  Our SI implementation followed *Petit et al. (2009),* using the solver transientSimpleDyMFoam and its libraries for handling (partly) rotating meshes. Rotor and stator parts of the mesh can be coupled via topological changes or general grid interface (GGI). The basic GGI is similar to the static sliding interface, although much simpler in the sense that no re-meshing is required for the neighboring cells of the interface. The gain in time is significant.

In both methods, the flow in the propeller domain is solved in a rotating reference frame while the flow in the outer domain is solved in an absolute reference frame. In the MRF method the rotation is accounted for only with a physical approximation by applying additional source terms, while in the SI method the position of propeller domain changes with time according to the rotation velocity. The flow variables are interpolated between the interface of the rotating and the static domains.

As the SI method does not introduce any approximations, it leads in general to more accurate results, but the computational costs are much higher than the MRF method. The SI methods would be still our preferred approach if pressure fluctuations on ship hull or rudder need to be captured accurately, possibly also for special cases involving ventilation and/or cavitation. But for the SI method, for each time step, the grid has to be updated and values between the two interfaces have to be interpolated anew.

Especially for simulations in irregular seaways, the computational requirements of RANS simulations are already very high for many industry constraints, even without consideration of a propeller. Therefore we investigated whether the MRF method could give sufficiently accurate results (at much lower computational cost), making it the right choice for many industry applications. The computations with the SI method were carried out with a transient solver based on the SIMPLE-algorithm. This solver was provided by the *OpenFOAM Turbomachinery* Working Group, and extended for 6 DoF free-surface simulations with two-phase flows. This extended solver was used also for the simulations using the MRF method. The grid sensitivity of both methods was investigated in a preliminary study.

The test case was a typical 8000 TEU container ship with a 6-bladed propeller. For this case, model-test results for open-water, resistance and propulsion tests were available. Fig.1 shows the geometry of the investigated propeller and an example of the computational grid. The coarsest grid of the sensitivity study consisted of 500,000 control volumes (CVs), the finest grid of approx. 11,000,000 CVs. The entire computational domain was extended four propeller diameters in front of the propeller and to the sides, and twelve diameters behind the propeller. The thickness of the first cell layer near the wall was chosen, that the mean y^+ value was below 0.5 in all computations. Therefore the computations were carried out without the use of a wall function. The simulations were carried out in model scale, a constant rpm of 600 was imposed for the propeller.

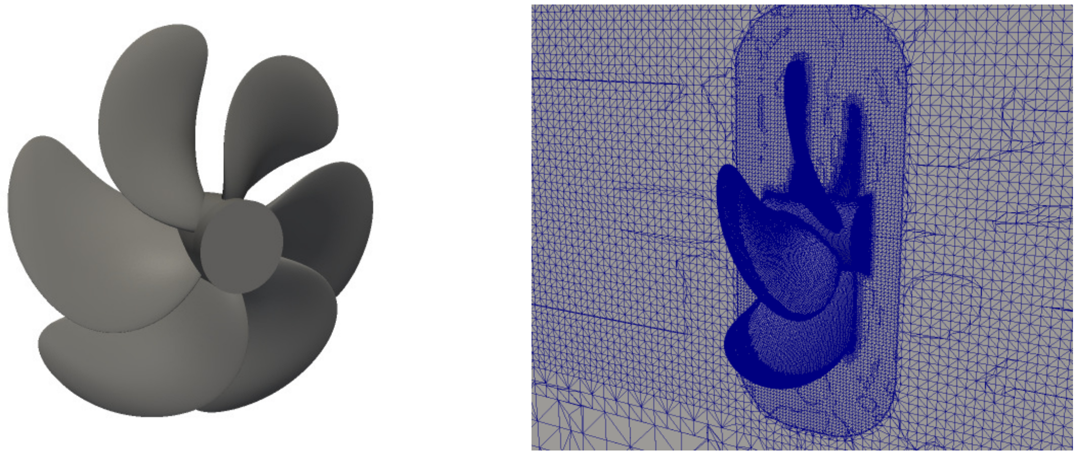

Fig.1: Propeller geometry (left) and grid around propeller (right)

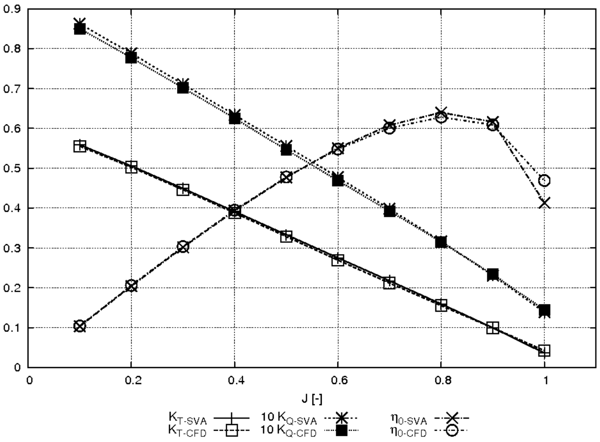

Fig.2: K_T, 10 K_Q and η_0 vs. advance number J; index: SVA = model tests; index CFD = MRF method

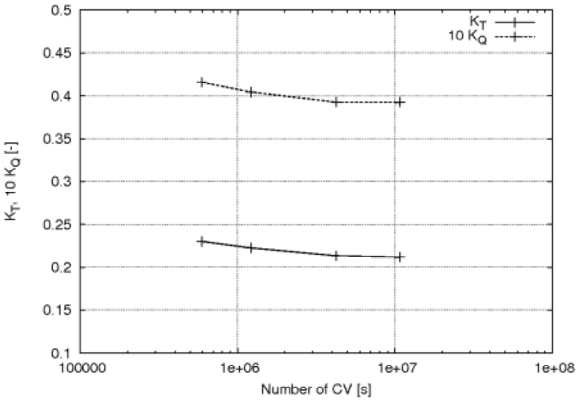

Fig.3: Influence of cell count on K_T and K_Q

Fig.2 shows the results of open-water simulations for the finest grid, namely thrust and torque coefficients K_T and 10 K_Q and the propeller efficiency η_0 over the advance coefficient J. The thrust and torque were determined by integrating the pressure and friction forces over the propeller surface, omitting the propeller hub. The results for the MRF method and the finest grid agree very well with the results of the model tests. The difference of the propeller efficiency is below 3% (except for the highest advance coefficient, where K_T and K_Q are very small). For one advance coefficient and a medium grid with 4,200,000 cells, the MRF method was compared with the SI method. The SI method showed a clear dependency on the time step. For a time step corresponding to a rotation of 1° per time step, the difference between the two methods was below 0.5%. Larger time steps led to a distinct under-prediction of the computed thrust with the SI method.

Computations for propeller-ship interaction were performed without free surface and as single-phase flow (no cavitation). Table 1 gives ship data, Table 2 propeller data. The grid had 4 million cells. The computations were performed at model scale with a speed of 2.02 m/s, corresponding to a full-scale ship speed of 25.25 knots. A constant rpm of 600.9 was imposed for the propeller. Model variations aimed to illustrate the influence of:

- propeller position relative to the inhomogeneous wake field (4 propeller positions in 15° steps)
- size of MRF zone (2 sizes), Fig.4
- time step size in SI (5 time steps)

Table 1: Ship data

	Ship	Model, λ=41.364
L_{pp}	319.00 m	7.712 m
L_{OA}	334.32 m	8.082 m
B	42.80 m	1.035 m
$T_A = T_F$	13.00 m	13.00 m
Displ.	116391 m^3	1.645 m^3
A_x	538.3 m^2	0.315 m^2
S_{BH}	16604 m^2	9.704 m^2
ρ	1.0258 t/m^3	0.998 t/m^3
LCB/L_{pp}	48.52%	

Table 2: Propeller data

D	0.22 m
P/D	1.0472
A_E/A_0	1.0308
D_N/D	0.2
$C_{0.75}$	0.0916 m
$T_{0.75}$	0.0028 m
z	6
Rake	24.51°

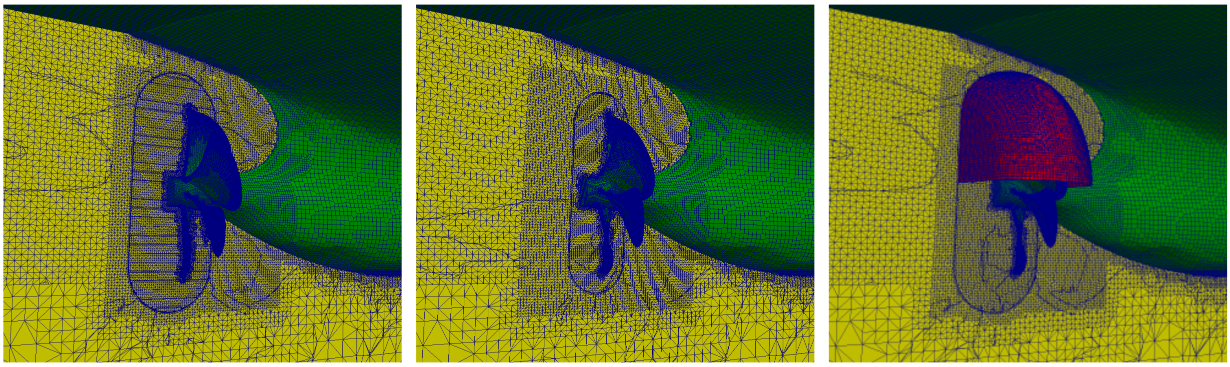

Fig.4: Grids with large (left) and small (middle) MRF zone and Sliding Interface (right)

Table 3 summarizes the results. The change in propeller position gave changes of ±1.3% in thrust. The smaller MRF zone significantly approached results from MRF to those of SI. For SI, finer time steps gave converging results. For practical purposes, time step of 1° is then recommended.

Table 3: Results of model parameter study

MRF	T	Q	SI	T	Q
Position 1	33.32 N	1.522 Nm	5.0° per time step	25.36 N	1.394 Nm
Position 2	33.63 N	1.532 Nm	2.0° per time step	34.26 N	1.584 Nm
Position 3	33.75 N	1.539 Nm	1.0° per time step	35.15 N	1.602 Nm
Position 4	33.95 N	1.545 Nm	0.5° per time step	35.67 N	1.620 Nm
Position 1 (small zone)	35.35 N	1.619 Nm	0.25° per time step	35.83 M	1.635 Nm

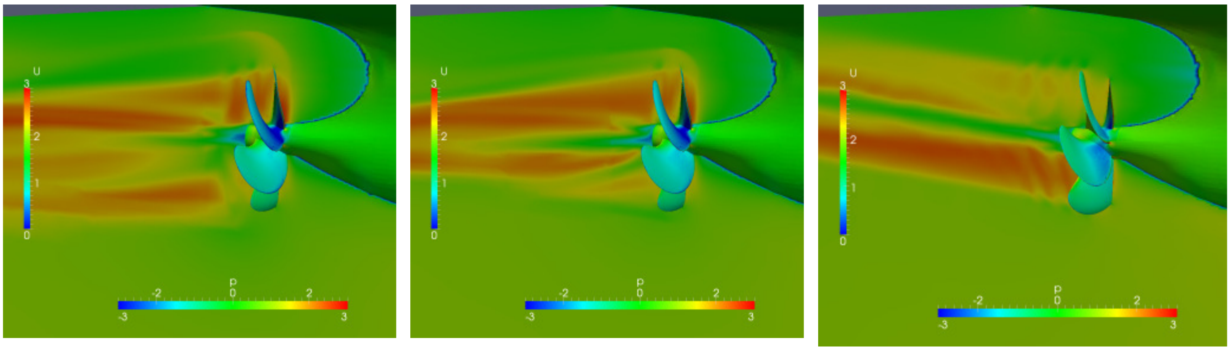

Fig.5: Pressure distribution on hull and propeller and velocity distribution on mid-ship plane MRF – Position 1 (left), MRF with smaller zone (middle) and SI (right)

Fig. 5 shows the velocity distribution in the centre-plane and the pressure distribution on the hull and propeller for the simulation with the two different MRF zones and the SI method. Disturbances due the MRF zone in the velocity distribution can be seen. The influence of the MRF zone size and form should be investigated in further studies in order to minimize the influence on the results.

AUVINEN, M.; ALA-JUUSELA, J.; PEDERSEN, N.; SIIKONEN, T. (2010), *Time-accurate turbomachinery simulations with open-source CFD; flow analysis of a single-channel pump with OpenFOAM,* ECCOMAS CFD 2010, Lisbon

DICK, E.; VIERENDEEL, J.; SERBRUYNS, S.; VANDE VOORDE, J. (2001), *Performance prediction of centrifugal pumps with CFD-tools*, TASK QUARTERLY 5/4, pp.579–594

JASAK, H. (2009), *Dynamic Mesh Handling in OpenFOAM*, Workshop of Flow Modelling in OpenFOAM, Darmstadt
http://www.csi.tu-darmstadt.de/media/csi/news_1/dbdopenfoamworkshop/jasak2_dynamicmesh.pdf

PETIT, O.; PAGE, M.; BEAUDOIN, M.; NILSSON, H. (2009), *The ERCOFTAC centrifugal pump OpenFOAM case-study*, 3rd IAHR Int. Meeting of the Workgroup on Cavitation and Dynamic Problems in Hydraulic Machinery and Systems, Brno
http://www.tfd.chalmers.se/~hani/pdf_files/Olivier_PETIT_IAHR2009.pdf

A Comparison of Propeller Representation Methods for Numerical Underwater Noise Prediction

Paula Kellett, Osman Turan, Atilla Incecik, Mahdi Khorasanchi
Department of Naval Architecture and Marine Engineering, University of Strathclyde, Glasgow, UK

Bernhard Godderidge
Shell Shipping, London, UK

Email: paula.kellett@strath.ac.uk

Underwater noise has recently become a key area of concern to the wider marine industry, with pressure from both government bodies and conservation groups urging the industry to examine the effects on wildlife and the marine environment and to take steps to minimise them. There are many potentially harmful effects which underwater noise can have on marine wildlife. These include changes to key life behaviours such as foraging and diving, avoidance of biologically important areas and migration routes, reductions in effective communication distances, and in some more extreme cases, hearing damage, stranding and death. This paper focuses on the prediction of radiated underwater from commercial ships during normal transit.

While the immediate impacts of shipping noise may be less extreme than sonar or airgun arrays, the long term impacts are potentially just as much of a concern. Shipping noise, while transient in a given location, is continual globally, and the lower frequencies associated with shipping noise - typically up to 1kHz - tend to travel long distances with little attenuation, and hence ensonify vast areas of ocean with a constant background noise. This research aims to provide a tool for predicting, in the early design stages, the radiated underwater noise characteristics of commercial vessels. This will allow the designer to estimate the underwater noise characteristics of a vessel, identify potential concerns, and also compare alternative designs to ensure the final design has the most suitable noise properties.

In order to be suitable for use by designers, the prediction tool is required to be reliable, applicable to a wide range of vessels, and able to provide accurate results for acceptable computational time and cost. This work is focussing on the propeller noise aspect of the prediction tool, aiming to establish a propeller noise representation method which fulfils these requirements most successfully.

This paper details a comparison of the three main approaches available for the prediction of propeller noise: a momentum source code, moving frame of reference with static propeller geometry, and a rotating propeller geometry and associated mesh. It will detail an investigation into the trade-off between computational requirement and accuracy presented by these three approaches for the prediction of propeller noise and induced flow excitation causing increased flow noise in hydroacoustic applications.

In order to ensure that the resulting noise prediction tool accurately represents actual ship noise characteristics, initial work is looking at recreating full scale measured data taken for an existing Liquid Natural Gas (LNG) Carrier; seen in **Figure 1** below. Measurements were taken with the LNG Carrier at anchor, and at 9 and 19 knots forward speed, at the trial draft of 9.69m. Numerical simulations are then carried out using commercial CFD software coupled with a built-in noise propagation method based on the Ffowcs-Williams Hawkings equation. Once the acoustic calculation has been carried out, a Fast Fourier Transform (FFT) is used to calculate the resulting spectra at the specified receiver locations. The influence of the three main types of noise sources associated with ship radiated underwater noise; machinery noise, propulsion noise, and hydrodynamic or flow noise can thus be investigated individually.

Figure 1 – Liquid Natural Gas Carrier

It is widely accepted that above cavitation inception speed (CIS), which for commercial vessels is typically below 10 knots, by far the most dominant source of underwater noise is the propeller and cavitation noise. Below CIS, machinery noise becomes dominant, with the main engines typically being the most significant sources onboard. Preliminary simulation work taking into account only the hydrodynamic and flow noise of the vessel was carried out to establish the initial suitability of the CFD model set-up and overall far-field noise propagation approach for this application. It seems likely that as CIS for this vessel occurs at around 8 knots, not accounting for the propeller and cavitation noise could be the cause of this discrepancy, as the propeller will be fully cavitating and dominant in terms of underwater noise at 19 knots.

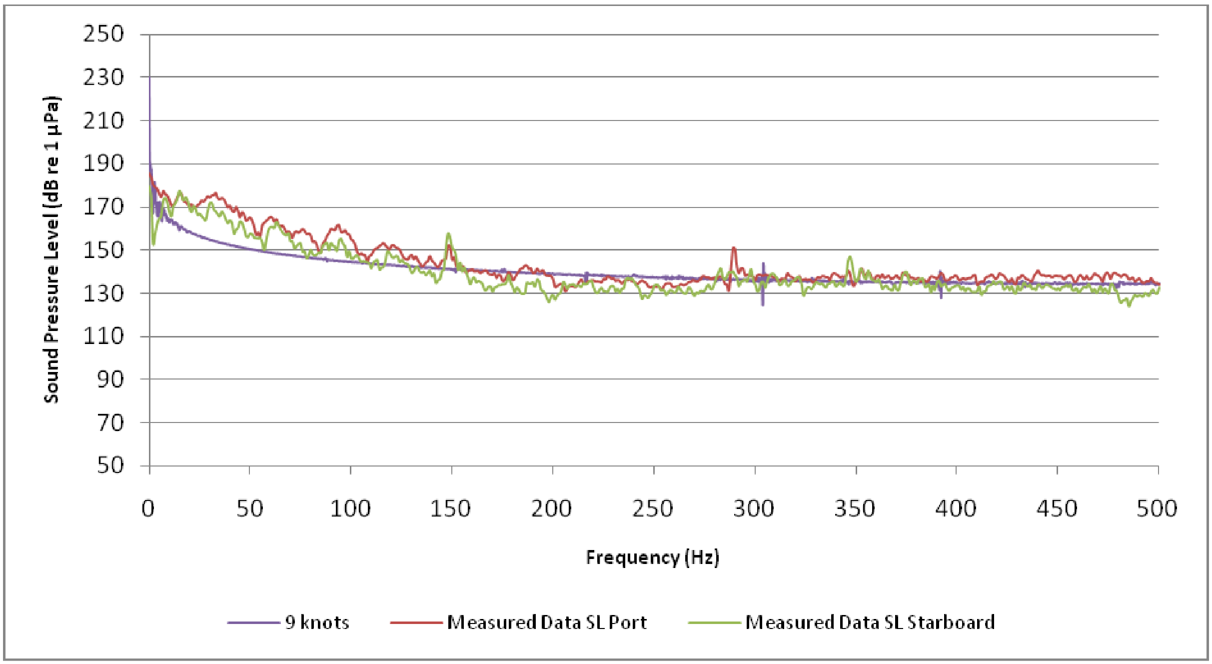

Figure 2 – Comparison of simulation and full scale data at 9 knots

Results indicated that while at the lower speed of 9 knots, the simulation gave a resulting sound pressure level (SPL) very close in terms of dB re 1µPa to the experimental data (seen in **Figure 2**), at the higher speed of 19 knots, a gap of around 30 dB was observed (seen in **Figure 3**), with the CFD simulation results giving the lower magnitude spectra. As decibels are a non-dimensional value, the reference pressure for the medium, in this case water, must be stated to give the decibel value meaning, hence a result given in dB re 1 µPa.

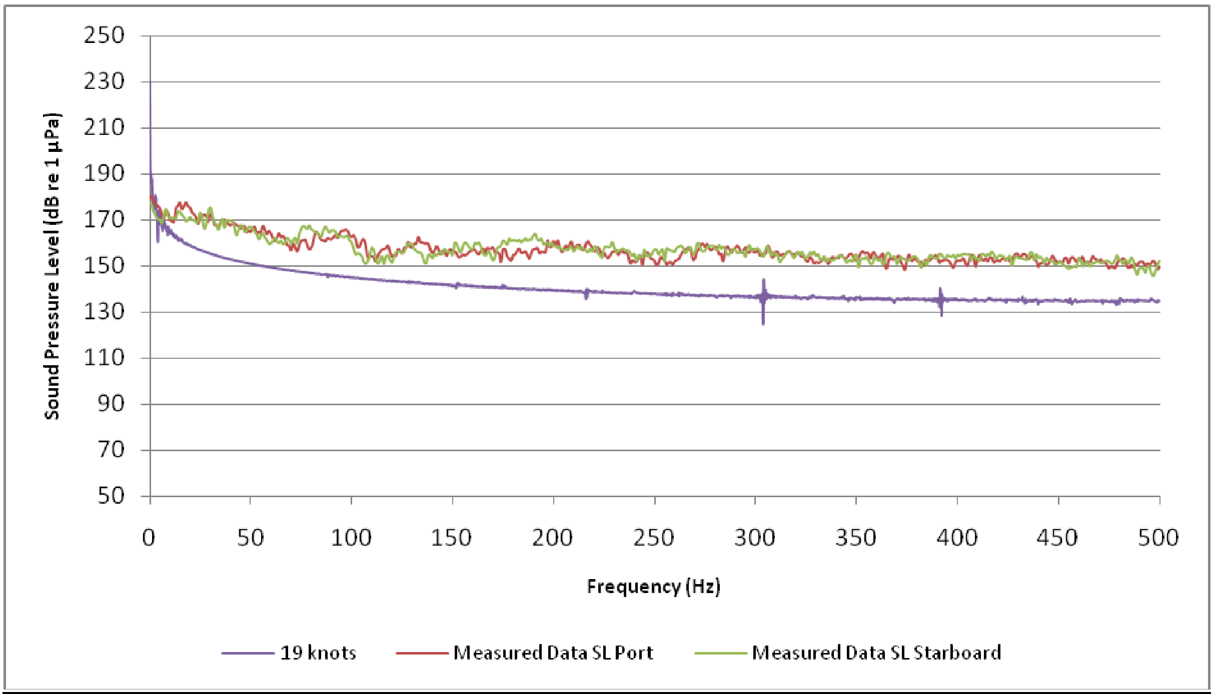

Figure 3 – Comparison of simulation and full scale data at 19 knots

The Ffowcs-Williams Hawkings (F-WH) Equation is the governing equation for sound propagation by a body moving in fluid flow. It uses the conservation of mass and conservation of momentum laws (Newton's 2nd Law), and the equation of state for fluids, to re-arrange the Navier-Stokes equations into an inhomogeneous wave equation. The equation characterises the acoustic pressure at a given location in the medium from three source terms, known as the thickness, loading and quadrupole terms, which describe the different noise generation and propagation mechanisms. The thickness noise term, or monopole source term, depends on the displacement of fluid by the body's geometry and motion in the fluid, and is typically calculated through surface integrals on the moving body surface, S. The loading noise term, or dipole source term, depends on the unsteady motion of the pressure distribution on the moving body, and like the thickness noise term, is usually calculated through surface integrals. The quadrupole source term, however, is related to non-linear effects, such as turbulence and cavitation within the flow. It's contribution is therefore calculated through volume integrals of the fluid domain. The contribution of these three sources are then calculated at a receiver location in the far-field at a given instant in time. The equation can be seen below in terms of generalized functions:

$$\Box\Box^{2}p'(x,t) = \frac{\bar{\partial}}{\partial t}\left\{\left[\rho_0 v_n + \rho(u_n - v_n)\right]\delta(f)\right\} - \frac{\bar{\partial}}{\partial x_i}\left\{\left[\Delta P_{ij}n_j + \rho v_i(u_n - v_n)\right]\delta(f)\right\} + \frac{\bar{\partial}^2}{\partial x_i \partial x_j}\left\{T_{ij}H(f)\right\}$$

Where: $\Box\Box^{2}$ *is the D'Alembert, or wave operator as defined below:*

$$\Box\Box^{2} = \left(\frac{1}{c^2}\right)\left(\frac{\bar{\partial}^2}{\partial t^2}\right) - \bar{\nabla}^2$$

c is the sound speed in a quiescent medium, i.e. a medium that is assumed to be stable and unlikely to change
$\bar{\nabla}$ *is the gradient operator*
p *' is the acoustic pressure disturbance*
(x, t) are the observer space-time variables
ρ_0 *is the density of the quiescent medium, or fluid static density*
ρ *is the fluid density*
u_n *and* v_n *are the local normal velocities of the fluid and source surface respectively*
$\delta(f)$ *is the Dirac delta function, where*

$\delta(f) = 0 \; for \; f \neq 0$
$\delta(f) = +\infty \; for \; f = 0$

$$\Delta P_{ij} = P_{ij} - p_0\delta_{ij}$$

P_{ij} *is the compressive stress tensor*
p_0 *is the ambient static pressure*
δ_{ij} *is the Kronecker delta, whereby* $\delta_{ij} = 1$ *when* $i = j$*, and otherwise* $\delta_{ij} = 0$
u_i *and* v_i*, and* u_j *and* v_j *are fluid and surface velocity components*
n_j *is the surface boundary normal vector*
T_{ij} *is the Lighthill stress tensor, usually taken as the molecular rate of transport of momentum, where:*

$T_{ij} = \rho u_i u_j + P_{ij} - c^2\rho'\delta_{ij}$

ρ' *is acoustic density fluctuation*
$H(f)$ *is the Heaviside Function, where*

$H(f) = 0 \; for \; f < 0$
$H(f) = 1 \; for \; f > 0$

As the area of water of importance in this work is almost uniform, with much lower variations in pressure, temperature and salinity than in deeper regions, it is suitable to use an approach which assumed propagation in a uniform medium.

Using a momentum source to define the behaviour of a propeller requires use of a User-Defined Function (UDF) to specify the geometrical and operational properties of the propeller, and how these should be incorporated into the simulation. This source code requires information such as the propeller disc location, and the propeller's thrust and torque distribution which is calculated using the thrust (kT) and torque (kQ) coefficient curves to define the performance, taken from open water tests. For simulations at different speeds, the rotational speed (rps) and normal velocity at the propeller inlet (Vn) must also be specified. In this application, the rps is specified in the model set-up using known values taken from full scale measurement data, and the inlet velocity used is taken from a mesh face in the stern of the vessel adjacent to the propeller. The x, y and z momentum source terms can then be calculated, specified as acting related to the propeller centroid. These source terms are specified for the disc in the model set-up. The main advantage of this approach is that it does not require the propeller geometry to be modelled, however this could also prove to be a major disadvantage, as the source code will struggle to capture the flow behaviour around and downstream of the propeller accurately. It is expected that this will prove to be the least suitable of the three approaches.

The rotating frame of reference approach requires the propeller geometry to be accurately modelled and meshed in the 3D CFD model, however this geometry will remain static in the simulation. The propeller's frame of reference is fixed to the propeller, and the Cartesian co-ordinate system (x, y, z) and rotational velocity for this reference frame is set to the required rotational speed for the propeller. Stationary components of the model are defined with respect to the global co-ordinate system. It should be noted that numerical complications can arise far from the rotating axis, and care must be taken when specifying the velocity values to be used for turbulence modelling; specifically for strain and vorticity rates.

The most complex of the three approaches is the rotating mesh method. Here, the propeller geometry is encased in a separate mesh, which rotates along with the geometry at the required rotational speed for the vessel speed being simulated. This requires a sliding interface between rotating and stationary mesh sections, which is suitably defined throughout the simulation. A disadvantage to this otherwise very suitable approach lies in the high computation time required due to the flow being modelled in a time-dependant manner.

Acknowledgements
This work is carried out at the University of Strathclyde, with support from Shell Shipping and the University of Strathclyde.

14th Numerical Towing Tank Symposium (NuTTS'11)
Poole, England, 22.-24th October 2011

Automation of Propeller Calculations and Application to the Potsdam Propeller Test Case - PPTC

Olof Klerebrant Klasson[1]

Tobias Huuva[1]

Magnus Pettersson[1]

[1]Core Competence Team, Berg Propulsion Technology AB, Hönö, Sweden

1 INTRODUCTION

1.1 Background

In propeller design there are a variety of tools to be used for early predictions of the propeller open water performance. At Berg Propulsion Technology AB (BERG) there are several alternatives among these tools. Some of the tools also have extensive setup times. The limitations of the tools are to some extent investigated, but no comparison between the tools has been performed at BERG.

The accuracy of numerical tools such as the boundary element method (BEM) and Reynolds-Averaged Navier-Stokes (RANS) are not solely dependent on the tools capabilities itself, but also on how they are set up by the user.

The Potsdam Propeller Test Case (PPTC) was intended to give research groups the possibility to validate their computational tools against both model tests and other software, setup by different users. This is a very valuable reference when studying the accuracy of the computational tools.

The setup time for different tools might be very long. One example is CFD, which might have several days, and even weeks, as setup time.

1.2 Objective

The objective was to investigate and validate the computational tools for open water propeller predictions at hand at BERG using the PPTC and make a user environment that automates pre- and post-processing for the tools.

1.3 Limitations

The tools to automate and compare were the Wageningen Propeller Series Program [1], the BEM tool PROCAL [2] and the open source Computational Fluid Dynamics (CFD) toolbox OpenFOAM [3]. The tools were compared to each other considering solely open water characteristics of propellers. OpenFOAM's ability to predict velocity fields forward the propeller disc was compared to model test results.

The automation regarded pre-processing and post processing for open water characteristics predictions. By post-processing, the generation of open water diagrams was regarded. Automatic pre-processing was intended as a way to from either a few user questions or by taking data directly from the blade design location, get a complete open water setup.

For the CFD, the analysis was of steady, non-periodic RANS-type without resolving the wall. The choice of non-periodic boundary condition depended on that the periodic boundary condition was not applicable for ANSA [4] interacting with OpenFoam when the project was performed.

1.4 The PPTC Propeller and Test Setups

This section describes the model tests of the PPTC that was predicted with CFD, BEM and WS. The PPTC propeller is a five bladed controllable pitch propeller (CP).

Table 1: Propeller characteristics of the PPTC propeller

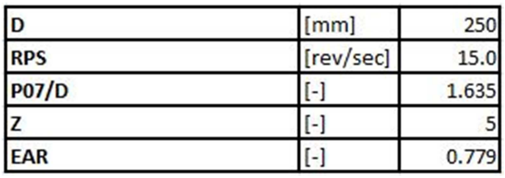

D	[mm]	250
RPS	[rev/sec]	15.0
P07/D	[-]	1.635
Z	[-]	5
EAR	[-]	0.779

One of the design criterions for the propeller was to generate a tip vortex. The propeller design was provided with different hub caps for push and pull arrangement. Some propeller characteristics can be seen in Table 1.

The open water test was carried out in a pull configuration with a hub designed to avoid a pressure build up upstream the disc. The test was performed as a slide test in the SVA towing tank with Breadth*Depth*Immersion = 9*4.5*0.375 m. The propeller was placed in the lateral centre of the tank. Before the open water test, the pressure probes were calibrated so that the results were considered to be solely generated by the propeller blades. Table 2 shows the operating conditions of the open water test.

Table 2: Operating conditions of the open water test

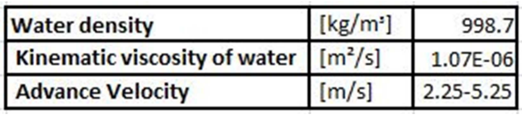

Water density	[kg/m³]	998.7
Kinematic viscosity of water	[m²/s]	1.07E-06
Advance Velocity	[m/s]	2.25-5.25

The results for comparison were K_T and K_Q at J=0.6-1.4 with an interval of 0.2.

The velocity field measurement was performed in the SVA Potsdam cavitation tunnel K15A. The tunnel has a cross section of 600*600 mm and a length of 2600 mm. The propeller was positioned in the vertical and lateral centre of the tunnel. The test setup was a push configuration. Another type of hub was used for this test to match the push configuration better.

The velocity field was measured using Laser Doppler Velocimetry (LDV). The inflow was homogenous and the LDV measurements were performed in the planes at axial distance 0.1D and 0.2D in front of the propeller disc, where D is the propeller diameter.

The measurements were angular based with the zero degree position defined as the 12 o' clock position. The velocities in all directions were measured at every 0.25° step. The test was performed in non-cavitating condition. The operating conditions are presented in Table 3.

Table 3: The operating conditions for the velocity field measurement

Water density	[kg/m3]	997.1
Kinematic viscosity of water	[m^2/s]	9.03E-07
Number of revolutions	[1/s]	23
Velocity	[m/s]	7.204
Advance coefficient	[-]	1.253
Thrust coefficient	[-]	0.25
Torque coefficient	[-]	0.725

The data provided was firstly axial, tangential and radial velocities for the angular interval $-50° \leq \Phi \leq 22°$ at 0.25° step size for the two planes in front of the propeller disc at radial positions R0.7, R0.97 and R1.0

The tip vortex at x/D=0.1 was also given as velocities in the Cartesian directions in the interval $-40° \leq \Phi \leq 0°$ and r/R in the interval $0.4 \leq r/R \leq 1.1$ [5]

2 Method

This section explains the practice of CFD, BEM and WS. In the subsections, first the general method of PPTC prediction is described and then the automation practice.

2.1 Open Water Test with CFD method

The preprocessing tool used for the mesh was ANSA. The geometry was simplified by removing a gap between the hub and the root and a gap in the intersection between hub and shaft, see Figure 1.

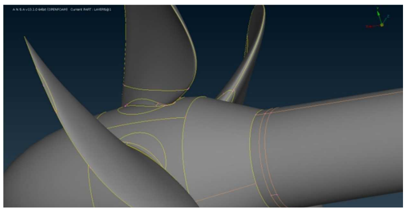

Figure 1: The modified geometry. Note that the gaps between hub and shaft and hub and blade root are filled.

The blade, hub and shaft were surface meshed with triads. The triads were smaller at high curvature and larger near mid surface sections.

As turbulence model, the K-omega SST model with the wall unresolved was applied. To model the boundary layer, wall functions were used. Five prism layers with 1.2 as growth ratio and a starting height of 0.5 mm were applied.

The rotation was modeled with Multiple Reference Frames, MRF. To make use of MRF, a volume surrounding the rotating parts was needed. As domain, a larger cylinder was used. For local mesh refinement near the hub and the blades, a size box was used. The whole setup can be seen in Figure 2. The dimensions of MRF-zone, size box and domain can be seen in Table 4.

Figure 2: The propeller inside the MRF-zone (small region with thin line), the domain (large region with thin line) and size box (thick line)

The surface of the MRF-zone and the domain was meshed with triads and the interior of both regions were meshed with hexahedrals, allowing a minimal amount of tetras and pyramids in the transition from the triad surface elements. The resulting number of elements can be seen in Table 5.

Table 4: Dimensions of size box, MRF zone and domain

Domain diameter	5D	MRF-zone length	7D
Domain length upstream	5D	Size box length	5D
Domain length downstream	10D	Size box diameter	D+0.25D
MRF-zone diameter	D+0.25D	Propeller diameter, D	250 mm

Table 5: Number of elements for the different grids

	OW coarse	OW fine	Velocity field coarse	Velocity field fine
Surface mesh elements	100000	150000	290000	200000
Prism layer elements	502920	600000	410000	1000000
Total elements	4500000	11000000	4600000	13600000

As interpolation schemes, first order accurate schemes were used for the turbulent quantities kinetic energy, inverse turbulent time scale and the turbulent viscosity. For the velocity, a second order upwind scheme was applied.

To ensure grid independent results, the mesh was refined at regions with large gradients. The mesh was made larger around shaft and hub, but refined with a factor of two at blade corners and blade tip. The maximum volume element length in the slip stream was also reduced by a factor two. The contingent difference between the coarse and the fine mesh should depend on the discretization error. [6]

The CFD package used was OpenFOAM with the solver MRFSimpleFoam. The simulation was of steady RANS type. The forces and moments were computed on the blades only.

As boundary conditions, the no-slip condition was applied on the propeller surface. The outlet was set as pressure outlet with zero gradient for the remaining quantities. The inlet was set up with uniform velocity and the remaining quantities were calculated in accordance with equation 1-4. [7]

$$k = \frac{3}{2} V_A^2 * I \tag{1}$$

$$\frac{\mu_t}{\mu} = 10 \tag{2}$$

$$\epsilon = \frac{0.09 \rho k^2}{\frac{\mu_t}{\mu} \mu} \tag{3}$$

$$\omega = \frac{\epsilon}{k} \tag{4}$$

Where k = the turbulent kinetic energy; V_A *= the advance velocity; I = the turbulent intensity;* μ_t *= the turbulent viscosity;* μ *= the fluid viscosity;* ϵ *= the turbulent dissipation;* ρ *= the density of the fluid and* ω *= the specific dissipation.*

For the domain, wall functions were used and the pressure was of zero gradient type.

The meshing method was automated by using the ANSA scripting language and batch mesh program. A script using the settings described above was made. It was made to perform a basic geometry cleanup and to merge the cleaned geometry with a template containing MRF-zone, domain and a batch mesh scenario. This was to set proper element types and sizes, yielding consequent meshes for any propeller. Many of the automatic geometry and mesh improvement functions in ANSA were implemented in the script.

2.2 Open Water Test with BEM

For the BEM prediction, first a geometry input file was extracted from the BERG standard blade design documents.

The propeller was meshed according to best practice to get an orthogonal mesh, which is preferable. [8]

The velocity was set to match the reasonably high load $0.5 * J_{\eta Max}$. A steady analysis was performed and the wake panel and axial force radial distribution were studied. If the curves showed reasonably smooth distributions and the Kutta-condition was converged, the solution was considered trustworthy. If the solution wasn't trustworthy, the mesh was altered. Great care was laid on getting the last trailing edge element skew angle to be sufficient. [8]

When the mesh was good enough the open water test could be performed by simply inserting the proper speeds matching the model test, i.e. $V_A = JnD$. If the solutions were considered trustworthy for all advance velocities, the solution was considered as completed.

This process was automated by writing Visual Basic (VBA) scripts that may export mesh settings and the geometry on a proper format into a calculation folder. Separate scripts were made to get grid dependence control-files and open water test control-files. A script to extract open water data from the output files and tabulate as advance ratio, thrust, torque and efficiency and plot them was made as well.

2.2 Open Water Test with WS

Since the Wageningen Propeller Series Program uses the polynomials, the best way to automate and use the program would be to program the polynomials directly into VBA. The polynomials are divided in two; one for K_T and one for K_Q. These polynomials were already at hand at BERG, so they were programmed into separate VBA-functions.

The polynomials were programmed so that pitch ratio, blade area ratio and number of blades were picked in the design-sheet. The outputs were K_T and K_Q as function of advance ratio, yielding an automated Wageningen Series script.

2.3 Velocity Field Measurement

The velocity field computation was performed in the same way as for the open water test with the CFD method. The domain and inner volume were rotated and elongated to fit the new arrangement and the longer shaft.

To comply with the thrust identity, the speed had to be lowered somewhat. Two different speeds were tested and then the linear relationship between J and K_T was used to find the proper velocity yielding the correct thrust.

3 Results

In this section, the results are presented for first the pure open water test with CFD, BEM and WS compared to model test results. After this the results of the velocity field measurement and prediction are presented. It should be noted that all predictions were performed as blind tests.

3.1 Open Water Tests

The final fine mesh for the open water test is visualized with a centre plane cut in Figure 3. As can be seen, the resolution is highest near the blade surface.

Figure 3: The coarse mesh for the open water test

The grid dependence comparison from J=0.6 to J=1.2 is presented in Figure 4. It is evident that the grid dependence is very small.

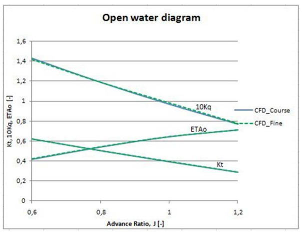

Figure 4: A comparison between the coarse and the fine mesh for the CFD simulation

The y^+ values for the coarse and the fine mesh is presented in Table 6. They are higher for the fine mesh, which might depend on the higher resolution, yielding less dissolved gradients near the wall.

Table 6: The y^+-value of the coarse and fine mesh at corresponding advance ratio.

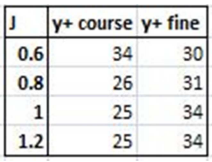

J	y+ course	y+ fine
0.6	34	30
0.8	26	31
1	25	34
1.2	25	34

The axial velocity distribution of the open water test at J=0.6 is visualized in Figure 5. It looks intuitive. A separation zone occurs behind the shaft, which might affect the force calculation. This should on the other hand be negligible since the hub is excluded from the force calculations.

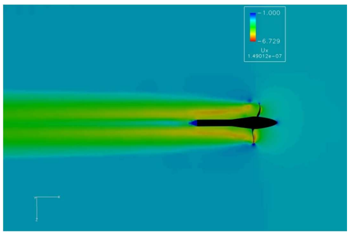

Figure 5: The axial velocity distribution for the open water test at J=0.6

The radial wake strength (PHIW) and radial axial force (F_x) distributions of the SMP'11 propeller at $0.5J_{\eta Max}$ in the BEM open water prediction can be seen in Figure 6. They are smooth and the highest load seems to occur at the expected radial section.

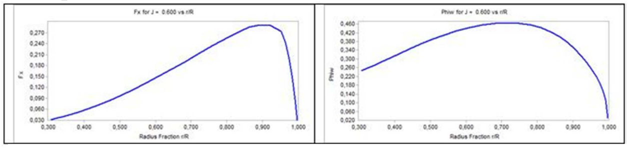

Figure 6: Radial axial force distribution to the left and wake strength distribution to the right

The open water test results of the CFD method, BEM and WS are compared to model test results in Figure 7 to Figure 9. It should be noted that the calculations were performed as blind tests. The CFD calculation is very accurate. The difference for BEM should depend on that the hub was excluded from the calculation. The same goes for WS together with geometrical differences.

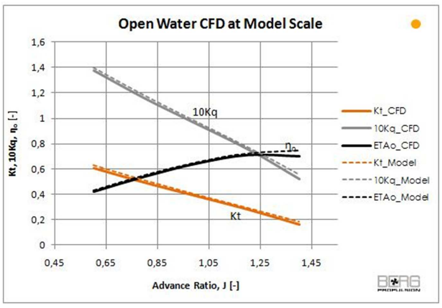

Figure 7: Open water chart with CFD results compared to model test results

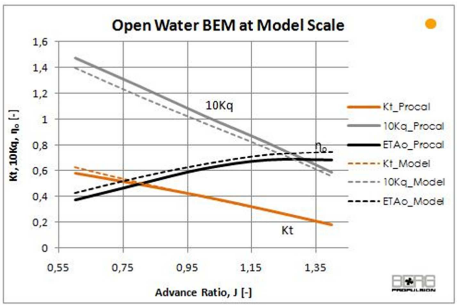

Figure 8: Open water chart with BEM results compared to model test results

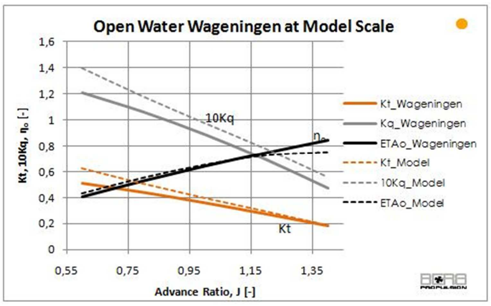

Figure 9: Open water chart with WS results compared to model test results

3.2 Velocity Field Measurement

The fine mesh used in the velocity field measurement prediction is shown in Figure 10.

Figure 10: The fine mesh used for the velocity field measurement prediction

The velocity, corresponding K_T and corresponding y^+ are tabulated in Table 7. The results are from the fine mesh. $V_A = 7.1867$ was chosen as working point.

Table 7: Velocities and corresponding J, K_T and y+ for the fine mesh of the velocity field measurement prediction.

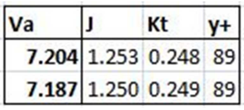

Va	J	Kt	y+
7.204	1.253	0.248	89
7.187	1.250	0.249	89

In Figure 11 an iso-surface with helicity of 150 $\mathbf{m^2/s^2}$ is shown to visualize the generated tip vortex. The generated tip vortex is evident. The velocity field measurement results at radial stations r/R=0.7, and 0.97 in plane x/D=0.1 downstream the propeller disc for the PPTC propeller with non-dimensional axial, tangential and radial velocities from the prediction plotted together with the model test results can be seen in Figure 12 and Figure 13.

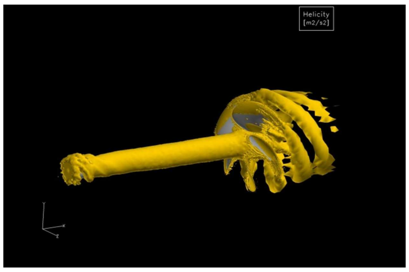

Figure 11: ISO surface of helicity 150 m^2/s^2 at the working point

The thick line represents the calculation and the thin, fluctuating line represents the model test. The fluctuations in the calculations should depend on that the solution is slightly unconverged. The tendency of the vortex was sufficiently captured.

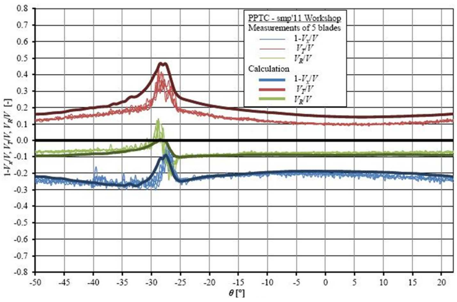

Figure 12: x/D=0.1, r/R=0.7

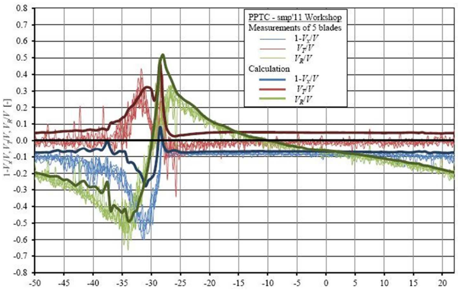

Figure 13: x/D=0.1, r/R=0.97

The tip vortex as measured by LDV and the result predicted by OpenFOAM can be seen in Figure 14.

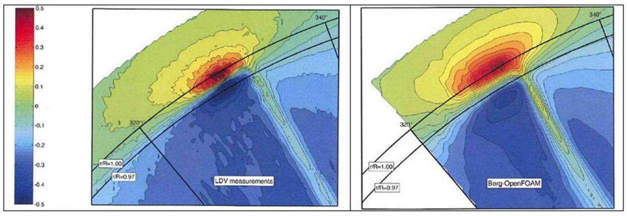

Figure 14: LDV measurements (left) compared to CFD prediction (right) of velocity field at plane x/D=0.1

As can be seen, the vortex is rather well predicted at every radial station. The largest difference lies within the expected; the LDV is fluctuating while the CFD shows a more averaged behavior.

3.3 The Automated CFD Script

This section describes what the CFD-automation script performs when it is used. First, a script generated blade from Solid Works (SW) on .IGS-format is provided, see Figure 15.

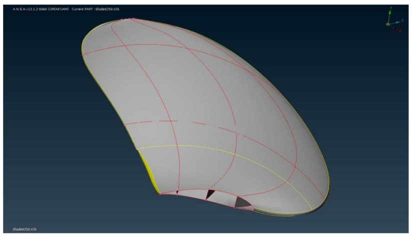

Figure 15: The blade as generated from SW.

When the first part of the script is started, unnecessary surfaces are removed and the domain, MRF-zone, shaft and hub are added and scaled to fit the propeller diameter, see Figure 16 for the result.

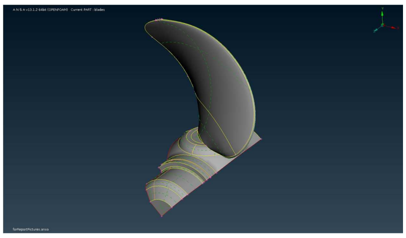

Figure 16: The cleaned geometry

This is a natural break of the script; it is often relevant to measure and set up the pitch. When geometrical aspects are satisfactory, the surface mesh generating part of the script could be started. The mesh quality could become poor or unmeshed in a few regions. This is the second and last natural breakpoint; one should always check that the surface mesh represents the physics and is of good quality. Figure 17 shows a completed surface mesh after the second part of the script.

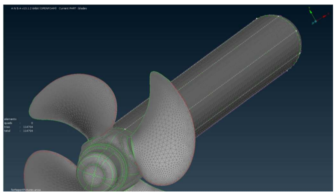

Figure 17: The completed surface mesh, ready for layers and volume mesh

When the third part of the script is started, the last steps of automatic surface mesh cleanup, layer generation and volume meshing is performed. The completed mesh can be seen in Figure 18.

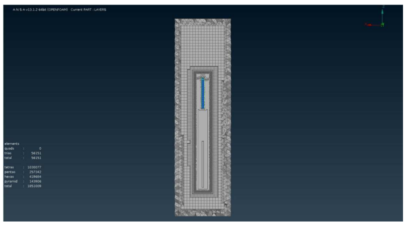

Figure 18: The completed volume mesh

The result could be outputted to e.g. the OpenFOAM template-folder containing the boundary conditions described in section 2.1. If no pitch setting is needed and the user is familiar with ANSA and no large problems with the geometry occur, the estimated work time using the script is 5-10 minutes. The whole mesh is completed within 15-25 minutes.

4 Conclusions and Future Work

The main conclusions that can be drawn about the CFD-method are that the CFD-method:

- is the most accurate among the compared methods regarding open water characteristics predictions, but has the very highest computational cost
- might have long setup times
- can accurately predict the velocity field downstream the propeller disc if the mesh resolution is high enough
- is good for "out of the box" predictions, such as predicting the characteristics from an odd design or removing the hub from the force results
- gives the possibility to visualize problem areas, such as separation zones
- could be automated regarding pre-processing for open water predictions, saving at least five hours of manual work and guaranteeing consequent setups. This conclusion only regards the method described in this paper.

The main conclusions that can be drawn from BEM are that BEM:

- is almost as accurate as CFD regarding open water characteristics predictions and has significantly lower computational cost
- has much shorter setup time than CFD
- is a good tool for early propeller performance predictions
- could be automated both in regard to pre- and post-processing, saving some time and, more importantly, reducing the risk of setup errors. This conclusion only regards the method described in this paper.

The main conclusions that can be drawn from the Wageningen Series are that the Wageningen Series:

- has an extremely low setup time
- does not need a complete geometry; only pitch, blade area ratio, number of blades and advance ratio are needed to make a prediction
- is very useful at an early design stage due to the low number of inputs
- is useful to get an indication of whether the PROCAL/CFD results are correct
- could be automated both in regard to pre- and post-processing, which saves some time.

The final recommendations of how the tools and specific methods studied in this thesis should be used are that:

- the Wageningen Series should be used for predictions at a very early design stage and to check whether the other predictions are within reasonable values
- the boundary element method should be used when the propeller design is finished and more reliable open water predictions are needed
- the CFD method should be used when more odd designs should be tested or when exact guarantees of open water performance should be left.

Some aspects should serve as recommended future work. The volume mesh close to the propeller disc in the velocity field measurement should be improved. This could solve the convergence issue at x/D=0.1. The wall could be entirely resolved to attain more accurate velocity field measurements. It would also be interesting to perform an analysis with a fully hexahedral mesh to improve the results. A comparison between the MRF results and results with a sliding mesh would also give better understanding of the level of approximation. The CFD script should be rewritten to handle the periodic boundary condition in ANSA. This allows as many more times higher cell resolution as the number of blades of the propeller. It is a qualified approximation as well; the analysis is steady and hence the results won't be affected by the symmetry assumption.

REFERENCES

[1] Wageningen propeller series program - v2003_1 – A program containing the Wageningen charts

[2] PROCAL v 2.0.2.0 – A boundary element method tool with GUI, post processor, grid generator and solver for the direct formulation of the potential flow problem for propeller. It can also solve for cavitation using the Morino formulation

[3] OpenFOAM v1.6 –An open source CFD toolbox. "It can solve anything from complex fluid flows involving chemical reactions, turbulence and heat transfer, to solid dynamics and electromagnetics." (quoted: http://www.openfoam.com/)

[4] ANSA v13.1.2 – A meshing program for CFD and FEM including CAD tools.

[5] SMP'11 PPTC description: http://www.sva-potsdam.de/assets/images/smp11

[6] Versteeg H.K., Malalasekera W., An Introduction to Computational Fluid Dynamics – The Finite Volume Method 2nd ed., Malaysia 2007

[7] Davidsson L., Numerical Methods for Turbulent Flow. Göteborg, Sweden, Chalmers University of Technology, Department of Thermo and Fluid Dynamics. January 7, 2005.

[8] Bosschers J., PROCAL v2.0 Theory Manual, MARIN, Report 20834-7-RD, Wageningen, June 2009

Analysis of the Floating Structures using Sliding Meshes

Marek Kraskowski, Ship Design and Research Centre S.A. (CTO), Poland
marek.kraskowski@cto.gda.pl

The paper presents the results of the CFD simulations of the motion of the objects floating in regular waves of high amplitude. Two types of objects were analyzed: a fishing vessel and a drilling platform. For the vessel, the results were validated basing on the experiment in the towing tank. A simplified method for taking into account the mooring system was proposed. All simulations were carried out at model scale, using sliding meshes and STAR CCM+ flow solver.

The choice of moving mesh type for particular type of simulation including fluid-structure interaction depends on pros and cons of these types; the most popular approaches are (see Fig.1):

- Rigid mesh moving together with moving object (no relative motion between mesh nodes) – simplest possible approach, characterized by lowest computational cost and fairly appropriate in cases like estimation of dynamic trim and sinkage of the vessel in calm water. However, the accuracy of this approach rapidly decreases for high motion amplitudes, especially large angles, due to violent motions of the domain boundaries;
- Deforming mesh – characterized by high accuracy, but appropriate only for cases where motion amplitudes are relatively low. Too large displacement of the object from its initial position causes unacceptable deformation of the mesh cells;
- Sliding mesh – the flow domain is divided in two subdomains; the inner domain, surrounding the analyzed object, is moving together with it, and the outer domain undergoes only linear motions. This approach is characterized by much higher tolerance for large amplitudes of linear motions than the rigid mesh, but also considerably higher computational cost;
- Overlapping meshes – robust and quite accurate, but usually unavailable in commercial software.

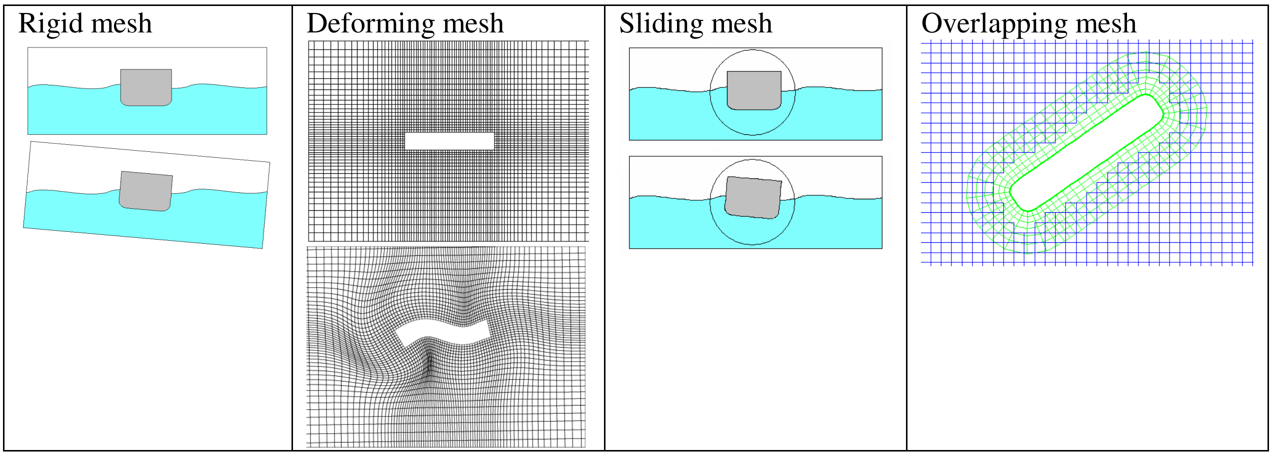
Rigid mesh
Deforming mesh
Sliding mesh
Overlapping mesh

Fig. 1: Types of meshes

The goal of the realized research was to elaborate a robust computational method capable of handling large angular motion amplitudes, so the choice of sliding meshes for the computations of floating objects in waves was considered an optimal solution among the options available in STAR CCM+ solver.

The first test case to be analyzed using sliding mesh was a fishing vessel; its geometry is presented in Figure 2.

Main features - full scale/model scale:
(scale factor: 21.45)

Length b.p.: Lpp = 65.4 m/3.049 m
Breadth: B = 19.0 m/0.886 m
Draught: T = 6.3 m/0.294 m

Fig. 2: Geometry of the analyzed vessel (main features listed)

The analysis of motion was limited to heave and pitch in head waves, at constant forward speed. Three regular waves were considered; their features (length and height at model scale) are listed in Table 1.

Table 1: Regular wave parameters

Length λ [m]	3.0	4.0	4.8
Height H [m]	0.136	0.139	0.174

As only one angular motion was considered, the inner computational domain of cylindrical shape could be used. Dimensions of the computational domain are presented in Figure 3.

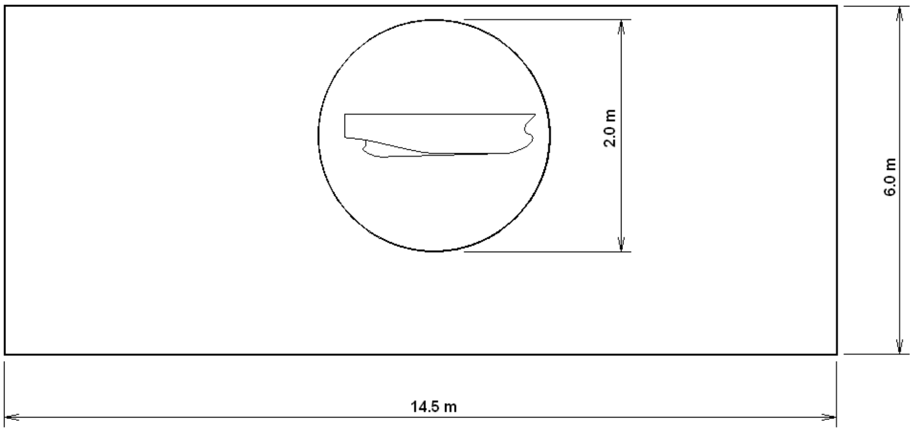

Fig. 3: Computational domain – dimensions (width: 4.66m)

Due to the need for additional iterations at sliding interfaces in each time step, economical mesh generation is crucial in case of using sliding meshes. In the present case, total number of mesh cells was about 830 000. Details of the computational mesh are presented in Figure 4.

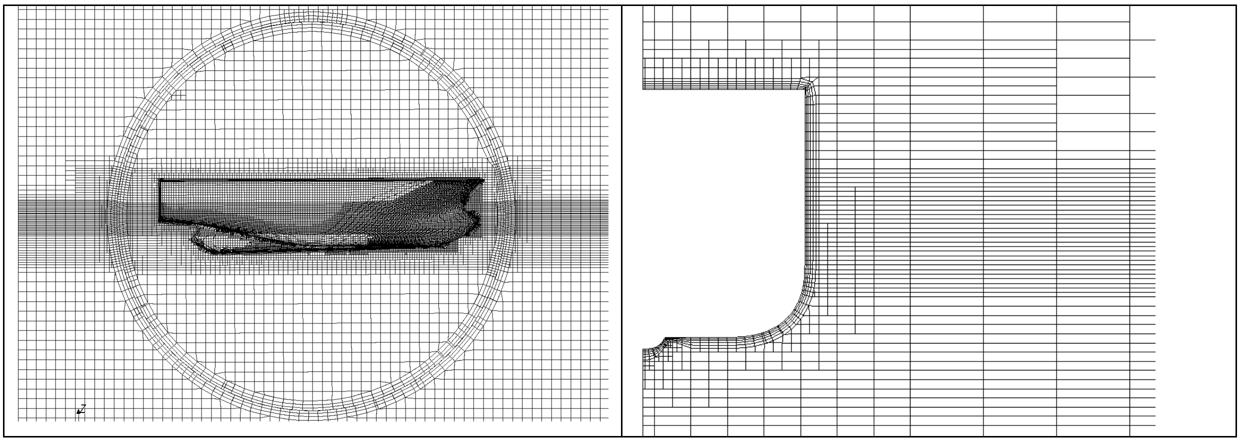

Fig. 4: Computational mesh - details

(It was discovered during test computations that few layers of O-grid on each side of the sliding interface is necessary to avoid unphysical flow behaviour at the interface.)

The experiment in the towing tank was carried out in order to provide a validation material for the computational method. The measured quantities were: time history of pitch, heave and resistance. A sample of comparison of CFD results with experimental results is presented in Figure 5.

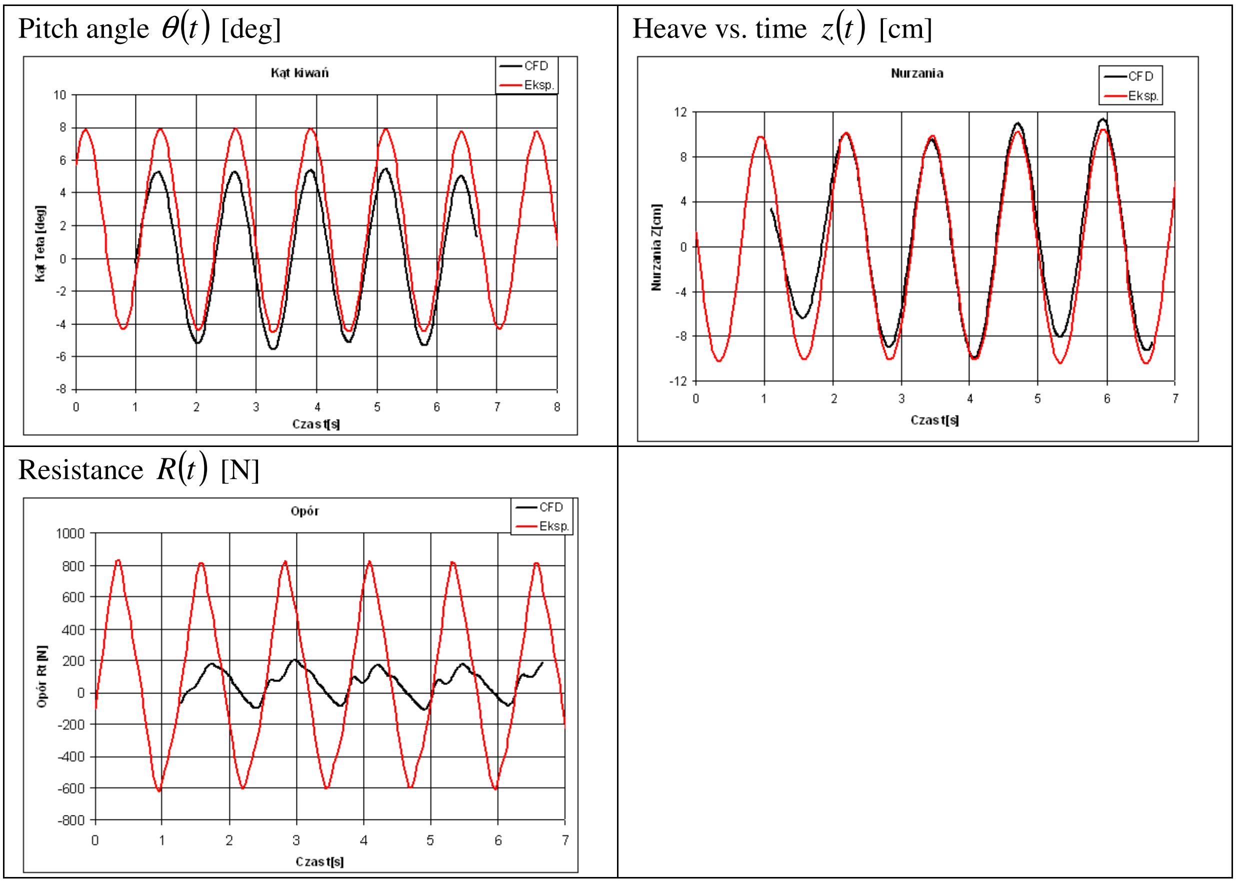
Pitch angle $\theta(t)$ [deg]

Heave vs. time $z(t)$ [cm]

Resistance $R(t)$ [N]

Fig. 3: Comparison of CFD and experimental results for fishing vessel

The comparison presented above yields the following conclusions:

- Although the mean computed resistance value is close to the mean measured value, huge underestimation of extreme values can be observed in the CFD results. The reason of this tendency was not explained yet, but seems to be a general feature of RANSE computations using VOF model, probably due to fuzzy interface between water and air;
- The CFD prediction of pitch angle is reasonable, but underestimated. One of the reasons for that is using the “numerical wave generator” based on linear wave theory, while the wave steepness considerably exceeds the limit of validity of this theory. In consequence, the resulting wave is noticeably different from the required one, i.e. the crests are higher and the hollows are shallower. Further attempts of using higher order wave theory to achieve the required wave parameters were not successful, so a provisional solution was applied, consisting in introducing minor corrections to the generated linear wave, so that the resulting wave gets closer to the required one. Such a rough method, however, causes strong oscillations of wave height in time. Thus, the problem of generating large amplitude waves in CFD computations remained unsolved so far;
- Despite the problems listed above, the agreement of computed and measured heave is surprisingly good.

Despite the encountered problems listed above, a positive remark can be done than the method for analysis of floating objects, based on sliding meshes, is characterized by sufficient robustness.

It has, however, an important drawback that should be mentioned here: it can be seen in figure 4 that in case of very slender vessel (characterized by large L/B and L/T), enclosing it into a cylindrical subdomain would result in large wastage of computational power due to large regions of unnecessary mesh.

Further author's work on development of the computational method for floating objects in waves is focused on adapting the CFD methods for the offshore industry objects. Therefore, the following elements should be modelled in the simulations:

- Mooring systems;
- Elastic and rigid risers;
- Tethers of the tension leg platforms (TLP);
- Dynamic positioning.

The work done so far includes introducing the equivalent forces simulating the action of the mooring system to the simulation of the motion of semi-submersible platform in waves. Some preliminary results of this simulation are presented below.

In case of a homogeneous mooring chain, the relation between chain tension and the moored object displacement is given in analytical form, e.g. (*Barltrop*, 1998):

$$S - S_0 = \frac{H}{w} \cdot \arcsin\left(\frac{wL}{H}\right) - \frac{H_0}{w} \cdot \arcsin\left(\frac{wL_0}{H_0}\right) + \frac{L_T}{AE}\left(H - H_0\right) - \left(L - L_0\right)$$

where:

S : horizontal displacement of the object;

H : horizontal component of the chain tension, $H = AE\sqrt{\left(\frac{T}{AE} + 1\right)^2 - \frac{2wh}{AE}} - AE$

T : chain tension, h : water depth;
w : unit weight in water;
L : chain length measured from the moored object to the seabed;
AE : chain elasticity parameter (A transversal section, E - Young modulus);
L_T : total length of the chain from the moored object to the anchor.
index 0 indicated the values in assumed equilibrium state.

An analytical formula like the one above is valid for quasi-static displacements of the object; in case of high-frequency motions, dynamic effects become important, i.e. the chain tension increases due to inertia and resistance forces. These effects were not taken into account yet in the proposed computational model, assuming that the influence of mooring system on wave frequency motions of the object is negligible. Such assumption is valid in large range of motion frequencies.

The relation given above is nonlinear and cannot be linearized for a wide range of object displacement, so the following model of chain force (taking advantage of basic features of STAR CCM+) was proposed:

- Each mooring chain is replaced by several linear springs;
- The relaxation length of the springs vary, so that when the object displacement increases, they are tightened successively (a scheme is presented in Figure 6);
- In such way, quite accurate piecewise linear interpolation of the nonlinear relation is achieved (see Figure 6).

In the simulation of semi-submersible platform, 8 mooring chains were introduced.

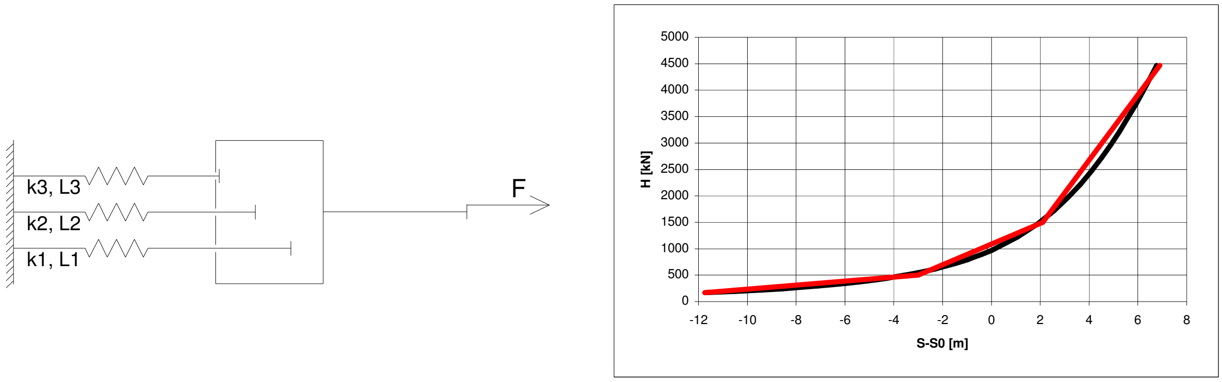

Fig. 4: Modelling the mooring chain with linear springs – scheme and characteristics

Simulation of the semi-submersible platform motion in waves was also carried out using the sliding mesh approach, however, in this case, all degrees of freedom were free; so the inner domain was spherical. The mesh details are presented in Figure 7.

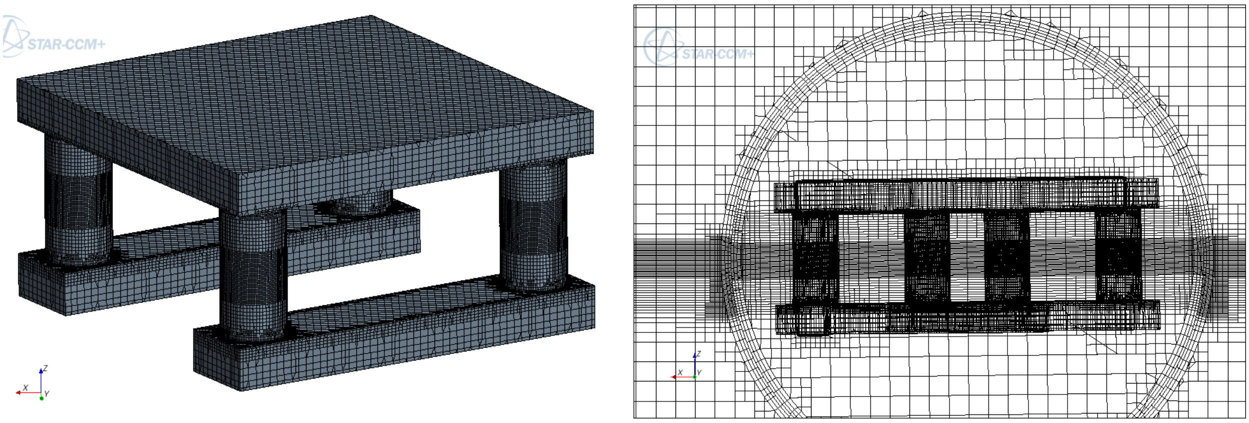

Fig. 5: Computational mesh for the semi-submersible platform

The simulation of the platform motion was carried out only to check the robustness and qualitative correctness of the model, as no experimental results are available yet. Figures 8 to 10 show examples of results. First observations based on the achieved results are as follows:

- Despite long time of simulation, no steady drift value was achieved due to strong oscillations appearing at the beginning of the simulation. Introducing the artificial damping in the initial stage can speed up the solution;
- Quite stable solution for pitch and roll was achieved.

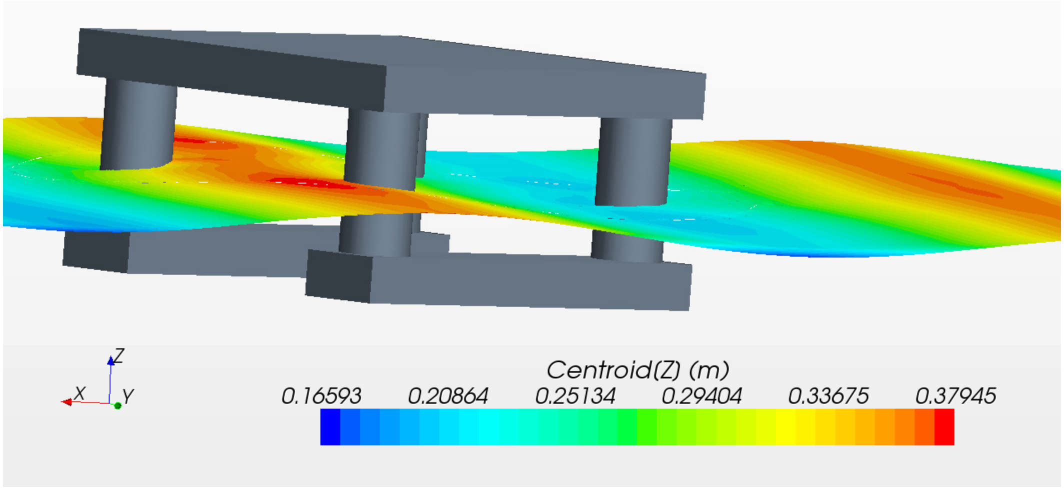

Fig. 6: Semi-submersible platform in waves

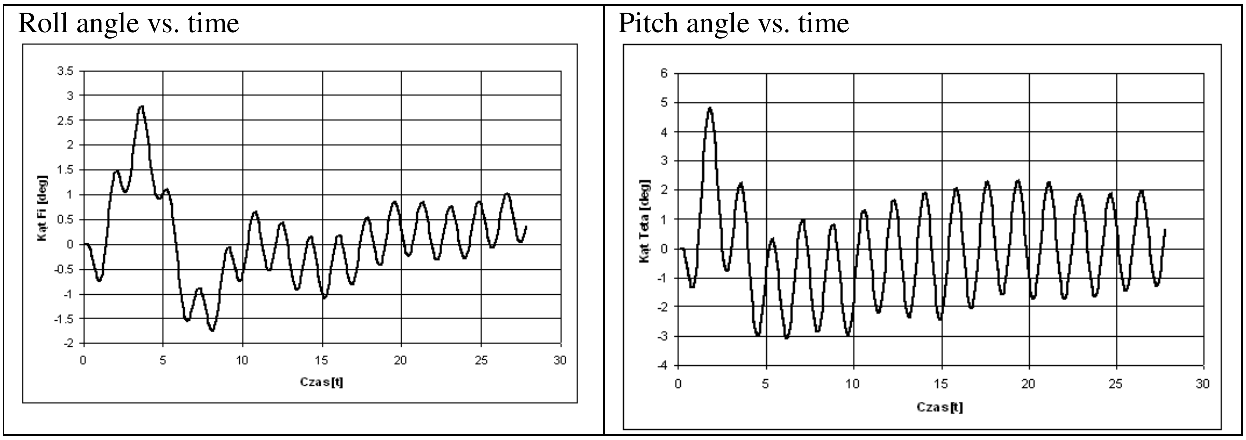
Roll angle vs. time

Pitch angle vs. time

Fig. 7: Roll and pitch angle of the semi-submersible platform

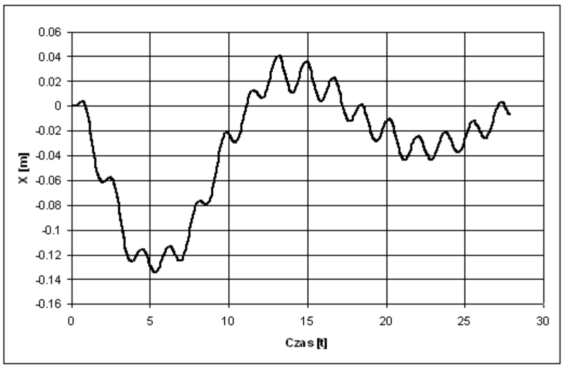

Fig. 8: Drift of the semi-submersible platform

The work done so far, focused on application of sliding meshes for floating objects in waves, can be summarized as follows:

- The method proved to be sufficiently robust to be used in 6DOF simulations characterized by large angular motions;
- For the vessel motion in head waves, reasonable agreement with model tests was observed;
- A method for modelling the mooring system in CFD was proposed, based on steady approach and a set of linear springs – to be validated;
- Some problems were encountered in generating steep waves in CFD; further research on this topic is planned, including application of high order models.

References

Barltrop N. D. P. et al., *Floating structures: a guide for design and analysis*, The Centre for Marine and Petroleum Technology, 1998

Validation of Viscous Free-Surface Flows around NPL Catamarans in Oblique Motion at Moderate Froude Number

Max Haase[1], Nikolai Kornev[2] and Robert Bronsart[2]

[1] *University of Tasmania, Australia, mhaase@amc.edu.au*

[2] *University of Rostock, Germany, nikolai.kornev@uni-rostock.de*

Introduction

Simulation of ship manoeuvres is one of the most important problems of ship hydrodynamics. Since time-domain simulation of ship manoeuvres still lack in computational efficiency, it is common to simulate the ship at quasi-staedy motions to then derive an Abkowitz-type model of hydrodynamic forces and moments to be coupled with the equations of motion. Considered degrees of freedom usually include surge, drift and sway, in this study static drift at different Froude numbers has been taken into account. In earlier work, it has been shown that even empirical methods can deliver reasonable results for free-sailing manoeuvres (Haase et al 2010). For catamarans an approach by Mastushkin (1976) to correct lateral force and yaw moment depending on the demihull separation could be experimentally validated for catamarans with large separation ratios (s/L = 0.45). For small values of s/L = 0.15 the yaw moment could be estimated sufficiently, but the lateral force was significantly overestimated (Winkler et al 2011). This leads to the assumption, that an interaction between the demihulls of catamarans in manoeuvring motions needs to be further investigated and an independent hydrodynamic model is required. A catamaran with a representative separation ratio of s/L = 0.15 utilizing NPL hullforms (National Physics Laboratory) has been investigated at static drift simulations for different velocities up to Fn = 0.4 and drift angles up to ß = 30 °. The simulations have been done using open source solvers of OpenFOAM 1.7.1 for steady single-phase and unsteady multi-phase RANSE computations, they have been validated with captive model test data by Winkler et al (2011).

The work has been done within the joint research project AGAPAS (Autonomously acting Rescue Robot for Persons in Distress at Sea) aiming at the development of a novel rescue boat using a catamaran configuration with the total length of L = 4.5 m. The boat has to operate in heavy seas under conditions of strong wave induced flow motion with velocities comparable with boat speed. Large effective drift angles are expected to be the common case in operation. The development of a methodology to estimate hydrodynamic forces and moments under such conditions was the motivation for the present study.

Ship Model Description

Table 1: Main particulars of the tested NPL 4a hull form.

Parameter			
Design length between perpendiculars	L_{pp}	[m]	1,6
Design breadth	B	[m]	0,15
Design draft	D	[m]	0,10
Block coefficient	C_B		0,40
Prismatic coefficient	C_P		0,67
Midship coefficient	C_M		0,56
Wetted surface area	S_w	[m²]	0,34
Longitudinal centre of buoyancy	LCB	[m]	0,69

A NPL 4a hullform with a representative length of 1,6 m was selected for the investigations, a demihull separation ratio of s/L = 0.15 has been chosen. The main particulars can be seen in table 1, the linesplan is shown in figure 1. The catamaran has been simulated at velocities of Fn = 0.3 and 0.4 at a variety of drift angles up to ß = 30 °. In the past researchers have utilized a variety of NPL hullforms for investigations on calm water resistance (Molland et al 1994) and seakeeping (Wellicome et al 1995) of fast displacement catamarans.

RANSE Simulation of Double-Body Flow

As no significant free-surface deformation is expected, it is advantageous to model the ship flow using the double-body concept according which the submerged body is mirrored with respect to the undisturbed water surface. The calculation is then performed for the double body in an unbounded fluid. Generally the double-body concept is valid for small Froude numbers Fn < 0.1 … 0.15. However this simplification can be quite acceptable for slender bodies at moderate Froude numbers around 0.3. Calculations were carried out using the solver simpleFoam within the open source code OpenFOAM 1.7.1. The solver utilizes pressure correction SIMPLE algorithm (Semi-Implicit Method for Pressure-Linked Equations, see Peric and Ferzinger (2001)). Turbulence has been taken into account by the SST k-ω turbulence model.

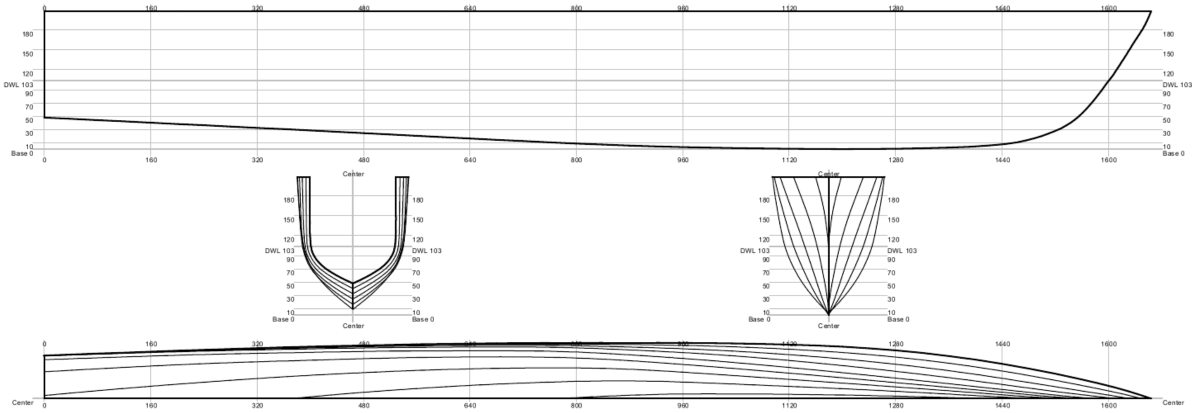

Figure 1: Lines plan NPL 4a.

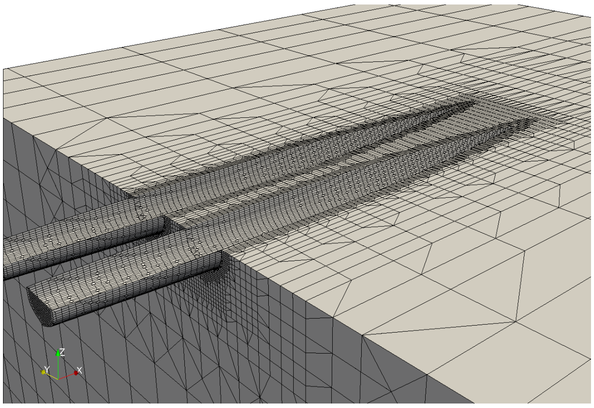

Figure 2: Grid structure used for double-body flow computation.

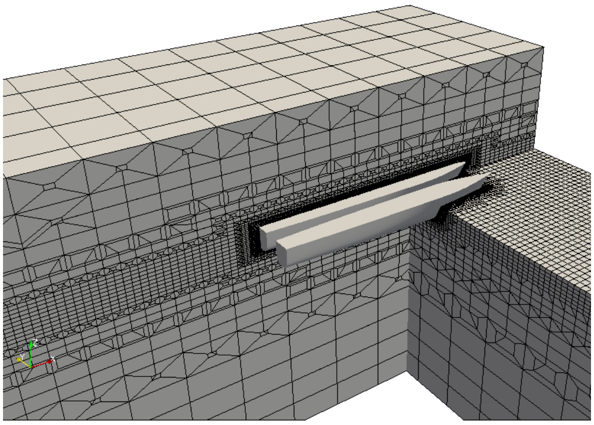

Figure 3: Grid structure used for free-surface flow computation.

A grid (figure 2) has been created using OpenFOAM tools, such as blockMesh, snappyHexMesh, or snapEdge. A coarse resolution in the far field, combined with fine resolution close to the hull has shown good results using only about 100,000 cells.

Generally, as can be seen in figure 4-6, the results of experiments and numerical computations agree quite well. The resistance force agrees quite well for drift angles up to 20 °. However, the non-linear character of the resistance increase observed in measurements was numerically not very well reproduced. The relative discrepancy between experiment and computation is between 5% and 10% for all cases and forces excepting the longitudinal force at drift angles larger than ß = 30 °. Also it is obvious, that the results for the transverse force agree with measurements better than these for the yaw moment coefficient. While experimental values for the yaw moment coefficients are generally larger than the computational one, experimental side force coefficients are slightly smaller compared to the computation. An exception is the transverse force at a drift angle of 30 °. The computations at ß = 30 ° has been conducted for two velocities corresponding to Froude numbers Fn = 0.3 and Fn = 0.4. There has been no noticeable difference between the two velocities regarding force and moment coefficients. Computational results for the drift angle of ß = 45 ° deviate significantly from the experimental ones, eventually due to increasing gravitational (Froude number) effects.

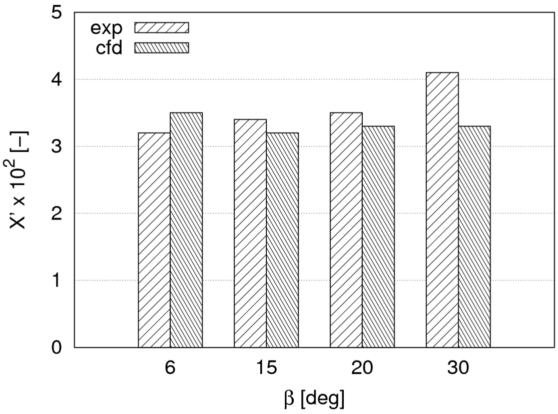

Figure 4: Comparison between experiments and double body computation for longitudinal force coefficient of NPL catamaran at different drift angles, V = 1.19 m/s.

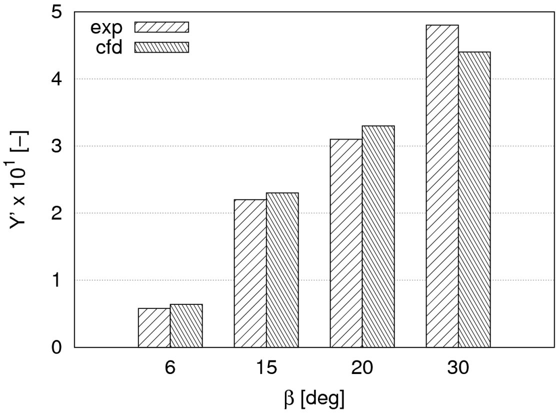

Figure 5: Comparison between experiments and double body computation for lateral force coefficient of NPL catamaran at different drift angles , V = 1.19 m/s.

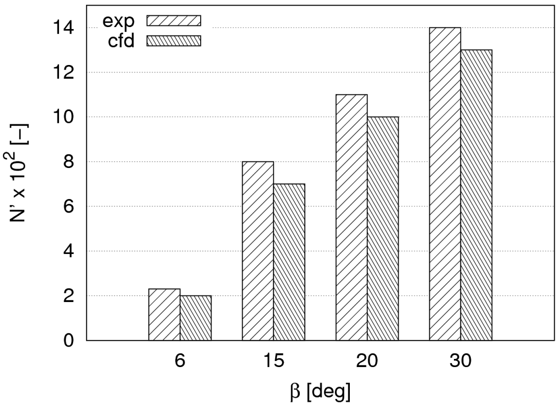

Figure 6: Comparison between experiments and double body computation for yaw moment coefficient of NPL catamaran at different drift angles, V = 1.19 m/s.

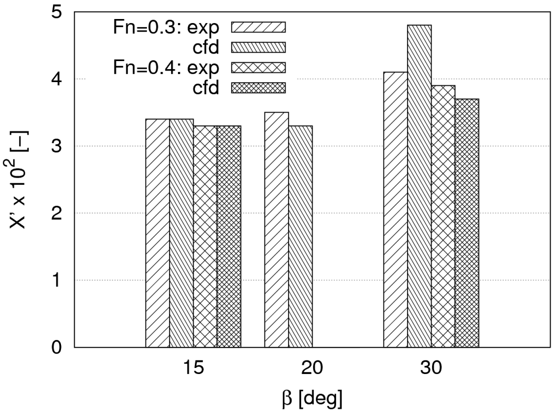

Figure 7: Comparison between experiments and free-surface flow computation for the longitudinal force coefficient of NPL catamaran at different drift angles and Froude numbers.

RANSE Simulation of Free-Surface Flow

To prove the effect of the Froude number on manoeuvring forces the calculations have also been carried out with modelling the free surface. The computations have been performed with the multi-phase solver interFoam of OpenFOAM 1.7.1 in unsteady mode. For a grid considering the free surface, also the emerged part of the ship and the domain needs to be modelled. To resolve the free surface elevation a vertical refinement around the expected free surface has been done. The commercial tool HexPress (Kleinsorge and Bronsart 2011) has been used to generate the grid consisting of 500,000 cells, as shown in figure 3.

In figure 7 it can be seen, that longitudinal force is well estimated using the free surface computation for moderate drift angles. At large drift angles the longitudinal force seems to be overestimated. Surprisingly, the results for the high Froude number of 0.4 agree with measurements better than these for Fn = 0.3, although the strong free surface effects are more pronounced at large Froude numbers and therefore the modelling errors are more probable. The discrepancy with measurement for the transverse force given in figure 8 is acceptable at moderate drift angles and not satisfactory for the large ones. Even the tendency of the force decrease with growing Froude number is not reproduced.

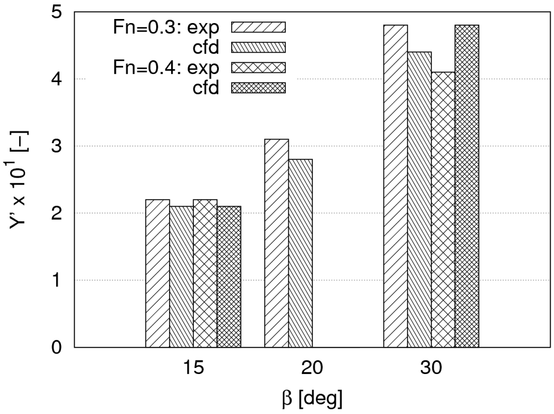

Figure 8: Comparison between experiments and free-surface flow computation for lateral force coefficient of NPL catamaran at different drift angles and Froude numbers.

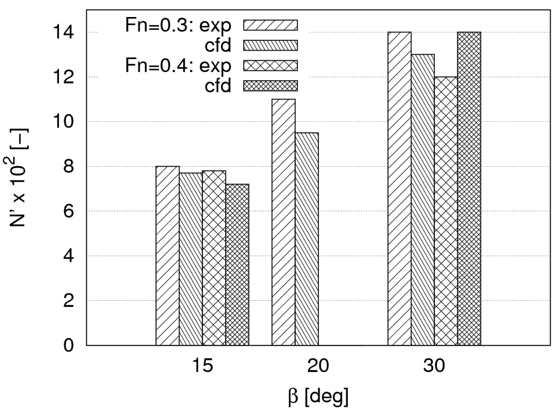

Figure 9: Comparison between experiments and free-surface flow computation for the yaw moment coefficient at different drift angles and Froude numbers.

For the yaw moment (figure 9), the agreement between simulations and experiments is quite good at ß = 15 ° at both Froude numbers and for ß = 30° at the slower speed, while the results for ß = 20 ° and for ß = 30 ° at Fn = 0.4 show a significant deviation from experimental ones. However, for drift angles ß = 15 ° the computations considering free-surface effects better correlates with measurements then double-body flow simulations.

Figure 10 shows the free-surface deformation caused by the NPL catamaran. The bow wave is well pronounced and its appearance agrees well with observations done during the model tests by Winkler (2011). Figure 11 demonstrates a strong vortex shedding from the bow section as well as the ventilation of the fore ship section at Fn = 0.4 and ß = 30 °. It can be seen, that due to the low pressure inside the vortex the ventilation continues into the core of the vortex, also the resulting influence of the bow vortex on the leeward demihull can be clearly seen at the pressure distribution in figure 12. Even if a very high accuracy in the resulting force and moment coefficients compared to experimental data could not be achieved, this suggests that the code is capable to resolve highly non-linear physical effects such as ventilation and wave-breaking at free-surface flows. In figure 13 the free-surface deformation has been validated for the AGAPAS catamaran, since no captive model test data of this model is available, the only way to validate the computation, is the comparison of the free-surface contour.

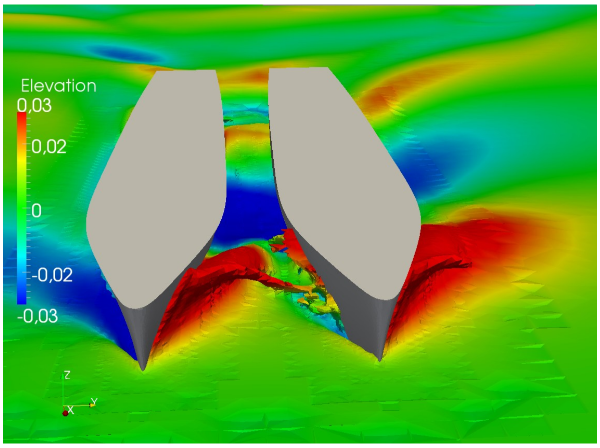

Figure 10: Bow wave and free surface elevation at ß = 15 ° and Fn = 0.4.

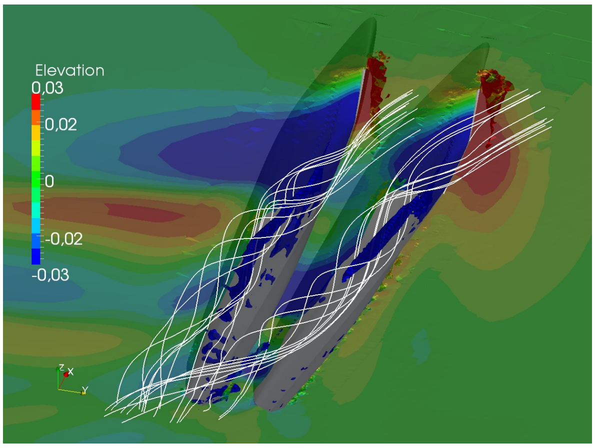

Figure 11: Vortex structure and ventilation at bow sections of each demihull at ß = 30 ° and Fn = 0,4.

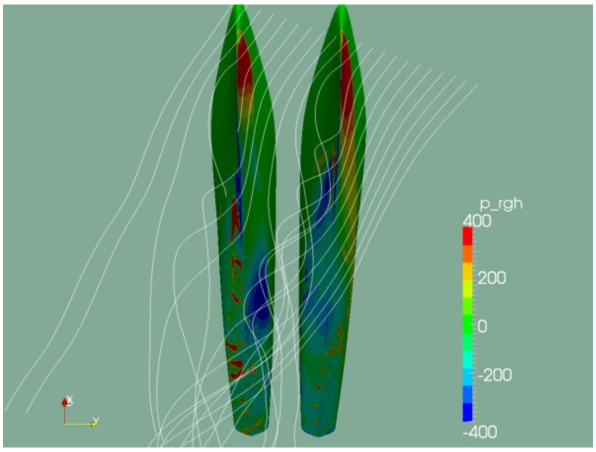

Figure 12: Pressure distribution and streamlines at NPL 4a catamaran with s/L = 0.45 at ß = 30 ° for Fn = 0.4.

Figure 13: Superposition of simulated free-surface contour and image of free surface for free sailing AGAPAS catamaran model with s/L = 0.45 at ß = 0° and Fn = 0.4.

Conclusions

Single-phase and multi-phase CFD calculations have been validated using experimental data of captive model tests. Numerical simulations of ships in oblique motion show good agreements with the experiments for drift angles up to ß = 20 °, which can be considered as a large one for conventional ships. While computations using the double-body concept deliver quite reliable results at moderate costs, relatively high computational resources are needed for free-surface computations. Consideration of free-surface effects results in the improvement of numerical results at drift angles larger than ß = 15 °, especially for the longitudinal force and yaw moment. A large discrepancy at large drift angles might be due to significant free-surface deformations which is known to be not sufficiently modelled using RANSE-based methods. In future work, the investigations presented in this paper will be continued for the cases of steady yaw at high Froude numbers. Special attention will be paid to study of grid dependency and influence of turbulence models.

Acknowledgements

This research has been performed within the framework of the interdisciplinary project AGAPAS, funded by the German Federal Ministry of Economics and Technology (BMWi). Max Haase likes to thank his former colleagues at the Chair of Ship Design and at the Chair of Modelling and Simulation at the University of Rostock for the good cooperation and warm and friendly atmosphere.

References

Bronsart, R. and Kleinsorge, L. (2011). CFD Meshing Tools and Their Integration into the Ship CAD Process, Proc. of RINA ICCAS, Trieste, Italy

Haase, M., Bronsart, R., Kornev, N. and Nikolakis, D. (2010). Simulation of the Dynamics of an Autonomously-Acting Small Catamaran for Search and Rescue Process, Proc. IFAC CAMS, Rostock, Germany

Mastushkin, Y. M. (1976). Calculating Controllability of Twin-Hull Ships. Shipbuilding no 6,

Molland, A., Wellicome, J. and Couser, P. (1994). Resistance Experiments on a Systematic Series of High-Speed Displacement Catamaran Forms: Variation of Length-Displacement Ratio and Breadth-Draught Ratio, Ship Science Report 71, Southampton, England

Peric, M. and Ferzinger, J. H. (2001). Computational Fluid Dynamics, Springer Verlag, 2001

Wellicome, J. F., Temarel, P., Molland, A. F. and Couser, P. R. (1995). Experimental Measurements of the Seakeeping Characteristics of Fast Displacement Catamarans in Long-crested Head Waves, Ship Science Report 89, Southampton, England

Winkler, S. (2011). PMM-Tests of NPL Catamarans, Proc of STG-Jahrbuch 2011, Rostock, Germany

A potential flow based underwater glider flight simulator

Surasak Phoemsapthawee, Marc Le Boulluec
IFREMER, RDT/HO, BP-70, 29280 Plouzané, France

Jean-Marc Laurens
ENSTA-Bretagne, 2 rue François Verny, 29806 Brest cedex9, France

François Deniset
IRENav, Ecole navale, Lanveoc, CC-600, 29240 Brest cedex9, France

1 Introduction

Underwater gliders are an Autonomous Underwater Vehicles (AUVs) used in ocean exploration and observation. They use small changes in their buoyancy to dive and to return to the ocean surface. During the change of altitude, the underwater gliders, like air gliders, use the hydrodynamic forces generated by their wings to move forward to the desired location. Since they use the buoyancy and the gravity force to propel themselves, their propulsion system consumes very low energy compared to the other AUVs. The low energy consumption of the propulsion system enables long duration operations [3]. Without any external moving part, except for the Slocum Electric which is equipped with an adjustable rudder, the underwater glider flights are controlled by changing the position of the center of gravity and/or buoyancy to adjust the trim and the heel angles [4]. Nowadays there are three well-known underwater gliders on the market: Seaglider, Slocum and Spray [7], but some are still under development, for example [2]. In France, there are also developments of this AUVs type, for example Sterne the underwater glider developed by Ensta-Bretagne (formerly Ensieta) [1, 12].

Many research studies with respect to the automatic flight control of underwater gliders have been undertaken [5]. However, most (if not all) of the underwater glider automatic flight controls employ a quasi-static empirical hydrodynamic model and need the hydrodynamic coefficients identifications [9]. We developed such a parametric underwater glider simulator in order to compare its predictions with our potential flow based simulator.

For better flight control, the hydrodynamic behavior and the flight mechanics of the underwater glider should be analyzed. To this end, we need to develop the equations of motion or the Euler-Newton equations that are suitable to the underwater glider problem. The Euler-Newton equations solver is then coupled with a hydrodynamic solver. Although it is possible to couple the motion solver with a RANSE solver, such a simulator consumes a lot of computation time and resource [11], and is not suitable for a long duration simulation. Moreover, the glider always operates at small incident angles and is not subject to significant flow separation. We then use an unsteady potential flow solver coupled with a viscous correction since it allows for a reasonable computation time.

2 Numerical model

The simulator is the result of a coupling between two solvers developed in-house: the dynamic solver and the hydrodynamic solver.

2.1 Dynamic model

The equations of motion, also known as the Euler-Newton equations, are developed for a glider of which the center of gravity, mass and moment of inertia can vary in the body reference frame. Since the variation of glider inertia and center of gravity with respect to the body reference frame can be determined from the flight control command, the unknowns of the system are the translation and the angular accelerations ($\dot{\vec{V}}_{O_b/R_b}$ and $\dot{\vec{\Omega}}_{R_b/R_g}$) of the body reference frame.

$$\begin{bmatrix} m\mathbb{E}_3 & -m[O_bG] \\ m[O_bG] & \mathbb{I}_{m/O_b} \end{bmatrix} \begin{Bmatrix} \dot{\vec{V}}_{O_b/R_b} \\ \dot{\vec{\Omega}}_{R_b/R_g} \end{Bmatrix} = \begin{Bmatrix} \sum \vec{F}_{ext} \\ \sum \vec{M}_{ext} \end{Bmatrix} - \begin{Bmatrix} \vec{F}_{fic} \\ \vec{M}_{fic} \end{Bmatrix} \tag{1}$$

where $\vec{F}_{fic}$ and $\vec{M}_{fic}$ are the fictitious force and moment The external forces ($\vec{F}_{ext}$, $\vec{M}_{ext}$) of the glider are the gravity forces, the buoyancy forces and the hydrodynamic forces.

2.2 Hydrodynamic model

As mentioned in the introduction, the hydrodynamic forces can be computed with an unsteady potential flow calculation or by using a parametric model.

For the potential flow calculation, an unsteady BEM code is used. The spatial and time discretization sensitivity of the code are well mastered. The code has been verified and experimentally validated several times in the past, for example [13]. It belongs to what [10] refers to as "Second generation" panel methods involving a Dirichlet condition. The surfaces of both lifting and non-lifting bodies are discretized into first order panels carrying constant source σ and doublet μ distributions. The wakes developed behind the lifting bodies are formed with sheets of first order panels carrying a constant doublet distribution. The wake geometry is naturally described since it is generated in a Lagrangian manner. The viscous effect is taken into account via the friction force. The local friction coefficient C_f is defined as a function of the local Reynolds number Re_s. If $Re_s < 5 \times 10^5$, the flow is supposed to be laminar and $C_f = 0.664/\sqrt{Re_s}$. Elsewhere, the flow is supposed to be turbulent and $C_f = 0.027/\sqrt[7]{Re_s}$. The 1st-order Euler explicit numerical scheme is applied for the time variation.

For the parametric model, the lift L and the drag D forces of the lifting bodies (main wing and stabilizer) are calculated from $L = \frac{1}{2}\rho V^2 A C_L$ and $D = \frac{1}{2}\rho V^2 A C_D$ where V is the foil incident velocity and A is the foil planform area. The lift coefficient C_L and the induced drag coefficient C_D are estimated using the Prandtl approximation: $C_L = 2\pi\alpha\Lambda/(\Lambda+2)$ and $C_D = C_L^2/(\pi\Lambda)$ where α is the angle of attack in radian and Λ is the aspect ratio. The rotation on the glider axis also induces the angle of attack of each section of the lifting bodies. This moment is estimated from the integration of 2D section lift as $M = -\frac{\pi}{6}\rho V\omega\, c\, b^2$ where ω is the glider angular velocity along the glider axis, c is the foil chord and b is the foil span. In addition to the pressure forces, friction forces must be taken into account. Like the potential flow calculation, the principal drag force of the glider is the friction on the glider surface along the glider axis. The flow is assumed turbulent and the friction force is computed from the ITTC-1957 formula. Regarding the other lateral drag and moment forces on the glider body, the glider body is assumed to be a cylinder and formulas based on cylinder section drag integration are applied. However, these lateral drag forces do not have much effect on the numerical results since the glider always operates at small incident angles. The added inertia forces over the glider body and the lifting bodies are taken into account as well.

2.3 Dynamic-hydrodynamic coupling method

The simulation scheme is explained here. Starting from the initial conditions (positions, velocities, hydrodynamic forces), the Euler-Newton equations are solved to obtain the new positions and the new velocities using the 4th-order Runge-Kutta method. After the Euler-Newton solver, the hydrodynamic forces are calculated from the new positions and the new velocities using the potential flow solver. The two solvers are independent from each other. Once the hydrodynamic forces are updated, the next time step is considered and the Euler-Newton equations are recalculated. The process continues in this way until the end of simulation. The size of the time step is dictated by the potential flow code requirement and is applied to the parametric model as well.

In the case of potential flow model, the error of the added inertia calculation in the hydrodynamic forces can cause the instability of the motion calculation. This numerical error can be reduced by adding the added inertia on both sides of the Euler-Newton equations.

$$(\mathbb{M} + \mathbb{M}_a)\dot{\mathcal{U}}|_n = \mathcal{F}_{ext}|_n - \mathcal{F}_{fic}|_n + \mathbb{M}_a\dot{\mathcal{U}}|_{n-1} \tag{2}$$

The stability of this numerical error reduction scheme is discussed in [8]. The article demonstrates that a large range of estimated added inertia produces the same motion as the genuine added inertia. In this paper, the estimated added inertia is pre-calculated by a non-lifting potential flow code using Rankine singularities.

In the case of parametric model, the added inertia force is taken into account by adding the added inertia directly into the inertia term. The added inertia is also pre-calculated by the non-lifting potential flow code:

$$(\mathbb{M} + \mathbb{M}_a)\dot{\mathcal{U}}|_n = \mathcal{F}_{ext}|_n - \mathcal{F}_{fic}|_n \tag{3}$$

3 Numerical simulations

A simple underwater glider model is simulated in this first numerical study of glider hydrodynamic behavior. The glider geometry is presented in Figure 1(a). The glider body can be separated into three parts: the head, the main body and the tail. The main body is a cylinder with a 0.2 m diameter and 1 m length. The head and the tail are hemi-ellipsoids with the same diameter as the main body and have a length of 0.5 m. The wing and the stabilizer section profiles are NACA0005. The volume and the mass of the lifting parts are neglected in the simulations. Hence, the glider volume and the displacement mass are solely calculated based on the glider body and the center of buoyancy B is positioned at the middle of the glider body. The ballast can take in or drain off the water of ± 0.5% of the glider volume ($\pm 0.5\% \ \nabla$). The glider moment of inertia is defined to be equal to the moment of inertia of a 0.2 m diameter and 2.0 m length cylinder of which the mass is equal to the glider displacement.

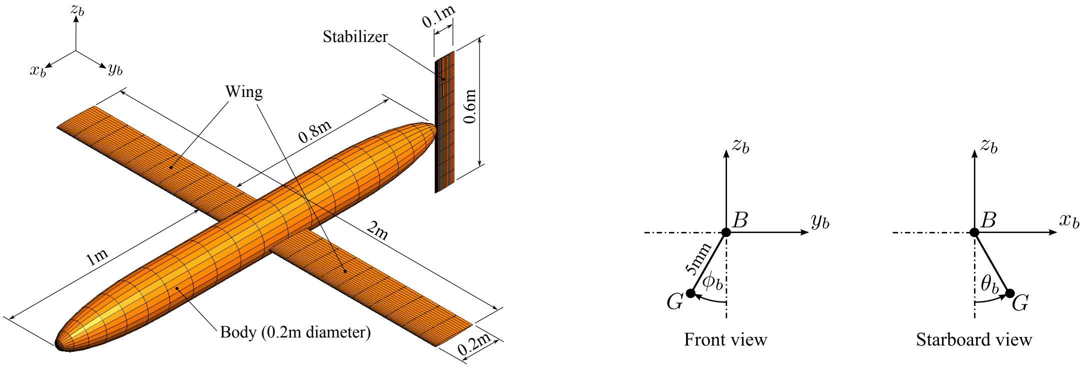

(a) Geometry (b) heel ϕ_b and trim θ_b command angles

Figure 1: Glider model geometry and definitions of command angles

The position of the center of gravity of the glider is the resultant of the fixed mass, the mass of ballast water and a moving mass. In the model, the resultant center of gravity G is directly taken into account. The moving mass can rotate around the glider axis at the fixed radius. It can also slide along the glider axis. As a result, the distance between the resultant center of gravity and the glider axis is constant and taken equal to 5 mm. The glider flight control command consists therefore of two components: the buoyancy control and the position of the center of gravity control. The position of the center of gravity can be represented by two angles: the heel command angle ϕ_b and the trim command angle θ_b. The definitions of the two angles are illustrated in Figure 1(b). In all simulations, the glider is initially launched with a 0.2 m/s horizontal velocity in the x_b-positive direction.

3.1 Sawtooth trajectory

First, we simulate the glider advancing in sawtooth trajectories. The ballast and the trim command angle are varied alternatively. When the ballast takes in the water ($+0.5\% \ \nabla$), the trim command is positive; we call these conditions the command state I. When the ballast drains out the water ($-0.5\% \ \nabla$), the trim command is negative; we call these conditions the command state II. Each command state lasts 99 seconds. The glider conditions are varied between the command state I and II in a sinusoidal manner to avoid a sharp variation. The transition time lasts 1 second. This sawtooth trajectory is simulated for different trim command angles θ_b of ±10, ±20, ±30 and ±40 degrees.

Figure 2 presents the sawtooth trajectories obtained by the two approaches for a 500 second simulation. Both approaches produce very similar results as expected. The velocity differences between the two approaches depend without any doubt on the friction computation. This will be the case for most trajectories simulations but in the next section, we will present a case for which both approaches yield very different results.

3.2 Helical trajectory

In the case presented in this section, we command the glider to dive with positive trim and heel command angles with the intention to change the glider direction. In the example presented here, trim and heel command angles are both equal to 10 degrees. Three different geometries of the stabilizer are considered. The dimensions of the three stabilizers are illustrated in Figure 3.

The glider is expected to turn because of the lateral component of the main wing lift force when the glider is heeling. In the case of a positive heel angle as in these simulations, the glider is then expected to

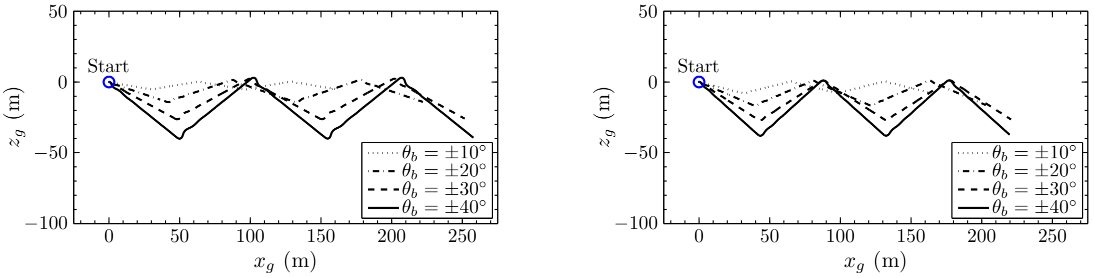

Figure 2: Sawtooth trajectory during 500 seconds for different trim command angles θ_b; left with the potential flow model, right with the parametric model

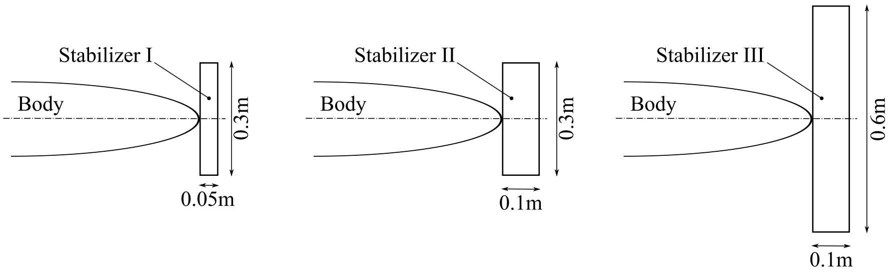

Figure 3: Dimensions of stabilizers

turn to the starboard direction. The obtained trajectories for both approaches are presented in Figure 4. Unlike the sawtooth simulations, the two approaches produce very different results.

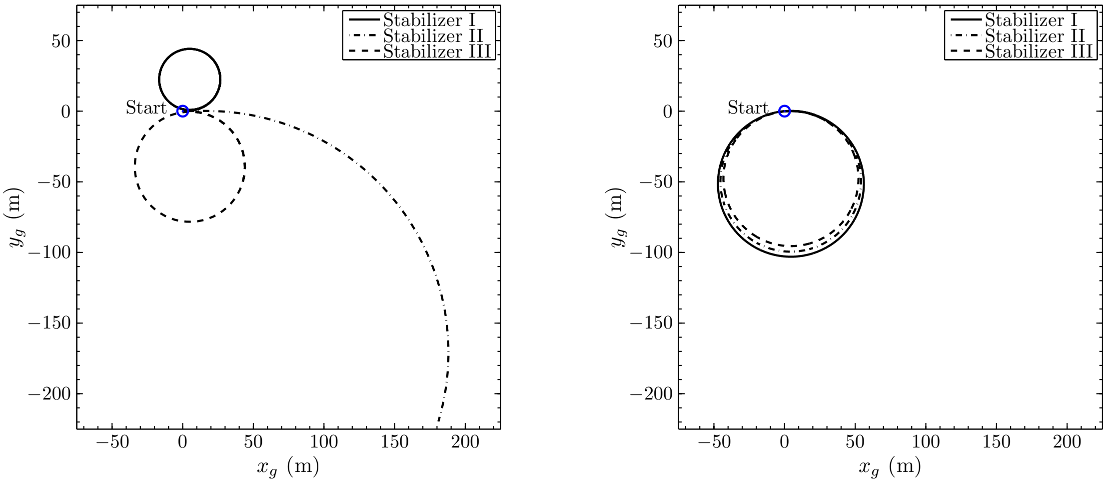

Figure 4: Top view of helical trajectory during 1000 seconds for 10° trim and 10° heel command angles; left with the potential flow model, right with the parametric model

According to the numerical results of the simple approach, the glider moves to starboard as expected. The stabilizer size is only of little effect; the three trajectories are almost the same. The glider turns with the steering force generated by the main wing and the stabilizer generates the hydrodynamic moment to adjust the glider orientation to the incident inflow. However, this behavior is not always observed in reality. The glider Sterne which was developed at Ensta-Bretagne experienced counter-steering behavior. The first Sterne model was lost during an experiment at sea because of this unexpected behavior. It was suspected that the stabilizer size was responsible for this. The new Sterne model equipped with a larger stabilizer does not present any counter-steering behavior. This is the reason why, in order to confirm the role of the stabilizer, we decided to cover different stabilizer geometries in this study.

The potential flow results demonstrate the experimentally observed counter-steering behavior. These numerical results confirm that the stabilizer size plays an important role in this behavior. The smallest stabilizer (stabilizer I) causes the glider to turn to the counter-steering direction (the port direction in this case) while the other two do not. When the stabilizer is large enough (stabilizer III), the glider behaves as expected and predicted by the simpler approach. In the case of the intermediate size (stabilizer II), the stabilizer is not large enough to steer the glider properly. When the stabilizer is too small, it cannot produce enough hydrodynamic moment to counteract the counter-steering hydrodynamic moment. The counter-steering hydrodynamic moment is generated by the main wing lift since the main wing is situated behind the center of gravity.

Although the simple approach includes the added mass coefficient, it does not fully show the fluid inertia effect. The hydrodynamic moment generated by stabilizer is fully perceived as soon as the glider heels without any delay. In the potential flow simulations, there is a delay between the geometric position and the hydrodynamic response. This delay exists because of fluid inertia. Because of this delay, if the stabilizer counteracting moment is not strong enough, the glider finds the time to position itself in the other equilibrium position causing the counter-steering behavior. The proper simulation is then only possible if the hydrodynamic solver is fully unsteady. In principle, it is possible to add such effects and other effects in a parametric model. For instance, we could add the interaction between the glider body and its appendages using a correction factor as suggested in [6]. Adding these parameters would not significantly increase the CPU time but it would render the simulator "glider-specific". Furthermore, such a development implies a lot of adjustment using experimental data or more economical means such as the simulator presented in this paper. In the potential flow simulator, the most important effects are properly taken into account without any adjustment and if the glider geometry changes, we only need to change the mesh. Nevertheless, although the CPU time for the simple approach is negligible, it is significant for the glider flight simulator based on the potential flow calculation.

4 Computation resource consumption

We now consider the underwater glider equipped with the stabilizer III to simulate a non-trivial trajectory. The objective is to simulate a diving helical trajectory followed by a surfacing contra-rotating helical trajectory. Like in the previous simulations, the glider is launched with a 0.2 m/s horizontal velocity in the x_b-positive direction. The heel command angle is set at 20 degrees. The trim command and the ballast are varied alternatively every 1100 seconds. For the first 1100 seconds, the trim command angle is 10 degrees and the ballast takes the water in for diving. For the next 1100 seconds, the trim command angle is -10 degrees and the ballast drains the water off for surfacing. The total duration of the simulation is 2332 seconds and takes 20000 time steps. This simulation involves about 24 hours of computation time on a standard workstation (CPU 4 cores with 2.66 GHz).

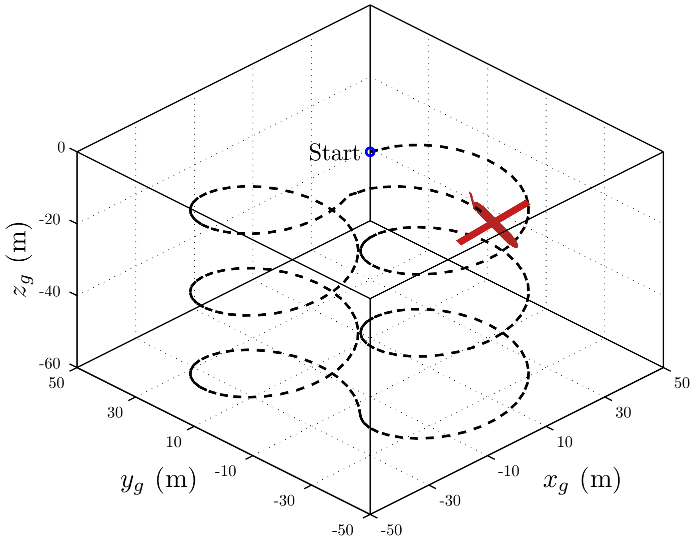

Figure 5: Example of trajectory simulation for a real-time duration of 2332 seconds. The CPU time in this case is about 24 hours on a standard workstation. The glider appears 10 times bigger than it is.

5 Conclusion and perspective

An Euler-Newton equations solver is coupled with a potential flow code to simulate 6-DOF trajectories of underwater gliders. This simulator can be used to study the hydrodynamic behavior of gliders in order to improve the glider automatic flight control and to optimize the glider geometry. A numerical study of the hydrodynamic behavior of an underwater glider has been conducted. All results were compared with a simple parametric simulator. A series of simulations considering sawtooth trajectories has first been conducted. In this case both simulators give very similar trajectories. As expected, the glider velocity varies as a function of the trim angle. To confirm a behavior observed experimentally, a second series of simulations concerning the glider steering has been launched. The potential flow simulator shows that the stabilizer geometry plays an important role in steering control. An inappropriate stabilizer geometry can cause counter-steering behavior that the parametric simulator cannot anticipate. A non trivial case has finally been presented to demonstrate the capabilities of the potential flow based glider simulator. The detailed results of this numerical study have been submitted to Journal of Ocean Engineering. Further validations using real data and experimental model testing are necessary to increase our confidence within the simulator.

Acknowledgement

This work is partially supported by the Europôle Mer (`http://www.europolemer.eu`).

References

[1] T. Ahmed-Ali, L. Cuillerier, and N. Seube. Glider observer and identifier based on sliding modes control. In *Proceedings of Manoeuvring and Control of Marine Craft*, Girona, Spain, 2003.

[2] A. Alvarez, A. Caffaz, A. Caiti, G. Casalino, L. Gualdesi, A. Turetta, and R. Viviani. Fòlaga: A low-cost autonomous underwater vehicle combining glider and AUV capabilities. *Journal of Ocean Engineering*, 36:24–38, 2009.

[3] R. Bachmayer, N. E. Leonard, J. Graver, E. Fiorelli, P. Bhatta, and D. Paley. Underwater gliders: recent developments and future applications. In *Proceedings of the IEEE International Symposium on Underwater Technology (UT'04)*, Tapei, Taiwan, 2004.

[4] A. Bender, D. M. Steinberg, A. L. Friedman, and S. B. Williams. Analysis of an autonomous underwater glider. In *Proceedings of the Australian Conference on Robotics and Automation*, 2008.

[5] P. Bhatta and N. E. Leonard. Nonlinear gliding stability and control for vehicles with hydrodynamic forcing. *Automatica*, 44(5):1240 – 1250, 2008.

[6] F. Caldeira-Savaira and D. Clarke. The active control of swath motions. In *Proceedings of International Conference of Swath Ships and Advanced Multi-hulled Vessels II*, 1988.

[7] C. C. Eriksen, T. J. Osse, R. D. Light, T. Wen, T. W. Lehman, P. L. Sabin, J. W. Ballard, and A. M. Chiodi. Seaglider: a long-range autonomous underwater vehicle for oceanographic research. *IEEE Journal of Oceanic Engineering*, 26(4):424–436, October 2001.

[8] F. Floc'h, J.-M. Laurens, J. B. Leroux, and S. Kerampran. Trajectory prediction by coupling Euler-Newton equations and flow models. In *Proceedings of 11th Numerical Towing Tank Symposium*, Brest, France, 7-9 september 2008.

[9] J. G. Graver. *Underwater gliders: dynamics, control and design.* PhD thesis, Department of Mechanical and Aerospace Engineering, Princeton University, 2005.

[10] H. Hoeijmakers. Panel methods for aerodynamic analysis and design. *AGARD Report*, 783:5.1–5.47, 1992.

[11] S. M. Murman, M. J. Aftosmis, and M. J. Berger. Simulations of 6-DOF motion with a cartesian method. In *Proceedings of 41st AIAA Aerospace Sciences Meeting*, Reno, NV, January 6-9 2003.

[12] S. Phoemsapthawee, M. LeBoulluec, J.-M. Laurens, and F. Deniset. Numerical study on hydrodynamic behavior of an underwater glider. In *Proceedings of the 30th International Conference on Ocean, Offshore and Arctic Engineering OMAE-2011*, Rotterdam, Netherlands, June 19-24 2011.

[13] S. Phoemsapthawee, J.-B. Leroux, J.-M. Laurens, and F. Deniset. A transpiration velocities based sheet cavitation model. *Ship Technology Research / Schiffstechnik*, 56(4):161–176, 2009.

Simulation of Ships in Severe and Extreme Sea Conditions

Jens Ley[*], *Miguel Onorato*[†], *Jan Oberhagemann*[‡], *Ould el Moctar*[§]

1 Introduction

Dealing with extreme wave events and their consequences for marine structures requires to go beyond classical approaches to wave-structure interaction. The probability of large-amplitude ship responses is small and cannot be predicted with linear statistics for ergodic random processes; wave-wave interaction becomes important as well as nonlinearities in the structure's response, just to mention some aspects. This has important implications on the numerical assessment of risks related to extreme wave events. Nonlinear statistics have to be used, and numerical methods for both the wave modelling and the computation of corresponding structural responses have to account for nonlinearities as well. Time domain simulations become the method of choice instead of less involved and less time-consuming frequency domain approaches.

Here we focus on the modelling of waves using computational fluid dynamics (CFD). Related ship responses are discussed as well. RANS (Reynolds-Averaged Navier-Stokes) methods are well suited to capture almost all of the flow features that are important for wave-wave and wave-structure interaction. As a drawback, the associated enormous computational costs limit the use of time domain RANS computations to only simulate selected scenarios, even on today's computer clusters.

In this paper, we present recent results of ongoing investigations as part of the research project *ExtremeSeas* funded by the European Community. In particular, we discuss appropriate wave modelling for RANS simulations in severe and extreme sea states.

2 Numerical Method

We use the RANS solver COMET for the solution of the RANS or Euler equations. COMET implements the SIMPLE (Semi-Implicit Pressure-Linked Equations) coupling scheme for incompressible fluids and a Volume of Fluid (VOF) approach for free-surface flows, see also Ferziger and Perić (2002).

The fluid equations solver is coupled with a nonlinear solver of the ship motions in six degrees of freedom (6DoF solver), see Brunswig and el Moctar (2004). Additionally, basic effects of ship hull girder elasticity can be included with a Timoshenko beam model. Oberhagemann and el Moctar (2007) describe the coupled algorithm, while representative code validation examples are published in Oberhagemann and el Moctar (2011).

3 Wave Modelling

The energy content of irregular wave processes is usually described with the spectral energy density distribution S as function of wave frequency ω. Several theoretical models provide semi-empirical formulae for $S(\omega)$, the most common of these are the Pierson-Moskowitz spectrum only depending on wind speed, Pierson and Moskowitz (1964), and the JONSWAP spectrum for limited fetch and wind duration, Hasselmann et al. (1973). The International Association of Classification Societies (IACS) recommends the application of Pierson-Moskowitz spectra for wave load predictions of ships, which corresponds to a JONSWAP spectrum with a reduced peak enhancement factor, $\gamma = 1$.

Ocean waves are not unidirectional but have a directional spreading of wave energy around the main direction of wind action. Usually a cosine square distribution of wave energy over wave encounter angle is assumed, but the actual spreading strongly depends on wind conditions. We consider only unidirectional waves for the sake of simplicity.

For finite volume methods (FVM), gravity waves are generated by providing wave elevation, velocity field and pressure field at the fluid domain bound-

---

[*] University of Duisburg-Essen, Duisburg, Germany

[†] Università di Torino, Italy

[‡] jan.oberhagemann@uni-due.de, University of Duisburg-Essen, Germany

[§] University of Duisburg-Essen, Germany aries. In the most common case, the wave process is represented by a superposition of n linear harmonic component waves according to Airy theory. The surface elevation of unidirectional waves reads

$$\zeta(x,t) = \sum_{i=1}^{n} A_i \, cos(k_i x - \omega_i t), \tag{1}$$

with the surface elevation $\zeta(x,t)$, complex component wave amplitudes A_i, wave frequencies ω_i and corresponding wave numbers $k_i = \frac{\omega_i^2}{g}$. Velocity and pressure field are composed accordingly from component waves. Sometimes higher-order wave theories up to fifth-order Stokes theory are used. All such kinds of component wave superposition neglect wave-wave interaction and thus are limited to small amplitude waves.

Inside the fluid domain, generated waves propagate according to the discretised Navier-Stokes equations. Wave evolution and wave-wave interaction are implicitly accounted for as well as trough-crest asymmetries, wave skewness and even wave breaking, provided the discretisation is sufficient. However, the initial and boundary conditions impose a wave regime according to eq. 1.

Long simulation times and large fluid domains may be required to yield a fully developed wave process including all nonlinearities. More advanced boundary conditions can help here. The simplest model that describes the weakly nonlinear evolution of a narrow band, unidirectional wave system in deep water is the Nonlinear Schrödinger (NLS) equation that has been derived by Zhakarov (1968),

$$i\left(\frac{\partial A}{\partial x} + \frac{1}{c_g}\frac{\partial A}{\partial t}\right) - \frac{k_0}{\omega_0^2}\frac{\partial^2 A}{\partial t^2} - k_0|A|^2 A = 0. \tag{2}$$

Here, c_g is the group velocity and $A(x,t)$ describes the complex envelope of the waves and is related to the surface elevation $\zeta(x,t)$,

$$\zeta(x,t) = |A(x,t)| \, cos(k_0 x - \omega_0 t). \tag{3}$$

$k_0$is the wave number corresponding to the dominant wave and $\omega_0 = \omega(k_0)$ the corresponding angular frequency. Eq. 2 describes the dynamics of the waves in a quasi-linear regime properly, and on average it can decently reproduce the statistical properties of the surface elevation (wave height) even for moderate steepness. The equation has a number of exact analytical solutions, known as breathers, which are prototypes of rogue waves, Osborne et al. (2000). Such breather solutions may also emerge spontaneously from a random sea state, provided that the spectrum is sufficiently narrow and waves are on average sufficiently steep, see Onorato et al. (2001).

For ocean waves, such conditions occur when the JONSWAP spectrum is energetic (large significant wave height H_s) and is characterized by large enhancement factor γ. The effect of increasing γ (and keeping fixed the other parameters in the spectrum) is twofold: on one side it increases the mean steepness and, on the other, it reduces the average width of the spectrum (increases the correlation length of the wave packets). For a Pierson-Moskowitz spectrum the spontaneous formation of breathers is very rare and follows the prediction of the linear theory (Rayleigh distribution).

Given a random realisation of a JONSWAP spectrum, the formation of rogue waves is not immediate; indeed, the generation of breathers is related to the so called Benjamin-Feir instability which requires space to develop in the order of 30 wavelengths, Onorato et al. (2006). Therefore, if one is interested in addressing the problem of the interaction of waves with a structure, such structure should be placed far enough to let the nonlinearity develop. From a numerical point of view, it is computationally expensive to evolve a sea state for 30 - 40 wavelengths if the primitive equations of motion are used. In this regard, the NLS equation provides an interesting new approach: due to its low computational cost (a spatial domain covering 100 wavelengths can be evolved for 50 wavelengths in about a minute in a modern PC), the NLS equation can be used for evolving a wave process and provide the initial conditions for a more accurate model that treats the wave-structure interactions properly.

Before applying NLS solutions as boundary conditions, we will have a look at discretisation requirements for wave sequence representation in FV fluid domains.

4 Wave Propagation in the Fluid Domain

Numerical diffusion causes a growing loss of wave energy, the further the solution proceeds from the initial and boundary conditions. Hence, for given discretisation schemes, numerical diffusion of wave energy is linked to the grid resolution in space and time. Fig. 1 exemplarily shows the energy loss as a function of temporal and spatial resolution for a regular wave with a relatively high steepness of $H/\lambda = 0.05$, evaluated after 10 wave periods from

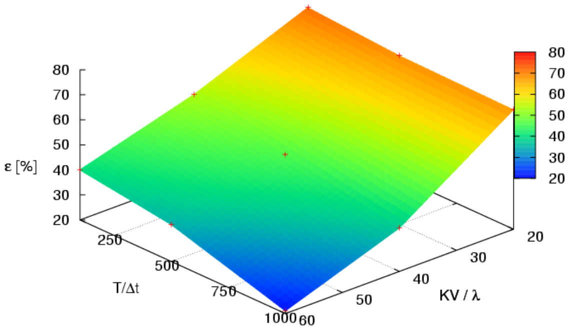

Fig. 1 Relative energy loss ε of a regular wave with $H/\lambda = 0.05$ as a function of nondimensional time step size and control volumes per wave length

the initial condition and 10 wave lengths from the inlet boundary, respectively. We define the relative energy loss ε as

$$\varepsilon = 1 - \frac{E'}{E}, \tag{4}$$

with the effective wave energy E', and its theoretical or reference value E. While the wave almost vanishes on the coarsest grid with the largest time steps, there is still a significant relative energy loss of 20% using a nondimensional time step size $\Delta t/T = 0.001$ and 60 control volumes per wave length (combined with 30 cells per wave height).

Although wave energy is dissipated in reality through friction as well, the decrease of wave energy will be almost exclusively related to numerical diffusion in this example.

Investigations showed that the requirements on grid and time step resolution increase with wave steepness, and results for smaller wave steepnesses give a more optimistic figure. Additionally, the distance from the inlet boundary to the location of interest was quite large in this example, compared with typical fluid domain configurations for simulations of ships in waves.

Numerical diffusion becomes even more important when simulating longer sequences of irregular wave processes. Especially high frequency wave components are prone to vanish soon due to insufficient grid resolution in time domain RANS simulations.

We examplify the above considerations for a realisation of a relatively steep sea state with peak period $T_P = 12.0s$, significant wave height $H_S = 12.0m$ and peak enhancement factor $\gamma = 3.3$, according to a JONSWAP spectral shape. Fig. 2 shows computed and measured time series of the surface elevation at three different sample locations

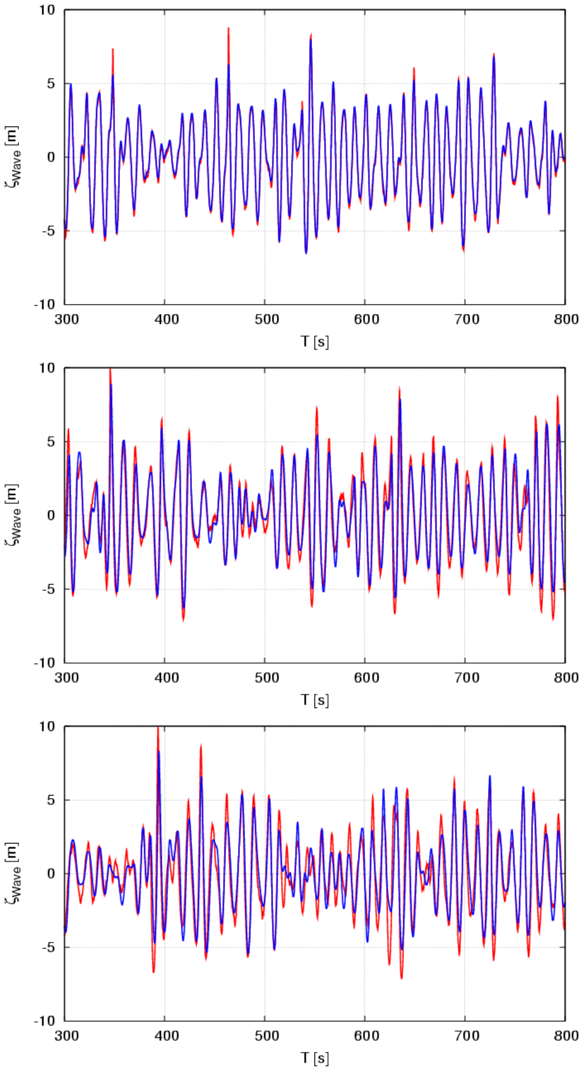

Fig. 2 Time series of surface elevations at three distances from the inlet / wave maker (top to bottom: sample locations x_0, x_1, x_2); comparison of computation (blue line) with model test data (red line); sea state $T_P = 12.0s$, $H_S = 12.0m$, $\gamma = 3.3$

$x_0 = 0m$, $x_1 = 800m$ and $x_2 = 1600m$ (full scale) from the inlet boundary, or, respectively, the wave maker. The input component waves for the computation were reconstructed with Fourier transformation from the experimental time series data. Initially, the computation replicates the experimental data fairly, although some peaks are smaller. Differences grow with increasing distance from the inlet, but there is still a general agreement with the measured surface elevations.

To quantify the energy loss, we start with defining spectral moments m_k of $S(\omega)$ as

$$m_k = \int_0^\infty \omega^k S(\omega)\, d\omega. \tag{5}$$

The total energy per unit area contained in the wave spectrum, E, is the integral over all frequencies,

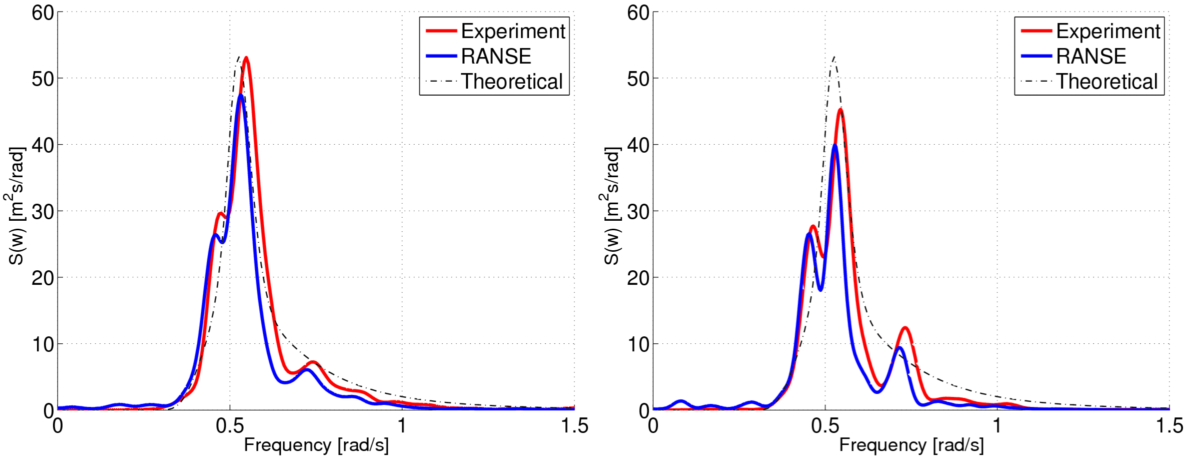

Fig. 3 Decrease of spectral energy density, evaluated at sample locations x_1 (left) and x_2 (right)

multiplied with the water density ρ and the gravitational acceleration g. It is closely linked to m_0:

$$E = \rho g \int_0^\infty S(\omega)\, d\omega = \rho g m_0. \tag{6}$$

For a computed or measured time signal of surface elevation at a certain location, one can compute the observed spectral energy distribution $S'(\omega)$ e.g. using Fast Fourier Transformation. Knowing either the theoretical or the input spectral density distribution $S(\omega)$, inserting eq. 6 in eq. 4 yields:

$$\varepsilon = 1 - \frac{\rho g m_0'}{\rho g m_0} = 1 - \frac{m_0'}{m_0}. \tag{7}$$

Spectral density distributions for the example sea state, obtained at locations $x = 800$ m and $x = 1600\,m$, are given in Fig. 3 and compared to the theoretical spectral density distribution at the wave maker. Obviously, the spectral density distribution obtained from the computation is consistently lower than the experimental data throughout the bulk part of the frequency range, indicating a lower energy content. Especially the spectral density for higher frequencies is considerably lower in the computation. Table 1 quantifies the observations, listing the experimental and numerical wave energy E'_{Exp} and E'_{CFD}, respectively, and the relative energy loss in the computation.[1] The comparisons showed that the numerical energy loss increases with simulation time and distance from the inlet, which is clearly related to numerical diffusion.

Tab. 1 Relative numerical spectral energy loss in an irregular sea state compared to experiments

	$x_1 = 800\,m$	$x_2 = 1600\,m$
$\frac{1}{\rho g} E'_{Exp}\,[m^2]$	8.752	7.254
$\frac{1}{\rho g} E'_{CFD}\,[m^2]$	7.302	5.764
$\varepsilon = 1 - \frac{E'_{CFD}}{E'_{Exp}}$	0.166	0.205

The grid resolution in this example was 40 cells per significant wave height and 167 cells per wave length λ_P corresponding to the peak period, while the temporal resolution was 950 time steps per peak period.

5 Ship Responses to Severe Seas

The investigations presented in this section intend to outline requirements on RANS simulations to determine short-term statistics of ship responses in severe sea states. Here we focus on the vertical hull girder bending moment M_y, the ship response which is considered most critical in these sea states.

The encountered sea state and the ship speed strongly influence the resulting ship response. For an ultra-large container vessel sailing at a speed of $v_S = 10\,kts$, Fig. 4 shows the results of RANS simulations in a sea state with $T_z = 11.5\,s$, $H_S = 14.5\,m$, $\gamma = 1.0$ and long-crested waves. Time series of midships M_y (20 realisations with $300\,s$ duration each) were evaluated with rainflow counting. Of each realisation, the initial run-up phase of $50\,s$ was removed prior to evaluation. The ship hull flexibility was accounted for with a beam representation. Additionally, parameter variations (speed reduction to $v_S = 5\,kts$, rigid hull girder and cosine square wave spectral spreading) are presented. The input wave components were the same, where appropriate.

---

[1] Instead of the theoretical E, we used the experimental E'_{Exp}, because E'_{Exp} is not constant for all measurement locations. Since the evaluated spectra only represent time records of each $8\,min$, E'_{Exp} fluctuates due to insufficient time record lengths for statistical convergence. Additionally, wave breaking occured with consecutive losses of wave energy.

Most significantly, the rigid hull girder simplification strongly reduces not only the overall number of encountered load cycles, but also the number of cycles exceeding a given load level. This emphasizes the importance of hull girder vibration. A directional spreading of the waves causes a comparable decrease of the load spectrum throughout the bigger part of the spectrum. In this case, a speed reduction apparently has a small influence. While bow flare slamming is less pronounced at reduced speed, stern slamming becomes an issue.

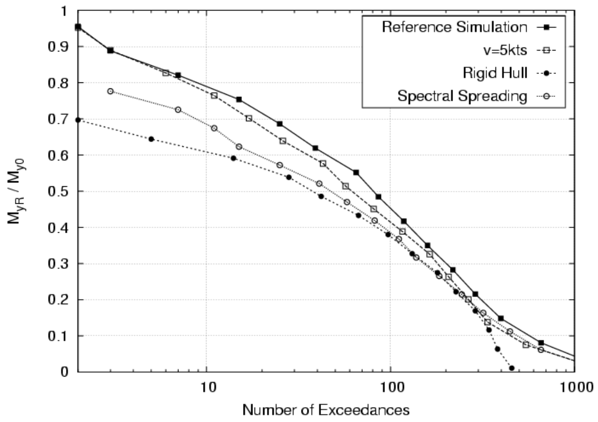

Fig. 4 Rainflow counting of M_y amplitudes, comparison of influential parameters on ship response statistics

Tab. 2 Sea states conditions

	T_P	T_z	H_S	γ	μ	v_S
A	$16.2s$	$11.5s$	$14.5m$	1.0	180^o	$0kts$
B	$15.0s$	$12.4s$	$14.5m$	6.0	180^o	$0kts$

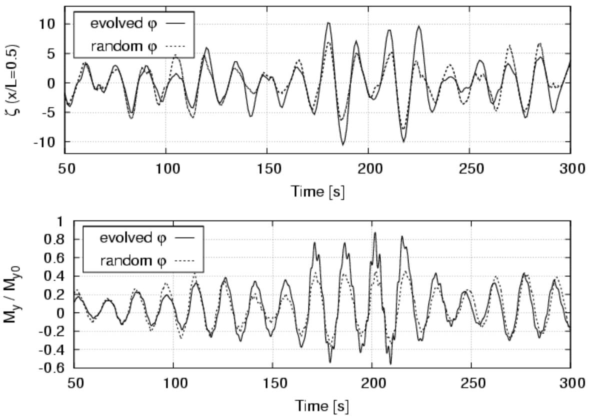

Fig. 5 Comparative time series of surface elevation (top) and M_y (bottom) in a sea state B realisation with random phases (dashed lines) and phases according to NLS solution (solid lines)

Another influential parameter of rather unexpected importance was investigated in further computations only comprising $2,500s$ evaluated time series.

For two sea states, see Table 2, we compared wave realisations with randomly phased wave components and corresponding wave sequences that were previously evolved with an NLS method solving eq. 2. Fig. 5 (top) examplifies, for one realisation, the difference between the input wave sequence according to the NLS solution and the corresponding random-phased wave sequence. The wave group at around $t = 200s$ is a result of phase modulation, yielding significantly higher crests and troughs, and as a consequence the midships vertical bending moment amplitudes increase as well, Fig. 5 (bottom). Additionally, vibration becomes more pronounced. Rainflow counting of M_y for all realisations, Fig. 6, gives a more general picture. Rare events, i.e. M_y amplitudes which are exceeded only a few times, are more severe in the phase-modulated sea state realisations. Especially for the very peaked sea state B with $\gamma = 6.0$, there is a remarkable gap between the curve corresponding to random phases and the one corresponding to the NLS pre-simulations. The gap for sea state A is smaller and only occurs for amplitudes exceeded less than 50 times, thus it has small statistical relevance. For sea state B, the gap already occurs for load levels that are exceeded more than 100 times, and it is much more pronounced.

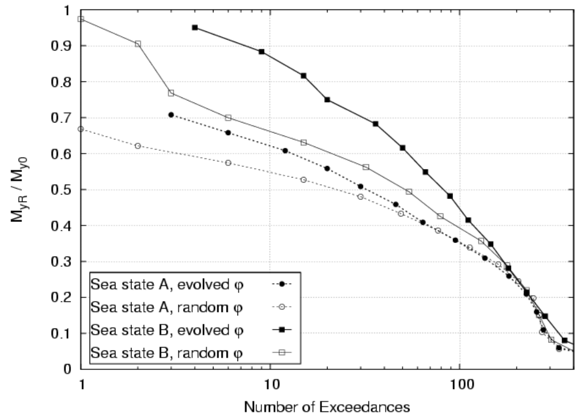

Fig. 6 Influence of component wave phases on M_y amplitudes, computed for two sea states A and B; initial random phases (empty symbols) and evolved sea state (full symbols)

So far, the results indicate a significant influence of wave process evolution on the hull girder loads in these severe sea states, especially for the very narrow-banded spectrum with $\gamma = 6$.

6 Discussion

The presented work aims at simulating ships in irregular waves to obtain statistical properties of ship responses in steep and severe sea states with better accuracy compared to less involved methods. Relevant nonlinearities related to wave-wave interaction, breaking waves and nonlinear ship responses including structural elasticity are implicitly accounted for. The presented examples, however, highlighted the necessity to mind the grid dependency of the numerical solution and carefully check the results with respect to achieved accuracy.

Extreme load predictions for ships are a challenging task and are associated with large uncertainties. Our investigations tried to outline important nonlinear contributions to extreme loads, namely hull girder elasticity and wave-wave interaction. Forward speed effects, wave directional spreading and wave nonlinearities, amongst others, are also important but have been previously investigated. The wave spectral shape and peak enhancement factor γ showed to have a significant impact on ship responses in our computations, but more investigations are required. In case our findings can be confirmed, present recommendations for sea state parameters in ship load analysis should be revised.

All nonlinearities implicate increased numerical effort, and those presented here can hardly be included on a regular basis, at least with available computer resources. Instead, sophisticated and efficient procedures should be established to reduce the required simulation times.

Comprehensive experiments with models of four different ships are part of the *ExtremeSeas* project. Comparisons with model test data are not yet available to quantify the accuracy of the presented coupled solver at predicting ship response statistics in severe or extreme seas. Another task is to combine experimental and numerical data to establish short-term statistical probability distributions of hull girder responses in such conditions.

A prolongated and more elaborate version of this paper has been submitted to Ship Technology Research.

Acknowledgements

A part of the research was supported by the European Community's Seventh Framework Programme FP7-SST-2008-RTD-1 under grant agreement No. 234175.

References

Brunswig, J and el Moctar, O (2004). "Prediction of Ship Motions in Waves using RANSE", *Proc. 7th Numerical Towing Tank Symposium*, Hamburg, pp. 9–13.

Ferziger, J H and Perić, M (2002). *Computational Methods for Fluid Dynamics* (3rd ed.). Berlin Heidelberg New York: Springer Verlag.

Hasselmann, K, Barnett, TP, Bouws, E, Carlson, H, Cartwright, DE, Enke, K, Ewing, JA, Gienapp, H, Hasselmann, DE, Kruseman, P, Meerburg, A, Müller, P, Olbers, DJ, Richter, K, Sell, W, and Walden, H (1973). "Measurements of wind-wave growth and swell decay during the Joint North Sea Wave Project (JONSWAP)", *Ergänzungsheft zur Deutschen Hydrographischen Zeitschrift Reihe Vol 12*, pp. 95.

Oberhagemann, J and el Moctar, O (2007). "A Simplified Approach to Investigate Fluid-Structure Coupling Effects on Slamming Loads of Ships", *Proc. 10th Numerical Towing Tank Symposium*, Hamburg, pp. 150–155.

Oberhagemann, J and el Moctar, O (2011). "Numerical and Experimental Investigations of Whipping and Springing of Ship Structures", *Proc. 21st ISOPE Conference*, Maui, pp. 461–468.

Onorato, M, Osborne, AR, Serio, M, and Bertone, S (2001). "Freak Wave in Random Oceanic Sea States", *Physical Review Letters Vol 86 (25)*, pp. 5831–5834.

Onorato, M, Osborne, AR, Serio, M, Cavaleri, L, and Stansberg, CT (2006). "Extreme Waves, Modulation Instability and Second Order Theory: Wave Flume Experiments on Irregular Waves", *European Journal of Mechanics B/Fluids Vol 25*, pp. 586–601.

Osborne, AR, Onorato, M, and Serio, M (2000). "The Nonlinear Dynamics of Rogue Waves and Holes in Deep-Water Gravity Wave Trains", *Physical Letters A Vol 275*, pp. 386–393.

Pierson, WJ and Moskowitz, LA (1964). "Proposed Spectral Form for Fully Developed Wind Seas Based on the Similarity Theory of S. A. Kitaigorodskii", *Journal of Geophysical Research Vol 69*, pp. 5181–5190.

Zhakarov, V (1968). "Stability of Period Waves of Finite Amplitude on Surface of a Deep Fluid", *Journal of Applied Mechanics and Technical Physics Vol 9*, pp. 190–194.

Unsteady CFD of a Marine Current Turbine using OpenFOAM with Generalised Grid Interface

Thomas P. Lloyd[†][*], **Stephen R. Turnock**[†] **and Victor F. Humphrey**[‡]

[†]Fluid-Structure Interactions Research Group; [‡]Institute of Sound and Vibration Research,
University of Southampton, Southampton, UK. SO17 1BJ

1 Introduction

Marine current turbines (MCTs), such as the 'Seaflow' and 'Seagen' devices (Fraenkel, 2007) represent an important technology for harnessing marine renewable energy. The hydrodynamic behaviour of such devices includes complex interactions between the turbine and ocean turbulence, as well as turbine wakes if sited in arrays. These should be accounted for in performance assessments.

Traditionally, blade element momentum (BEM) models have been used to assess turbine performance, either in isolation (Batten et al., 2007) or array configuration (Turnock et al., 2011), the later study combining this approach with computational flud dynamics (CFD) simulations to model turbine wakes. Recently however, modelling the unsteady performance of turbines using viscous CFD has become more popular for the assessment of transient performance and blade fatigue loads (Faudot and Dahlhaug, 2011; Lawson et al., 2011) which are important for determining operational lifecycles. This is possible through the use of unsteady CFD techniques such as unsteady Reynolds-averaged Navier Stokes (URANS) solvers and dynamic meshing.

This paper presents the initial findings of a study carried out using the CFD library OpenFOAM® to predict the performance of a single turbine in a test tunnel environment, with comparison to the experiments of Bahaj et al. (2007). The main aim is to establish the use of dynamic meshing for conducting unsteady CFD simulations of turbomachines, with possible other applications including ship hull-propeller-rudder interaction.

2 The OpenFOAM Generalised Grid Interface

OpenFOAM is an open source CFD 'library' written using the object-oriented language C++ to solve computational continuum mechanics (CCM) problems (Weller et al., 1998). The advantage of this approach is that the user can easily interact with the top-level code and existing applications to solve CCM problems, or modify the code to create new solvers and utilities for specific user requirements. Users are also free to share their code developments with the OpenFOAM community. This has led to various 'development' releases of the code, such as that distributed under the OpenFOAM®-Extend Project.

A notable development of the code, utilised here, is the Generalised Grid Interface (GGI) (Beaudoin and Jasak, 2008), available through the Extend Project. This provides the ability to couple non-conformal mesh regions, and has been applied to numerous turbomachinery problems for handling the interface between rotating and stationary domains (e.g. see Petit et al. (2011)). The GGI passes flow variables across the interface between 'master' and 'slave' patches at each simulation time step.

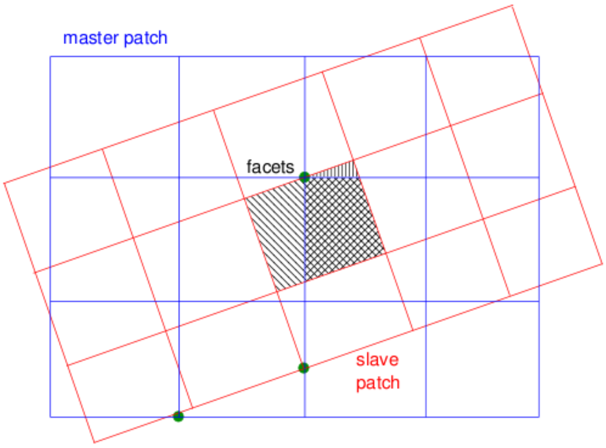

Figure 1: Schematic of master and slave patch face cutting (taken from Jasak (2011))

---

[*] *corresponding author's e-mail*: T.P.Lloyd@soton.ac.uk

This is achieved by:

1. cutting faces on the interface into facets, as shown in Figure 1;
2. calculating interpolation weights between master and slave patches based on facet areas;
3. transferring flow variables between master and slave patches using calculated weights.

Constraints for consistency and conservativeness are also invoked.

3 Case Setup

The simulated case uses the rotor geometry and experimental performance data of Bahaj et al. (2007), who tested a model-scale turbine in the QinetiQ cavitation tunnel at Haslar, Gosport, for a number of tip speed ratios (TSRs) and hub pitch angles. The main parameters of the experiments are provided in Table 1. Figure 2 shows the turbine as tested in the cavitation tunnel. The speed value quoted in Table 1 corresponds to a single tested case, with the hub pitch angle set accordingly to match the setup of Bahaj et al. (2007).

Table 1: Cavitation tunnel and turbine particulars

Tunnel	
Length	5 m
Breadth	2.4 m
Height	1.2 m
Maximum speed	8 ms^{-1}
Pressure	0.2-1.2 atm.
Turbine	
Rotor radius (R)	0.4 m
Hub pitch angle	25 deg
Blade shape	NACA 63-8xx
Speed (U_∞)	1.54 ms^{-1}
Tip speed ratio	6

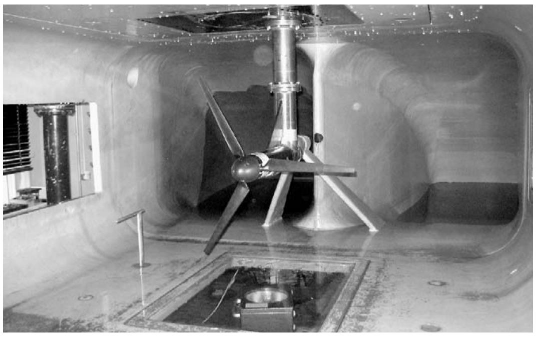

Figure 2: Model-scale turbine in cavitation tunnel (taken from Bahaj et al. (2007))

The simulation is set up using two mesh domains created using the 'blockMesh' utility, as show in Figure 3a, to replicate the dimensions given in Table 1. Mesh refinement around the turbine blades and hub is achieved using 'snappyHexMesh'. An additional refinement is included in the form of a cylinder extending downstream from the blade tips, in an attempt to capture the tip vortices (see Figure 3b). The mesh in the far field remains unrefined, meaning the tunnel wall boundary layers are not fully resolved. The implications of this are discussed in Section 4. The simplified geometry, created using *.stl* files, is also shown in Figure 3b, assuming the hub radius to be at 20% of the radius. The boundary conditions for velocity are summarised in Table 2, referring to Figure 3. Note that the GGI upstream of the rotor is located at $x/D = -0.625$, whilst the rotating domain has a diameter of 1 metre.

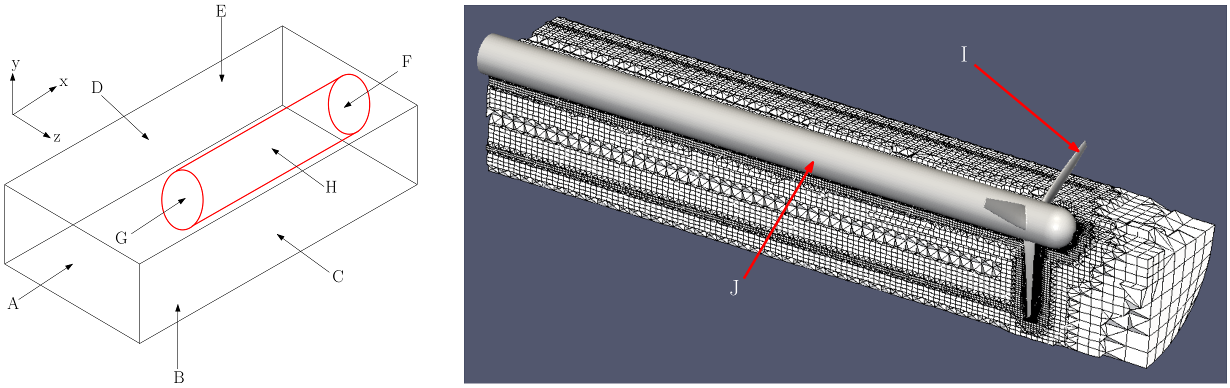

(a) Overall domain schematic

(b) Mesh cutaway view near turbine

Figure 3: Views of simulation domain with labelled patches, corresponding to Table 2

The velocity across the inlet is specified as uniform since no information is available regarding velocity profile or fluctuations from the experiments. Similarly k and ω values are assigned using the empirical formulae $k = 1.5(|u|I)^2$ and $\omega = C_\mu^{-1/4} k^{1/2}/L$, where $C_\mu = 0.09$ (Tu et al., 2008).

Table 2: Summary of boundary conditions applied to simulation domain (see Figure 3 for patch designations)

Designation	Description	BC type	Designation	Description	BC type
A	inlet	Dirichlet (fixed value)	F	outlet	Neumann
B	bottom	no slip (fixed wall)	G	GGI	ggi
C	side	no slip (fixed wall)	H	GGI	ggi
D	side	no slip (fixed wall)	I	blades	no slip (moving wall)
E	top	no slip (fixed wall)	J	hub	no slip (moving wall)

The main mesh and solver settings are presented in Table 3. The time step is controlled by imposing a limit on the maximum Courant number (Co) of 10. The resulting mean Co is approximately 0.15. This high Courant number is permitted by using the 'transientSimpleDyMFoam' solver available through the Extend Project. This allows large time steps to be used for unsteady simulations by utilising the Semi-Implicit Pressure-Linked Equations (SIMPLE) solution method.

Table 3: Mesh and simulation settings

Parameter	Setting
Mesh type	hexahedra
Mesh size	~700,000
Simulation type	URANS
Turbulence model	$k-\omega$ SST
Coupling	SIMPLE
Δt	~0.001s

4 Results and Discussion

The mesh used in this paper is considered to be extremely coarse, whilst simulations using larger meshes, ~6M cells, are currently in progress. However, the results which can be extracted from the current simulation allow insight into modifications required to improve the flow feature capture and design of GGI meshes.

Figure 4 shows the time histories of turbine power coefficient and efficiency, which are defined as $C_P = P/0.5\pi\rho U_\infty^3 R^2$ and $\eta = P/\Delta P_f$ respectively, where ρ is fluid density and ΔP_f is the rate of work input from the fluid. These measures are output from the code using the 'turboPerformance' utility, available through the Extend Project.

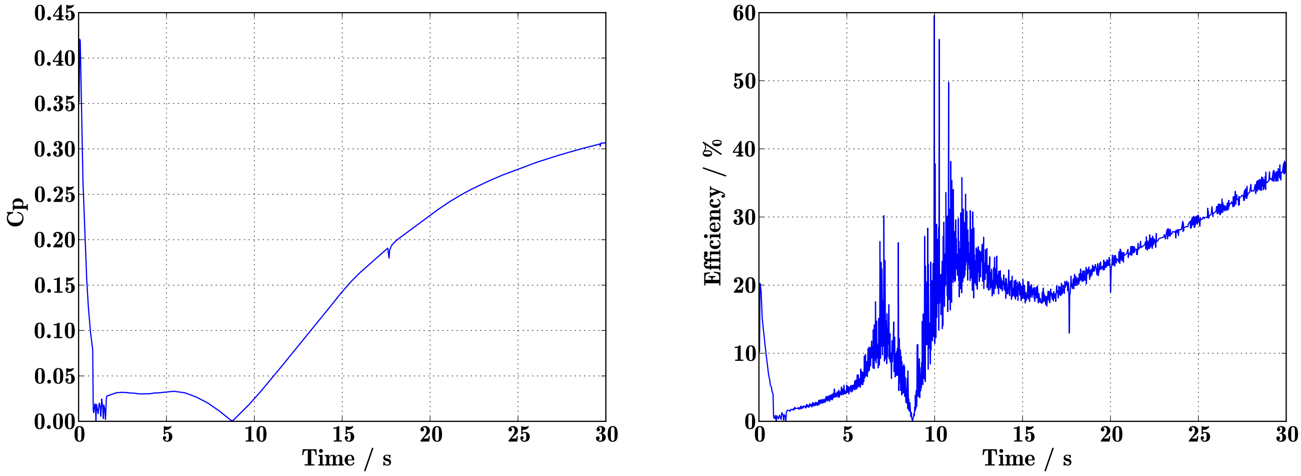

(a) Turbine power coefficient

(b) Turbine efficiency

Figure 4: Non-dimensional turbine performance parameter evolution

The large fluctuations and lack of steady mean show that the solution has not fully converged. This is confirmed by examining the simulation residuals, whereby the lateral and vertical velocity components have only reduced by 10^{-3}. It is expected that this it due to the coarse mesh used outside of the turbine diameter. However, it can be seen that the C_P does appear to be tending towards a constant value, suggesting that the turbine torque is converging. Thus the almost linear increase in η may be attributed to the non-converging mass flux through the domain, suggesting a longer domain should be used.

Figure 5a shows an axial slice through the domain, with axial velocity non-dimensionalised as $u_x^* = u_x/U_\infty$. This plot shows clearly the interaction between the turbine blades and the tunnel wall boundary layer. Thus the mesh density in this region should be increased to better capture this behaviour. It also reveals a velocity jump across the GGI due to the coarse mesh used. Further refinement at the interface is required.

Figures 5b and 5c provide views of the spatial evolution of the turbine wake. Figure 5b clearly shows the velocity deficit due to the rotating blades. A wake mean velocity deficit is also evident in Figure 5c for each of the downstream cut planes. However, the is a sharp velocity change across the GGI due to the coarse mesh, which could influence the wake development.

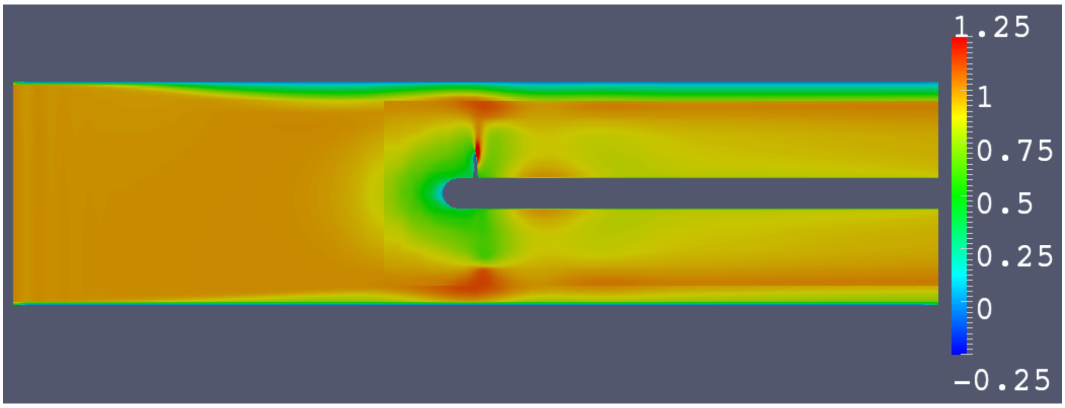

(a) Streamwise slice: domain centreline

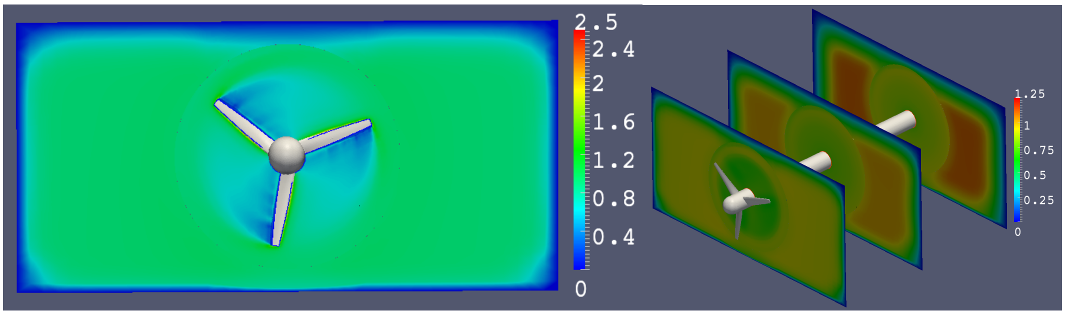

(b) Transverse slice: turbine rotor

(c) Transverse wake slices located at: $x/D = 0.125, 1.25$ and 2.5

Figure 5: Domain slices, displaying non-dimensional axial velocity

Of further interest is the capture of the turbulent structures in the wake, and especially the tip vortices. In order to assess this, the second invariant of the velocity tensor is used. This is calculated as $Q = 0.5(\Omega_{ij}\Omega_{ij} - S_{ij}S_{ij})$, and provides identification of vortical structures. As illustrated in Figure 6, the tip vortices of the turbine blades are captured reasonably well. However, these structures are not transported downstream a significant distance, showing the mesh to be too coarse in this region, despite some refinement being employed here (see Figure 3b). Thus furhter mesh refinement is required, which may benefit from the application of a 'vortex refinement' technique, such as that of Pemberton et al. (2002).

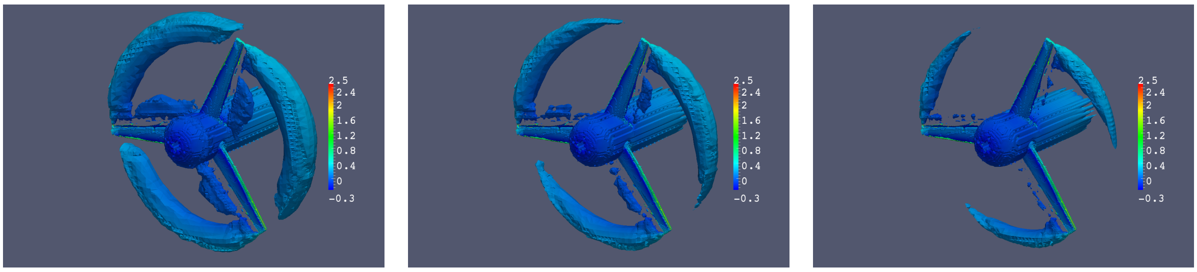

(a) $Q = 10s^{-1}$ (b) $Q = 20s^{-1}$ (c) $Q = 50s^{-1}$

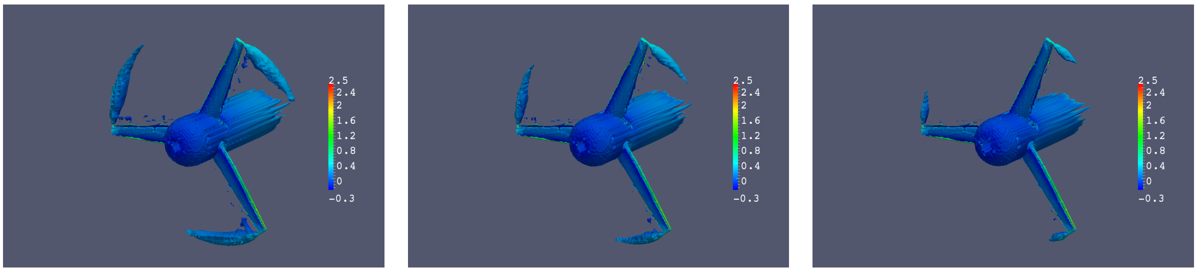

(d) $Q = 100s^{-1}$ (e) $Q = 200s^{-1}$ (f) $Q = 500s^{-1}$

Figure 6: Plots of second invariant of velocity tensor, Q, coloured by non-dimensional velocity magnitude

5 Conclusions

The CFD simulation of marine current turbines under realistic conditions presents numerous challenges. The use of unsteady solution methods is important, and becoming more popular. However, accurately capturing flow features and modelling realistic conditions is not a simple task. This study has presented preliminary findings concerning the simulation of an MCT to replicate experimental performance data.

The main challenge highlighted by the results is appropriate mesh design. The coarse mesh used here has led to complex flow features and hydrodynamic interactions being lost in the simulation. The focus of future work will be on improving mesh design and using larger meshes. Furthermore, to accurately capture turbine response to realistic environmental conditions, other unsteady methods such as large- and detached-eddy simulation will be required, in order to both model ocean turbulence by specifying inlet turbulent velocities, and predict turbine response fluctuations over smaller time steps.

Acknowledgements

Thanks to all those involved in the OpenFOAM®-Extend Project and the Turbomachinery Special Interest Group for the development and support of the GGI and other 'Turbo Tools', particularly Martin Beaudoin, Hrvoje Jasak and Håkan Nilsson. Mr Lloyd acknowledges the financial support of a University of Southampton Postgraduate Scholarship, as well as funding from dstl and QinetiQ.

Nomenclature

$Co = \frac{u\Delta t}{\Delta s}$	Courant number $[-]$	$S_{ij} = \frac{1}{2}\left(\frac{\partial u_i}{\partial x_j} + \frac{\partial u_i}{\partial x_j}\right)$	Strain rate tensor $[s^{-1}]$
D	Turbine diameter $[m]$	Δs	Cell dimension $[m]$
I	Turbulence intensity $[-]$	Δt	Time step $[s]$
k	Kinetic energy $[m^2 s^{-2}]$	U_∞	Reference velocity $[ms^{-1}]$
$L = 0.07D$	Turbulence length scale $[m]$	u	Velocity $[ms^{-1}]$
P	Turbine power $[kgm^2 s^{-2}]$	x	Distance downstream of rotor [m]
Q	Second invariant of velocity tensor $[s^{-1}]$	$\Omega_{ij} = \frac{1}{2}\left(\frac{\partial u_i}{\partial x_j} - \frac{\partial u_i}{\partial x_j}\right)$	Rotation rate tensor $[s^{-1}]$
R	Turbine radius $[m]$	ω	Specific dissipation $[s^{-1}]$

References

Bahaj, A., Molland, A., Chaplin, J. and Batten, W. (2007), 'Power and thrust measurements of marine current turbines under various hydrodynamic flow conditions in a cavitation tunnel and a towing tank', *Renewable Energy* **32**(3), 407–426.

Batten, W., Bahaj, A., Molland, A. and Chaplin, J. (2007), 'Experimentally validated numerical method for the hydrodynamic design of horizontal axis tidal turbines', *Ocean Engineering* **34**(7), 1013–1020.

Beaudoin, M. and Jasak, H. (2008), Development of a generalized grid interface for turbomachinery simulations with OpenFOAM, *in* 'Open Source CFD International Conference 2008', number December 2008, 4th-5th December, Berlin.

Faudot, C. and Dahlhaug, O. G. (2011), Tidal turbine blades: design and dynamic loads estimation using CFD and blade element momentum theory, *in* 'Proceedings of the 30th International Conference on Ocean, Offshore and Arctic Engineering', 19th-24th June, Rotterdam.

Fraenkel, P. L. (2007), 'Marine current turbines: pioneering the development of marine kinetic energy converters', *Proceedings of the Institution of Mechanical Engineers, Part A: Journal of Power and Energy* **221**(2), 159–169.

Jasak, H. (2011), Turbo Tools and General Grid Interface Theoretical Basis and Implementation, *in* '6th OpenFOAM workshop', number June, 13th-16th June, Penn State University.

Lawson, M. J., Li, Y. and Sale, D. C. (2011), Development and verification of a computational fluid dynamics model of a horizontal-axis tidal current turbine, *in* 'Proceedings of the 30th International Conference on Ocean, Offshore and Arctic Engineering', 19th-24th June, Rotterdam.

Pemberton, R., Turnock, S. R., Dodd, T. and Rogers, E. (2002), 'a Novel Method for Identifying Vortical Structures', *Journal of Fluids and Structures* **16**(8), 1051–1057.

Petit, O., Bosioc, A. I., Nilsson, H. k., Muntean, S. and Susan-resiga, R. F. (2011), ‘Unsteady simulations of the flow in a swirl generator , using OpenFOAM’, *International Journal of Fluid Machinery and Systems* **4**(1), 199–208.

Tu, J., Yeoh, G. H. and Liu, C. (2008), *Computational Fluid Dynamics: A Practical Approach*, Elsevier Ltd, Oxford.

Turnock, S. R., Phillips, A. B., Banks, J. and Nicholls-Lee, R. (2011), ‘Modelling tidal current turbine wakes using a coupled RANS-BEMT approach as a tool for analysing power capture of arrays of turbines’, *Ocean Engineering* **38**(11-12), 1300–1307.

Weller, H. G., Tabor, G. R., Jasak, H. and Fureby, C. (1998), ‘A tensorial approach to computational continuum mechanics using object-oriented techniques’, *Computers in Physics* **12**(6), 620–631.

Potsdam Propeller Test Case (PPTC)

Ulf Barkmann, Hans-Jürgen Heinke, Lars Lübke
SVA, Potsdam Model Basin, Germany (pptc@sva-potsdam.de)

Introduction

In course of the Second International Symposium on Marine Propulsors (smp'11) the organizing committee decided to arrange a propeller workshop. The intention of the workshop was to offer universities and research groups the opportunity to validate their numerical tools and setups for propeller flows.

The Potsdam Model Basin (SVA) was asked to contribute experimental data. It was decided to publish the data of the controllable pitch propeller VP1304 under the acronym "Potsdam Propeller Test Case" (PPTC). In course of the workshop the SVA hosted the test case 2. The requested computations included open water tests (case 2.1), the evaluation of the velocity field behind the propeller (case2.2) and cavitation tests (case2.3). The experimental data was not known to the participants in advanced, making the different cases blind tests.

The paper is intended to give a brief overview of the workshop test case data and the computational results. The entire workshop date, covering the geometry, reports, experimental data and the workshop evaluations, can be found under the following link: www.sva-potsdam/pptc.html. Questions concerning the data can be addressed to: pptc@sva-potsdam.de

Geometry

The propeller is a controllable pitch propeller. This affects the propeller blade design near the hub and results in a 0.3 mm gap between hub and the root of the propeller blade near the leading and trailing edge. The hub cap and aft fairing where designed according to the 22nd ITTC (1999) proceedings. The gap between aft fairing and hub has a width of 3 mm. Also a dummy hub, having the same dimensions and mass as the propeller hub, was manufactured, which was used during the so called pre-tests. The main data of the propeller is given in the following Table.

			VP1304
Diameter	D	[m]	0.250
Pitch ratio $r/R = 0.7$	$P_{0.7}/D$	[–]	1.635
Area ratio	A_E/A_0	[–]	0.77896
Chord length $r/R = 0.7$	$c_{0.7}$	[m]	0.10417
Skew	θ_{EXT}	[°]	18.837
Hub ratio	d_h/D	[–]	0.300
Number of blades	Z	[–]	5
Sense of rotation		[–]	right
Type		[–]	controllable pitch propeller

The propeller surface model, a propeller description by radius, the hub cap geometry and the geometry of the cavitation tunnel were provided by the SVA.

Test case 2.1: Open Water Tests

For the determination of the open water curves, the propeller was investigated in a pull configuration in the towing tank of the SVA. For the open water tests the dynamometer H39 from Kempf & Remmers was used. During the tests the propeller shaft was submerged by 1.5 D. Measurements with a dummy hub were conducted, in order to derive the idle torque, the force in the gap between the hub and the aft fairing and the resistance of the hub cap. The open water tests were carried out at two different numbers of revolutions in order to evaluate the dependency on the Reynolds number. For the evaluation of the computational results however solely the tests with $n = 15\ \mathrm{s}^{-1}$ are taken into account.

For the workshop it was requested to calculate the open water characteristics of the propeller blades only for different advanced coefficients. The thrust T, the torque Q and the efficiency η_O should be expressed in the following way, employing the rate of revolution n, the propeller diameter D, the advance speed V_A and the water density ρ:

Advance coefficient	Thrust coefficient	Torque coefficient	Open water efficiency
$J = \frac{V_A}{n \cdot D}$	$K_T = \frac{T}{\rho \cdot n^2 \cdot D^4}$	$K_Q = \frac{Q}{\rho \cdot n^2 \cdot D^5}$	$\eta_O = \frac{J}{2\pi} \cdot \frac{K_T}{K_Q}$

The measured torque and thrust were corrected with the data from the pre-tests (according to the ITTC recommendations) giving the blade forces only. The corrected open water characteristics for $n = 15\ \mathrm{s}^{-1}$ are given in the following. In [1] the measurements are described in more detail.

J	K_T	$10K_Q$	η_O
0.60	0.6288	1.3964	0.4300
0.80	0.5100	1.1780	0.5512
1.00	0.3994	0.9749	0.6520
1.20	0.2949	0.7760	0.7258
1.40	0.1878	0.5588	0.7487

For the workshop 14 participants handed in 19 different open water curves, computed with 13 different solvers. Among the solvers were 5 potential flow codes and hence 8 different viscous flow solvers. For the viscous flow calculations up to 4.3 Million elements were used to mesh one blade passage. In the following Figure the boundaries of the standard deviation (straight black lines) and the mean values (dashed black lines) of all computations are plotted for the thrust and torque coefficient, as well as the open water efficiency. The corresponding measurements are given as dashed red lines.

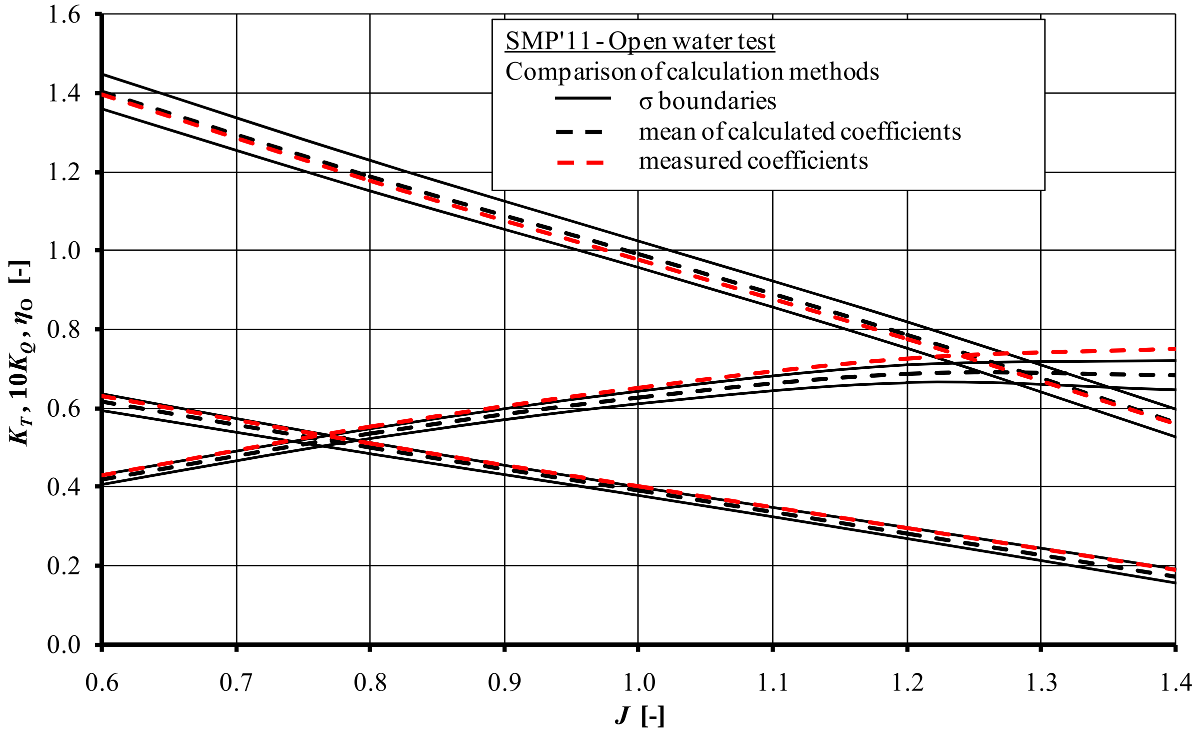

It shows that the computational methods are able to predict the open water characteristics in the requested advance coefficient range quit good. It has to be considered however, that the extreme ends of the usual advance coefficient range was not asked for (J < 0.6 – J > 1.4). In this region the discrepancies can expected to be larger. In general the deviations between measured and computed values are smaller for the thrust in comparison to the torque coefficient. The thrust coefficient is under predicted by the computational methods, while the computed torque coefficient scatters around the measured value. This leads in general to an under prediction of the open water efficiency as well.

Test case 2.2: Velocity field

The velocity field was measured by means of LDV in the cavitation tunnel K 15 A (Kempf & Remmers) of the SVA Potsdam, utilising a test section with the length of 2600 mm and a cross section of 600x600 mm. The dynamometer J25 was arranged in front of the propeller model. The shaft inclination was zero degrees.

Angular based measurements of the transient flow field behind the rotating propeller operating in homogeneous inflow were carried out, employing a 2D-LDV measuring system from TSI. Special attention was laid upon resolving the tip vortex. The velocity field around the model propeller VP1304 was measured in different planes (see Table below). One revolution of the propeller was resolved within 1440 angle classes, giving an angular resolution of 0.25°. The resolution in radial direction is given in the Table below.

measuring plane	start radius	end radius	distance	
	r/R	r/R	$\Delta r/R$	[mm]
in front of the propeller x/D = -0.20	0.40	1.10	0.050	6.250
behind the propeller x/D = 0.094, 0.10, 0.11, 0.13, 0.16, 0.20	0.40	0.70	0.050	6.250
	0.70	0.90	0.025	3.125
	0.90	0.95	0.010	1.250
	0.95	1.05	0.002	0.250
	1.05	1.10	0.025	3.125

Inflow speed	V_A	[m/s]	7.204
Number of revolutions	n	$[s^{-1}]$	23
Advance coefficient	J	[–]	1.253
Thrust coefficient	K_T	[–]	0.250
Torque coefficient	$10K_Q$	[–]	0.725
Water density (for t_w = 24.7°C)	ρ	$[kg/m^3]$	997.1
Kinematic viscosity of water (for t_w = 24.7°C)	ν	$[m^2/s]$	0.903E-6

The LDV measurements were carried out along a line of constant angular position $\Theta = 225°$, for the working point given above. The data is than related to the propeller construction line. The tests were conducted with a non-cavitating propeller. Test results are summarized in the SVA report [2].

For the workshop it was requested to calculate the velocity field around the propeller. The calculations should be conducted according to the thrust identity. It was requested to provide the velocity distribution in two different planes located 0.1 and 0.2 propeller diameter behind the propeller plane. The data should be derived on different radii, as well as in the entire plane with arbitrary step sizes, see Table below:

	r/R [-]	x/D [-]	θ [°]
Case 2.2.1	0.70	0.1, 0.2	-50° - 22°
Case 2.2.2	0.97	0.1, 0.2	-50° - 22°
Case 2.2.3	1.00	0.1, 0.2	-50° - 22°
Case 2.2.4	0.40 - 1.10	0.1, 0.2	

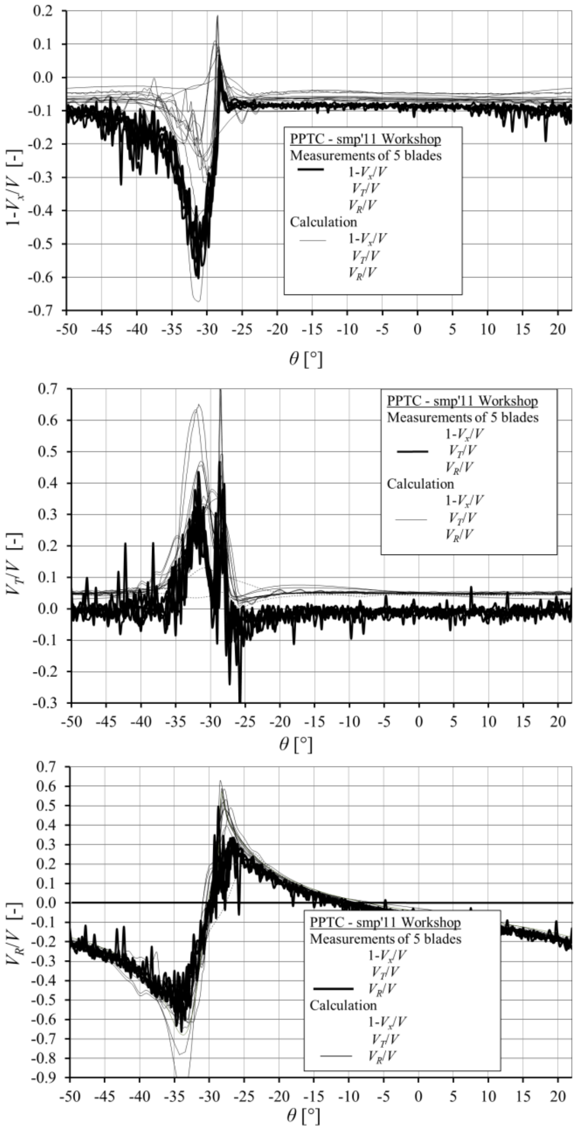

Comparison of axial (top), tangential (middle) and radial (bottom) velocities

It was requested to provide the velocities in axial, tangential and radial direction. The axial velocities are defined positive in flow direction, the radial velocities for increasing radii and the tangential velocities in direction of rotation.

For case 2.2 11 groups handed in 13 different velocity field calculations, computed with 10 different solvers, among which are 2 potential flow codes. The number of elements used in the computational meshes for the viscous flow solvers varied from 1.0 to 4.6 Million cells.

In the Figures on the side, the computed axial, tangential and radial velocities for radius $r/R = 0.97$ in plane $x/D = 0.1$ are compared with the corresponding measurements exemplarily (case 2.2.2). It shows that the agreement between calculations and measurements is in general good. The radial velocity component is calculated more accurately than the other two components. The tip vortex in plane $x/D = 0.1$ is fairly good resolved in all calculations.

The evaluation of the computational results for plane $x/D = 0.2$ behind the propeller plane shows however, that the vortex core is shifted slightly more inwards in the calculations in comparison to the experimental data. This implies a different slipstream contraction. Furthermore numerical diffusion probably also has a mayor effect on the development of the tip vortex further downstream, resulting in smaller velocity gradients.

Automatic grid refinement in the tip vortex region was not tried in any of the computations.

Test case 2.3: Cavitation tests

The cavitation tests were conducted in the cavitation tunnel K 15 A, in the same section than the velocity field measurements. The dynamometer J25 from Kempf & Remmers was arranged in front of the propeller model. The shaft inclination was zero degrees.

			Case 2.3.1	Case 2.3.2	Case 2.3.3
Advanced coefficient	J	[-]	1.019	1.269	1.408
Cavitation number based on *n*	σ_n	[-]	2.024	1.424	2.000
Thrust coefficient (non-cavitating!)	K_T	[-]	0.387	0.245	0.167
Number of revolutions	n	[1/s]	24.987	24.986	25.014
Water density (for $t_w = 23.2$°C)	ρ	[kg/m^3]	997.44	997.44	997.37
Kinematic viscosity water (for $t_w = 23.2$°C)	ν	[m²/s]	$9.337 \cdot 10^{-7}$	$9.337 \cdot 10^{-7}$	$9.272 \cdot 10^{-7}$
Vapour pressure (for $t_w = 23.2$°C)	p_v	[Pa]	2818	2818	2869
Air content	α/α_s	[%]	53.5	53.5	58.50

The propeller characteristics were measured for different numbers of revolution. The cavitation bucket was observed for $n = 25\ \mathrm{s}^{-1}$. Two blades had been selected for the cavitation tests. The cavitation behavior of the propeller was observed in different working points, given in the Table above. A description of the cavitation tests in detail is given in SVA report [3].

For the workshop the participants were asked to conduct the calculations according to the thrust identity. For the three working points it was requested to visualize the cavity surface for vapor fractions of 20, 50 and 80%. In order to quantify the thrust deduction it was additionally asked to provide the thrust coefficient of the propeller in cavitating condition. It was also requested to provide the pressure distribution on different propeller radii ($r/R =$ 0.7, 0.97 and 1.00) with and without cavitation. The data was requested to be made dimensionless with the section advance speed, with p being the tunnel pressure, p_v the vapour pressure, p_0 the static pressure and r the radius:

Cavitation number with respect to n

$$\sigma_n = \frac{(p - p_v)}{0.5 \cdot \rho \cdot (nD)^2}$$

Pressure coefficient

$$c_P = \frac{(p - p_0)}{0.5 \cdot \rho \cdot \left(V^2 + (2 \cdot \pi \cdot n \cdot r)^2\right)}$$

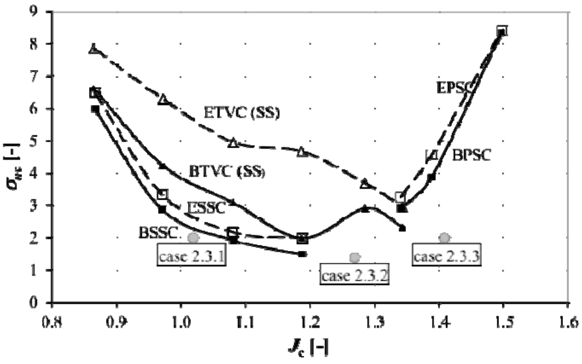

Cavitation bucket, blade 1

For the cavitation test case (2.3) 11 groups handed in 15 results, employing 12 different solvers of which 5 were potential flow codes. In the Figure on the left the cavitation bucket is shown, giving the cavitation inception points for the beginning (B) and end (E) of the tip vortex cavitation (TVC), the suction side cavitation (SSC) and the pressure side cavitation (PSC). The operation points (with respect to σ_n and J) for the different test cases are also marked in the Figure. For case 2.3.1 and case 2.3.2 suction side and tip vortex cavitation are encountered, while for case 2.3.3 also pressure side cavitation occurs. For case 2.3.1 also hub vortex cavitation could be observed.

In the investigated operation points thrust deduction due to cavitation was observed. In the Table on the left, the measured thrust coefficient with and without cavitation is given, followed by the computed thrust coefficient for the cavitating propeller. The used solver for the calculations is given after the group number.

	case 2.3.1	**case 2.3.2**	**case 2.3.3**
	K_T [-]	**K_T [-]**	**K_T [-]**
Exp. (non-cavitating)	**0.3870**	**0.2450**	**0.1670**
Exp. (cavitating)	**0.3725**	**0.2064**	**0.1362**
G1-Procal	0.3760		
G2-SC/Tetra	0.3750	0.1990	0.1380
G3-Fluent	0.3740	0.1940	0.1320
G4-PFC	0.3570	0.2330	0.1610
G5-Fluent	0.3880	0.2050	0.1440
G6-FreSCO+	0.3830		0.1440
G7-Panel	0.3922	0.2369	0.1378
G8-StarCCM	0.3782	0.2035	0.1306
G9-CFX(FCM)	0.3740	0.2030	0.1300
G9-CFX(Kunz)	0.3750	0.2100	0.1330
G9-CFX(Zwart)	0.3730	0.1960	0.1330
G10-Comet	0.3852	0.2101	0.1513
G11-FinFlo	0.3860	0.2020	0.1420

All participants detected a thrust deduction by cavitation in their calculations. The discrepancies between measurement and calculation were in general lower than 5%, showing how well the thrust break down was in general predicted.

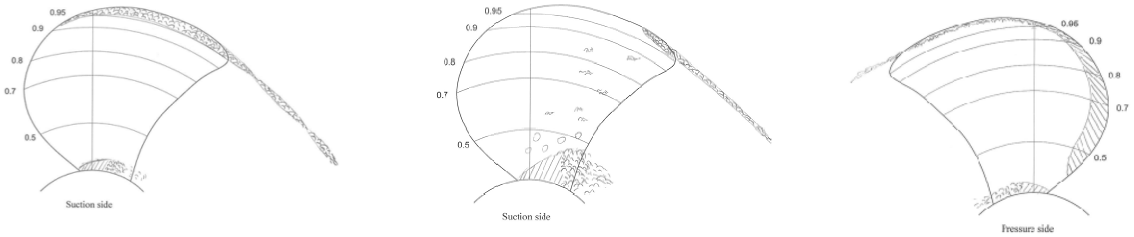

Cavitation sketches, case 2.3.1 suction side (left), case 2.3.2 suction side (middle), case 2.3.3 (right) pressure side

The cavitation behavior for all three operation points is shown in the sketches above. The evaluation of all calculations showed the difficulty in predicting the cavitating tip vortex. For case 2.3.1 there was a tendency to over prediction the risk on suction side cavitation.

Final Remark

The PPTC is intended to aid developers and CFD groups to validate their programs and setups for the calculation of the flow around propellers. In this context the PPTC was introduced in course of the smp'11 propeller workshop. During the workshop up to 14 groups participated in one of three test cases. The test results were unknown to the participants making the test cases blind tests. The test results [1][2][3] were made public (www.sva-potsdam.de/pptc.html) on the website of the SVA after the workshop. All data will remain available there for future use. Furthermore the workshop evaluations, containing all computational results, can also be downloaded. The test results contain also high speed videos of the cavitating propeller as well as the entire LDV data.

The propeller workshop gave insight in state of the art propeller calculations. The following remarks can be drawn:

- The agreement between measurements and calculations for the open water characteristics can be considered good in the investigated advance coefficient range. The highest discrepancies were observed for the open water efficiency.
- The viscous flow calculations proved to be in general insignificantly more accurate than the potential flow calculations for the calculations of the open water curves. For the prediction of the velocity field and cavitation the viscous flow codes proved to be advantageous.
- The calculations predicted in general the flow field (tip vortex) 0.1 propeller diameters behind the propeller plane quit well. Further downstream a shift in vortex core position between measurements and calculations becomes apparent. The numerical calculations also show clear effects of numerical diffusion.
- The computations are in general able to predict the thrust deduction due to cavitation quit accurately. Due to the difficulty to judge which vapour fraction corresponds to the visible cavitation bubbles in the experiment, the prediction of thrust deduction is considered as major criteria for the successful calculation of the cavitating propeller.
- The tip vortex cavitation could only be predicted close to the propeller.

The authors would also like to acknowledge the support given by the organizing committee of the smp'11 and especially Prof. Maksoud for his advice and support during the workshop. Furthermore the authors would also like to thank Dr. Streckwall and Mr. Druckenbrod for their help.

References

[1] U. Barkmann, Potsdam Propeller Test Case (PPTC) - Open Water Tests with the Model Propeller VP1304, Report 3752, Schiffbau-Versuchsanstalt Potsdam, April 2011

[2] K. Mach, Potsdam Propeller Test Case (PPTC) - LDV with the Model Propeller VP1304, Report 3754, Schiffbau-Versuchsanstalt Potsdam, April 2011 (unpublished)

[3] H.-J. Heinke, Potsdam Propeller Test Case (PPTC) - Cavitation Tests with the Model Propeller VP1304, Report 3753, Schiffbau-Versuchsanstalt Potsdam, April 2011

CFD-BASED METHODS FOR NUMERICAL MODELLING OF SCOUR

Greg Melling[1], Justin Dix[1], Stephen Turnock[2], University of Southampton - gjm1v07@noc.soton.ac.uk
Richard Whitehouse, HR Wallingford

1. Introduction

Marine local scour is understood as the removal of sediment from around the base of an object on the seabed caused by waves and currents. The introduction of a flow obstruction to the seafloor will have a significant impact on the local hydrodynamics, causing acceleration, pressure gradients, boundary-layer separation and increased turbulence at the seabed and in the wake of the object. Where the seabed cannot resist the increased magnitude of impinging shear forces, e.g. in non-cohesive mobile sediment such as sands, sediment will be eroded to form a characteristic scour hole. Scour, left unchecked can cause structural damage and major economic losses. The ability to predict scour, both vertical and lateral, is thus a prerequisite for the optimised design of a structure and provision of scour protection.

At present, empirical equations are used for simple two-dimensional objects such as vertical and horizontal cylindrical type in the forecast of maximum scour depths. Fewer relations are available for the quantification lateral scour extent and evolution of the scour pit with time. For a more comprehensive scour prediction or assessment of more complex structures, expensive and time-consuming physical model experiments are required.

The aim of this PhD project is to develop a numeric method for scour modelling in openFOAM CFD which will be capable of predicting scour around complex three-dimensional seabed structures. In this study, we will focus on the discussion of the available approaches for scour modelling using CFD methods.

2. CFD-based scour modelling

The first CFD-based methods were tentatively used for scour modelling in the 1990s. Two general approaches have crystallised that can be distinguished as fundamentally different (Fig. 1). Earlier methods were concerned with flow simulations coupled with a morphological description that drives the deformation of the bottom computational mesh to produce a scour hole. Successive refinement in the following years saw routines of varying complexity being employed for the calculation of the mesh deformation tensor. A boundary adjustment technique (e.g. Li and Cheng, 1999; Lu et al., 2005) has been employed which relates the magnitude of deformation to the equilibrium of the bottom shear stress τ and critical threshold for incipient sediment motion τ_c, i.e. the mesh vertices are adjusted in vertical direction in response to the impinging flow until the condition $\tau = \tau_c$ is reached. More common has been method based on sediment transport theory in which the morphological model consists of bedload and/or suspended sediment equations and the bed evolution is determined by solving the mass balance of sediment equation (e.g. Olsen and Melaaen, 1993; Brørs, 1999; Liang and Cheng, 2005; Liu and Garcia, 2008).

More recently, scour predictions based on two-phase flow considerations have been presented (Zhao and Fernando, 2007; Amoudry et al., 2008; Yeganeh-Bakhtiary et al., 2011). Euler-Euler models treat the fluid and solids as phases as interpenetrating continua capable of exchanging properties like mass and momentum. The advantage of two-phase models is that fluid-solid and solid-solid interactions are considered and no empirical relations are required.

---

[1] Geology/Geophysics Research Group, School of Ocean and Earth Sciences, University of Southampton

[2] Fluid Structure Interaction Research Group, Faculty of Engineering and Environment, University of Southampton

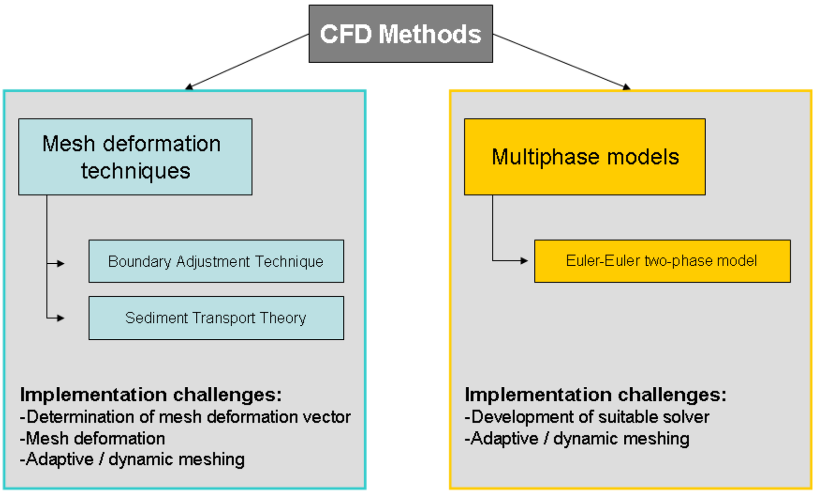

Fig. 1 CFD-based scour modelling methods

3. Numerical Investigations

3.1. Mesh deformation techniques – capturing the basics

a. Resolving the flow

The prerequisite for any scour simulation is the appropriate representation of the factors that cause sediment redistribution. These include the local hydrodynamics, resolved to an appropriate level, associated vortical structures, pressure gradients and bed shear stresses. Preliminary investigations were undertaken on capturing the required details of the flow. To validate the flow simulation physical model data of Dargahi (1989) for the turbulent flow around a vertical surface-piercing cylinder.

The RANS k-ω approach was employed successfully to capture the pressure gradient on the cylinder (Fig. 2). The separation of the upstream boundary layer and development of a junction vortex at the object-wall interface was observed. The plateau in Fig. 3 illustrates the location of the horseshoe vortex; the agreement with empirical data is good. The slight discrepancies in the bottom boundary layer can have two potential causes, the uncertainty of the exact velocity profile used by Dargahi (1989) and deficiency of the mesh.

b. Predicting bed shear stresses

For the purpose of wall shear stress prediction simulations were conducted to replicate flume tests of Sullivan (2008) which offered laser scan data of scour holes around a submerged wreck model. Calculated stresses were qualitatively compared with the topography in the experiment under the premise that areas of high bed shear can be correlated with areas of erosion in the tests.

Numerical simulations were carried out on two orientations of the wreck to the flow for which experimental data was available (Fig. 4). The wreck model was created from the laser scan point cloud data which was processed in solid modelling software. Unstructured gridding routines were used to devise a mesh. Due to the complexity of the object, many iterations were required before a succesful mesh was found. Due to a lack of validation data, a qualitative evaluation of the flow around the wreck model was undertaken with respect to the boundary layer separation and expected gross flow features. Further, the adequacy of the hydrodynamics were “validated” indirectly in light of the resulting pattern of bed shear stresses, as these are the results of some discernible flow feature such as enhanced levels of flow or vorticity. The visualisations in Figs. 5 and 6 show the major flow features and the presence of flow separation in both simulations. A counter-rotating vortex is resolved at the wall-object interface for both cases. The upright wreck results in a recirculation zone in the lee of the object.

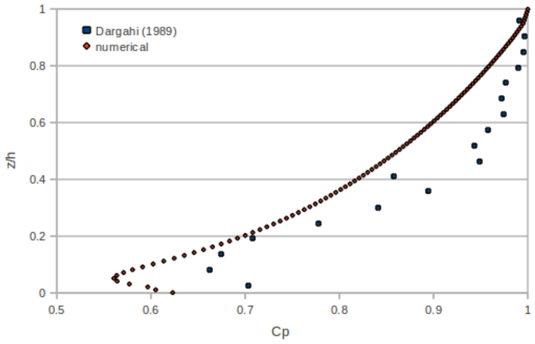

Fig. 2 Validation of pressure gradients on stagnation line

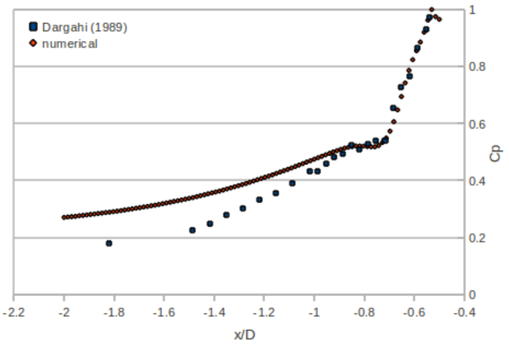

Fig. 3 Validation of pressure gradient at the base of the cylinder in x-direction

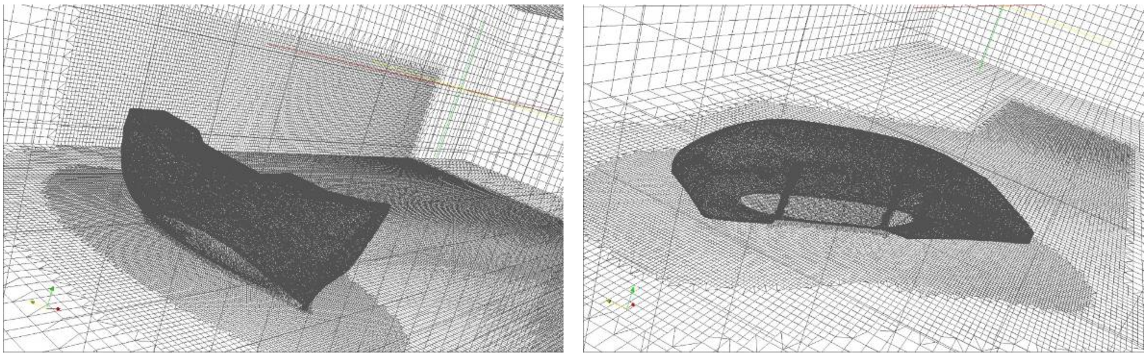

Fig. 4 Wreck model meshes: upright, 90° to flow (left) and on port side, 45° to flow

Interesting turbulent wake patterns are visualised by the streamtubes. On the upright wreck eddies originate from flow spinning off the lateral ends of the object. Where the flow passes over the object similar eddies are observed in the vertical plane. For the wreck oblique to the incoming flow, it was observed that a large part of the flow passes directly over the object, with a smaller proportion passing around the sides. A vortex is shown corkscrewing off the wreck as a result of the interaction between the downward flow in the lee of the wreck and accelerated flows around the ends. As will be shown in the visualisation of wall shear forces, it is the presence of these areas of increased turbulent energy that are responsible for driving the scour process.

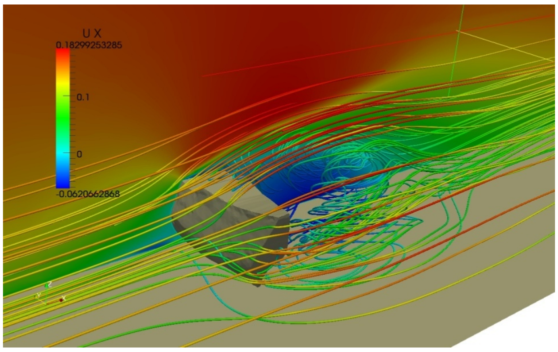

Fig. 5 Slice and stream tubes of U(x)

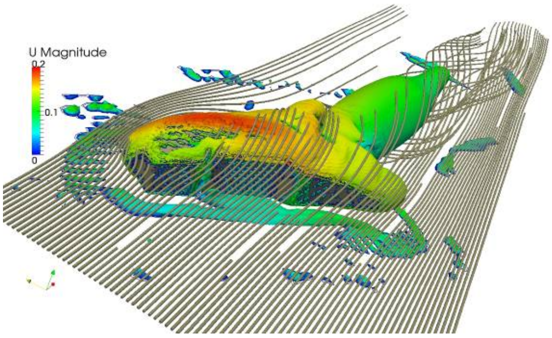

Fig. 6 Isosurface of Q coloured in U and streamlines

Fig. 7 offers a comparison of the laser scan data with calculated wall shear stresses. There is general agreement between areas of high shear and zones of erosion (brown and green circles). Similarly, quiescent accumulation zones show low shear stresses (pink circles). It is however evident that the turbulent energy of the wake is not fully captured (green circles). This could be improved by increasing the mesh resolution and a vortex-following mesh-adaptive algorithm.

In summary, the building blocks for the implementation of a moving mesh technique have been investigated. As illustrated above, once the model and mesh requirements for resolution of flow and bed shear stresses have been established, a routine for mesh movement can be developed.

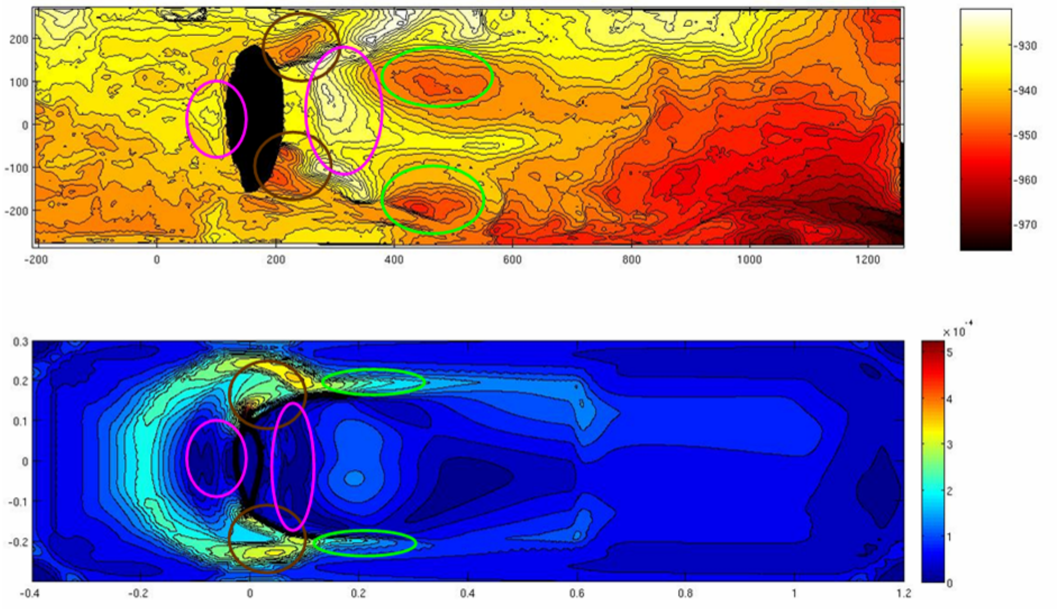

Fig. 7 **Comparison of laser scan data (top) and wall shear stresses (bottom)**

3.2. **Eulerian multi-phase model – investigating capability**

The Euler-Euler method has recently been applied to scour studies around marine pipelines (Zhao and Fernando, 2007; Yeganeh-Bakhtiary, 2011) with promising success. The Eulerian method establishes conservation equations for both phases based on single-phase conservation equations with additional terms for interphase exchanges of mass and momentum. The particle-particle interaction is governed by the kinetic theory of granular flow which describes viscosities for the kinetic, collisional and frictional regimes.

Preliminary investigations into the suitability of the implementation of the Eulerian solver in openFOAM have been carried out and are discussed. A horizontal pipeline case is used to illustrate the capabilities and shortcomings of the solver. A case was set up with uniform inlet velocity of U_b=0.25m/s, pipe diameter D=0.1m and solid fraction of α=0.6 (with a maximum fraction of α_{max}=0.65). Fig. 8 shows the evolution of α and velocity of fluid fraction U_b with time. The results for α reveal that the bed rapidly experiences overpacking ($\alpha > \alpha_{max}$). This causes the bed to reduce in volume and results in errors in morphology. For U_b the maximum flow velocity is expected in the gap between the pipe and the bed (as pictured in the initial condition t=0). However, the flow is reduced significantly with time which causes the bedforms to smooth out.

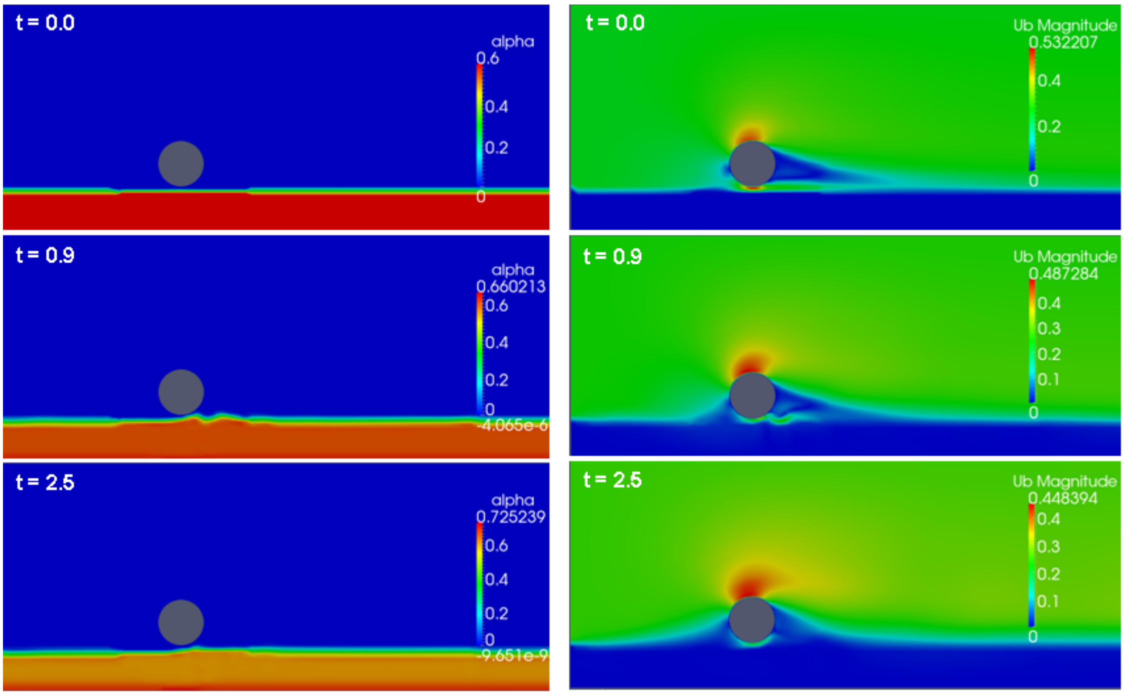

Fig. 8 Evolution of phase fraction α and velocity of fluid fraction Ub

Several issues have been identified with the standard solver. Using kinetic theory alone to control the maximum solid fraction, the bed is subject to strong overpacking. The attenuation of flow in the near-bed area is caused by an inadequate representation of the particle-turbulence interaction which causes a strong reduction in flow velocity leading to rapid settling out of particles near the pipe. Another issue is a discrepancy in timescales. The characteristic timescale of particle-turbulence interaction is shorter than the time required for the flow to adjust to the bed morphology change, causing errors in the scour calculation. This has also been reported by Zhao and Fernando (2007). A number of modifications are required. To alleviate overpacking, a particle normal force model is used that introduces a solids pressure term in the conservation equation. Initial inclusion has shown to improve the control of the maximum solid fraction. For issues with particle-turbulence interaction a number of potential remedies have been identified. Elghobashi and Abou-Arab (1983) have developed a two-phase turbulence model which includes terms for the effect of particles on turbulence. This could be implemented. Another option could be a “frozen bed switch” which entails not solving for the solid phase while the hydrodynamics are calculated; once the flow is fully developed, both phases are solved to allow for bed adjustment before returning to the previous step (Fig. 9). Similarly, iterative mapping between a transient single-phase and the Euler-Euler solver could be used to provide accurate hydrodynamics while respecting the disparity between the characteristic timescales (Fig. 10).

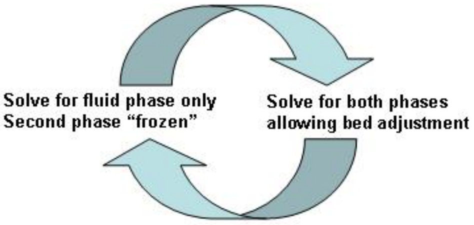

Fig. 9 “Frozen bed switch”

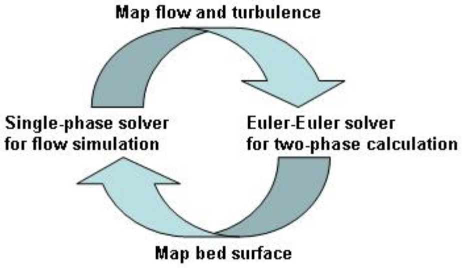

Fig. 10 Iterative mapping between solvers

4. Conclusions

Two possible approaches to scour modelling using CFD methods have been outlined: mesh deformation techniques and multi-phase models. For the prior, the basic components – accurate prediction of hydrodynamics and bed shear stresses – of such an approach have been investigated in openFOAM CFD and discussed in light of physical model data. Based on the presented numerical experiments, a moving mesh approach can be developed and implemented. Multi-phase approaches have only recently been used in scour prediction; previous studies have shown the Euler-Euler method to be suitable. The capabilities of the openFOAM implementation of the Eulerian solver are explored using a two-dimensional pipeline case. Several shortcomings have been illustrated and modifications have been suggested to develop the solver for the purposes of scour modelling.

References

Amoudry, L. O., Hsu, T.-J., & Liu, P. L.-F. (2008). Two-phase model for sand transport in sheet flow regime. Journal of Geophysical Research, 113(C3), 1-15. doi:10.1029/2007JC004179

Brørs, B. (1999). Numerical modelling of flow and scour at pipelines. Journal of Hydraulic Engineering, 125(5), 511-523.

Dargahi, B. (1989). The turbulent flow field around a circular cylinder. Experiments in Fluids, 8(1), 1–12.

Elghobashi, S., & Abou-Arab, T. (1983). A two-equation turbulence model for two-phase flows. Physics of Fluids, 26(4), 931-938.

Li, F., & Cheng, L. (1999). Numerical model for local scour under offshore pipelines. Journal of Hydraulic Engineering, 125(4), 400-406.

Liang, D., Cheng, L., & Li, F. (2005). Numerical modeling of flow and scour below a pipeline in currents Part II. Scour simulation. Coastal Engineering, 52(1), 43-62.

Liu, X., & García, M. H. (2008). Three-Dimensional Numerical Model with Free Water Surface and Mesh Deformation for Local Sediment Scour. Journal of Waterway, Port, Coastal, and Ocean Engineering, 134(4), 203-217.

Lu, L., Li, Y., & Qin, J. (2005). Numerical simulation of the equilibrium profile of local scour around submarine pipelines based on renormalized group turbulence model. Ocean Engineering, 32(17-18), 2007-2019.

Olsen, N., & Melaaen, M. C. (1993). Three-Dimensional Calculation of Scour Around Cylinders. Journal of Hydraulic Engineering, 119(9), 1048-1054.

Sullivan, R., (2008). Physical Modelling of Scour Under Bidirectional Flow Conditions Around Submerged Three Dimensional Objects. MSc Thesis, School of Ocean and Earth Sciences, University of Southampton.

Yeganeh-Bakhtiary, A., Kazeminezhad, M. H., Etemad-Shahidi, A., Baas, J. H., & Cheng, L. (2011). Euler–Euler two-phase flow simulation of tunnel erosion beneath marine pipelines. Applied Ocean Research, 33(2), 137-146.

Zhao, Z., & Fernando, H. J. S. (2007). Numerical simulation of scour around pipelines using an Euler–Euler coupled two-phase model. Environmental Fluid Mechanics, 7(2), 121-142.

Numerical Analysis of propeller loads for a drifting container vessel using RANSE

Philipp Mucha [a], Ould el Moctar [b]

Institute of Ship Technology, Ocean Engineering and Transport Systems
University of Duisburg-Essen
[a]philipp.mucha@stud.uni-due.de, [b]ould.el-moctar@uni-due.de

The state-of-the art of propulsion system design for ships mainly bases on calm water performance. However, propeller blades are subject to extreme loads during manoeuvring or rigid body motions of the ship, thus affecting fatigue strength. In the current design practice, the problem of taking into account the dynamic load raising is met by high safety factors which increases operational costs. Within the framework of the research project Propulsion in Seaways (PropSeas), this work deals with the numerical simulation of various scenarios of extreme loading of propeller blades for a container vessel using a commercial RANS solver. The objective of the investigation of these scenarios is to derive important data regarding fatigue strength. In this context, assessing transverse forces on propeller blades is of paramount importance since they have a crucial influence on loads at the blade's root. This paper presents the results of computations for a drifting container vessel without the effects of the free surface.

The container vessel used for the analysis is the Duisburg Test Case (DTC) the main particulars of which are given in Table 1. The propeller used is the five bladed propeller P1570 with fixed pitch from Potsdam model basin (SVA). Results from model tests for P1570 are available serving as a benchmark for the numerical method employed.

During drifting, the propeller experiences an oblique inflow resulting in a variation of the effective angle of attack α_e as a function of the blade's circumferential position θ. This gives rise to transverse forces on the propeller shaft, a transverse shift of the centre of thrust and reversing loads on the propeller blades, particularly affecting fatigue strength and the manoeuvring performance of the ship. Figure 1 deals with the kinematics of oblique inflow for a sectional representation of a blade profile, mainly referring to el Moctar (2001). Here, α_g is the geometric angle of attack, Φ the local nose-tail pitch angle, β_γ the angle of advance, v_i the propeller induced velocity, v_r the resulting velocity and n the rate of revolution. The Cartesian coordinate system is located at radius r=0.7R.

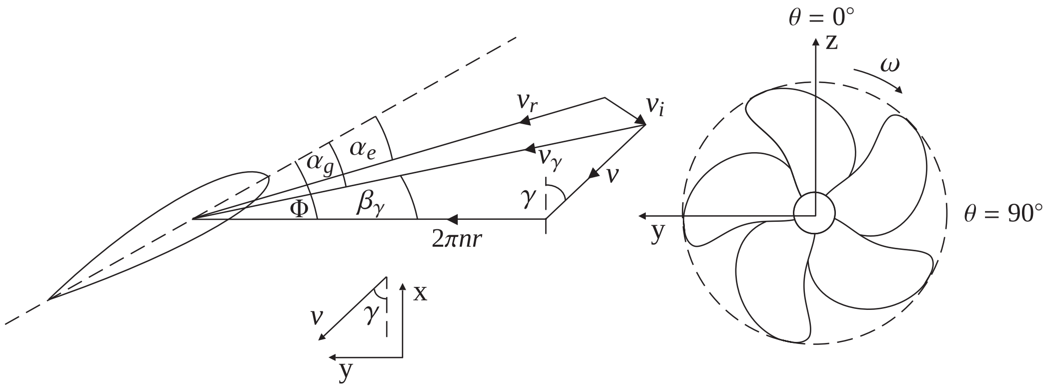

Figure 1: Kinematics of oblique inflow

The x-axis points in the ship's forward direction, the y-axis points to portside and the z-axis points upwards. The sign of the angle of inflow γ is positive in Figure 1. In a cylindrical coordinate system fixed to the propeller axis, the inflow velocity v_γ for the sectional view yields

$$v(r,\theta) \quad = \quad v\sqrt{(cos\gamma)^2 + \left(\frac{2\pi nr}{v} + sin\gamma cos\theta\right)^2 + (sin\gamma sin\theta)^2} \tag{1}$$

Equation (1) contains the axial, tangential and radial components of v_γ. A more elaborate discussion of propellers in oblique flow can be found in el Moctar (2001) or el Moctar and Bertram (2000).

The RANS solver STARCCM+ (6.02.007) is used for the given problem. The solution draws up on the integral representation of the mass (2) and momentum conservation (3) equations satisfying

$$\frac{d}{dt}\int_V \rho \,\mathrm{d}V + \oint_S \cdot \,\mathrm{d}S \quad = \quad 0 \tag{2}$$

$$\frac{d}{dt}\int_V \rho \,\mathrm{d}V + \oint_S \rho v(v\cdot n)\,\mathrm{d}S \quad = \quad \oint_S (T - pI)\cdot ndS + \int_V \rho b \,\mathrm{d}V \tag{3}$$

where ρ is the density and the vector v the velocity of the fluid. n is the normal vector of S, which represents the area of the surface of the control volume V. T denotes the stress tensor, I is the unit tensor, p is the pressure and b a vector of a force per unit mass. A SIMPLE method couples the pressure and velocity fields, see STARCCM+ User Guide (2011). The additional transport of momentum due to the turbulent nature of the flow is accounted for by a k-ϵ model involving two more transport equations. A generic representation of these with ϕ being a scalar quantity such as k or ϵ respectively yields

$$\frac{d}{dt}\int_V \rho\phi \,\mathrm{d}V + \oint_S \rho\phi(v\cdot n)\,\mathrm{d}S \quad = \quad \oint_S \Gamma\nabla\phi dS + \int_V \rho b_\phi \,\mathrm{d}V \tag{4}$$

In (4), Γ denotes the diffusivity coefficient and b_ϕ represents either sinks or sources of the considered scalar quantity. A discussion and a quantification of the empirical coefficients which arise when substituting ϕ for k or ϵ can be found in STARCCM+ User Guide (2011).

The equations which govern the flow are approximated by the Finite Volume Method for the control volumes (CV) the solution domain is subdivided into. The CV's can be of arbitrary shape. The values for each variable are computed at the cell centre. The respective values at the surface of each volume are found from interpolation, surface and volume integrals are approximated by appropriate square methods providing a set of algebraic equations. A detailed description can be found in Ferziger and Peric (1996).

In the given problem, unstructured and automatically generated hexahedral grids are used for the solution domain the properties of which are given further down the line. The propeller is described by tetrahedral cells. Regions where high gradients of the flow quantities are likely to occur are locally refined.

The effect of the free surface on the propeller inflow is considered negligible here. Therefore, the solution domain is cut off at the ship's draught employing a symmetry boundary condition. At the outlet a zero gradient condition is set. The sides and the bottom of the solution domain represent walls with slip conditions. The ship is placed in the solution domain in such a way as to adjust the desired drifting angle. The unsteady nature of the flow demands a simulation in time domain. The rotation of the propeller is simulated as an unsteady rigid body motion. A cylindrical mesh enclosing the propeller is dynamically linked to the local flow field by sliding interfaces which are updated in every time step.

Previous to the above simulation, grids for the ship and the propeller are generated and investigated independently. Convergence of the grid is checked by a stepwise refinement of cell sizes with constant properties within the boundary layer. The latter is resolved by prism layers. For the ship, the average non-dimensional wall distance $Y+$ yields 150. For the propeller, $Y+$ is 300 on average. Solutions are considered convergent in case of a decrease of the normalized residuals by five orders of magnitude. The grids used for the simulation of the drifting ship are:

- DTC without P1570: $3.3 \cdot 10^6$ [solution domain: (length, breadth, depth)=(6L, 2L+B, L)]
- P1570: $7.5 \cdot 10^6$ cells

L	B	d	c_B	v	∇	D	A_E/A_0	$c_{0.7}$	$P_{0.7}/D$	$Skew$
355 m	51 m	14.50 m	0.65	20 kn	166095 m^3	8.91 m	0.82	3.19 m	0.99	31.70°

Table 1: Main particulars of DTC and P1570

An open water test is performed for P1570 at full scale and compared to the results from the model tests. Here, the flow velocity is varied at a constant rate of propeller revolution of $n = 12$ rps. Since the propeller operates in axial inflow, the flow can be considered stationary within a coordinate system which is fixed to the hub and which participates in the propeller's rotation. The results from the open water test agree well with the model tests, especially for advance coefficients $J = v/nD$ in a range of $0.4 \leq J \leq 0.8$ within which the propeller will operate in. Scale effect corrections for the model propeller (scale $\lambda = 59.407$) are included in Figure 2.

The r.h.s. of Figure 2 shows the convergence history of the non-dimensional transverse force coefficient

$$K_{y,i} \quad = \quad \frac{Y_{P,i}}{\rho n^2 D^4} \tag{5}$$

for the simulation of the drifting DTC (γ=-15°) with rotating P1570. $Y_{P,i}$ is the transverse force on propeller blade i. The propeller's rate of revolution is 0.72 rps. $K_{y,i}$ varies with the propeller's frequency of rotation. Time steps are chosen corresponding to a rotation of 2° and 5°, respectively, to investigate the influence of temporal discretisation. A stable oscillation of $K_{y,i}$ starts after approximately 1.5 revolutions, valid for both time steps. Figure 3 provides a more detailed insight into the trend. At positive peaks of the oscillation, the value of $K_{y,i}$ from the computation with the coarse time step (dotted line) is a factor 0.0282/0.0257 ($\approx$1.1) higher than the one computed with the finer time step (solid line). The finer time step is chosen for further simulations in favour of accuracy.

The r.h.s. of Figure 3 compares $K_{y,i}$ for various angles of attack. Besides the case of the DTC at straight course (γ=0°), a small angle of attack (γ=-5°) is additionally considered. The amplitude of $K_{y,i}$ is considerably higher for the drift motion compared to the straight course (Figure 3). Figure 4 illustrates the difference of $K_{y,i}$ over one rotation for γ=-5° and γ=-15°. The blade is loaded significantly higher when running against the direction of the flow. Despite the large difference between both angles, $K_{y,i}$(-15°) increases moderately compared to $K_{y,i}$(-5°). The r.h.s. of Figure 4 deals with the same problem but for P1570 in homogeneous oblique flow. Here, the difference in $K_{y,i}$ is substantially higher. Obviously, the presence of the hull diminishes the dependency of $K_{y,i}$ on γ because of the flow directing function of the aft body. For a discussion of the influence of J and γ, the reader is referred to el Moctar (2001).

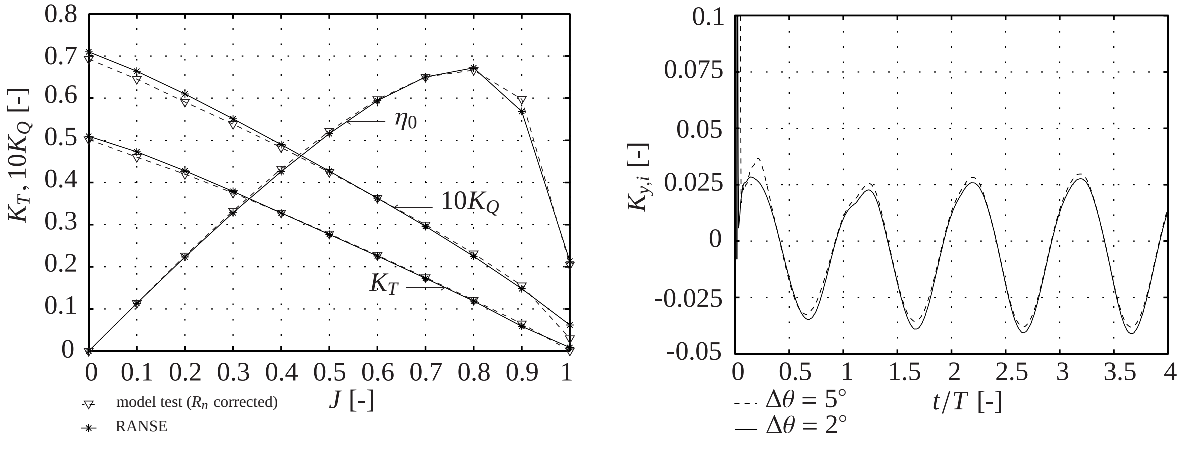

Figure 2: Open Water test (axial inflow, n=12 rps) and convergence history of $K_{y,i}$ for P1570 behind DTC (0.72 rps, v=6kn, $\gamma = -15°$)

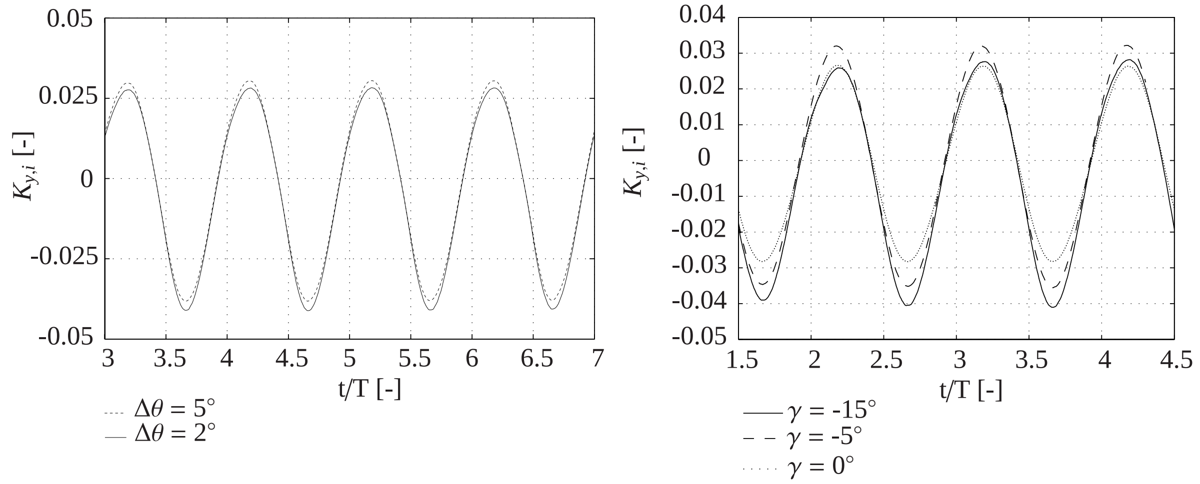

Figure 3: The plot on the l.h.s. shows the variation of $K_{y,i}$ over time/period. The r.h.s. of the figure illustrates the dependency of $K_{y,i}$ on γ.

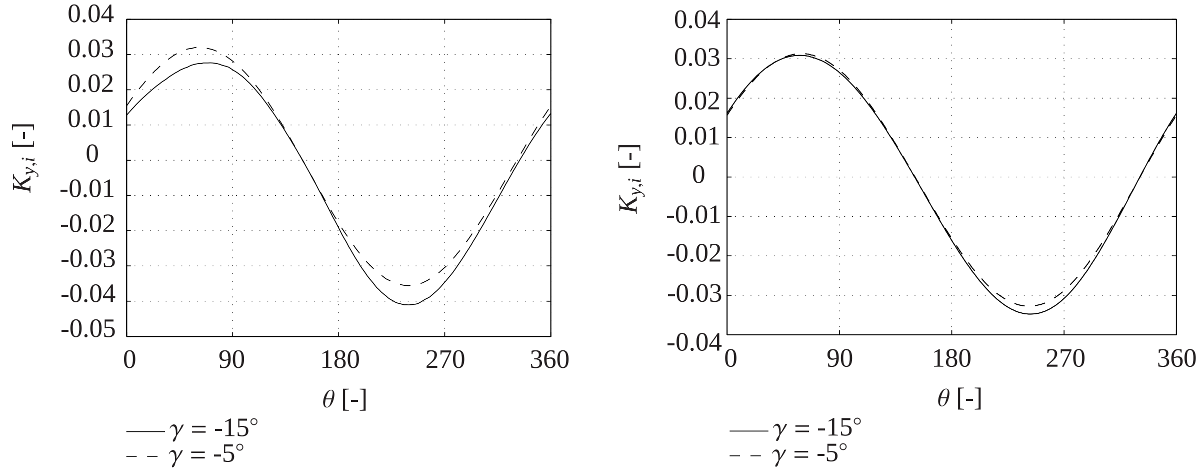

Figure 4: The plot on the l.h.s. compares $K_{y,i}$ for two different angles of attack and for P1570 behind the DTC. The r.h.s. illustrates this problem for P1570 in homogenous oblique flow.

The work presented is still in progress. Further investigations comprise the determination of propeller loads during a turning cycle manoeuver and rigid body motions of the ship. Finally, a load collective is derived in accordance to a typical operational profile for a ship like the DTC. The author hopes to present this work at the symposium.

PROPULSION IN SEAWAYS: http://www.propseas.com/, called 07-01-2011

EL MOCTAR, O.: *Numerische Berechnung von Strömungskräften beim Manövrieren von Schiffen*, Ph.D. thesis at Technical University Hamburg-Harburg, 2001

EL MOCTAR, O., BERTRAM, V.: *RANS Simulation of Propeller in Oblique Flow*, Proceedings of the 3rd Numerical Towing Tank Symposium (NuTTS), Tjärnö, 2000

CD-ADAPCO: *STARCCM+ User Guide 6.02.007*, 2011

FERZIGER, J., PERIC, M.: *Computational methods for fluid dynamics*, Springer, 1996

Influence of shape variation on hydrodynamic damping of rigid body motion

Henry Piehl[*], Jens Höpken[†], Ould el Moctar[‡]

1 Introduction

Objective of this text is to present an estimation technique for predicting the roll damping coefficients of a ship hull and to outline the numerical tools and procedures used in this study. To show the dependency of the damping coefficient from the shape of a ship hull the new methods are applied on a two dimensional test case.

The term *roll damping* defines the loss of motion energy of a ship rotating about its longitudinal axis due to viscous flow effects. In general the viscous damping forces acting on a ship hull are small compared to the pressure or inertia forces. But for the roll motion of a ship the uprighting moment and the inertia is considerably smaller. This leads to an oscillating (rolling) system which is easily excited by the sea state, exhibits large motion angles and is only slightly damped.

In order to improve the safety of ships it is essential to understand the working principles of roll motion and thereby find ways to predict and increase the roll damping of ships.

There exist three common test methods with which the roll damping behavior of a ship can be measured. Aside *roll decay* test and *restrained forced moments* test (see Blume [2]) a third test method is the *forced motion* test. This type of test has the great advantage that the input variable (roll angle) and the constant test parameter (roll period, roll amplitude, roll axis) can be controlled precisely and that the reaction moment can be measured in a fairly straight forward manner.

Simulating a forced roll motion has another advantage over simulations accounting for the free roll decay: Only the Navier-Stokes Equations has to be solved. Since the motion of the hull is predefined, neither a fluid-body interaction routine nor a rigid body motion equation has to be implemented into the solving process.

Motivation and background for this study is the project MatRoll, which is part of the joint research project BestRoll [1]. The main objective of this project is the development a prediction method for the roll damping of modern ship forms. The project includes a large number of numerical simulations as well as experimental model tests for several different ship types and their hull shape variations. The results obtained from these simulations build a hydrodynamic data base that is used as an input for various system identification methods and statistical models.

The aim is the development a mathematical model that is able to predict the roll damping coefficients of a modern hull during the design phase. Such models do already exist, but do not capture modern hulls appropriately and do not account e.g. for non linear effects (cp. Ikeda et al. [4]).

The number of simulations, the size of the data base and the amount of memory requires a framework within which test setup, computation and analysis can be executed with a high degree of automation. This demand defines the secondary objective of this study: to implement and test an efficient simulation framework.

---

[*] henry.piehl@uni-due.de, University of Duisburg-Essen, Duisburg, Germany

[†] jens.hoepken@uni-due.de, University of Duisburg-Essen, Duisburg, Germany

[‡] ould.el-moctar@uni-due.de, University of Duisburg-Essen, Duisburg, Germany

2 Case Setup

2.1 Model Assumptions

The simulation of a roll damping test requires several model assumptions. The first and major constraint is the use of a two-dimensional mesh. This fact means that turbulent effects and vortex transport are at least questionable. Furthermore the 2D setup does not allow a forward ship speed, hence all simulations are done with zero ship velocity.

2.2 Geometry

Fig. 1 outlines the general geometrical layout used for a forced motion simulation. During the test procedure, the hull oscillates around a fixed roll axis and the reaction moment generated by fluid forces is sampled. The base shape of the hull is a quadratic box, with its bearing located in the center of the box, that in turn is fixed on height of the initially undisturbed free surface. The hull has a design edge length of 20 m and is simulated at a model scale of $\lambda = 20$.

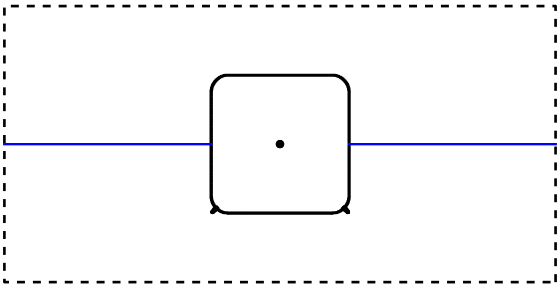

Fig. 1 Geometric setup: −− domain boundary, − hull, − waterline, • roll axis

2.3 Simulation Setup

The ship hull is assumed to be a rigid body, moving according to a prescribed motion. The motion is defined by its position and velocity. Since all three degrees of freedom, except for the rotation are locked, the equation of motion is reduced to one dimension. The forced roll motion is described by an equation of a simple sinusoidal shape, that solely depends on the maximal roll angle $\hat{\phi} = 10\,^\circ$ and the angular frequency $\omega = 2\pi/T_{\mathrm{roll}}$ with $T_{\mathrm{roll}} = 5\,\mathrm{s}$, reading:

$$\phi\left(t\right) = \hat{\phi}\sin\left(\omega\, t\right)\frac{1}{1+e^{-\delta\left(t-t_0\right)}} \tag{1}$$

For stability reasons during the initial simulation phase, a sigmoid function is used to successively blend the sinus function to its full extend.

$$\begin{aligned}\dot{\phi}\left(t\right) \;=\; \hat{\phi}\Bigg[&\frac{\omega\cos\left(\omega\, t\right)}{1+e^{-\delta\left(t-t_0\right)}}\\ &+\frac{-\delta\sin\left(\omega\, t\right)\left(e^{-\delta\left(t-t_0\right)}\right)}{\left(1+e^{-\delta\left(t-t_0\right)}\right)^2}\Bigg]\end{aligned} \tag{2}$$

The blending time and rate can be configured by t_0 and δ. Since it is necessary to define the motion state of the rigid body by parametric equations, an additional equation for the rotation velocity is required by the case setup (eq. (2)).

3 Methods

3.1 Parametric Geometry

By variating the hull shape systematically, the influence of the hull shape on the damping behavior can be investigated. The OpenFOAM mesh generator described in section 3.3 requires the geometry to be present in the STL format. In order to generate these files efficiently, a Python routine was written, which allows to define a parametric geometry and export the data into the STL format.

In a first step, the dimensions of the geometry are defined. Depending on these measures, the vertices are generated accordingly and are connected either by straight lines or bezier splines. To obtain a surface rather than a line, these 2D line segments are finally extruded into the third dimension and tessellated with triangles.

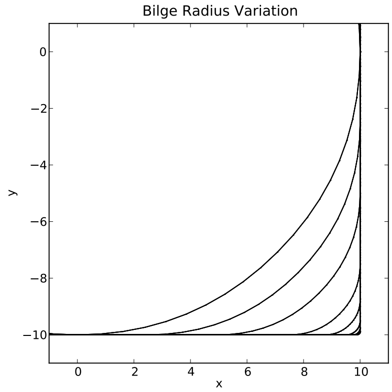

Fig. 2 Bilge radius variation

The outlines of the lower right bilge radii for all variations are shown in Fig. 2. The bilge radius was variated from $r_b = 10\,\mathrm{m}$ (perfect circle) down to $r_b = 0\,\mathrm{m}$ (quadratic box). In a second sequence, a bilge keel was introduced and attached to the hull with a constant bilge radius of $r_b = 2.5\,\mathrm{m}$.

The length of the bilge keel l_b was variated in nine steps between 0.1 m and 0.9 m. Fig. 3 shows the hull with three different bilge keel lengths.

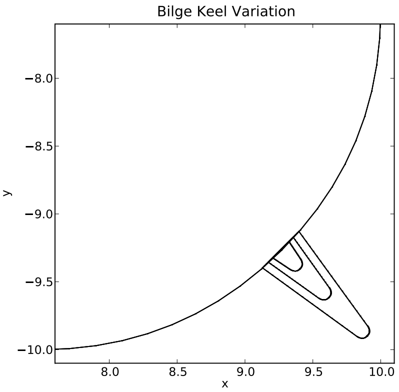

Fig. 3 Bilge keel variation

3.2 Numerical Method

The used solver is derived from the known OpenFOAM solver `interDyMFoam`, that solves the Reynolds Averaged Navier-Stokes (RANS) equations for two incompressible, inmiscible, isothermal fluids on a finite number of control volumes. A *PISO* algorithm is employed for the pressure-velocity coupling and the used turbulence model is a k-ω-SST model.

The two phases are handled by the Volume-of-Fluid (VOF) method Hirt and Nichols [3] which introduces an additional transport equation for the volume fraction α. This volume fraction represents the relative filling of a cell with water and can hence only be $\alpha \in [0, 1]$. Consequently, the interface between both phases is located in partly filled cells with $\alpha \in]0, 1[$. Rusche [5] used an artificial compressibility term to reduce the smearing of the interface:

$$\frac{\partial \alpha}{\partial t} + \nabla (\alpha \mathbf{u}) + \nabla (\alpha (1 - \alpha) \mathbf{u}_r) = 0 \qquad (3)$$

The motion of the hull is prescribed by Eq. (1) and (2) and implemented as a rigid body motion. In order to realise the motion of the hull, a mesh morphing algorithm is employed. To ensure a sufficiently high cell quality near the hull, even at large displacements, a blending function is used. In principle, this function is a Radial-Basis-Function (RBF) and defines if and how the nodes are moved. Near the hull, all nodes are moved according to the motion of the hull. At the outer boundaries, all points are fixed in space and in between these regions, the nodes are displaced to compensate the hull motion.

3.3 2D FVM mesh

Although OpenFOAM is a CFD code for arbitrarily unstructured 3D finite volume meshes, it is possible to perform 2D simulations as well. Therefore one cell in the planar direction must exist and special boundary conditions need to be applied.

The mesh itself is generated by the means of OpenFOAM utilities and three major steps are required. Firstly a hexahedral background mesh, consisting of one cell in planar direction is generated using `blockMesh`. In order to improve the cell quality of the final mesh, square cell cross sections of the cells near the hull are essential.

After the background mesh is generated, the actual geometry is discretised by `snappyHexMesh` and custom refinements are employed to compensate for the motion of the cells around the free surface, due to the mesh morphing. As `snappyHexMesh` splits the background cells in all three spatial directions, a transverse patch has to be extruded in the final step, in order to ensure that only one cell in planar direction exists.

The computational domain has transverse length of 8B, a vertical height of 6B, a thickness of 1 m and consists of roughly $150 \cdot 10^3$ cells. The majority of the cells is located around the hull as well as around the free surface area and the bilge keels (see figures 4 to 6).

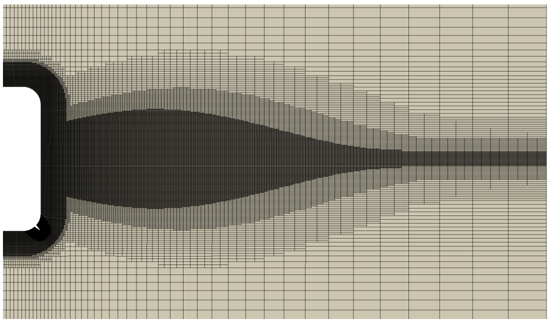

Fig. 4 Mesh refinement zone for mesh deformation

3.4 Runtime Data Processing

As outlined in section 1, an extensive matrix of simulations has to be dealt with. In order to

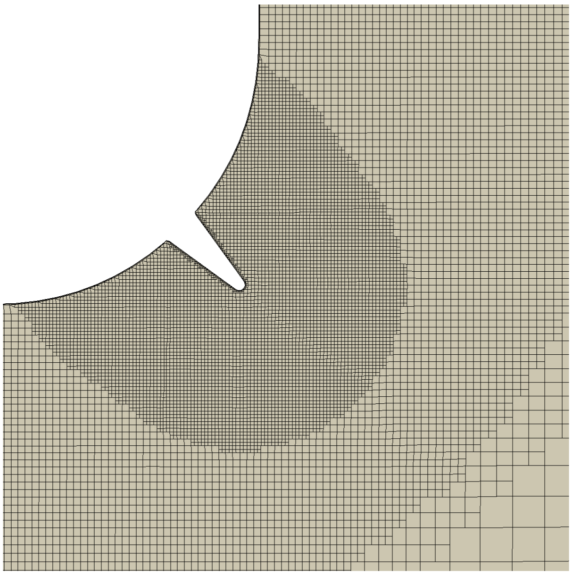

Fig. 5 Mesh refinement zones

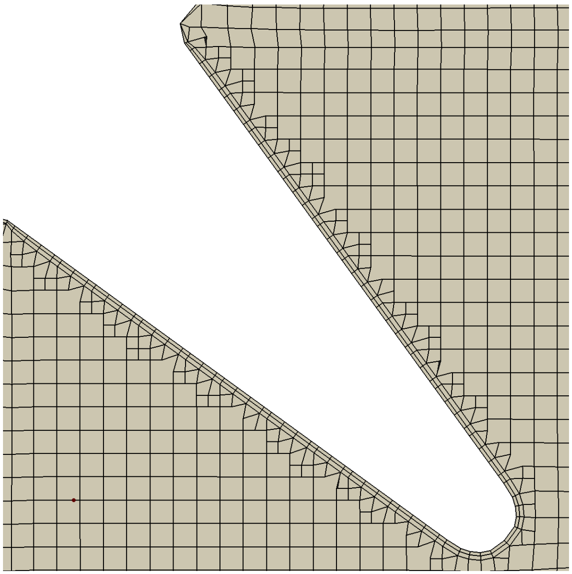

Fig. 6 Mesh around bilge keel with prismatic boundary layer

suffice the demands of the planned mathematical model in terms of input parameters and to distinguish between the contribution of different appendages and the hull itself to the damping, the flow fields have to be saved at a fairly high sampling rate. Writing the entire field, or even a small subset of it, at that rate would result in a significant memory overhead.

To avoid that, a `functionObject` was developed, that samples all relevant fields on the hull as well as on the appendages at a much higher frequency as it could be done for the entire flow fields. The data is stored in the VTK format. The fields are namely, p, α and the stress tensor τ.

3.5 Time Series Analysis

During the simulation, the rigid body was moved according to the roll angle and the velocity (see Eq. (1) and (2)). The motion of the body induces a reaction moment of the surrounding fluid.

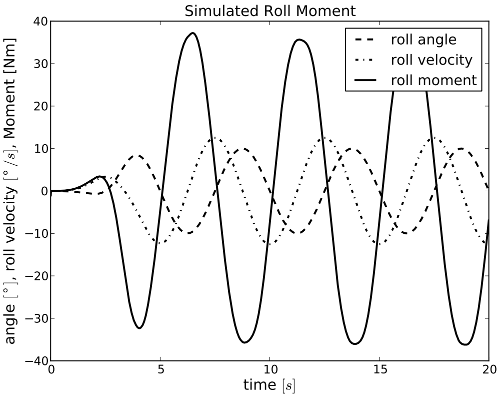

Fig. 7 Roll angle, roll velocity and resulting moment with ramp function

Fig. 7 shows the time series of a complete simulation. The increasing amplitude during the first seconds of simulation is the result of the blending function. For the analysis of the damping coefficients, the first two roll periods are omitted, in order to to only include the roll periods where a harmonic state is reached.

In order to extract the roll damping coefficient from the time series, an analytical equation for the roll motion is formulated (see Eq. (4)). Since the simulations employ a fixed roll axis, Eq. (4) is similar to the one dimensional Abkowitz type differential equation for roll motion.

The left side of the equation is a 2nd order Newton equation with terms for the fluid inertia (the formulation uses a zero mass inertia for the rigid body since the acceleration of the body is forced as well), the damping moment and the hydrostatic uprighting moment. The single term on right hand side of the equation defines the time dependent roll moment.

$$\underbrace{I_{\text{fluid}}\ddot{\phi}}_{\text{inertia}} + \underbrace{\mathrm{B}\dot{\phi}}_{\text{damping}} + \underbrace{\Delta\mathrm{GZ}\left(\phi\right)\phi}_{\text{hydrostatic}} = \underbrace{\mathrm{M}_{\phi}\left(t\right)}_{\text{roll moment}} \qquad (4)$$

As already mentioned in section 1, the case setup for the simulation of forced roll motion has a great advantage over the one for roll decay tests.

Due to its sole degree of freedom, the ODE (cp. Eq. (4)) is reduced to a simple algebraic equation by overriding the free variable ϕ with the given equations (5a) and its derivatives (5b) and (5c).

$$\begin{aligned} \phi(t) &= \hat{\phi}\sin(\omega\, t) && (5a) \\ \dot{\phi}(t) &= \hat{\phi}\omega\cos(\omega\, t) && (5b) \\ \ddot{\phi}(t) &= -\hat{\phi}\omega^2\sin(\omega\, t) && (5c) \end{aligned}$$

Inserting Eq. (5a) to (5c) into Eq. (4) leads to the following algebraic equation:

$$\begin{aligned} -I_{\text{fluid}}\hat{\phi}\omega^2\sin(\omega\, t) &+ \mathrm{B}\hat{\phi}\omega\cos(\omega\, t) && (6) \\ &+ \Delta\mathrm{GZ}\hat{\phi}\sin(\omega\, t) = \mathrm{M}_{\phi}(t) \end{aligned}$$

By subtracting the hydrostatic uprighting moment, Eq. (6) can be further simplified, giving Eq.(7). The uprighting moment depends on the $GZ(\phi)$ (see figure 8), which is calculated based on the hull geometry, draft and roll angle.

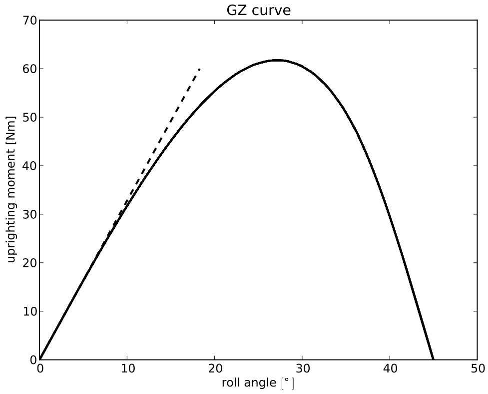

Fig. 8 GZ curve for a hull with 2.5 m bilge radius

Inside the interval $\phi \in [0°, 10°]$, $GZ(\phi)$ is of an almost linear shape. Due to the sinusoidal excitation, the resulting hydrostatic moment is itself sinosodially shaped. The final equation (7) states the dynamic moment and contains only two unkowns: the coefficient I_{fluid} due to the fluid inertia and B the roll damping coefficient.

$$\begin{aligned} &-I_{\text{fluid}}\hat{\phi}\omega^2\sin(\omega\, t) \\ &\quad +\mathrm{B}\hat{\phi}\omega\cos(\omega\, t) = \mathrm{M}_{\text{dyn}}(t) && (7) \end{aligned}$$

These unkowns can be calculated by using Eq. (7) as an ansatz function for a least squares fit on the M_{dyn} time series. The property that the velocity and acceleration terms in (7) are phase shifted by 90° enables the least squares method to calculate a unique solution for the coefficients. Fig. 9 shows the simulated roll moment, the harmonic components and a synthesized roll moment which is the simple superposition of the three harmonic components.

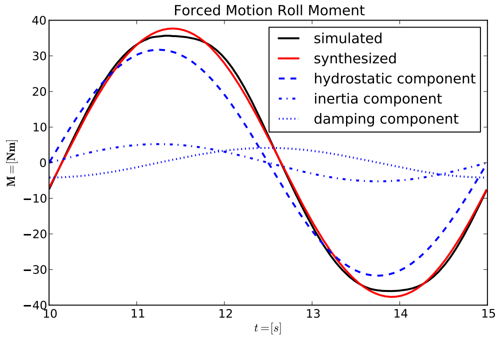

Fig. 9 Simulated and synthetic roll moment and its sinoidal components

The procedure to calculate the roll damping can be summarised as follows:

1. Transform time series from adaptive time step to a uniform sample rate.
2. Smooth time series to filter high frequency error.
3. Downsample time step.
4. Select time interval of one roll period.
5. Calculate time series of hydrostatic moment.
6. Subtract hydrostatic moment from simulated moment.
7. Apply least squares fit to dynamic moment.

4 Results

Fig. 10 and 11 show the results of the time series analysis. The resulting coefficients are plotted against the shape variations of the bilge radius and the bilge keel length. The results show the expected damping behavior and confirm that smaller bilge radii and longer bilge keels generate larger damping coefficients. The coefficient calculated for the rolling hull with the perfect circular shape show nearly zero inertial effects as one would expect.

It can be observed, that increasing the bilge keel length results in a strongly non-linear increase of the damping coefficient.

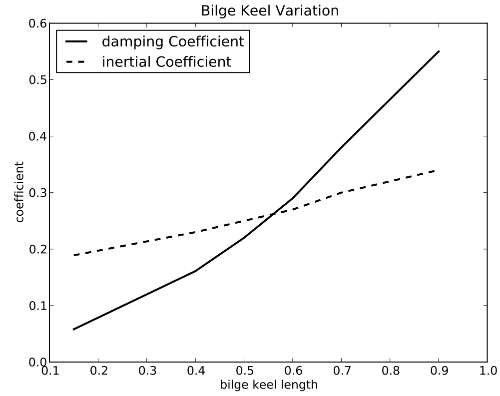

Fig. 10 Damping coefficients for bilge length variation

Two other effects can are noticeable: Firstly an increase of the bilge keel length is more effective than the variation of the bilge radius. And secondly the bilge keel must have a certain length to become effective. Otherwise a shadowing effect of the bilge radius surpresses the damping effect of the bilge keel.

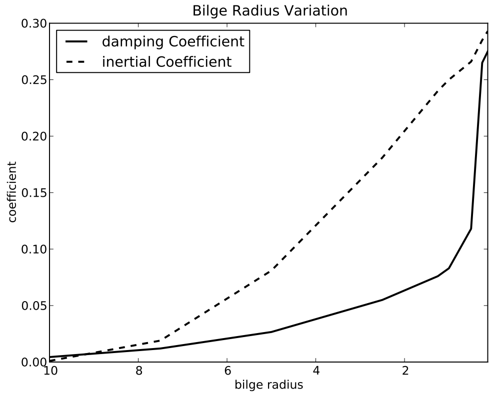

Fig. 11 Damping coefficients for bilge radius variation

In order to investigate the reason for the different damping coefficients B, a plot of the reaction moment over the simulation time is shown in figure 12. The data is obtained from simulations of all bilge keels, attached to a hull with a bilge radius of 2.5 m. It can be concluded, that the higher damping coefficients are not due to a higher maximal moment but from a broader peak.

Fig. 13 shows the difference between simulated and analytical roll moment, calculated by Eq. (7). The shape of the difference between the synthesized and simulated roll moment has the shape of a 2nd harmonic mode which can be correlated to a ϕ^3 term which is often used in nonlinear roll damping equations.

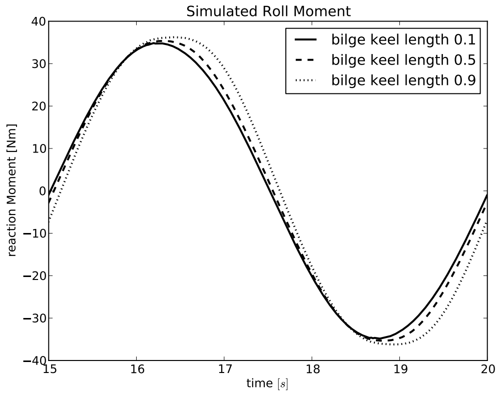

Fig. 12 Roll moment for various bilge keel lengths

In comparison to the RANS simulation, Eq. (7) leads to an overestimation of the maximum damping moment and a smaller underestimation of the damping moment's broadness.

An exemplary view on the area around the bilge keel, right after passing one of the rotation's dead centre is shown in figure 14. A large vortex, shedding from the tip of the bilge keel can be observed. In this type of simulation, these vortexes stay visible for a significant amount of time. In reality, these vortexes are transported downstream, due to the forward speed.

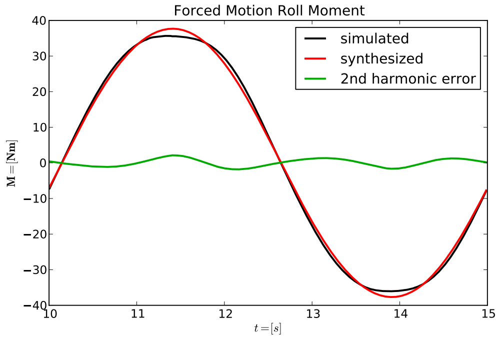

Fig. 13 2nd harmonic mode indicates higher order damping term

5 Conclusions

The simulations showed that the effect of a smaller bilge keel radius is not as significant as a longer bilge keel is. A longer bilge keel does not increase the maximum reaction moment, but broadens the shape of it over time.

However, all conclusions have to be reinvestigated for a full ship with forward speed, as the ship's velocity influences the roll damping considerably.

The developed simulation and postprocessing

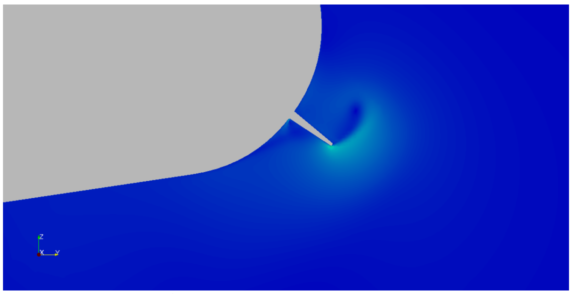

Fig. 14 Detail of the velocity magnitude around the bilge keel

framework has proven to work as designated and can be applied to the systematic simulation of complete hull shapes.

Acknowledgements

This study is supported by the project BestRoll which is part of the BMWi development program “Schifffahrt und Meerestechnik für das 21. Jahrhundert”

References

[1] Project bestroll. URL `www.tu-harburg.de/roll-damping.html`.

[2] P. Blume. Experimentelle Bestimmung von Koeffizienten der wirksamen Rolldämpfung und ihre Anwendung zu Abschätzung extremer Rollwinkel. *Schiffstechnik*, (26), 1979.

[3] C.W. Hirt and B.D. Nichols. Volume of Fluid (VOF) Methods for the Dynamics of Free Boundaries. *Journal of Computational Physics*, 39:201–225, 1981.

[4] Y. Ikeda, Y. Himeno, and N. Tanaka. A prediction method for ship roll damping. Technical report, Department of Naval Architecture, University of Osaka Perfecture, 1978.

[5] Henrik Rusche. *Computational Fluid Dynamics of Dispersed Two-Phase Flows at High Phase Fractions*. PhD thesis, Imperial college of Science, Technology and Medicine, London, 2002.

Investigations for Wake Field of Single-Screw and Twin-Skeg Container Ships in Model and Full-Scale by Unstructured Grid based RANS Solver

Nobuaki SAKAMOTO[†], Yasutaka KAWANAMI[†] and Shotaro UTO[†]
[†]National Maritime Research Institute, Mitaka, TOKYO 180-0004 JAPAN
sakamoto@nmri.go.jp, kawanami@nmri.go.jp, uto@nmri.go.jp

1. Introduction

In designing surface vessels with better propulsive efficiency, ships' wake field near propeller plane is of the great interest. Leveraging viscous computational fluid dynamics (CFD) simulation as a tool to estimate the wake characteristics, there are two approaches, i.e. 1) model-scale based estimation, and 2) full-scale based estimation. In 1), resistance and self-propulsion simulations are performed in model-scale, and attentions are paid to wake distribution and self-propulsion factors, e.g. thrust deduction factor 1-*t*, effective wake factor $1\text{-}w_T$ and relative rotative efficiency η_R. It is well-known that the wake distribution, 1-w_T and propeller open water efficiency η_o are subjected to scale effect, and thus several scaling methods have been proposed (ITTC 2011). In 2), resistance and self-propulsion simulations are performed in full-scale, and wake distribution and 1-w_T can be calculated without scaling.

National Maritime Research Institute (NMRI) in Tokyo JAPAN has been investigating twin-skeg ships with an electrical propulsion system supported by two off-centered podded propulsors (Sasaki 2010). Although the initial building cost for such ships is relatively higher than a conventional single-screw ship, there are several advantages in connection to ship's resistance and propulsive performance: 1) propeller loading of a twin-skeg ship is almost half of a single-screw ship which can contribute to improve η_o; 2) off-centered podded propulsion system makes it possible to search optimal location to minimize 1-w_T as well as to maximize hull efficiency η_H. In order to verify whether newly designed twin-skeg ship has these advantages or not, it is efficient to perform complementary study between experiment and viscous CFD simulation. In the meantime, the scale effect in the wake distribution and 1-w_T for twin-skeg ships must be investigated since it is open-to-question that the existing scaling criteria can be applicable for twin-skeg ships since some of them are based on empirical database of single-screw ships.

Based on these backgrounds, there are two objectives in the current research; 1) examine the capability of unstructured grid based viscous CFD solver, SURF ver.6.44 developed at NMRI (Hino 1997) to simulate flow around single-screw and twin-skeg ships in model and full scale; and 2) investigate the wake and its scale effect for a twin-skeg ship in model and full-scale. At the beginning, resistance and self-propulsion simulations are performed with single-screw container ship (Sydney Express) in model and full-scale, and results of wake distributions are compared with the experimental data provided by the courtesies of Hamburg Ship Model Basin (HSVA) to confirm accuracy of the CFD solver. Then, the similar simulations are performed with twin-skeg container ship (MS791), and the results from model-scale simulations are compared with the available experimental data (Sasaki 2010). In the mean time the scale effect in the wake field is investigated using the results from model and full-scale simulations.

2. Computational Method

The governing equations are the continuity equation and Reynolds-averaged Navier-Stokes (RANS) equation. They are non-dimensionalized by fluid density ρ, the fluid kinematic viscosity ν, the characteristic length which is equivalent to L_pp, and the characteristic velocity U_0 which is equivalent to the ship speed relative to the water. Spatial discretization for the governing equations is accomplished using a cell-centered finite volume method with unstructured grids. Artificial compressibility approach (Chorin 1969) is utilized for velocity-pressure coupling. The turbulence is modeled by modified Spalart-Allmaras (MSA) one-equation model (Spalart and Allmaras 1994; Hirata and Hino 2000) without wall function. The free surface is modeled by single-phase level-set method.

The presence of rotating propeller is represented by simplified body-force model based on an infinitely bladed-propeller theory. In the model, the propeller is approximated as an actuator disk, and the body force distribution on the disk is calculated by a simplified propeller theory in which a propeller thrust and torque are determined from the information of the propeller inflow velocity vector and operating conditions.

The inviscid fluxes in momentum transport equations are evaluated by the 2nd-order upwinding scheme based on the flux-difference splitting of Roe (Roe 1986). In turbulence and level-set transport equations, the convective fluxes are evaluated by the 1st-order upwinding scheme. Viscous fluxes appeared in momentum and turbulence transport equations are evaluated by the 2nd-order central differencing scheme. Temporal discretization is accomplished using 1st-order Euler backward differencing scheme with fully implicit manner. The discretized equations are solved by the multi-color symmetric Gauss-Seidel method. The code is parallelized utilizing OpenMP®, and all the simulations presented in this article are carried out by a shared-memory type workstation with 12 CPU cores (Interl Xeon® E5530 2.40GHz).

3. Simulation Design

3.1 Geometry and test case

Two hulls are of the interest in the current study. Sydney Express is a conventional single-screw container ship (C_B=0.616) with rudder, and there are measurement data (Kux et al. 1982) as well as computational results in model and full scale (Schweighofer et al. 2005). MS791 is a twin-skeg container ship (C_B=0.656) with podded propulsion system investigated by NMRI, yet the bare hull is considered in the current study. Table 1 summarizes the present test cases together with the available validation data.

Table 1 Test cases

#	(Fn, Rn)	Simulation type*	Total # of cells	Validation data
Sydney Express				
1.1	0.0, 1.245×10^7	R	2.0M (half)	Nominal wake
1.2	0.0, 1.859×10^9	R, S.P.	4.0M (both)	Total wake, propeller rps
MS791				
2.1	0.235, 7.48×10^6	R, S.P.	1.3M (half)	Nominal wake, self-prop. factors
2.2	0.0, 7.48×10^6	R, S.P.	3.8M (half)	N/A
2.3	0, 1.70×10^9	R, S.P.	3.8M (half)	N/A

*: R=Resistance simulation, S.P.=Self-propulsion simulation

3.2 Computational setup

Figures 1a and 1b show the computational grid in the stern vicinity. Both grids have multi-block topology (C-H/H-O hybrid type for Sydney Express, O-O/H-O hybrid type for MS791), and all the blocks consist of hexahedra cells without hanging nodes. The total number of cells is approximately 1.3M to 4.0M, and the minimum spacing normal to the wall is calculated as was done by Hirata and Hino (2007) which provides y^+~1.03. Figure 1c is the propeller locations for MS791 self-propulsion simulation in model-scale. Eight locations are of the interest to search the propeller location which provides minimum $1\text{-}w_T$ and the asterisk represents the optimal location found by model scale experimental (Sasaki 2010) and computational results (Sakamoto et al. 2011). This location is also utilized to perform self-propulsion simulation in full-scale.

All the simulations are performed at full-load and even-keel condition. The effect of free surface is ignored except #2.1. Instead of considering free surface, the model-ship correlation allowance (ΔCf) is made use of to take wave making resistance into account in which the values are obtained from the experiments (Ukon 1991; Sasaki 2010). In the current full-scale cases, the surface roughness is not considered. Propeller rotates clockwise observed from stern for both Sydney Express and MS791. The self-propulsion point is set to ship-point in the model-scale computation and experiment.

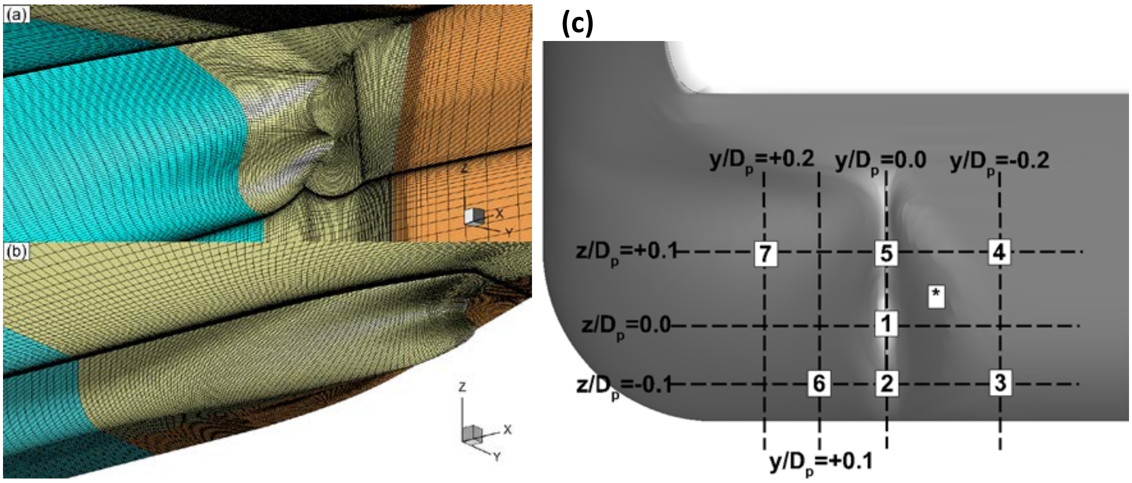

Figure 1 Grids and propeller location: (a) Grid for Sydney Express,(b) Grid for MS791, (c) Propeller location for MS791 model-scale simulation/experiment

4. Results

4.1 Sydney Express

Figure 2 shows the computational and the experimental results of nominal wake and total velocity distributions in model and full-scale, respectively. Both computational results agree well to the experimental data. In the nominal wake of model-scale, the computational result shows hook shape due to separated flow from the stern larger than the experiment which is likely due to the model constant used for rotational correction in the turbulence model. In addition, the computational result of U~0.9 isoline tends to spread wider than the experimental result. In the total velocity distribution of full-scale, the computational result predicts the peak of maximum axial velocity larger than the experimental result, yet the simulation is able to resolve overall trends of distribution in the axial velocity well compared with experiment. In the full-scale condition, the propeller revolution per second (rps) from self-propulsion simulation is 1.60Hz which shows an excellent agreement with the rps reported during the navigation (1.63Hz). It supports the fact that the current full-scale simulation is successfully conducted and provides an accurate propeller inflow velocity.

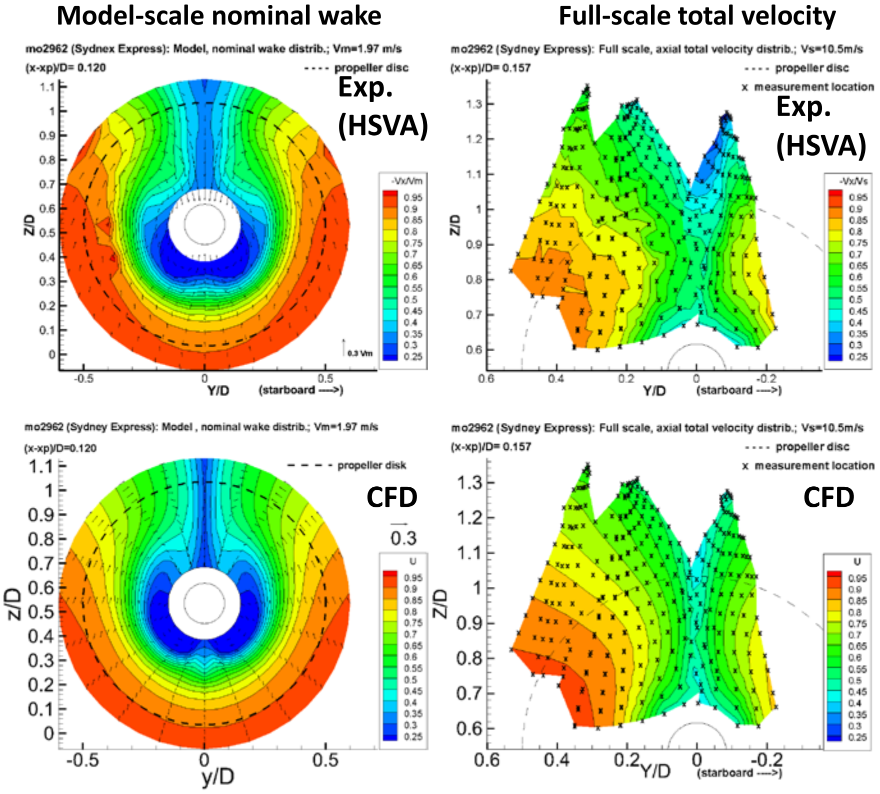

Figure 2 Comparisons of nominal wake and total velocity distribution in model and full-scale

4.2 MS791

Figure 3a present the computational and experimental results of the velocity distribution at propeller plane in model-scale. For the axial velocity distribution, the computational result reproduces the bended contour of low-velocity behind the skeg very well compared to the experiment up to U~0.8, although the U~0.9 contour becomes diffusive inside and outside of the skeg which is the similar trend to the Sydney Express. The diffusible contour line of U~0.9 inside the skeg is likely due to the vortices generated at the fore part of the ship bottom and transported to downstream. Outside of the skeg, the reason for the phenomenon is under investigation, and so far it has been figured out that the phenomenon is neither due to the order of spacial discretization scheme for convection term in turbulence equation nor the grid density. The computational result of the cross flow vector clearly shows the circulatory flow pattern rotating counter-clockwise observing from port-side stern which is due to the upward velocity component enhanced by the tunnel buttock, and these phenomena agree quite well with what observed in the experiment. Figure 3b shows experimental and computational results of 1-w_T at eight locations associated to Fig. 1c in model-scale. The computational results estimate 1-w_T very well compared to the experimental data when the center of propeller locates at the center line of the skeg, optimal location and at y/D_p=0.1. On the other hand, the results become larger than the experimental data when the center of propeller is close to the ship centerline. The experimental configuration utilizes only one propeller open water testing dynamometer at port side of the ship, while the symmetric boundary condition is applied to xz-plane in the simulation. This allows ship to have propellers on both sides which may cause the effect of propeller interference and in consequence yields such difference.

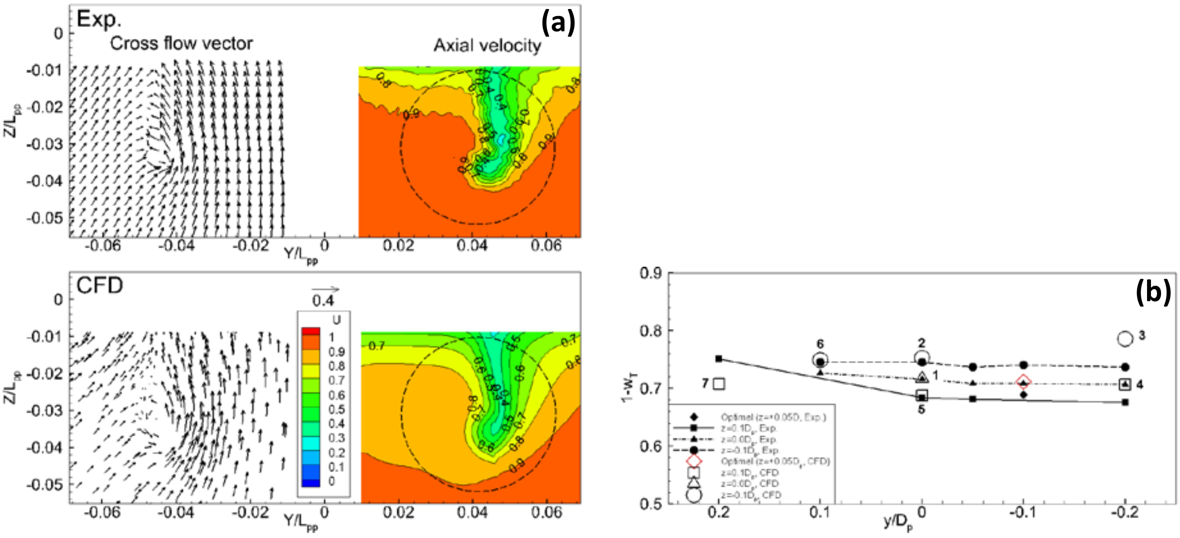

Figure 3 Nominal wake distribution around propeller plane (left) and effective wake factor at different propeller location (right) at model-scale: (a) Comparison of nominal wake distribution, Exp. vs CFD, (b) Comparison of 1-w_T at different propeller location, Exp. vs CFD

Figure 4a shows the scale effect in the axial velocity and cross flow vector together with turbulent eddy viscosity around propeller plane. Notice that model and full-scale simulations utilize the same grid. The scale effect in turbulent eddy viscosity is significant at inside the skeg tunnel especially close to the hull and upper outside of the skeg tunnel. The axial velocity profile shrinks in conjunction with the distribution of turbulent eddy viscosity. In cross-flow vector, the scale effect is likely to become most significant at (y/L_{pp}, z/L_{pp})~(0.044, -0.025). Figure 4b shows the circumferential mean velocity (CMV) distribution along radial direction and tangential velocity distribution at r/R~0.7 along circumferential direction to quantify the scale effect in circulatory flow. The CMV in full-scale becomes 23% larger than that of the model-scale at r/R~0.3, and then the difference becomes smaller down to 16%. The difference in tangential velocity distribution at r/R~0.7 can be observed at $0^o < \theta < 180^o$ which indicates that the scale effect is significant at outside of the skeg rather than inside.

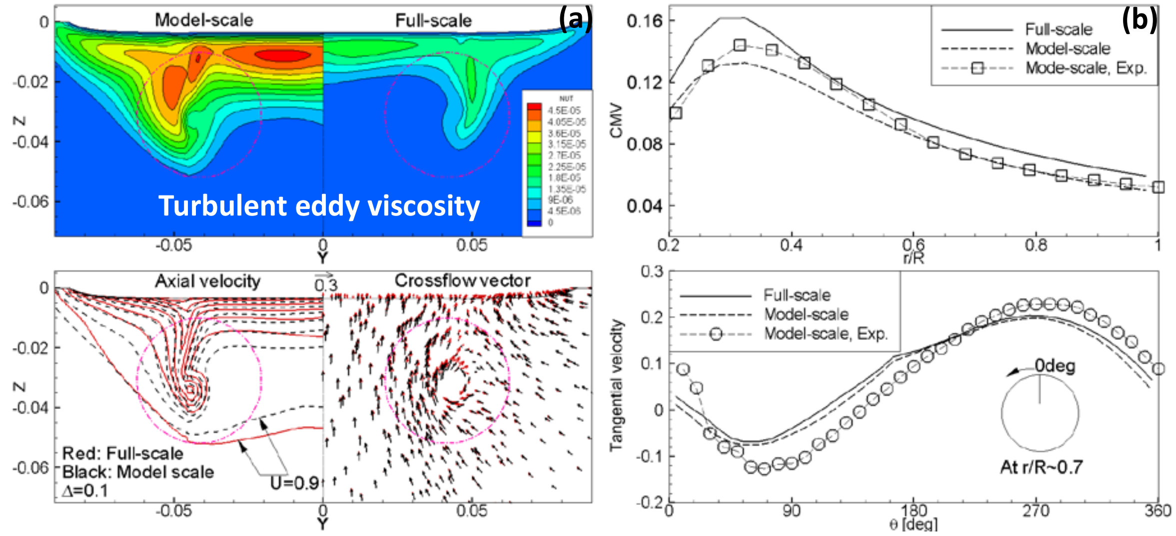

Figure 4 Scale effect in the velocity distributions around propeller plane: (a) Axial velocity distribution and cross flow vectors together with the turbulent eddy viscosity, (b) Circumferential mean velocity and tangential velocity distribution

Figure 5 shows 1-w$_T$ in full-scale obtained by three different methods, e.g. full-scale CFD simulation, Yazaki's method (Yazaki 1969) and ITTC 1978 method without rudder effect. The numbers above the bar-chart describe the difference between full-scale computational result and scaled computational/experimental results. The form factor utilized in ITTC 1978 method is brought from Sasaki (2010) and Sakamoto et al. (2011). Please notice that 1-w$_T$ in model-scale CFD and experiment are 0.71 and 0.69, respectively. The current results show that the two existing methods provide reasonably scaled results in both computational and experimental results. Yet the difference is slightly larger than the other cases when ITTC 1978 method is used. Although Yazaki's method is originated from the correlation between main particulars (Breadth/Draught) of single-screw ships, their model-scale and full-scale effective wake fraction, it could provide realistic results in current twin-skeg ship as long as half-breadth is utilized.

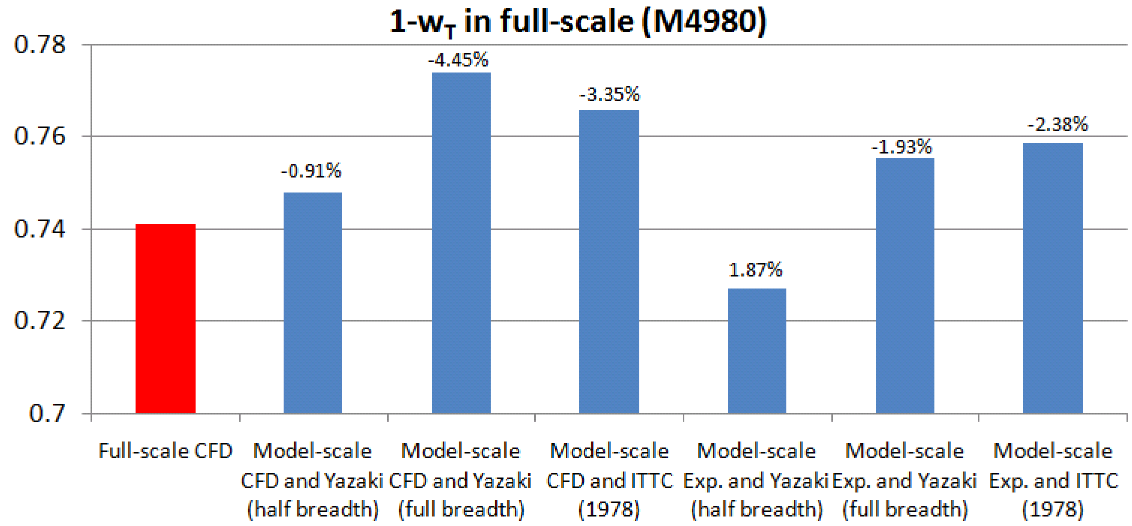

Figure 5 Effective wake scaling, Full-scale CFD vs Yazaki and ITTC 1978 criteria with model-scale computational and experimental results, numbers above the bar-charts describe the difference between full-scale computational result and scaled computational/experimental results.

5. Concluding Remarks

Resistance and self-propulsion simulations are performed for single-screw and twin-skeg container ship in model and full-scale by unstructured grid based RANS solver SURF ver.6.44. Two objectives in the present research are: 1) examine the accuracy of the code for full-scale simulation and 2) investigate the wake and its scale effect of a twin-skeg ship.

For the single-screw ship, the model and full-scale computational results agree well to the PIV/LDV measurement data as well as the propeller rps in full-scale. For the twin-skeg ship, the computational results also agree well with the experimental data, although the diffusive nature in U~0.9 must be investigated. The scale effect in circulatory flow is not negligible but is relatively localized. Two existing methods for wake scaling are utilized, and it is found that Yazaki's method with half-breadth would be acceptable for wake scaling in the current twin-skeg ship, although this is quite intuitive assumption and thus further diagnostics would be necessary using different types of twin-skeg ships. The computational cost is relatively high (for instance, approximately 48hrs to obtain converged solution in self-propulsion simulation for Sydney Express using 12cores), therefore speeding up the code (e.g. domain decomposition with MPI parallelization) would be also suggested as one of the future works. The current computational results for the twin-skeg ship are to be made use of to formulate scaling methods for nominal wake specifically for twin-skeg ships, and such research is in-progress at NMRI.

Acknowledgement

The wake measurement data for Sydney Express is provided by the courtesies of Hamburg Ship Model Basin (HSVA), and their cooperation would be greatly appreciated.

References

1. The Specialist Committee on Scaling of Wake Field, 2011, Final report and recommendations to the 26th ITTC, In: Proc. 26th International Towing Tank Conference, Rio de Janeiro, Brazil.
2. Sasaki, N., 2010, What is the best propeller for ZEUS?, In: Proc. International Propulsion Symposium, 116-123, Okayama, Japan.
3. Hino, T., 1997, A 3D unstructured grid method for incompressible viscous flows, Journal of the Society of Naval Architects of Japan, 182, 9-15.
4. Chorin, A.J., 1969, A numerical methods for solving incompressible viscous flow problems, Journal of Computational Physics, 2, 12-26.
5. Spalart, P.R. and Allmaras S.R., 1994, A one-equation turbulence model for aerodynamic flows, La Reschereche Aerospatiale, 1, 5-21.
6. Hirata, N., and Hino, T., 2000, A comparative study of zero- and one-equation turbulence models for ship flows, Journal of Kansai Society of Naval Architects, Japan, No. 234, pp.17-24.
7. Roe, P.L., 1986, Characteristic-based scheme for the Euler equations, Annual Review of Fluid Mechanics, 18, 337-365.
8. Kux, J., Niemeier, Th., Stohrmann, H., 1982, LDV-Nachstrommessungen auf der “Sydney Express”, Technische Universitat Hamburg-Harburg.
9. Schweighofer, J., Regnstrom, B., Starke, A.R. and Tzabirasm G., 2005, Viscous flow computations of two existing vessels at model- and full-scale ship Reynolds numbers – A study carried out within the European Union project EFFORT., In: Proc. International Conference on computational Method in Marine Engineering, Barcelona, Spain.
10. Hirata, N. and Hino, T., 2007, Numerical computations of ship flows in full scale, In: Proc. Computational Methods in marine Engineering, Barcelona, Spain.
11. Ukon, Y., 1991, Study on experimental prediction on ship hull vibration induced by propeller can cavitation, Annual Report of Ship Research Institute, 28, 4..
12. Yazaki, A., 1969, A diagram to estimate the wake fraction for an actual ship from a model tank test, In: Proc. 12th International Towing Tank Conference, Rome, Italy..
13. Sakamoto, N., Kawanami, Y. and Uto, S., 2011, Estimation of resistance and self-propulsion characteristics for low L/B twin-skeg container ship by unstructured-grid based RANS solver, Journal of Ship Research, under review.

Study of an Air Cavity in Water Tunnel

Abolfazl Shiri * and Rickard E. Bensow
Chalmers University of Technology, Götebory, Sweden

Michael Leer-Anderssen
SSPA AB, Götebory, Sweden

Jacob Norrby
STENA Rederi AB, Götebory, Sweden

1 Introduction

There are several methods of using air lubrication to decrease the viscous friction resistance on a ship hull. Amongst these, the choice of decreasing the area of wetted surface under the hull by implementing an air filled cavity, is the concern of this study. The optimal flow regime of interest for an air cavity concept corresponds to the stable air-water interface that attaches to the rear section of the cavity without continuously releasing the air. This method minimizes the energy loss by maintaining the air pressure inside the chamber, hence maximizing the efficiency.

Although the idea of using air lubrication dates back to the 19th century, the experiments on implementing air cavity under planing and semi-planing hulls started in the middle of the 20th century [1]. The studies on displacement ships revealed difficulties maintaining the air inside the cavity thus the efficiency of the method was questioned. Since then, the application of the air cavity in high speed boats has been more of the interest. Different experimental and numerical investigations have been performed by Matveev et al. [2] to study the characteristics of a simple stepped planing hull model in a water channel with different lengths and trims. Their investigations confirmed the theoretical limiting characteristic length defined for the cavities which form under the stepped plate (cf. Matveev [3]). An inviscid two-dimensional CFD model was verified by experimental studies of the stable and oscillating partial cavity, performed by Lay et al. [4]. The results showed high drag reduction, while considerable air flux was needed to establish a stable cavity.

The above studies suggest a characteristic length for partial cavity arrangement that limits the use of a stable cavity under a large displacement ship. For this kind of hulls the option of a full cavity that sustains the air volume with a longer distance under the hull is proposed. The depth of the cavity allows the water waves to form several wavelengths before it re-attaches to the inclined rear section of the cavity. Therefore the length of the full cavity is not theoretically limited, as long as the wave remains stable and the cavity does not collapse.

Studies of air cavity ships was initiated at SSPA in the early 1940s and there have been several investigation on this concept using ship models in the towing tank with different configurations of the cavity and geometrical parameters. The success in substantial drag reduction in high speed air cushioned vessels, raised the interest to investigate the possible application of air lubrication in the slow speed displacement vessels. Previous investigations of air film lubrication at SSPA have indicated that a large number of transverse air outlets longitudinally are required, effectively rendering the air film/micro-bubble approach impractical for large displacement ships. For such displacement vessels the area under the hull is large and to use a continuous air layer requires more energy compared to smaller vessels. The alternative method of using one or more pressurized cavities under the hull may provide a better solution. The shape and size of the hull also indicates the type of the cavity which can be used for viscous drag reduction.

Various studies have been carried out at SSPA regarding the hull shape and cavity geometry for the Stena P-MAX air project, including extensive model tests in the tank and performing series of measurements on a large 1:12 scale prototype (STENA AIRMAX) in open water. Although the results

---

*abolfazl@chalmers.se ; Tel: +46 31 772 90 69

of these studies provide some basis for full-scale hull design, a more detailed investigation was deemed necessary to exploit the physics of the air-water interface behavior and the parameters involved for the stability of the cavity. The main goal of this study is to discuss these parameters through computational and experimental investigations. To simplify the problem, an experimental investigation was proposed in SSPA's cavitation tunnel to study a single cavity inside a water tunnel. The result of the experiment complements the numerical studies of the same geometry and operating conditions.

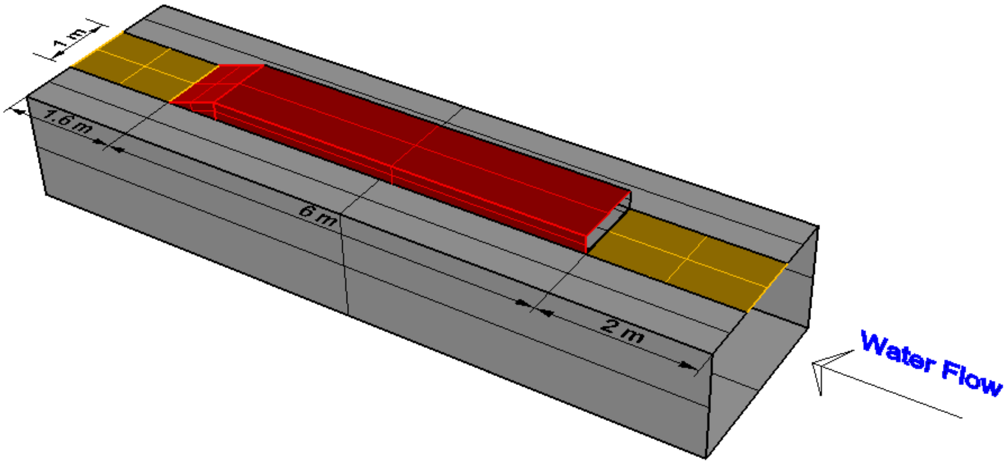

Figure 1: Schematic of the cavitation tunnel test section with the the cavity chamber.

2 Experimental Setup

In order to have more control on the parameters which dictate the formation of a stable cavity, a simple model of cavity was designed to be tested in a water tunnel. The experiment is being performed in the cavitation tunnel at SSPA, Sweden. To accommodate the cavity and experimental rig, the largest test section available with the size of $W = 2.6\ m \times H = 1.6\ m \times L = 9.6\ m$ was chosen. The model box consists of different sections: front plate, cavity box, beach plate and rear plate, which are connected to the force gauges in order to measure the drag force on different surfaces (see Figure 1). The water enters the test section through an expansion part that converts the circular cross-section into a rectangular one. The boundary layer thickness developed on the bottom and side surfaces is estimated as $\delta = 0.37 \times L \times Re^{-0.2} \approx 12\ cm$ which is far enough from the cavity box on the top surface of the test section. To provide a base for comparison, the surface friction resistance coefficient is calculated as [5]

$$C_{FM} = \frac{0.075}{(\log(Re) - 2)^2} \approx 0.0027 \tag{1}$$

which gives the surface friction resistance force for an intact test section with the size of (L=9.6m, W=1m) as $R = C_{FM} \times 1/2\rho U^2 \times S \approx 52\ N$.

The water inlet velocity and cavity length are selected to match the Froude number of $Fr = 0.26$, such that more than one wavelength is present in the cavity (in fact around 2.5 to achieve beneficiary free surface slope at the beach at the end of the cavity). This is important as we want to determine the characteristic of a long cavity, compared to a cavity formed behind a wedge in planing hulls. An inclined wall at the rear section of the cavity (beach section) allows the water to re-attach to the surface with minimum disturbances. The angle of this beach wall is adjustable together with the depth of the cavity. Air flux and drag forces will be measured for different air inlet pressure, cavity depth and beach angel. The free surface is monitored through the side windows on the test section and controlled by the air pressure and the cavity depth. The air pressure is adjusted with the air supplier connected to the front end of the cavity above the step.

3 Computational Study

The computational study was carried out using a two-phase RANS solver in OpenFOAM. The water and air phases are assumed to be immiscible, therefore the solver employed the Volume of Fluid (VOF) method to simulate the unsteady water-air interface inside the cavity. The VOF method defines a volume fraction (α_1) of each phase in the cell as the indicator of the interface hence capturing the interface shape by calculating this variable in the flow field. The advantage of VOF method to the interface fitting methods is that it can simulate more complex geometries in regions with wave breakdown, without grid regeneration (cf. Wackers et al. [6]), deemed advantageous in this setting where air may escape the cavity and we may even see a collapse with the water attaching to the cavity ceiling.

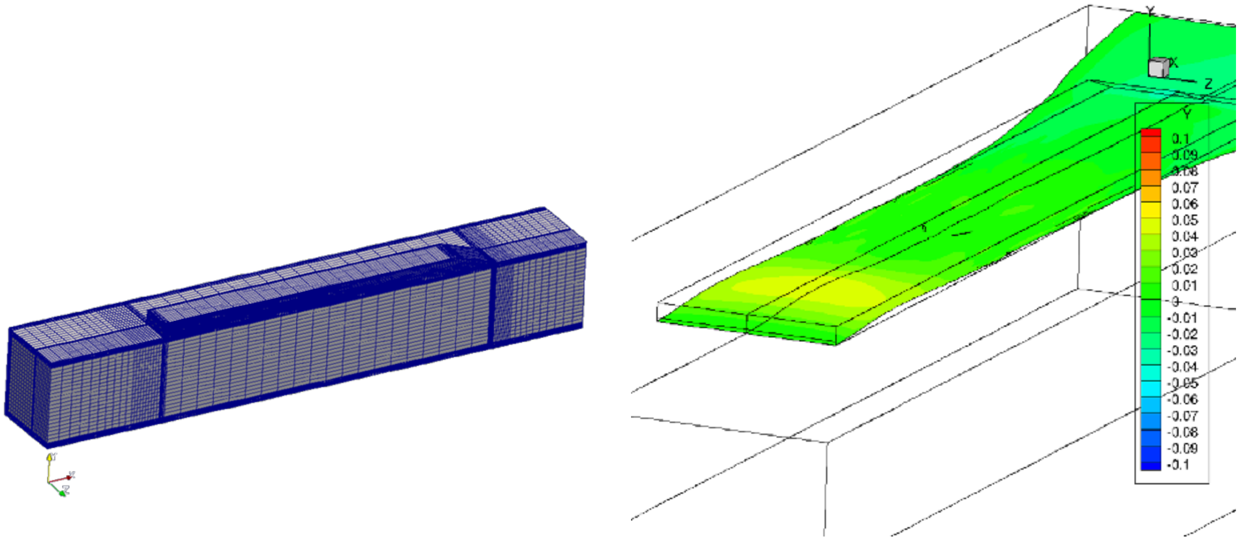

Figure 2: Left: Computational mesh used in CFD simulation. Right: Water-air interface based on $\alpha_1 = 0.5$. The surfaced is colored based on the height.

Using the same grid and boundary conditions (cf. Figure 2, left), complimentary simulations are done in FLUENT as well as OpenFOAM to compare the results of different CFD software. To decrease the number of cells in the calculation, a symmetry boundary condition is considered in the middle of the flow field. The simulation is carried out for different air inlet pressure and different cavity depth. The geometry of the computational model was based on the test model in the cavitation tunnel (see Figure 1). The transient calculation is performed following the same procedure as the experiment, i.e. the cavity is filled with air and then the water starts to flow in the tunnel. Different boundary conditions are considered for the air inlet, such as constant pressure or constant flow rate. The calculation continues until the interface between air and water reaches a stable state. The proper combination of parameters such as air inlet boundary condition should be considered, otherwise the solution never gets to a steady point; either the cavity will be filled with water or the excessive air will continuously escape the cavity (see Figure 2, right). The water free surface can be estimated based on the volume fraction of each cell and the interface is assumed to be where $\alpha_1 = 0.5$. For all the cases a constant velocity is implemented at the water inlet boundary condition.

Two important parameters to characterize the flow in the cavity are the Froude number based on the cavity length [5]

$$Fr = \frac{U}{\sqrt{gL}} \tag{2}$$

and cavitation number based on the cavity pressure:

$$\sigma = \frac{p_0 - p_c}{\rho_w U^2/2} \tag{3}$$

where L is cavity length, U is water velocity, p_c is air pressure at the cavity inlet and p_0 is the reference pressure. The transverse waves generated inside the cavity are assumed to have a wave length of $\lambda = 2\pi U^2/g$.

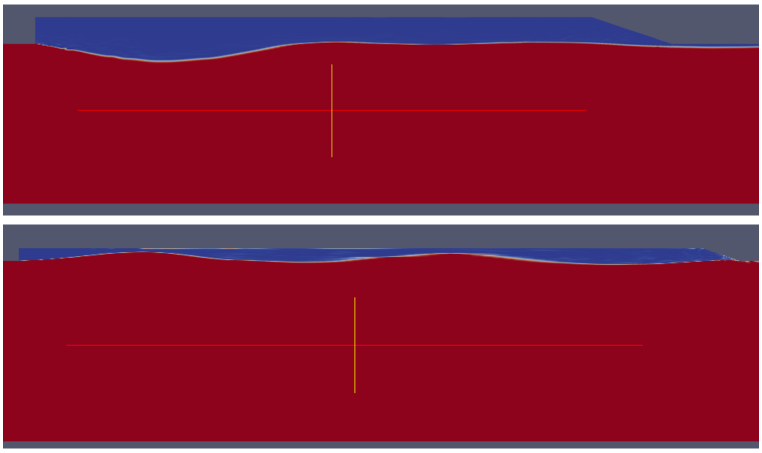

Figure 3: Water wave formation inside the cavity. The blue color indicates the air phase and the red color is water phase.

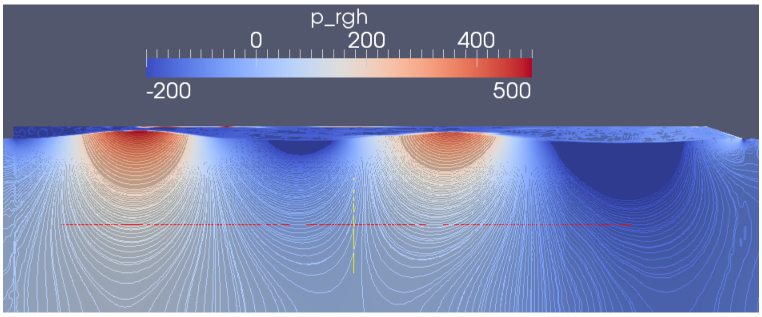

Figure 4: Relative pressure distribution. The hydrostatic pressure is subtracted from the total pressure $(p - \rho g h)$.

4 Results and discussion

Both experiments and computational investigations show that cavity pressure (p_c) plays an important role in the wave's shape and the stability of the water surface inside the cavity. The result of the CFD simulation is shown in Figures 3 and 4 for two-dimensional cases of the simulation. Figure 3 shows the water-air interface with a stable wave that re-attaches to the beach with different inlet air pressure and Figure 4 shows the relative pressure distribution in the case of lower air pressure. Different range of pressure were considered to examine the stability of the water waves in the cavity. As shown in Figure 3, above, by increasing the air pressure, the cavity starts to become unstable and the amplitude of the wave increases. The air leakage also increases and although the drag forces may decrease due to release of air, a stable condition can not be achieved due to the cavity collapse. There is a range of pressure in which the cavity becomes stable with a smooth water surface. In a lower range of the pressure the amplitude of wave increases, before water touches the ceiling and cavity collapses.

In three dimensional simulations, the water free surface has a complicated shape. As shown in Figure 5, the air escapes from sides of the cavity. The collapse in the cavity causes the water to touch the cavity roof and the air flow rate increases. Although the total horizontal drag forces may decrease considerably (see table 1) , the air is not contained in the cavity and energy loss due to air supply compensate for the air lubrication gain. Also the pressure forces on the beach section increases when the water flow over this section. The experimental investigation corresponding to these three dimensional simulations are currently being performed .

Acknowledgments

The study is supported by STENA Rederi AB and the Swedish Energy Agancy, grant 34047-1. The authors would like to thank the technical staff in SSPA AB cavitation tunnel for their support.

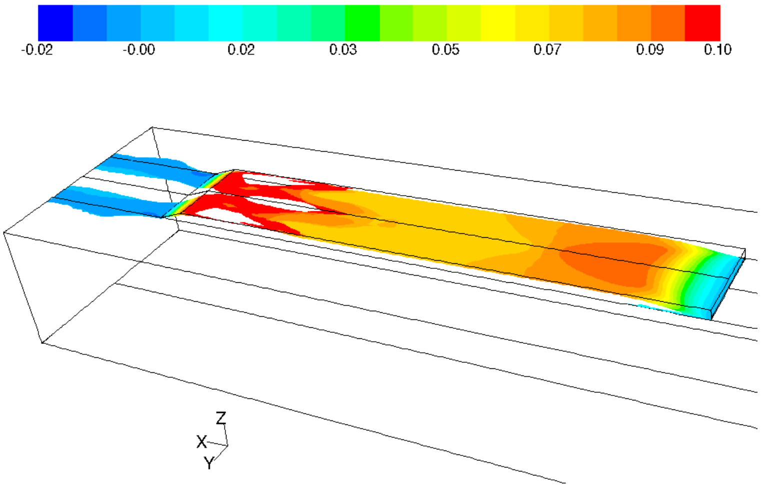

Figure 5: Three dimensional simulation with the case of constant air flow. Water-air interface based on $\alpha_1 = 0.5$ and the surfaced is colored based on the height

Section	Viscous force (N)
Beach wall	0.4
Cavity roof	2.5
Front plate	6.9
Rear plate	1.8
Total	11.6

Table 1: Horizontal viscous forces corresponding to the case shown in Figure 5. The pressure forces and the vertical forces on the beach section is not included.

References

[1] Matveev, K. I., "Two-Dimensional Modeling of the Limiting Air Cavity System," *41st Aerospace Sciences Meeting and Exhibit, 6-9 January*, 2003, Reno, Nevada.

[2] Matveev, K., Burnett, T., and Ockfen, A., "Study of air-ventilated cavity under model hull on water surface," *Ocean Engineering*, Vol. 36, No. 12-13, 2009, pp. 930–940.

[3] Matveev, K. I., "On the limiting parameters of artificial cavitation," *Ocean Engineering*, Vol. 30, No. 9, 2003, pp. 1179–1190.

[4] Lay, K., Yakushiji, R., Makiharju, S., Perlin, M., and Ceccio, S. L., "Partial Cavity Drag Reduction at High Reynolds Numbers," *Journal of Ship Research*, Vol. 54, No. 2, 2010, pp. 109–119.

[5] Larsson, L. and Raven, H. C., *Ship Resistance and Flow*, The Principles of Naval Architecture Series, The Society of Naval Architects and Marine Engineers, 2010.

[6] Wackers, J., Koren, B., Raven, H., Ploeg, A., Starke, A.and Deng, G. Q. P., Visonneau, M., Hino, T., and Ohashi, K., "Free-Surface Viscous Flow Solution Methods for Ship Hydrodynamics," *Archives of Computational Methods in Engineering*, Vol. 18, No. 1, 2011, pp. 1–41.

Development of hybrid URANS-LES methods for flow simulation in the ship stern area

N. Kornev*, A. Taranov, E. Shchukin
Chair of Modelling and Simulation, University of Rostock, 18057 Rostock, Germany

INTRODUCTION. Ship wake has strong influence on the ship performance, so it is very important to accurately determine the velocity field in the wake. From one side, the wake is responsible for the flow velocity decrease in the propeller disk, which results in the thrust increase and in the improvement of the overall propulsion efficiency. From the other side, a nonuniform velocity field causes variation of the propeller thrust in time and thus strong vibrations in the stern area. Propeller cavitation is another critical phenomenon in ship hydromechanics which is strongly influenced by the wake.

Numerical simulation of the wake has attracted the attention of CFD experts for a long time. A substantial success has been achieved in this field in the last two decades. Today, the averaged velocity field can be computed with high accuracy and the discrepancy between the numerics and the measurements is comparable with the tolerance of the experimental equipment. To get overview of the state of the art in this area, the reader is referred to contributions presented in the Gothenborg Workshop [1].

An important feature of the works done so far is the application of URANS (Unsteady Reynolds Averaged Navier Stokes) method which is capable of capturing steady effects and large scale unsteadiness. However, this technique is not able to resolve small scale flow oscillations due to large diffusivity which is an unavoidable feature of URANS closure models. These oscillations are caused by complicated vortex structures arisen due to flow separations on the hull and shedding of the boundary layer in the stern area. The time averaged vortex structure is well reproduced in URANS calculations, which is confirmed by a good agreement between the numerical simulations and the measurements of the mean velocities. Also, the time averaged fluctuation parameters like Reynolds stresses and the turbulent kinetic energy are predicted relatively well using advanced turbulent models such as the Reynolds stress models, see [2]. This allows one to accurately compute the variances of fluctuations, but not their amplitudes or spatial and temporal distributions. It can be a critical point for propeller design since flow, cavitation and thrust depend on the instantaneous spatial distributions of velocity in the incident flow.

In present practical design methods the unsteady effects are partly taken into account. The velocity vector $\mathbf{u}$ at any point $\mathbf{x}$ on the propeller blade depends on the angular position of the blade θ which itself depends on time, i.e. $\mathbf{u} = \mathbf{u}(\mathbf{x}, \theta(t))$. Unsteadiness of the propeller flow is purely due to the rotation of the propeller blade through the nonuniform time independent ("frozen") wake (see, for instance, the chapter 12 in [4]). We usually can assume that the incident flow does not explicitly depend on the time. This assumption is quite acceptable for ships with moderate block coefficients since the physical phenomena causing flow oscillations do not play a big role for such ships. However, the case of full-bottomed ships should be reconsidered. Because of the disadvantages of URANS modeling mentioned above, the most promising approach to work with such ships is Large Eddy Simulation (LES), which is already widely used for research purposes. On the contrary to other engineering fields, typical Reynolds numbers in ship hydromechanics are very large even at model scales. The grid resolution necessary for a pure LES is so huge that it makes the direct application of LES impossible. A practical solution

---

* nikolai.kornev@uni-rostock.de

of this problem is the use of hybrid URANS-LES methods, where the near body flow region is treated using URANS and far flow regions are treated with LES.

This paper presents the latest results of the development of hybrid methods for ship hydromechanics applications undertaken at the Chair of Modelling and Simulation of the Rostock University. Prediction of the unsteady wake behind the tanker KVLCC2 with the hybrid methods and the influence of the unsteady wake on the propeller thrust are considered. For the short review of the modern hybrid techniques see Kornev et al. [5].

DESCRIPTION OF THE HYBRID MODEL. Our hybrid model is based on the observation that the basic transport equations have the same form in LES and RANS

$$\frac{\partial \overline{u}_i}{\partial t} + \frac{\partial(\overline{u}_i \overline{u}_j)}{\partial x_j} = -\frac{\partial \overline{p}^*}{\partial x_i} + \frac{\partial(\tau_{ij}^l + \tau_{ij}^t)}{\partial x_j}, \tag{1}$$

but the interpretation of the overline differs. In LES it means filtering, but in RANS it stands for the Reynolds, or ensemble, averaging. Here we used the standard notation of p^* for the pseudo-pressure, and τ_{ij}^l and τ_{ij}^t for the laminar and turbulent stresses respectively. Note that the turbulent stresses are calculated in different ways in LES and URANS regions.

The computational domain in our model is dynamically (i.e. at each time step) divided into the LES and URANS regions. A cell of the mesh belongs to one or the other region depending on the relation between the integral length scale L and the extended LES filter Δ according to the following rule:

$$\begin{aligned} &\text{if } L > \Delta \text{ then the cell is in the LES region,} \\ &\text{if } L < \Delta \text{ then the cell is in the URANS region.} \end{aligned} \tag{2}$$

The integral length scale is calculated from the known formula of Kolmogorov and Prandtl with the correction factor 0.168 taken from [7]

$$L = 0.168 \frac{k^{3/2}}{\varepsilon}, \tag{3}$$

where k is the turbulent kinetic energy and ε is the dissipation rate. L varies from one time step to another, which results in varying decomposition of the computational domain into the LES and URANS regions. The extended LES filter for each cell is computed as $\Delta = \sqrt{d_{\max}^2 + \delta^2}$, where $d_{\max}$ is the maximal length of the cell edges $d_{\max} = \max(d_x, d_y, d_z)$ and $\delta = \sqrt[3]{(\text{the cell volume})}$ is the common filter width used in LES. This choice ensures that very flat cells in the boundary layer (for which $\delta \approx 0$ but $d_{\max} > 0$) are treated correctly. Δ depends only on the mesh and it is precomputed only once before the main computation.

We have implemented our hybrid approach in open source CFD software OpenFOAM and tested combinations of several LES and URANS models to find the best one. The LES models we have used are the simple and dynamic Smagorinsky models and the dynamic one equation eddy model. The URANS models used in the combinations are the linear and nonlinear k-ε, k-ω SST and $k\varepsilon v^2 f$ models. The combinations of these LES and URANS models have been applied to two test-cases — flat plate and asymmetric diffuser. The best results (in the sense of numerical stability and accuracy) have been obtained for the combination of the Smagorinsky dynamic model with the k-ω SST turbulent model and it is this combination that has been further studied and applied to the calculation of KVLCC2 tanker.

The turbulent stresses τ_{ij}^t are calculated from the Boussinesq approximation using the concept of the turbulent viscosity. The only difference between LES and URANS is the definition of the kinematic viscosity. Within LES it is considered as the subgrid viscosity and calculated according to the dynamic model of Smagorinsky:

$$\nu_{\text{SGS}} = c_D \delta^2 |S_{ij}|, \quad S_{ij} = \frac{1}{2}\left(\frac{\partial u_j}{\partial x_i} + \frac{\partial u_i}{\partial x_j}\right), \tag{4}$$

where S_{ij} is the strain velocity tensor and c_D is the dynamic constant. In the URANS region the viscosity is calculated from the k-ω SST turbulent model. The smooth transition of the turbulent viscosity between the two regions is provided by the expression

$$\nu(y) = \frac{\nu_t - \nu_{SGS}}{\pi} \arctan\left(100y - 100\right) + \frac{1}{2}\left(\nu_t + \nu_{SGS}\right), \tag{5}$$

where y is the distance from the cell to the closest wall.

NUMERICAL RESULTS FOR THE TANKER KVLCC2. The doubled model of the KRISO tanker KVLCC2 [3, 6] with the scale 1/58 has been chosen as a test object since it is a common CFD-benchmark which is widely used in the shipbuilding community [1]. The model has length of 5.517 m, breadth of 1 m, draught of 0.359 m and block coefficient of 0.8098. Study of the double model has been performed for the constant velocity of 1.047 m/s corresponding to the Reynolds number of $\text{Re} = 5 \times 10^6$. The Froude number $\text{Fn} = 0.142$ is small which makes it possible to neglect the water surface deformation effects.

Unstructured 3D-grid with 1.8×10^6 cells was generated by the Ship Model Basin Potsdam (SVA Potsdam) using ICEM CFD mesh generator. The computational grid has $y_1^+ \approx 0.1 - 4$ in the wall region of aftership and $y_1^+ \approx 10$ in the foreship area. The hybrid URANS-LES model was used with wall functions in URANS region. The computations have been carried out with fixed maximal Courant number of 0.6, which corresponds to the time step about 0.0005 s.

The central difference scheme is used for all terms in the momentum equation for the space discretization. Time discretizations was done using the Crank-Nicholson scheme. For the initialization of the flow in the computational domain the steady RANS solutions was used. To obtain the good time-averaged solutions the starting, strong unsteady, phase of the flow (wich corresponds to 3-4 ships lengths) has been deleted from the statistics. The time-averaging was done within 40-50 seconds (or 8-10 lengths of the ship).

The axial mean velocity field in the propeller plane for the KVLCC2 shown in Fig. 1 is compared with the experimental data of KRISO [6]. The axial velocity u_x is normalized to the ship model velocity u_0 and the coordinates are normalized to the length between perpendiculars of the ship model L_{pp}. The mean velocity field is very similar to the experimental one. The lines of the constant velocity have the typical form and reflect the formation of a large longitudinal bilge vortex in the propeller disk. The second longitudinal vortex is formed near the water plane, but it has a much smaller strength compared to the bilge one. Fig. 1(b) shows the resolved turbulent kinetic energy normalized to u_0^2 for both computational grids in comparison with experimental data of KRISO. Topologically, the isolines are similar to those of the axial mean velocity shown in the Fig. 1(a). The position of the area with the strongest fluctuations and the magnitudes of these fluctuations are reproduced satisfactorily, especially bearing in mind that according to [6], the uncertainty of the measured TKE is $\sim 12\%$.

CALCULATION OF THE THRUST VARIATIONS DUE TO UNSTEADY WAKE FLOW. The main task of this work is determination of the thrust variation on the propeller working in the unsteady flow. The possibility to calculate the forces and moment on the rotating propeller using the OpenFOAM was checked before the investigation of the interaction between ship and propeller. Description of the test propeller is presented in the Table 1

Number of blades	Diameter	Pitch ratio	EAR	D_{hub}	max. Skew
5	0.25	0.996	0.8	0.18	32 deg

Table 1: General propeller parameters

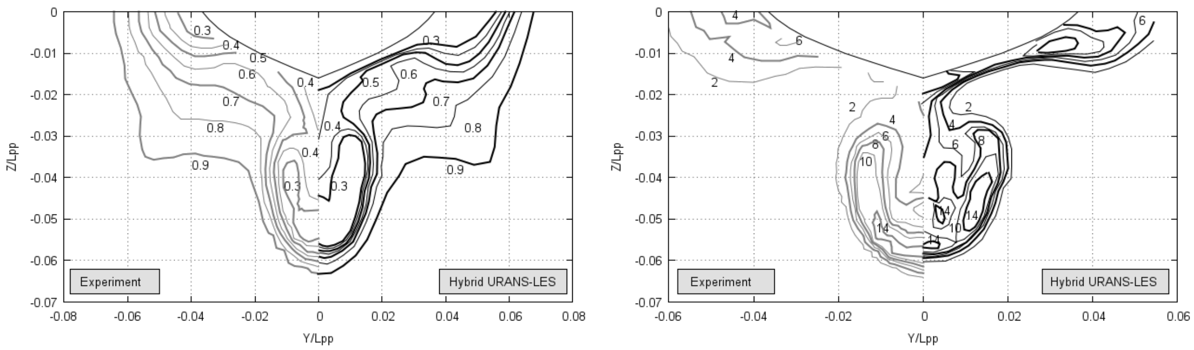

(a)

(b)

Figure 1: Mean axial velocity field U_x/U_0 (a) and normalized Reynolds stress field $R_{xx} = \overline{U_x'U_x'}/U_0^2$ multiplied with 10^3 (b) in the propeller plane of the tanker KVLCC2 at $\mathrm{Re} = 5 \times 10^6$ and $\mathrm{Fn} = 0.142$.

The grid for the propeller was generated using the snappyHexMesh-mesher provided by OpenFOAM. The grid contains 3.8×10^6 cells. Time step was about 0.0008. The open-water diagram for the propeller is showed in the Fig. 2.

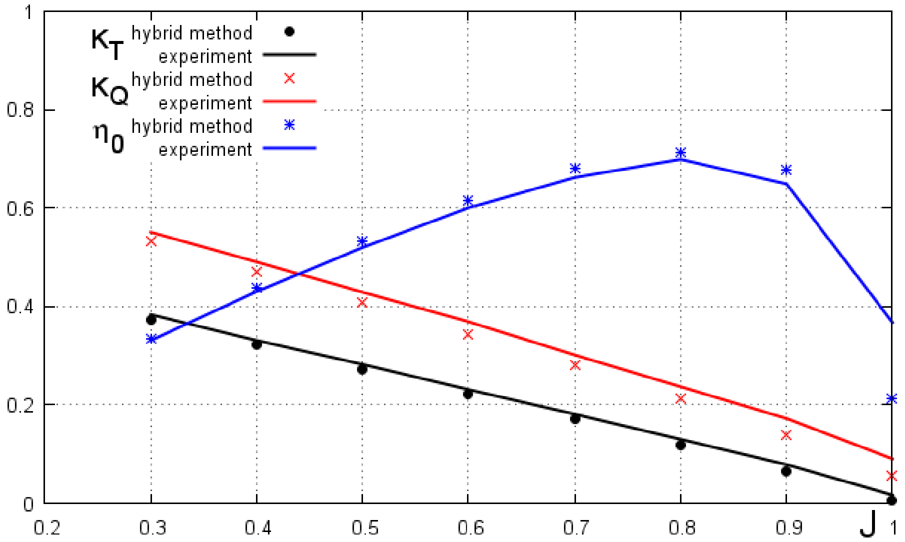

Figure 2: Open-water diagram of the test propeller comparing with measurements of SVA Potsdam

Finally we have calculated the KVLCC2 hull with rotating propeller. General grid interface (GGI) provided by OpenFOAM has been used to model the interface between stator (hull) and rotor (propeller) grids. The stator grid was generated using the Ansys ICEM software and contains about 2×10^6 cells. The rotor grid was generated using the snappyHexMesh-mesher provided by OpenFOAM and contains another 2×10^6 cells. The both grids have been successfully combined using the OpenFOAM. The combined grid is presented on the Fig. 3(a), the rotor grid is showed in yellow color. The isosurfaces of the λ_2 criterion (see Fig. 3(b)) shows vortex structures behind the propeller and strong instability of the flow behind the transom.

Fig. 4 presents the thrust on the propeller obtained from the hybrid method. The thrust vari-

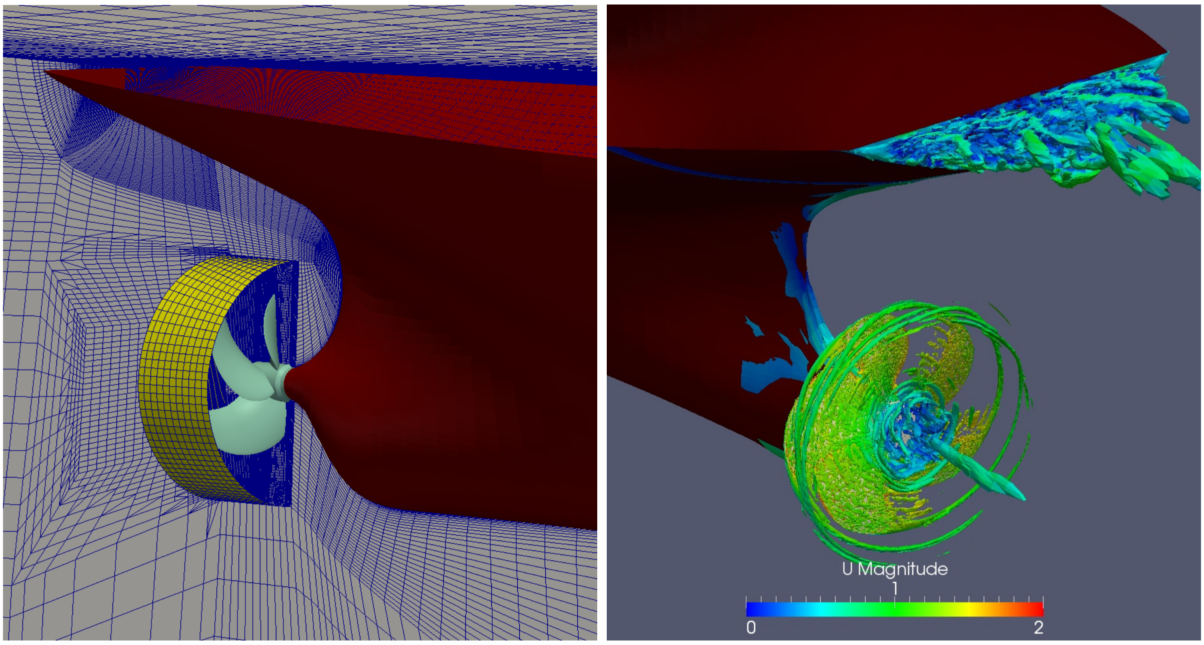

(a) (b)

Figure 3: Fragments of the computational domain (a) and isosurfaces of the λ_2 criterion in ship stern area (b)

ations presented on the Fig. 4 have fluctuations upto 14% from the middle value with standard deviation of 4.2%.

CONCLUSION. Unsteady loadings are of a great interest for many practical applications in marine engineering. Modelling of these phenomena requires new theoretical tools capable of resolving concentrated vortex structures which are responsible for large scale flow fluctuations. The focus of the present paper is the study of unsteady effects in the wake of ships with large block coefficients. The estimations presented in Kornev etl. [5] show that the pure LES demands a huge resolution which makes the LES application for shipbuilding purposes impractical even at small Re numbers typical for ship models. So far, the only reasonable solution is the application of hybrid methods. In this paper we presented a hybrid method based on the combination of the dynamic Smagorinsky SGS model (DSM) and the $k-\omega$ SST URANS approach. The method is applied to the calculation of the resistance and the wake flow of the tanker KVLCC2. The hybrid

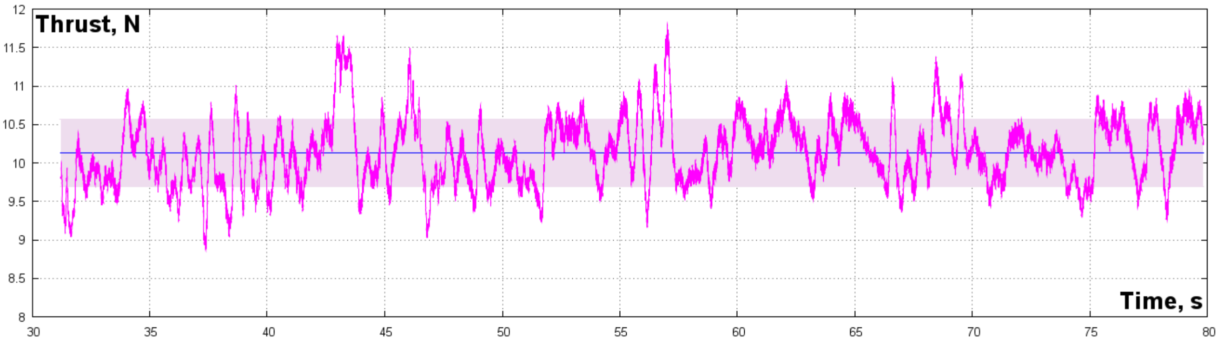

Figure 4: Variation of the thrust on the time

method provides very good results for the resistance. Also the fields of the mean axial velocity and the turbulent kinetic energy agree well with the measurement in the propeller plane. The hybrid method predicts the unsteadiness of the wake flow satisfactorly. Analysis shows that the instantaneous velocities deviate sufficiently from the mean values which are usually used as the estimated velocities in modern engineering methodologies. This fact can negatively influence the accuracy of propulsion and unsteady loads prediction.

ACKNOWLEDGMENT. The authors acknowledge gratefully the support of the German Federal Ministry of Economics and Technology (BMWi). This work has been performed within the framework of the project ShipLES monitored by Dr. A. Nitz. LES calculations have been performed on IBM pSeries 690 Supercomputer at the North German Alliance for the Advancement of High-Performance Computing (HLRN). The authors wish to acknowledge the community developing the OpenFOAM.

References

[1] Gothenburg 2010: A Workshop on CFD in Ship Hydrodynamics, Chalmers University of Technology, Gothenburg, 2010.

[2] Kim, S., Rhee, S. H., 2002. Assessment of eight turbulence models for a three-dimensional boundary layer involving crossflow and streamwise vortices. Fluent Technical Notes 165, 1–25.

[3] Kim, W. J., Van, S. H., Kim, D. H., 2001. Measurement of flows around modern commercial ship models. Exp. in Fluids 31, 567–578.

[4] Kornev, N., 2010. Propeller theory. Shaker Verlag.

[5] Kornev N., Taranov A., Shchukin E., Kleinsorge L., Development of hybrid URANS-LES methods for flow simulation in the ship stern area, NuTTS 2010: 13-th numerical towing tank symposium, Duisburg 2010.

[6] Lee, S. J., Kim, H. R., Kim, W. J., Van, S. H., 2003. Wind tunnel tests on flow characteristics of the KRISO 3600 TEU containership and 300 KVLCC double-deck ship models. J. Ship Res. 47, 24–38.

[7] Schlichting, H., 2000. Boundary layer theory. Springer.

Propeller Blade Optimisation applying Response Surface Methodology

Florian Vesting[1], **Rickard Bensow**[1]

[1]Chalmers University of Technology, Gothenburg, Sweden

1 INTRODUCTION

In order to further increase the applicability of optimisation within the propeller design process, an approach for response surface methodology, the Kriging algorithm, was applied to the propeller blade optimisation problem. The software package DACE (Design and Analysis of Computer Experiments), which is a Matlab toolbox for working with Kriging approximations for computer models, was applied in conjunction with the FRIENDSHIP-Framework. The accuracy of the response surface methodology (RSM) was evaluated against RANSE flow simulations coupled with a vortex-lattice propeller model (VLM).

2 MOTIVATION

A good design is almost always about finding a compromise between the competing objectives, constraints and variables. Their relationship is typically nonlinear and the approach of finding a range of satisfying solutions, is based on systematic design space investigation. This helps the designer identifying indicators and trends. However, systematic variations and optimisations on parametric designs, including numerical flow simulations, are still too demanding for an early design stage. Thus within this paper we are testing the feasibility to apply the RSM to a propeller optimisation challenge. Beside the dynamic of the propeller-ship system, the cavitation prediction is also part of the scope in this investigation.

3 KRIGIN PREDICTOR

The basic idea of a response surface is to develop a stochastic process Y for modelling an independent response $y(x)$. The regression model is in general a linear combination of chosen functions $f(x)^T\beta$ with regression parameters β and a random process $Z(x)$, which is assumed to have zero mean and a covariance which is a product of the process variance σ^2 and a correlation function [5, 4],

$$Y(x) = \sum_{i=1}^{n} \beta_i f_i(x) + Z(x), \tag{1}$$

$$E[Z(w)Z(x)] = \sigma^2 R(\theta, w, x). \tag{2}$$

One method for analysing such a model is known as Kriging. Assuming a 3-dimensional situation, the Kriging predictor, which was utilized in this case study, estimates the value at an untried location x as a weighted sum of the data values surrounding the location x. That is, from a given set of designs S, where each is of the form $(x_i; y_i; P_i)$ where x_i and y_i are the coordinates and P_i the depending variable. We can then estimate the value of an unknown point $\hat{y}$ by calculating the weighted sum of the known points:

$$\hat{y} = \sum_{i=1}^{n} w_i P_i \tag{3}$$

with w_i being the weights. The Kriging approach can be used either to evaluate the accuracy of any linear estimator with given coefficients or to determine a set of weights for the minimum variance unbiased linear estimator. For both cases the error variance σ^2 is needed, which depends on the given samples S, the fitted variogram or rather correlation and the weights. The best unbiased predictor is obtained by minimizing the vector of weights (4) with the demand (5) [5]:

$$MSE[\hat{y}] = E[(\hat{y}(x) - Y(x))^2], \tag{4}$$

$$E[\hat{y}(x)] = E[Y(x)]. \tag{5}$$

The method of mean squared error (MSE) to produce an unbiased estimator was used in the applied response surface. Equation (4) can be rewritten as (6) with $\mathbf{R}$ being a n x n matrix for the correlations between the given samples results and $r(x)$ being the correlation between the untried location and the known results. Both are obtained from the correlation model $R(\theta, w, x)$. By introducing the Lagrangian multiplier, (6), is minimized with respect to w and (5); for further details refer to [5, 2, 4].

$$MSE[\hat{y}] = \sigma^2(1 + w^T(x)\mathbf{R}w(x) - 2w^T(x)r(x)) \tag{6}$$

However, an important part within the Kriging approach is the correlation model R that has to be specified. It describes the influence of a known design on $\hat{y}$ with respect to the distance between them. The most commonly correlation models are the exponential, spherical or Gaussian models. The utilized toolbox contains seven choices wherein θ has been introduced in addition to the ones in [5] as a parameter for anisotropic behaviour [4].

4 3-DIMENSIONAL CASE STUDY

The Branins's rcos function was selected to assess the settings for the Kriging predictor. This established optimisation test function contains three global optima $f(x_1, x_2) = 0.397887$ at:

$$\begin{aligned}(x_1, x_2) &= (-\pi, 12.275)\\ &= (\pi, 2.275)\\ &= (9.42478, 2.475)\end{aligned}$$

$$f(x_1,x_2) = a\cdot(x_2 - b\cdot x_1^2 + c\cdot x_1 - d)^2 + e\cdot(1-g)\cdot\cos(x_1) + e$$

$$a = 1, b = \frac{5.1}{4\cdot\pi^2}, c = \frac{5}{\pi}, d = 6, e = 10, g = \frac{1}{8\cdot\pi}$$

The DACE toolbox contains different models for the correlation between the known and the unknown points. All of them describe the decreasing influence of a known point with increasing distance. However, they differ in their behaviour close to the origin and can be separated into two groups. One with type of functions that have a parabolic behaviour, e.g. gauss, cubic or spline and the other one with functions showing a linear behaviour near the origin (exp, lin and spherical).

Different correlations are suitable depending on the underlying phenomenon that will be mimicked. If the underlying phenomenon is continuously differentiable, the correlation function will likely show a parabolic behaviour near the origin. In that case the Gaussian, cubic or spline correlation function is recommended. The influence of a known point would decreases slower with increasing distance to the unknown location. Conversely, physical phenomena that shows also sporadic characteristics, usually have a linear correlation near the origin. In that case the exponential, linear or spherical correlation functions would be expected to perform better [4].

Often a phenomenon is anisotropic, which means correlations are different in different directions. However, this implies a priori a sophisticated knowledge of the correlations. Therefore, in this configuration an isotropy with spherical correlation model was selected.

Figure 1 plots the 3-dimensional results for the Branins's rcos function with the underlying RS. The three different plots refer to the different response surfaces, obtained with different densities of spatial input data (black dots). The plots show already with just 100 variants a fair representation of the contour in the centre. However, the distribution is not adequate enough closer to the boundaries. The highest density of 500 known points shows nearly the contour of the surface. Apparently, the distribution on 100 known points can not predict the absolute minimum values.

Figure 1 provides also the solution of the optimisation based on the response surface. These were performed with a genetic algorithm NSGA-II, computing 400 variants over all on each response surfaces. Within these figures the three fat green bullets mark the three global minima. At a glance one can see, that the algorithm converged for all three approaches close to one minimum. The optimisation with the underlying response surface (RS) based on 200 base points, converged to a region with the closest distance to the actual minimum. However, none of the optimisations was able to find the exact result. In fact, with less generation and population size, the algorithms had problems to converge close to a minimum at all. Figure 2 compares the final solutions of the optimisation. In this set-up, the configuration with 200 samples performed best. Configuration based on the coarse distribution of known points, shows an evened response surface and hence is not able to predict absolute min-

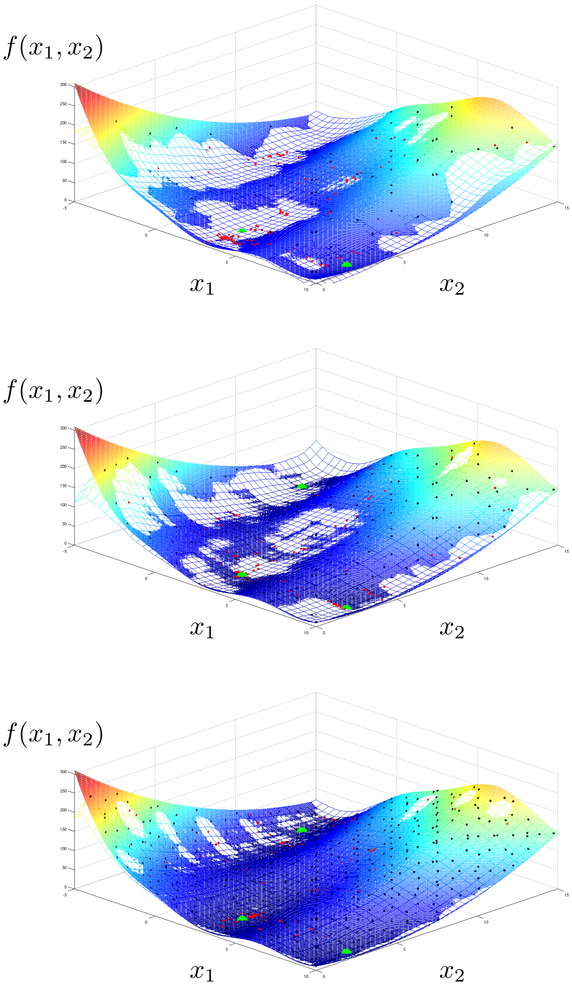

Figure 1: RS model for different design space investigation densities, with the dashed lines indicating the analytical function; top: 100 variants, middle: 200 variant, bottom: 500 variants

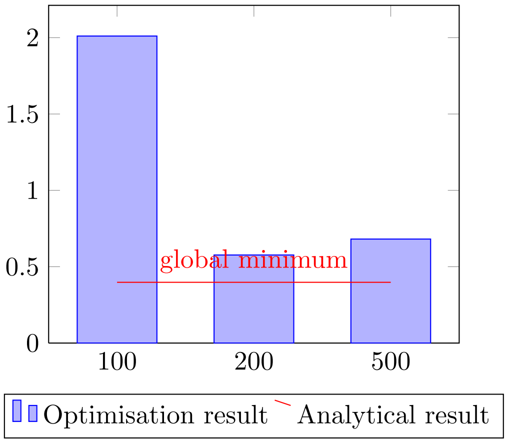

Figure 2: Final solution of the NSGA-II optimisation for the different response surfaces

imum. One should keep in mind that the objective function in this case study is rather smooth and continuous differentiable. This might be different in the applied propeller optimisation.

5 OBJECTIVES AND CONTRAINTS

In this section the selected constrains for a propeller blade optimisation based on the RSM are described. The constraints in the given samples S are supposed to be as continuous as possible to be able to create a decent response surface. The input or samples are obtained from a design of experiment (DoE) table, utilizing an iterative coupling between a RANSE solver (SHIPFLOW) for the flow field around the ship and a vortex lattice method (MPUF-3A) for cavitation prediction. A set of 220 variants were created in a deterministic approach utilizing a quasi-random sequence to create a DoE table gathering information about the objective function. Names written in light grey are output entities from MPUF-3A used to create the constraints. Some ideas are:

- A crux of the automated evaluation of cavitation, predicted with a VLM code, remains to be the propeller blade position with the occurrence of maximal cavity volume ('key-blade'). Thus for the constraints identification the blade position with the maximal volume will be determined. Starting from this position, the next 6 as well as the previous 4 blade positions are appraised to get a broader range of cavity information.
- In [6] the conjunction between the cavity volume at the 'key-blade' and the pressure pulses was quiet clear although not entirely resolved. It might be instead the cavity volume change $\frac{\delta Vol}{\delta t}$ which has a greater influence on the pressure pulses than the volume alone [3].
- The cavity closure line constraint in [6] was one of the most violated constraint. However, a convex shape of the cavity accompanied with a risk for shedding could not be shown.
- In [6] the thickness of the sheet cavity, in particular at the blade tip region, was not constraint. Although an influence was absolutely possible.
- According to [1] is the upstream desinence of initially attached cavity amongst others, one of the main ways by which focusing and erosive cavities formed.

5.1 Volume change

The overall performance of a propeller was better in [6] with less cavity volume. Although the amount of improvement regarding the pressure pulses was not directly connected to the maximal volume.To include the fluctuations of the cavity volume, in this continuation the change of non-dimensional cavity volume ($\frac{Vol}{R^3}$) is computed and included as well for the blade positions in the vicinity of the 'key blade' according to equation (7). Since this formulation does not consider changes in rotational speed, a time depending formulation for the cavity-volume-change was included as well (8).

$$\frac{\frac{Vol}{R^3}_{i}}{\frac{Vol}{R^3}_{i-1}} \tag{7}$$

$$\frac{\Delta Vol \cdot 2\pi n}{\Delta \theta} \tag{8}$$

5.2 Length ratio

Although a convex cavity closure line could not be shown in [6], an expeditious growing cavity length in span-wise direction can be an indicator for a shedding phenomenon which might occur on the midsection of the blade or in the tip region. Latter would be an indication of a possible tip vortex cavitation. Thus the cavitation length ratio was computed for all cavitation sections with a cavity area > 0 (9). All blade positions in vicinity of the key blade were taken into account and the maximal value was restricted.

$$\frac{CAVL/C_{i}}{CAVL/C_{i-1}} \tag{9}$$

5.3 Sheet thickness

The results of previous investigation [6] showed a trend for increasing pressure pulses with large cavity thickness predominant in the tip region. Thus three new constraints were included monitoring the cavity sheet thickness on the three outermost radii. The thickness is estimated for the main blade and all other blades in vicinity by (10):

$$t = \frac{CAVAREA}{cavL}, \tag{10}$$

with

$$cavL = CAVL/C \cdot C(r). \tag{11}$$

5.4 Desinence ratio

Assuming the formation of the sheet cavity is properly predicted by the VLM, an upstream desinence can be assumed as shown in figure 3. The cavity predicted is still attached to the leading edge in the first frame. However, moving the blade further through the wake, it disappears from the leading edge and only downstream there remains a cavity area (frame 2 and 3). In this situation the predicted cavity length is in most cases longer than $0.7C$, but the corresponding cavity area is rather small. Thus a ratio between the cavitation area and the non-dimensional cavitation length is monitored and limited to a maximum value (12).

$$\frac{CAVAREA}{CAVL/C} \tag{12}$$

5.5 Objectives

In the continuation of this project, the objectives are the amplitude of the first blade harmonic at the point with maximal first blade frequency pressure and the required shaft power P_D

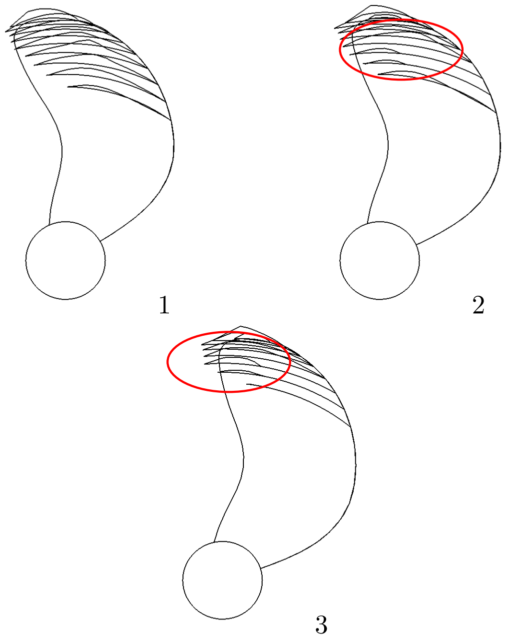

Figure 3: Leading edge desinence, where the sheet cavitation disappears from the leading edge.

$$P_D = 2\pi n Q \tag{13}$$

with:

$$Q = K_Q \rho D^5 n^2 \tag{14}$$

5.6 Classrules

Each design is evaluated with the classification notes 41.5 for 'Calculation of Marine Propellers' according to Det Norske Veritas (DNV). The created design is supposed to fulfill the high cycle stress criterion for dynamic stress amplitudes in the propeller blade as well as the low cycle stress criterion.

6 SELECTION OF CONSTRAINTS

In this section we discuss the influence of different constraints on the propeller performance regarding the objectives, with the help of the variants created in a DoE. The results were obtained from the RANSE-VLM coupling as it was used in [6]. From these results, all variants with poor performance regarding cavitation or highly unsteady cavities, were neglected. Thus only 157 variants were considered.

For the best variants (in both minimal pressure pulses and minimal required power) a clear trend for an increased geometry parameter Δ Camber of $+\ 0.002 - 0.006$ could be observed. All these variants are accompanied with a significant low first blade harmonic and a small cavity-volume-change. A slight trend could also be seen for the required power which tends to be accompanied by small values for the growing factor (≤ 1.4). The best variants in blade harmonics on the other hand show much more favourable trends towards a small cavity-volume-change (≤ 0.85), which can be seen on designs 169 and 138 in table 1. Generally a small maximum cavity volume have a positive effect on the pressure fluctuations, which is shown by variants 121, 147 and 169. It can also be verified with table 1, that even a higher cavity-volume-change in time, can still lead to a small pressure fluctuation if the cavity thickness at the blade tip (Tip1, Tip2, Tip3) are small (see designs 96, 136, 79). However, a high tip thickness (≈ 0.02) at position Tip1 has minor influence and can be evened out by a small volume change ($\approx 0.7 - 0.9$). This can be seen from variant 31 and 63. both show high values for Tip1 but medium cavity volume, Tip2, Tip3 and growing with the results of acceptable small pressure fluctuations.

Towards this, a higher thickness at positions Tip2 and Tip3 can be contrary regarding the the pressure pulses, see design 152, 203 and 209. For design 152 the pressure pulses are still smaller, which is due to the fact of a small cavity volume. The variants 203 and 209 have both a high volume and a high thickness which results in high fluctuations. These two variants underline also the small impact of Tip1 one, which is significantly small for both. At a glance, small values for the cavity thickness at the tip seem to be advantageously (see design 79). According to this, the positions Tip2 and Tip3 appear more regular at the same blade position and thus have a higher or more direct impact the pressure pulses than thickness at Tip1. If they come together with a small cavity-volume-change or a small maximum volume, it leads more often to a better result (147, 169). The constraints for the optimisation were selected according to these observed trends.

The designs show from the DoE show a uniform distribution for most of the constraints and the objectives, which will be used for the correlation model in the RS. The variance is significantly small for K_T, K_Q, Dt (cavity-volume-change), MaxVOL, η and thickness constraints. However, the desinence ratio varies within a wider range and can not be included in the response surface model, see figure 4. The variance for the maximal growing factor is only slightly better but will be included in the RS model.

7 PROPELLER OPTIMISATION

For a propeller optimisation the set-up was selected according to [6] with slight modifications on the design variables. Now, a set of ten design variables are selected changing the blade geometry. The 157 known points were used as input for the multi dimensional response surface model, with the settings discussed above. Based on this response surface an optimisation was carried out with regard to minimize the pressure pulses and the required power. A NSGA-II algorithm was employed with a population size of 20 and a total number of generations of 20. Due to the quick response of the result this comprehensive variant creation could be computed in an insignificant amount of time.

In order to generate a good correlation model for the Kriging predictor, a homogeneous distribution of the input values is unavoidable. Figure 4 shows also the distribution for the input parameter Δ Chord X2, exemplary for all 10 input parameters. From this a uni-

Name	Dt	MaxGrow	MaxVOL	Tip1	Tip2	Tip3	objectiveEFF	objectivePRES	PD
des0031	43.7	7.7	47.4	78.1	60.7	70.1	97.6	34.7	92.3
des0063	50.7	7.9	47.1	75.5	58.1	68.5	98.4	39.6	91.5
des0079	38.5	8.2	38.3	48.3	59.8	57.6	98.2	32.6	91.7
des0096	42.7	7.9	42.9	39.6	65.4	67.9	97.5	39.7	92.3
des0136	61.4	11.3	56	38.9	53	52.2	96.4	41.1	86.8
des0138	43.2	70.7	38.8	49.8	68.4	71.7	21.2	30.8	94.2
des0152	38.8	7.8	38	45.3	72.2	74.5	96	47	93.7
des0034	47.6	7.8	42.7	59.6	65.4	76.1	95.5	32.2	94.1
des0121	36.5	7.6	35.8	44.9	62	66.3	96.4	31	93.3
des0169	39.5	8.6	37.1	46.4	59	57.1	96.3	30.1	93.5
des0147	38.5	8.1	34.7	38.9	55.1	52.2	96.9	38.6	93
des0203	56.3	8.1	59.3	15.1	67.9	82.1	97.7	62.2	92.1
des0209	65.6	9.8	66.2	17	65.4	77.2	95.1	59.9	94.6

Table 1: Selected Results from DoE, values in % with respect to its maximum occurred

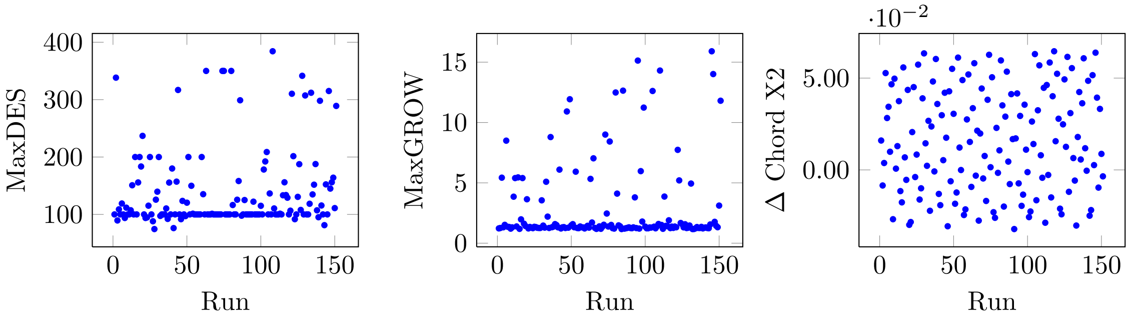

Figure 4: Distribution of input parameters

form distribution can be seen for all parameters. However, the resulting objectives and outputs show a more clustered distribution especially for seldom cavitation like desinence ratio. Thus for the Kriging predictor only selected input were applied to avoid a distortion of the RS model.

The 15 best solutions from the response surface in both objective functions were evaluated by SHIPFLOW-MPUF-3A coupled simulations. Figure 5 combine the results for the prediction and the computed results. At a glance one can see that the RS can not capture significant cavitation like the cavity length growing. A particular high growing value could not be predicted and thus the limitation for the design towards this constraint failed obviously. On the other hand was a prediction for the maximal cavity volume, the tip thickness region and the volume change promising. The pressure pulses were almost always under predicted with occasional intense differences. However, a trend could be captured well. The efficiency was close to the real values but sometimes with opposite trends. The same holds also for the second objective, the required power with a variance of the samples of 110 kN (¡ 1%). The optimal acceptable design show an increase regarding the pressure pulses of about 18%, which was predicted with an increase of 7.3%. The required power was on the other hand reduced by 8.5% (predicted reduction: 7.8%). This shows the optimisation algorithm searched predominantly to improve P_D. However, the penalty limit for the cavity volume was rather high and might be the motive for this result. Except for the cavity growing factor, the prediction for the best variant followed always the right trend within a tolerance of maximal 5%.

8 CONCLUSION

An optimisation was carried out employing a response surface methodology for the prediction of the performance of a propeller. Beside the objectives were also the constraints predicted by the RS model. The selected set-up could capture trends of the performance in a acceptable range. However, detailed information about the cavitation could not be obtained and sporadic occurrence of cavitation phenomena, for instance the cavity length growing could not be captured. More continuous cavitation phenomena, for instance the cavity thickness at the tip (Tip2 and Tip3) could be predicted with a variance of the samples of $4.62 \cdot 10^{-4}$ and $7.21 \cdot 10^{-5}$.

The optimisation suffered due to the failed prediction for the cavity growing factor and a obviously too lose selected limit for the maximal allowed cavity volume. However, the influence of the cavity volume can be essential, as the results from the DoE in section 6 showed.

The prediction of erosive cavities is with the selected constraints and a RSM not possible. However, for the selected limit is the favourable decrease in required power with an increase in cavity an expected result. For further work to improve the RS, anisotropy with respect to the observed trends could be included and a reduction of input parameters should be considered. The constraints regarding erosive cavitation must be revised to obtain more continuous values for the input to the RS. An imaginable possibility might be an averaged value over more blade positions or more sections for instance for a desinence constraint.

REFERENCES

Bark, G., Grekula, M., Bensow, R. & Berchiche, N. (2009). 'On Some Physics to Consider in Numerical Simulation of Erosive Cavitation'. Proceedings of the 7^{th} Internal Symposium on Cavitation

Clark, I. (2001). Practical Geostatistics. Scotland: Geostokos Limited

Kupier, G. (2010). 'New development and propeller design'. 9^{th} International Conference on Hydrodynamics, Shanghai, China

Lophaven, S., Nielsen, H. & Søndergaard, J. (2002). DACE A Matlab Kriging Toolbox. Lyngby: Technical University of Denmark

Sacks, J., Welch, W., Mitchell, T. & Wynn, H. (1989). 'Desing and Analysis of Computer Experiments'. Statistical Science, **4** (4), pp. 409-435

Vesting, F. & Bensow, R. (2011). 'Optimisation Considering Sheet Cavitation and Hull Interaction'. Proceedings of the Symposium on Marine Propulsion

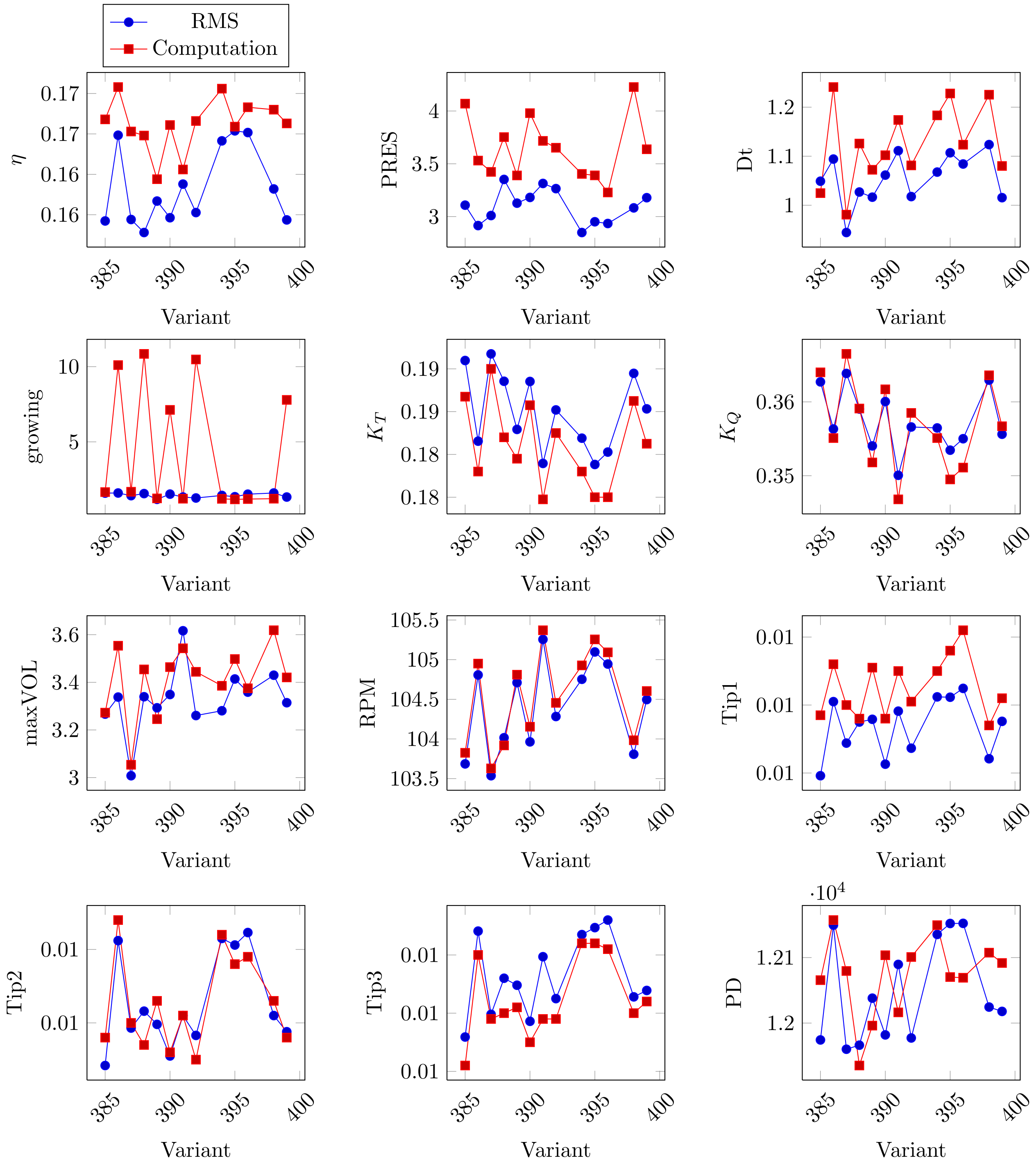

Figure 5: Comparison of the results

Case Study – Coupling CFD+DEM with FEM

Erik Vroegrijk
Lloyd's Register EMEA Technical Investigation Department (TID), London UK, erik.vroegrijk@lr.org

Introduction

The increase in Arctic trade over recent years and the possible introduction of new trade routes has sparked the need to assess and further enhance our existing Ice Class Rules and their applicability to a wide range of commercial ship types. Sailing through Arctic conditions requires modifications to the standard ship form in terms of structural strength and hull lines. In the past these modifications were based on best practice assumptions and ice towing tank tests results. With the increase in computation power and algorithm efficiency, numerical methods have now reached the level where they can be used in this development process.

For numerical methods to yield acceptable results the characteristics of sea ice must be understood and correctly implemented. The properties of sea ice, however, vary widely, as comprehensively summarised by Timco and Weeks **[1]**. Sea ice strength depends, for example, on factors like brine content, ice age, morphology, temperature and loading rate. The variation in mechanical properties makes sea ice incredibly difficult, perhaps impossible, to scale in model tests. Most ice towing tanks use refrigerated water with additives to simulate sea ice characteristics. As the base material for sea and model ice is the same (water), the model ice is commonly too strong. By adding air and performing controlled thermal treatment the model ice is weakened, after it is grown, until it reaches its target strength. Depending on the duration of the tests the model ice properties will change significantly. This is a direct result from the temperature gradient that exists through the ice thickness. As a result, ice towing tank tests often show a large scatter in measured data and low repeatability.

To circumnavigate the scaling problems it was argued by Vroegrijk **[2]** that currently available numerical methods, especially the explicit Finite Element Method (FEM), could be applied to most ship-ice and propeller-ice interaction topics. However, a comprehensive material model that resembled the actual behaviour of sea ice under different loading conditions could not be found. The mathematical model introduced in **[2]** aimed to represent all available strength data as a realisation of the brittle failure surface. In such it resembles more a methodology to represent ice characteristics in a numerical model while remaining accessible for improvement and discussion.

The drawback of using only FEM models in ship-ice and propeller-ice interaction is that the contribution of fluid forces prior to impact is neglected. It is argued here that for ice particles in, for example, brash ice channels, this is a too crude assumption. In reality the trajectory ice particles follow, before impacting on hull or propeller, is largely influenced by the flow conditions. The accelerated flow around the hull will influence their path as well as their angular velocities. This will change the orientation of the particles upon impact and therefore the contact area and resulting forces. The case study presented in this paper aimed to test the application of Computational Fluid Dynamics (CFD) in the calculation of ice particle tracks prior to impact, which will then be used as input in the FEM model.

Case study

The case study performed for this paper was deliberately chosen to be as simple as possible. The study aimed to show the influence of local flow conditions on a particle's track and orientation prior to its impact with bodies in the flow. For that, a simple flow solution was calculated around two basic geometrical shapes, a cylinder and a prism. The cylinder had a diameter of 2 *m* and was placed 8 *m* upstream and 1 *m* aside the domain centre line. The prism had sides of 3, 4 and 5 *m* with the origin of the coordinate system placed at the still water line at the intersection of the shortest and longest side of the prism. The flow domain had a height of 8 *m*, with the free surface located in the middle, representing a water depth of 4 *m*. The entire flow field stretched 24 x 50 *m*, in width and length respectively. A plot of the location of the origin, cylinder and prism is provided in **Figure 1**.

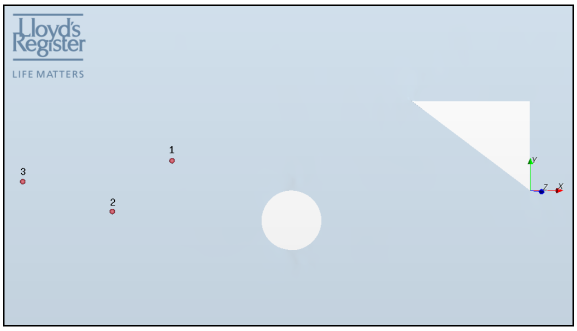

Figure 1. Test case set up

The Discrete Element Method (DEM) introduced in CD-adapco's StarCCM+ 6.02.009 works with spherical particles **[3]**. Within this method it is possible to combine multiple spheres of different diameters in so called *composite particles* to construct arbitrary shapes. For this case study a relatively simple composite particle was used consisting of three spheres, two with a 0.5 *m* diameter and one of a 0.4 *m* diameter. The smallest sphere was placed in the middle, with the bigger spheres placed on either side in domain transverse direction. To form a single body the spheres, displayed in **Figure 2**, overlapped 0.1 *m* on the particle centre line. The composite particles were introduced in the solution by three injectors, located at the still water free surface at x,y-locations: (-12,1), (-14, -0.7) and (-17, 0.3). In **Figure 1** the injectors are plotted with red dots. The injection velocity was set equal to the velocity of the unidirectional flow, which entered the domain from the left hand side of **Figure 1** with 1 *m/s*.

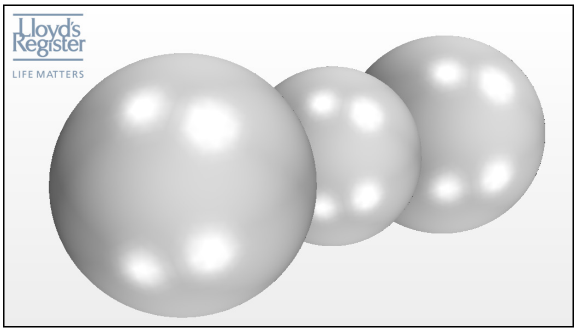

Figure 2. DEM particle

VOF with DEM

The free surface flow around the cylinder and prism was calculated using the Volume of Fluid (VOF) method. This method allows the interface between two fluid phases to be calculated accurately, as long as the fluid phases remain largely separated **[3]**. It was ensured that a 2nd-order discretization scheme was used close to the free surface, as 1st-order schemes are known to lead to too much diffusion in the past. With the free surface representation, the buoyancy forces acting on the particles can be calculated. It must be stressed that the computation of the free surface was not the primary objective in this case study. For that reason the mesh used around the cylinder and prism was relatively coarse, though sufficiently dense to capture the free surface.

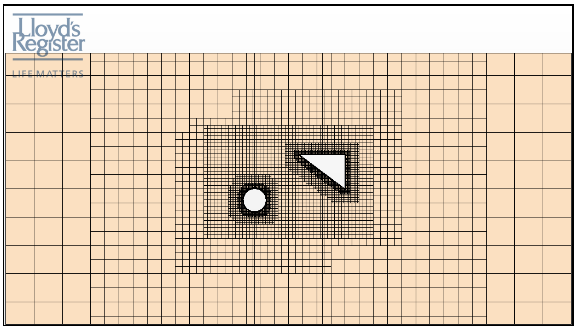

Figure 3. Trimmed mesh

The total number of hexahedral volume cells used in the flow domain was just over 210,000. The prism mesh applied on the surface of the cylinder and prism had a thickness of 0.1 *m* and consisted of 10 layers. The cell size in the region between the cylinder and the prism was further limited to 0.5 *m* in both length and width direction. The height of the cells around the free surface was refined to 0.1 *m*, such that the generated waves were captured with sufficient accuracy. A top view of the mesh is provided in **Figure 3**.

Before the particles were injected a converged flow solution was established. The velocity contours, for a cut just below the free surface, are provided in **Figure 4**. Clearly, the mesh dampens the vortex generated in the prism wake, as the mesh coarsens quickly downstream. Although this would affect the drag force experienced by the prism, the effects up stream will be relatively small. As the focus was on the software's ability to track DEM particles up to impact, the damping introduced by the coarse mesh downstream was considered to be acceptable.

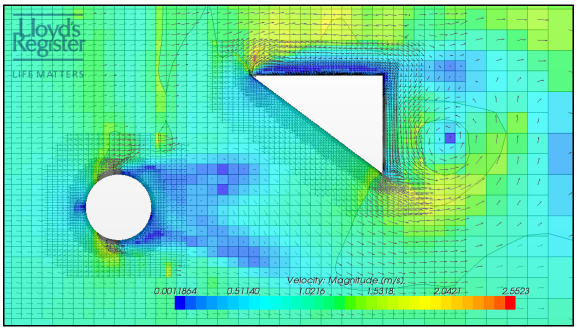

Figure 4. Velocity field underneath free surface

The motion of injected particles is solved on a secondary grid using standard momentum balance equations. Users can choose whether the interaction between fluid and particles is one-way (fluid forces acting on particle), or two-way. In the latter case the fluid will be forced to flow around the particles, while simultaneously influencing their motions. This is done by placing sufficiently strong momentum sources in the volume cells occupied by the particles. For this case study, however, only one-way coupling was activated, for it was sufficient to show the general principles.

The momentum balance solved in the DEM equations resembles a non-linear variant of the sliding-spring-dashpot system and is based on the Hertz-Mindlin theory **[3]**. The spring term in the system will generate a repulsive force based on the overlap, where the dashpot represents the structural damping. The amount of damping is user specified with coefficients of restitution in both normal and tangential direction. The slider allows for the tangential displacement of the contact point, and its stiffness is defined with the static friction coefficient. In this way all sorts of non-perfectly elastic collisions can be modelled. The only drawback of the method is that the contact area is not part of the equations. As a result accurate pressure distribution can't be calculated, hence the desire to couple the method with finite element method (FEM) software.

The DEM solution is updated after each time step taken in the fluid domain. During this update the DEM solver iterates with an automatically calculated stable DEM time-step. This DEM time-step is determined by the smallest detail in the solution, typically the particle diameter. Therefore, if one wants to influence the computational costs of the DEM solution, one has to alter the particle diameter. The path particles took was recorded in a track file, which contained quantities like particle position, velocity, angular velocity, kinetic energy, etc. At the end of the simulation the particle tracks can be visualised, as shown in **Figure 5**.

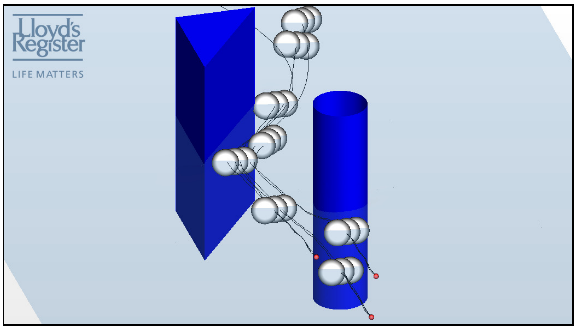

Figure 5. Particle tracks around obstacles

FEM solution

A wide range of commercially available and purpose-built finite element codes could be used to compute contact loads resulting from body impact. With a view to potentially applying this method to ship-ice and propeller-ice interaction, an explicit FEM variant was selected. Explicit FEM codes are especially suitable for problems that simultaneously encompass complex body interaction and highly nonlinear material behaviour. Within Lloyd's Register EMEA's Technical Investigation Department (TID) Abaqus/Explicit has been used in combination with StarCCM+ for fluid-structure interaction problems such as sloshing.

As in transient CFD analysis, explicit FEM advances the solution in time. This holds that the boundary and loading conditions can easily be expressed as a function of time. Abaqus/Explicit uses amplitudes for that purpose, which, for example, can be mathematical functions or tables **[4]**. In case tables are chosen the data is automatically interpolated to form continuous amplitudes through time. As a result, the track file data calculated by StarCCM+ could be directly implemented in Abaqus/Explicit using a simple I/O process.

The test case geometry was remodelled in Abaqus/Explicit and subsequently meshed. Both cylinder and prism were meshed using shell elements of 0.05 and 0.025 *m* thickness, respectively. The target quadrilateral element size was 0.1 x 0.1 *m* for both cylinder and prism. The ice particles, for the test case modelled as rigid bodies, were meshed using tetrahedrals with target sides of 0.05 *m*. An overview of the mesh is displayed in **Figure 6**.

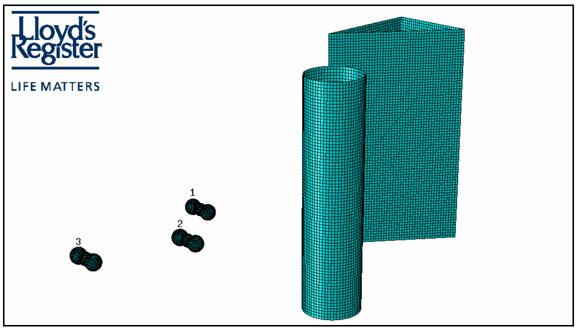

Figure 6. FEM mesh

For both cylinder and prism, isotropic linear elastic material behaviour was assumed, with strength parameters similar to steel. In future applications the material model applied to the ice particles could range from simple linear elastic to fully anisotropic rate dependent. For the latter, Vroegrijk's **[2]** material model was specifically written for implementation in explicit FEM.

To emphasise the differences in structural loads resulting from the simple sliding-spring-dashpot representation of StarCCM+ and the contact algorithm in Abaqus/Explicit, two scenarios were analysed. In the first scenario ice particle 2, see **Figure 6**, was set to follow the path calculated by StarCCM+. In the second scenario the boundary conditions acting on ice particle 2 were released prior to impact. In both scenarios the boundary conditions acting on ice particles 1 and 3 were released prior to impact.

The differences observed in the results are remarkable but not completely unexpected. The soft approach used in StarCCM+ allows for solid boundaries to overlap during interaction. Based on the amount of overlap the repulsive forces are

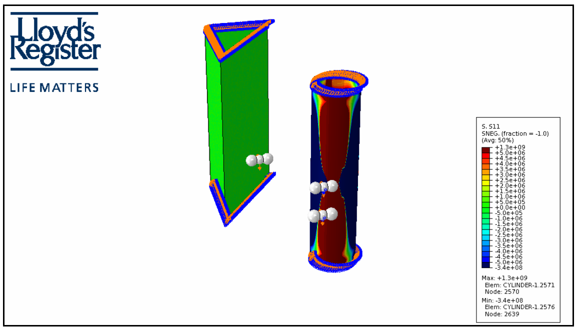

Figure 7. Scenario 1 – Impact ice particle 2

calculated and introduced back into the momentum balance. The result of constraining ice particle 2 to its path is that it forces the cylinder wall to deflect, as overlap is not allowed in the contact definitions in Abaqus/Explicit. The differences in the resulting stresses are profound, with the maximum first principal stress being 3 orders larger in scenario 1. For comparison the first principal stress plots are provided in **Figure 7** and **Figure 8**, for scenario 1 and 2, respectively, using the same colour scaling.

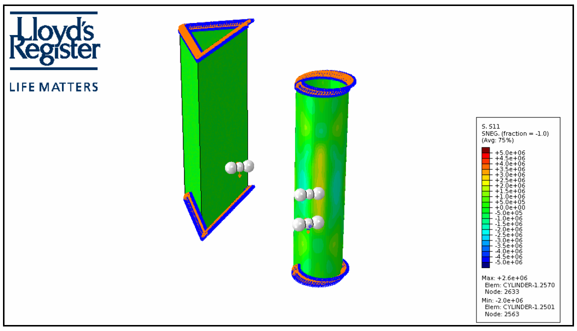

Figure 8. Scenario 2 – Impact ice particle 2

After the collision of ice particle 2 with the cylinder, its path remains unconstrained in scenario 2. As a result, ice particle 2 will not follow a path dictated by the flow anymore. For comparison the positions of the particles are plotted at the moment ice particle 1 impacts on the prism in **Figure 9** and **Figure 10**, for scenarios 1 and 2, respectively.

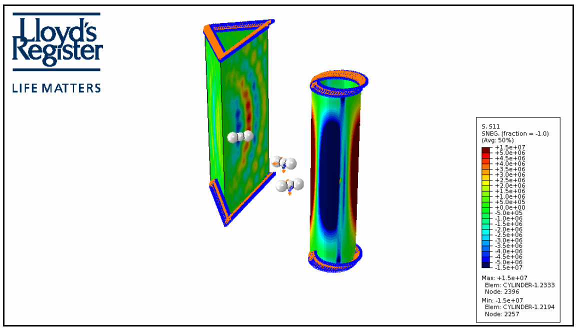

Figure 9. Scenario 1 – Impact ice particle 1

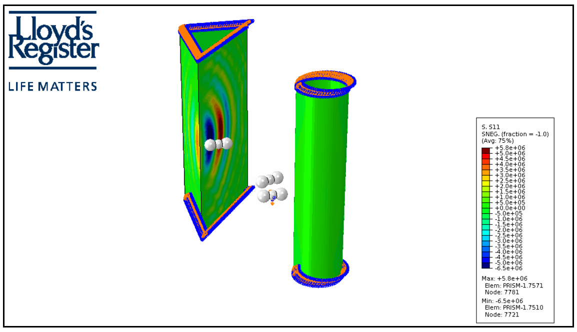

Figure 10. Scenario 2 – Impact ice particle 1

Discussion

The simplicity of the case study presented here might raise a question of why not use either one CFD or FEM package to solve the entire problem in the same package. For simple cases this would indeed be a more sensible modelling approach. However, the intention is to expand this very simple case study to full scale ice-breaking simulation in which ship-ice and propeller-ice interaction occur simultaneously. In such a simulation the flow around the ship will be far more complex, due to channel effects and propeller action. Thereby, the ice particles will not stay intact during interaction, but crush and crack upon impact. Currently no commercially available software package has the capacity to solve both problems simultaneously. On a more fundamental note, the problem we try to solve embraces both complex hydromechanics and mechanics. The former is still most reliably and quickly solved on an Eulerian grid, where for the latter the Lagrangian formulation is more practical. In that sense the presented case study enables users to utilise the full potential of both worlds, CFD and FEM.

The results presented here clearly show that the motion of large particles in a flow is certainly not random, but based on physics. The impact velocity, as well as the orientation of the particle in respect to the object it collides with, can significantly change due to flow conditions and should not be neglected. The weakness of the current approach is that only one-way coupling (CFD → FEM) has been employed. As shown this works well up to the moment just after impact. From there onwards fluid forces can not longer be anymore and should again be taken into account. The suggestion was made to CD-adapco to introduce a two-way coupling (CFD ↔ FEM), such that a particle would be removed prior to impact from the flow domain and reintroduced to the flow domain after impact with the restitution velocities and rotations as calculated by the FEM package.

Conclusion

It can be concluded with a high level of confidence that the coupling of CFD+DEM with explicit FEM is very straightforward and delivers realistic results up to just after impact. By taking the influence of hydrodynamic forces into account, a more accurate collision path can be determined. Therefore the particles kinetic energy prior to impact will be more realistic, resulting in more reliable collision forces and structural responses.

It must be emphasised that the DEM model has just been added to CD-Adapco's StarCCM+ software. As such the software is still in the early stages of development and is likely to improve, especially if a two-way coupling between the DEM and FEM is realised in the near future. This would open possibilities for modelling the complex ship-ice and propeller-ice interaction problems.

Acknowledgements

The author would like to thank LR and his colleagues within the Fluid Dynamics group of TID for their continuous support.

References

[1] G.W. Timco and W.F. Weeks - *A review of the engineering properties of sea ice* - Cold Regions Science and Technology 60 (2010), 107–129.

[2] E.A.J. Vroegrijk – *Ice breaking numerics* – Delft University of Technology (2011)

[3] CD-adapco – *StarCCM+ User Guide* – Version 6.02.009 (2011)

[4] Dassault Systmes Simulia Corp. - *Abaqus Users manual* – Version 6.10 (2010)

Coupled sliding grids and adaptive grid refinement for RANS simulation of ship-propeller interaction

Patrick Queutey, Ganbo Deng and Jeroen Wackers
Laboratoire de Mecanique des Fluides, Ecole Centrale de Nantes
CNRS-UMR 6598, 44321 Nantes Cedex 3, France
Patrick.Queutey@ec-nantes.fr, Ganbo.Deng@ec-nantes.fr, Jeroen.Wackers@ec-nantes.fr

1 Introduction

Currently, one of the main goals of EMN (the CFD Department of the LMF) is the simulation of ship propulsors in extreme operating conditions, with accurate modelling of all the physics involved. This requires the capability to simulate a propulsor rotating behind a ship hull, combined with effects of free-surface deformation, ventilation, and cavitation. These capabilities are being developed for inclusion in ISIS-CFD [2, 6], the unstructured finite-volume flow solver created by EMN.

An essential building block for these simulations is a sliding grid technique, which allows a part of the grid (containing the propulsor) to rotate within the main part of the grid, while keeping a connection between the two parts (see figure 1). Also, since many of the phenomena to be studied originate from highly localised low pressure zones, the accurate simulation of these phenomena can be obtained by automatic adaptive grid refinement. However, the sliding grid approach and the adaptive grid refinement have to be general enough to work together.

We have recently developed a sliding grid capability, that has been specifically constructed to work together with our existing grid refinement method [7, 8]. Both techniques are powerful enough to deal with the fully unstructured hexahedral grids that we generally use. The goal of this paper is to introduce the sliding grid method and to show how the two techniques work together.

Sliding grid methods can be constructed for unstructured grids, these procedures are far more complicated than for structured grid solvers. Among others, the connection between the two subdomains of the grid has to be reconstructed often, as it does not follow a regular pattern. Also, it is not easy to ensure flux conservation over the interface. We have chosen a connection between the domains that does not explicitly guarantee conservation; it is based on connectivities between the cells and faces on the interface that mimic as closely as possible the connectivities for all other cells in ISIS-CFD.

The paper first introduces the ISIS-CFD solver (section 2) concentrating on the computation of the fluxes as this part is essential for the sliding interface approach. Then section 3 presents the sliding grid method that we developed. The following section 4 explains the grid refinement method and the way it is combined with the sliding grid approach. The paper ends with numerical examples (section 5) and a conclusion.

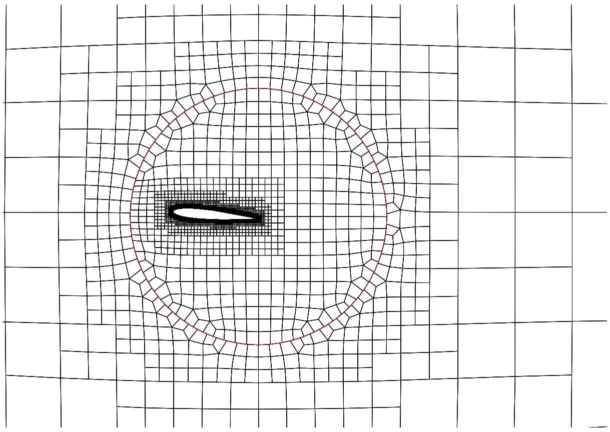

Figure 1: Example of a sliding grid around a pitching airfoil. The sliding interface is indicated in red.

2 The ISIS-CFD flow solver

ISIS-CFD, available as a part of the FINE$^{\text{TM}}$/Marine computing suite, is an incompressible unsteady Reynolds-averaged Navier-Stokes (RANS) method [2, 6]. The solver is based on the finite volume method to build the spatial discretisation of the transport equations. Pressure-velocity coupling is obtained through a Rhie & Chow SIMPLE-type method: in each time step, the velocity updates come from the momentum equations and the pressure is given by the mass conservation law, transformed into a pressure equation.

The discretisation is face-based. While all unknown state variables are cell-centered, the systems of equations used in the implicit time stepping procedure are constructed face by face. Fluxes are computed in a loop over the faces and the contribution of each face is then added to the two cells next to the face. This technique poses no specific requirements on the topology of the cells. Therefore, the grids can be completely unstructured, cells with an arbitrary number of arbitrarily-shaped faces are accepted.

Free-surface flow is simulated with a multi-phase flow approach: the water surface is captured with a conservation equation for the volume fraction of water, discretised with specific compressive discretisation schemes [6]. Furthermore, the method features sophisticated turbulence models [2] and 6 DOF motion simulation for free-moving ships [3].

Parallelisation is based on domain decomposition. The grid is divided into different partitions; these partitions contain the cells. The interface faces on the boundaries between the partitions are shared between the partitions, information on these faces is exchanged with the MPI (Message Passing Interface) protocol.

2.1 Reconstructions on the faces

To compute the fluxes, the quantities in the cell centres are reconstructed to the faces (see figure 2). For the diffusive fluxes and the coefficients in the pressure equation, the quantities on a face and the normal derivatives are computed with central schemes using the L and R cell centre states; if these centres are not aligned with the face normal, then non-orthogonality corrections are added which use the gradients computed in the cell centres. For the convective fluxes, we use the AVLSMART scheme [5] in the NVD context for unstructured grids established by Jasak, where limited schemes are constructed based on a weighted blending of the central difference scheme and an extrapolation using the gradient in the upwind cell. The reconstructions are detailed in [6].

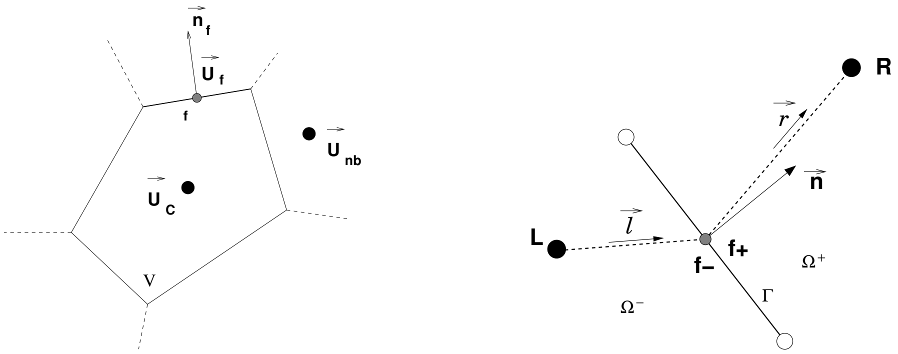

Figure 2: Cell, faces and neighbours (left), reconstruction on a face (right).

For the following discussion, the essential point is that all fluxes on a face can be constructed from the states and gradients in the centres of its two neighbour cells, plus the positions of these centres. In our domain decomposition approach for parallel computing, this neighbour cell information is the only thing which is exchanged over the interface faces.

3 Sliding Interface implementation

To compute the fluxes over the sliding interface, we need to establish connections between cells on the two sides of the interface. The procedure to connect these cells is performed at each time step in order to account for the rotation of the two subdomains with respect to each other. This procedure is chosen to remain as close as possible to what is done for standard cells. Thus, no specific interpolations are used. Instead, for a cell and face on the interface, we search the cell centre (in the other subdomain) which best matches the face. This cell is then used as neighbour cell for a flux computation exactly like in section 2.1.

The matching neighbour steps are searched in three steps (see figure 3).

1. A temporary ‘ghost’ point is constructed on the outside of each sliding face. This point is the mirror image of the inside neighbour cell centre, except near sharp corners of the sliding interface where the normal vector to the face is used. Ghost points are constructed on each side of the interface, for the two subdomains (figure 3 shows only the point for the left subdomain). The ghost points are not used for interpolation, only for the remainder of the search.

2. The current position of the sliding faces is gathered over all all partitions to form a global table. Then, in each partition, a search algorithm is used to find the global sliding face closest to each local ghost point.

3. The inside neighbour cells of the faces found are used as outside neighbours for the local sliding faces. If the neighbour is on another processor, an MPI communication is established just like the one for the normal

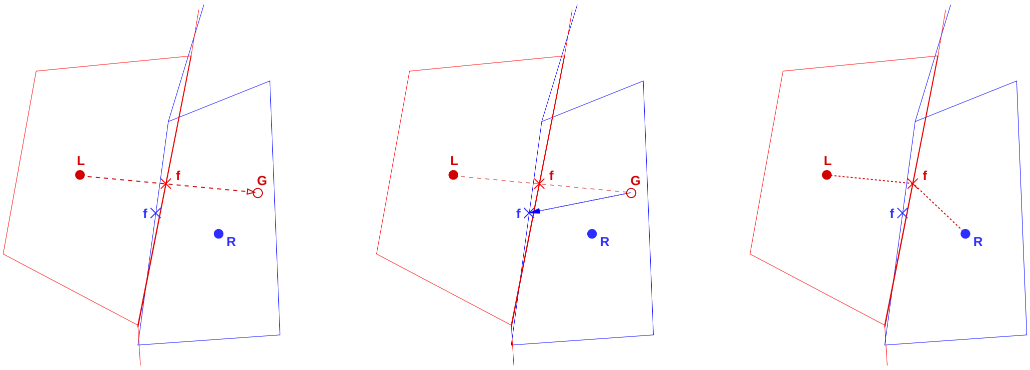

Figure 3: Sliding faces: construction of ghost points (left), searching the global faces (centre), the new neighbour cell (right).

domain decomposition. If the two cells are on the same processor, the communication is performed locally. As opposed to the normal domain decomposition, a cell on a sliding interface may be a neighbour for more than one cell, or for none at all.

As one sees, we do not explicitly split the grid in two parts by assigning a number of processors to each subdomain and partitioning each subdomain separately. Instead, the grid can be arbitrarily spread over the processors, a ‘colour’ is assigned to each cell to indicate to which subdomain it belongs. This gives the flexibility to run the code on a single processor and also to perform grid refinement; when a part of the grid is refined, the balance would be lost if each subdomain were assigned to a constant number of processors. With our approach, we can redistribute freely (section 4.1).

4 Automatic grid refinement

The automatic adaptive grid refinement technique included in the solver ISIS-CFD is for example described in [7, 8, 9]. The technique is meant to be used for all the different applications of the flow solver and has therefore been made as general as possible. The method supports the isotropic and anisotropic refinement of unstructured hexahedral meshes, i.e. cells can be refined by dividing them in all directions or in one direction only. Earlier refinements can be undone in order to adapt the grid to unsteady problems. The refinement criterion, which indicates where the grid must be refined, can be modified very easily; different refinement criteria have already been tested [8]. And finally, the grid refinement is fully parallel and includes an automatic dynamic load balancing in order to redistribute the refined grid over the processors when some partitions have been refined more than the others.

4.1 Coupling with sliding grids

Since the coupling between sliding faces is recomputed before each time step, no coupling information needs to be preserved when the grid is refined. Therefore, the coupling between the two techniques is relatively straightforward. However, several points deserve attention.

The first is the refinement of the sliding faces. Unlike the interface faces between partitions, which require a complex refinement procedure to preserve the connection to the faces on the other processor, the coupling between sliding faces is not kept during refinement. Therefore, the sliding faces are refined independently, just like boundary faces such as wall, inflow, or outflow faces. There is no explicit guarantee that the resulting refined cells on the two sides of the sliding interface have the same size. However, the refinement criterion which imposes the cell sizes is computed from the flow field, which is smooth over the interface. Thus, we may also expect a smooth variation of the cell size over the sliding interface.

A second point is the dynamic load balancing. As a part of this procedure, the grid is repartitioned using ParMETIS [4]. This tool is a graph partitioner that searches a balanced distribution of the nodes and a minimum number of edges cut; its input graph has the cell centres as nodes and the cell – neighbour cell connections as edges. To construct the graph, no edges are created for the sliding faces: all connections via sliding faces are ignored. Thus, ParMETIS naturally tends to put the interfaces between partitions on the sliding faces, as this costs nothing in terms of edges cut. This is an advantage for the convergence of the linear solvers in ISIS-CFD, since data on both sliding faces and interface faces between processors are updated in our linear solvers... but not in the innermost loop. Thus, faster convergence is obtained if these faces coincide, as this keeps their total number low.

4.2 Combined refinement criterion

When computing the interaction of a propulsor with the water surface, the volume fraction equation which gives the surface position needs to be accurately resolved. The precise computation of the vortical structures around the propulsor is also of prime importance; our preliminary research suggests for example that the onset of ventilation is largely determined by the minimum pressure on the propulsor blades. Thus, the grid must be refined both at the water surface and below the surface, in order to get good accuracy.

Therefore, we choose a refinement criterion which is a combination of two sensors. The first creates anisotropic grid refinement around the free surface. The second is based on the Hessian matrix of second derivatives of the pressure, which is similar to criteria being used for tetrahedral grid refinement [1]. This second criterion detects the presence of for example vortices. The final criterion is taken as the (approximate) maximum of these two sensors. A more complete description of the combined criterion is given in [9].

5 Numerical tests

In this section, two numerical test cases are presented in order to show that the combination of sliding interfaces and grid refinement is successful.

5.1 Pitching airfoil

The first testcase is the two-dimensional flow around a pitching NACA0012 airfoil. The airfoil is placed in a uniform flow and then rotated continuously round its trailing edge, thus shedding strong counter-rotating vortices. The Reynolds number based on the chord and the freestream velocity is $Re = 40$. The case is modelled with a circular sliding grid that rotates inside the man grid, see also figure 1. Grid refinement is based purely on the Hessian criterion, as this is a case without free surface.

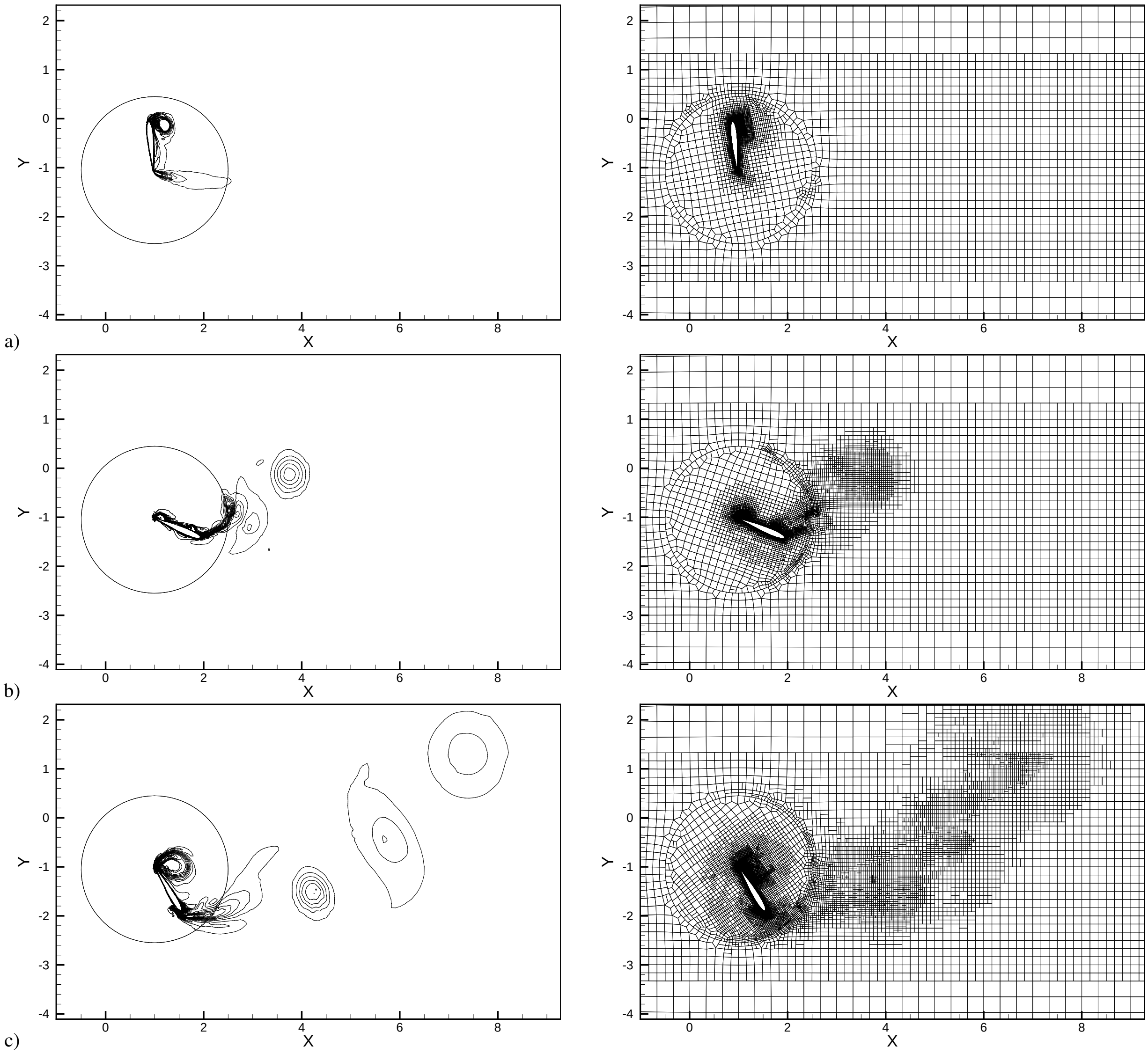

Figure 4: Vorticity contours and refined meshes for the pitching airfoil case, at $t = 0.7$ (a), at $t = 1.05$ (b) and during the second revolution at $t = 2.2$ (c).

Figure 4 shows snapshots of the flow at three different instants. The turning airfoil creates both isolated vortices and trailing vortex sheets. While some minor perturbations occur, these structures cross the sliding interface without problems and they persist in the far field. The meshes show, that the criterion correctly identifies the vortex zones, both close to the airfoil and far away. Without any explicit adjustment (section 4.1) the grid size varies smoothly over the sliding interface. Also, earlier refinements are undone correctly: no refinement remains on the upstream side of the sliding grid, while this part of the grid was refined when it was on the downstream side.

5.2 Propulsor with free surface

Our objective is not to simulate a surface-piercing propeller with a super-cavitating type profile that is designed to operate in partially submerged conditions for high speed craft, but to simulate the ventilation of a conventional propeller initially designed to operate in fully submerged conditions. Ventilation can occur when such a propeller operates too close to the free surface, or in heavy sea states. Such ventilation results in thrust loss and may induce violent impact loading, leading to propeller damage. Hence, successful prediction of such ventilation phenomena is useful for practical applications.

We compute the same test case as that investigated by Califano [10] during his PHD work. Experimental studies have been conducted with 9 different combinations of free-stream velocity U and shaft frequency n. Only one of them is simulated in the present preliminary study, namely the case with U=0.35m/s and n=14 Hz, which gives an advance ratio J=0.1. Only one submergence ratio h/R = 1.64 (h being the distance between the shaft centre to the free-surface, and R the radius of the propeller) has been computed to investigate the combination of sliding interfaces and grid refinement in a realistic situation.

The propeller with a diameter of D=0.25m is included in a rotating cylindrical domain with a diameter of 0.3m and a thickness of 0.2m. The original grid contains only about 1.54M cells for this domain with suitable grid resolution on the walls for low-Reynolds turbulent flow simulation. The second fixed domain contains about 0.36M cells with extension from $-7m < x < 3m$, $-2m < y < 2m$ and $-3m < z < 1m$. The grid is partitioned in four computational blocs. The time step employed is 0.0005s, which corresponds to about 142 time step per iteration. The free-stream velocity and the propeller rotation are accelerated to their maximum speed in 0.2s, while in the measurement, the acceleration period is about 0.42s. We have intentionally reduced the time resolution to reduce the CPU time for this preliminary investigation.

Figure 5 presents views of the instantaneous free-surface after three revolutions only of the propeller where important air entrainment is already predicted. The strong wave elevation as seen in figure 5(b) behind the propeller is created by the rapid acceleration used to rotate the propeller from rest and should be moved out downstream later. However the flow is not established after three revolutions, the current result is therefore convincing to demonstrate the efficiency of the refinement procedure together with the sliding interface approach. Figure 6 focuses in the median plane $y = 0$ at three successive time steps: the thick (blue) line represents the iso-volume fraction equals to 0.5. The grid cuts in the figure are obtained from triangulation during the computation and are only representative of the density of the pure hexahedral volume grid. At the third rotation the grid size has increased by 15% only and contains 2.2M cells.

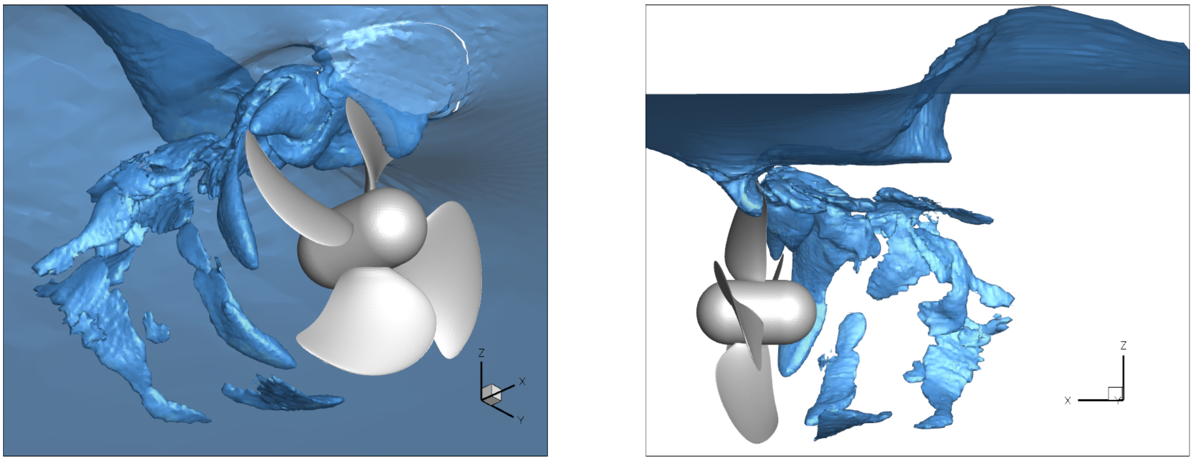

(a) 3D view. (b) 3D view from the median plan Y=0

Figure 5: Overview of the computed free-surface after three rotations of the propeller.

6 Conclusion

A sliding grid method has been presented for the simulation of marine propulsion. The method works in parallel and the different sub-domains can be distributed arbitrarily over the processors. No explicit interpolation is used to

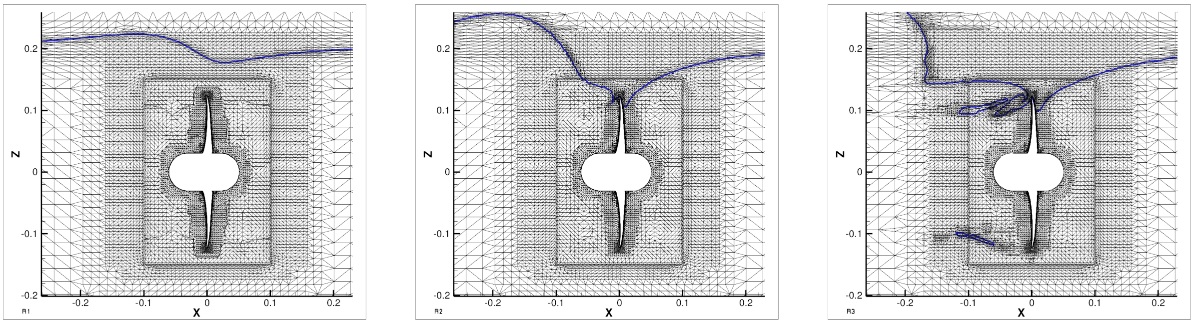

(a) 1 rotation.

(b) 2 rotations.

(c) 3 rotations.

Figure 6: Grid density and water/air interface in a median plane cut $y = 0$ at three time steps. The sliding interface corresponds to the limits of the squared region surrounding the propeller.

find the states on the sliding faces; instead, the coupling algorithm identifies real cells that are used as neighbours for the cells in the other sub-domain.

The combination with adaptive grid refinement is obtained by treating the sliding faces like standard boundary faces, when refining. The cell sizes are not explicitly synchronised over the sliding faces, instead the continuity of the refinement criterion over the interface guarantees smoothly varying cell sizes.

Two test cases show, that the combination of sliding interfaces and grid refinement is successful for the simulation of flows with vorticity and a free surface.

7 Acknowledgement

The authors are grateful to Dr. Andrea Califano and to Professor Sverre Steen at NTNU for providing us with the geometry of the propeller. We are also indebted to the French computer center IDRIS and CINES for providing us with computer resources.

References

[1] F. Alauzet and A. Loseille. High-order sonic boom modeling based on adaptive methods. *J. Comp. Phys.*, **229**(3), 561–593 (2010).

[2] R. Duvigneau, M. Visonneau, and G.B. Deng. On the role played by turbulence closures in hull shape optimization at model and full scale. *J. Marine Science and Technology*, **8**(1), 1–25 (2003).

[3] A. Leroyer and M. Visonneau. Numerical methods for RANSE simulations of a self-propelled fish-like body. *J. Fluid & Structures*, **20**(3), 975–991 (2005).

[4] http://glaros.dtc.umn.edu/gkhome/metis/parmetis/overview.

[5] V. Przulj and B. Basara. Bounded convection schemes for unstructured grids. *AIAA Paper No. 2001-2593*, (2001).

[6] P. Queutey and M. Visonneau. An interface capturing method for free-surface hydrodynamic flows. *Computers & Fluids*, **36**(9), 1481–1510 (2007).

[7] J. Wackers, K. Ait Said, G.B. Deng, I. Mizine, P. Queutey and M. Visonneau. Adaptive grid refinement applied to RANS ship flow computation. In *Proceedings of the 28th ONR Workshop on Naval Hydrodynamics*, Pasadena, California (2010).

[8] J. Wackers, G.B. Deng and M. Visonneau. Tensor-based grid refinement criteria for ship flow simulation. In *Proceedings of the 12th Numerical Towing Tank Symposium (NuTTS '10)*, Duisburg, Germany (2010).

[9] J. Wackers, G.B. Deng, and M. Visonneau. Combined tensor-based refinement criteria for anisotropic mesh adaptation in ship wave simulation. In *Proceedings of ADMOS 2011*, Paris, France (2011).

[10] A. Califano. Dynamic loads on marine propellers due to intermittent ventilation. *PHD thesis, Norwegian University of Science and Technology (NTNU)*, Faculty of Engineering Science and Technology, Department of Marine Technology, Oct. 2010, Trondheim, Norway.

Numerical Simulation of high-Reynolds number flow around Flettner rotors

Wei Zhang, Rickard Bensow
Department of Shipping and Marine Technology,
Chalmers University of Technology, SE 412 96 Gothenburg, Sweden
Email: zhang.wei@chalmers.se

The Flettner rotor, a vertical rotating cylinder, is an old type wind propulsion mechanism for shipping technology. It has attained renewed interest recently following the increased attention to fuel consumption and anticipated legislation. The "Magnus effect," the phenomenon giving the thrust, was first studied by G. Magnus who performed several laboratory experiments for a group of similar phenomena. Later, Prandtl (1926) references a paper by Helmholtz *et al.* where the "Magnus effect" is explained by an "ideal fluid" method without taking the viscosity into the consideration. Also for the reason of wind propulsion of ships, Prandtl starts to study the "Magnus effect" by the theory of viscous flow (Prandtl, 1926). With modern CFD technology, many have studied the "Magnus effect" for different topics (Tokumaru & Dimotakis, 1993; Mittal &Kumar,2003), but most of these studies focus on low Reynolds number, while more realistic case in transitional or fully turbulent flows are rarely found. Recently, Karabelas (2010) studied the high-Reynolds number flow pasting a rotating cylinder using LES, but it was more or less a 2D case.

There is thus a need to study cases similar to a real installation onboard, giving more reliable thrust estimates and yielding input into the assessment of effects on seakeeping and manoeuvrability of a ship with Flettner rotors. In this work, we use the CFD tools to design an experimental wind tunnel study of a Flettner rotor, at high-Reynolds number, and taking the 3D effect in to consideration. The experimental results will then be used to validate the computational model. Future work will include studies on scaling properties of lift, drag, and moment, as well as the interaction between several rotors and between the ship structures, like the free board and superstructure, and rotor installations.

In this computational study, four different diameters of the rotor (D = 50 mm, 60 mm, 70 mm, 80 mm), three different aspect ratios (AR = 3, 6, 9, where AR=H/D, with H is the height of the rotor) and two different Reynolds numbers ($Re = 0.5*10^5$, $1.0*10^5$), defined by the inlet velocity (U_{inlet})and rotor diameter, were selected for numerical simulation. A hexahedral mesh structure with O-grid around the rotor was chosen to discretize the computational domain. The same structure was used for all cases with a total cell count of 2.4 million cells, see Fig. 1.

As the CFD work in this study were performed for designing the wind tunnel experiment, the computational domain was chosen to mimic the real wind tunnel setup in the laboratory. So different from the realistic case of Flettner rotor, the sidewall effect of the wind tunnel was taken in to the consideration as the all side boundaries were set to the wall type boundary condition.

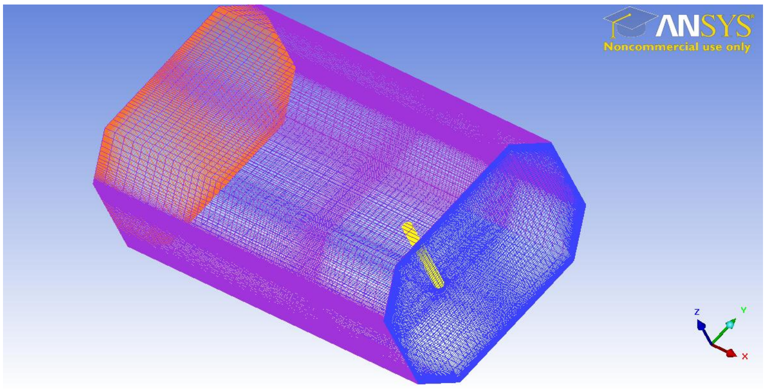

Fig. 1: view of mesh

All the cases were performed using the open source CFD code OpenFOAM, which is a finite volume based CFD solver, while for the case D = 70mm, with different aspect ratio and Reynolds number, simulations were performed also by the commercial codes ANSYS CFX and ANSYS Fluent, for the comparison. In the numerical studies, steady Reynolds Average Navier-Stokes modelling was chosen with the SST k- ω model (Menter, 1994) to model the Reynolds stresses.

For OpenFOAM and ANSYS Fluent, the steady state RANS equation was solved via the SIMPLE method, while the approach in ANSYS CFX used a coupled solver, in which all basic equations are solved as a single system. The discrete schemes for the advection terms are shown in Table 1.

Table 1. Discrete scheme for different solver

OpenFOAM	Gauss linearUpwindV Gauss linear
Fluent	QUICK
CFX	High Resolution

According to the Buckingham **π** theorem, the lift, drag, and moment coefficient (C_l, C_d and C_m) are dependent of the three dimensionless parameter relevant for the case of a Flettner rotor, that is the Reynolds Number, $Re=U_{inlet}D/\upsilon$, the aspect ratio, AR and spin ratio, $SR=\omega D/2U_{inlet}$. Based on the CFD result from OpenFOAM, the effects of Re, AR and SR are discussed, followed by a comparison for the case D = 70 mm for different software and an existing regression formula. This regression formula is based on existing published experimental studies and is close to the formulas presented by Reid (1925).

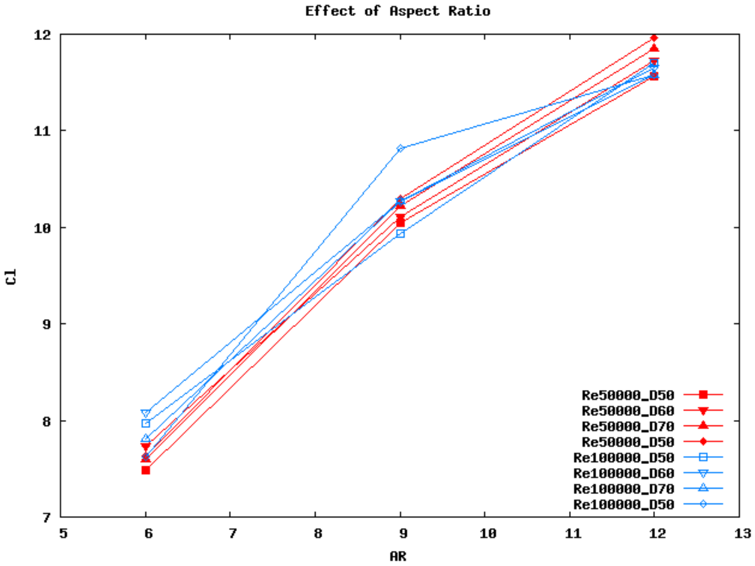

Figure 2: $C_{l,max}$ for different diameters and Re in this study.

According to the potential flow theory, the lift coefficient should be increase infinitely with the rotating speed of the rotor. But in viscous flow, according to Prandtl (1926) the upper limit of the lift coefficient $C_{l,max}$ is 4π (~12.6). However, in the recent study of a rotating cylinder, (Tokumaru & Dimotakis, 1993), it was showed that this upper limit $C_{l,max}$ could be exceeded, and idea proposed was that it was due to the three dimensional effects. In this study, all the attained max values of lift coefficient, for different D and Re, were below Prandtl's limitation (Fig. 2). Furthermore, $C_{l,max}$ increased with increasing aspect ratio and there is no indication for this trend to flatten out, approaching Prandtl's results, thus it can be expected that $C_{l,max}$ could exceed 4π with larger aspect ratio. It was also found that, regarding $C_{l,max}$, all the curves of different Re collapse, indicating that the $C_{l,max}$ is not sensitive to the Re.

In contrast to $C_{l,max}$, the max values for Cd (Fig. 3) and Cm (Fig. 4) are sensitive to Re, and this effect was more clearly seen for $C_{m,max}$ than $C_{d,max}$. Moreover, we noted an odd effect for the case Re=100,000 where $C_{d,max}$ is sensitive also to the diameter of the rotor; the reason is unclear and should be looked into in later work.

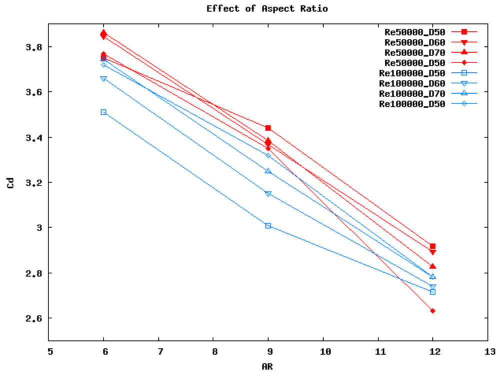

Fig. 3: $C_{d,max}$ of different Diameter and Re

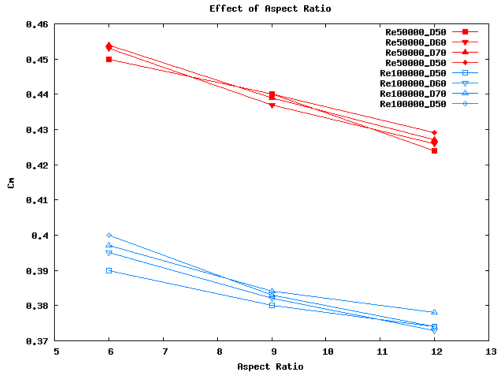

Fig. 4: $C_{m,max}$ of different Diameter and Re

The effect of the Spin Ratio is shown in Fig. 5. Although the results show some differences depending on different software, the basic trends for the effect of Spin Ratio are the same. The lift coefficient results of Fluent and CFX for AR=12 are close to the regression formula, while the rest are not. Another interesting thing regarding the lift coefficient behaviour is that rate of increase for the two different Re initially are the same. Considering that the regression formula do not take the effect of aspect ratio and Reynolds number into the consideration, this result still need to be better validated.

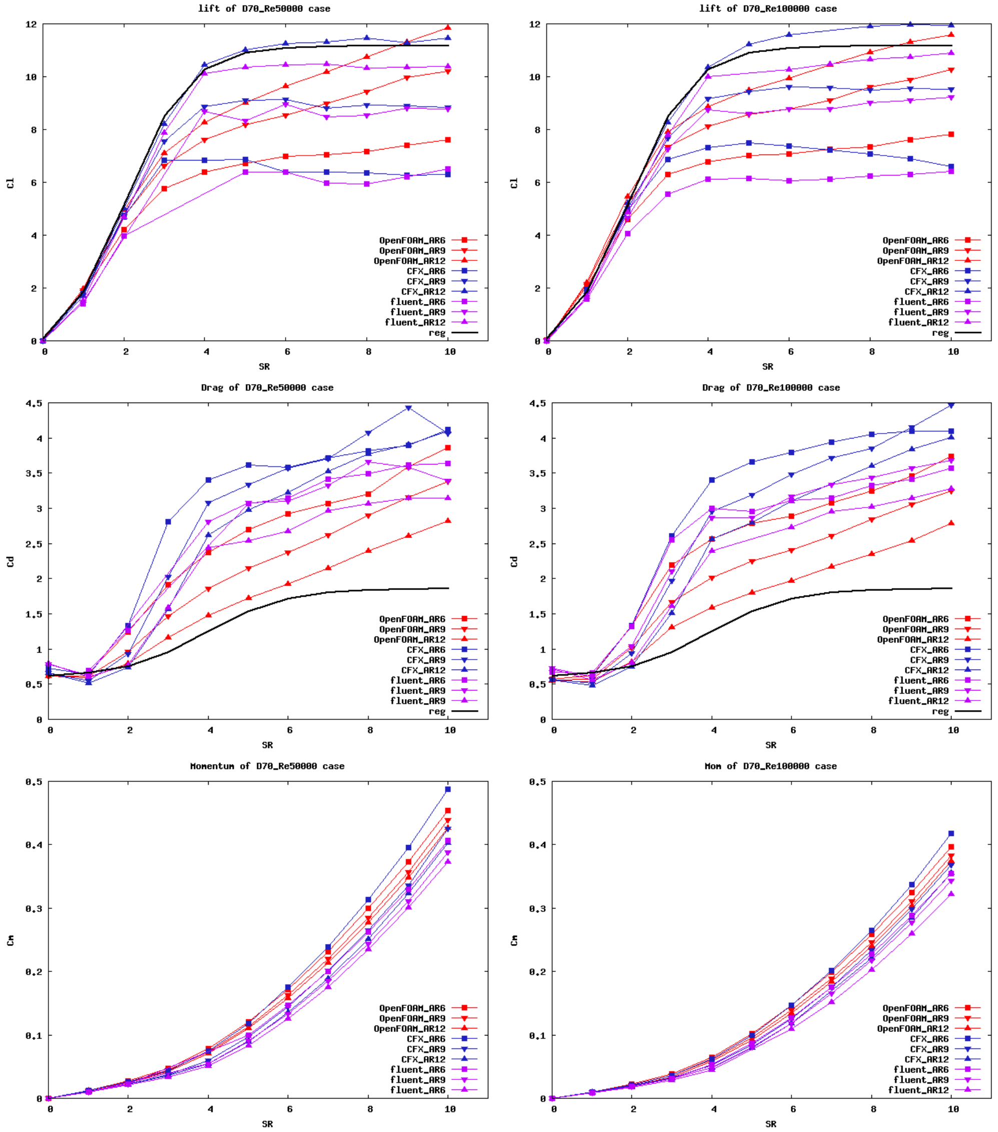

Fig. 5: Effect of Spin Ratio

Compared with results of C_l and C_m, the computed values for C_d show less agreement between software. The reason could be that C_d is more sensitive to the prediction of the actual flow structures creating the forces. Thus the predicted vortices in the wake of the Flettner rotor were also compared in Fig. 6 with four-selected Spin Ratio; the vortical stuctures behind the Flettner rotor is showed using an iso-surface of the second invariant of velocity gradient tensor coloured by turbulent kinemics energy.

First we note the obvious significant difference between rotating and non-rotating cases, present in all software. When the cylinder starts rotating, the well known "vortex street" type shedding disappears, while some vortices in streamwise direction appears along the rotor height on one side. This has not been reported before for such large Reynolds number and aspect ratio, at least to the author's knowledge. An effort will be made to validate this in the planned experimental work. The separating point moves in counter-rotating direction with increasing spin ratio. Furthermore, the complexity of the structures increases, at least from the result of OpenFOAM and ANSYS Fluent, with more and more vortices appearing. For ANSYS CFX, the results are smoother with limited increase in complexity. For example, with SR=10, only two vortices are predicted, while ANSYS Fluent and OpenFOAM show more than five. However, the later two still show differences in predicting the separation point.

We also compare the vortical stuctures behind the Flettner rotor for different aspect ratio at a fixed Reynolds number and spin ratio in Fig. 7 and Fig. 8. There are two large vortices at both end of the Flettner rotor that are almost the same in the size for all AR, while with increasing AR several smaller structures appear. This could be the reason for the increasing of the lift coefficient with the aspect ratio. Another interesting phenomena we note is that all the smaller vortices appearing along the rotor, except these at two ends, are in couple (Fig. 8), where the two vortices in one couple have different rotating direction. This indicates that a more complex instationary phenomenon occurs around the rotor.

At this point of the study, it is clear that the wake changes significantly not only with the defining parameters, but also due to variations between the tested software. The predicted trends for C_l and C_m are similar while the spread in predicted C_d is high. Two objectives for the upcoming experimental study, apart from adding experimental data to the force results, is thus to try to clarify both what is the complexity of the wake, and how does it vary, with changing the defining parameters, and why is the drag so sensitive to the wake prediction while the lift and moment is not.

Acknowledgements

This work is funded through the EU-project ULYSSES within the 7th Framework Programme. The authors wish to thank Mr Björn Allenström and Dr Da-Qing Li at SSPA Sweden AB for and Valery Chernoray at Chalmers for background discussions.

Reference:

[1] Prandtl, L., 1925, "The Magnus effect and Windpowered ships,"Naturwissenschaften,13,pp. 93-108

[2] Mittal, S. and Kumar,B., 2003,"Flow pass a Rotating Cylinder" J.Fluid Mech., 476,pp. 303-334

[3] Tokumaru, P.T. and Dimotakis, P.E., 1993, "The lift of a cylinder excuting rotary motions in a uniform flow" J.Fuid.Mech, 255,pp. 1-10.

[4] Karabelas, S.J., 2010, "Large Eddy Simulation of high-Reynolds number flow pass a rotating cylinder" Int. J. of Heat and Fluid Flow, pp. 518-527

[5] Menter, F.R., 1994, "Two-equation eddy-viscosity turbulence models for engineering applications" AIAA-Journal, 32(8), pp. 598-1605.

[6] Reid, E.G., 1925, "Tests of rotating cylinders" Flight , pp.17-20.

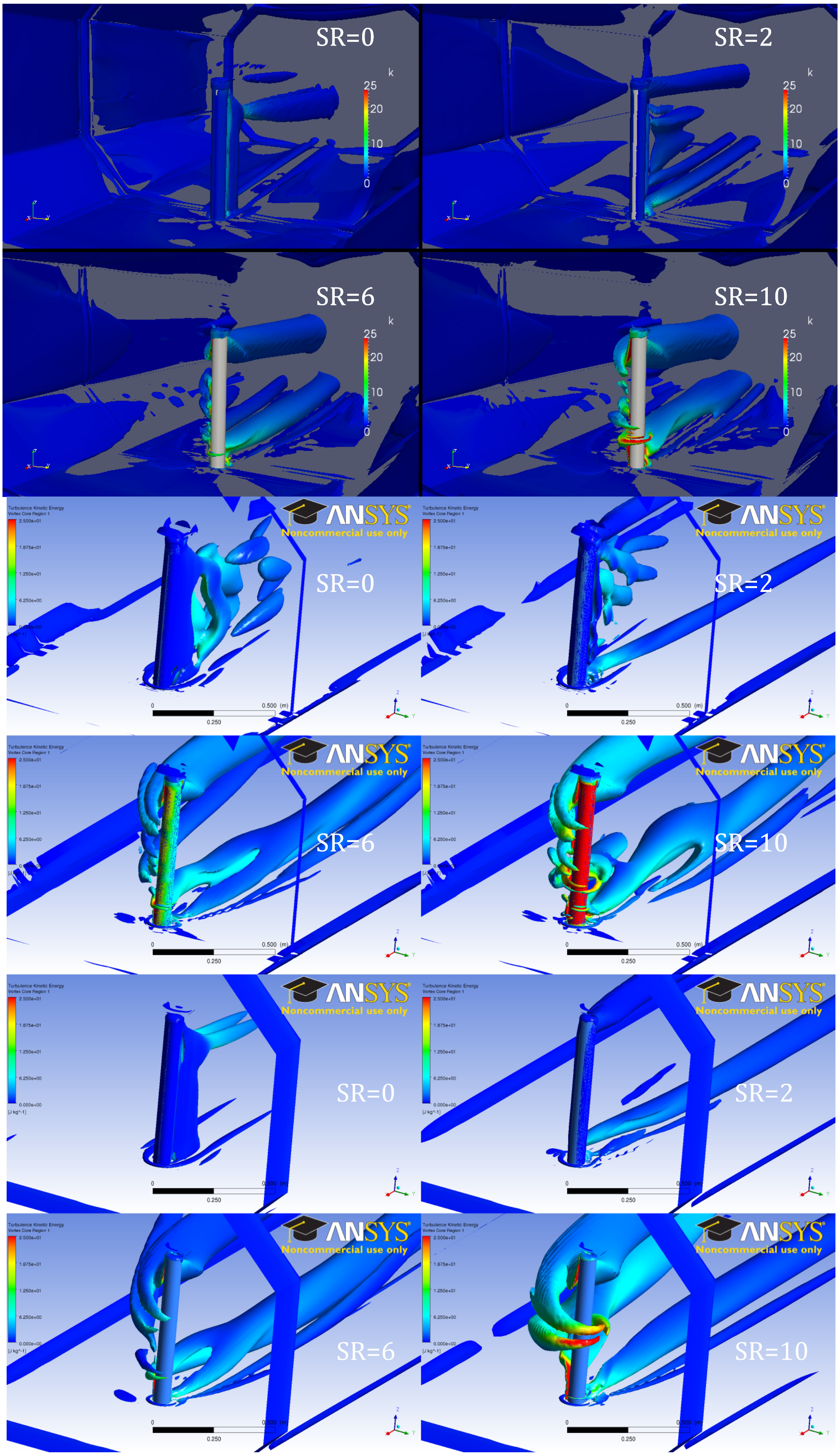

Fig. 6: Vortex behind the Flettner rotor(from top to bottom are result of :OpenFOAM, ANSYS Fluent and ANSYS CFX, for AR=9 Re=100,000)

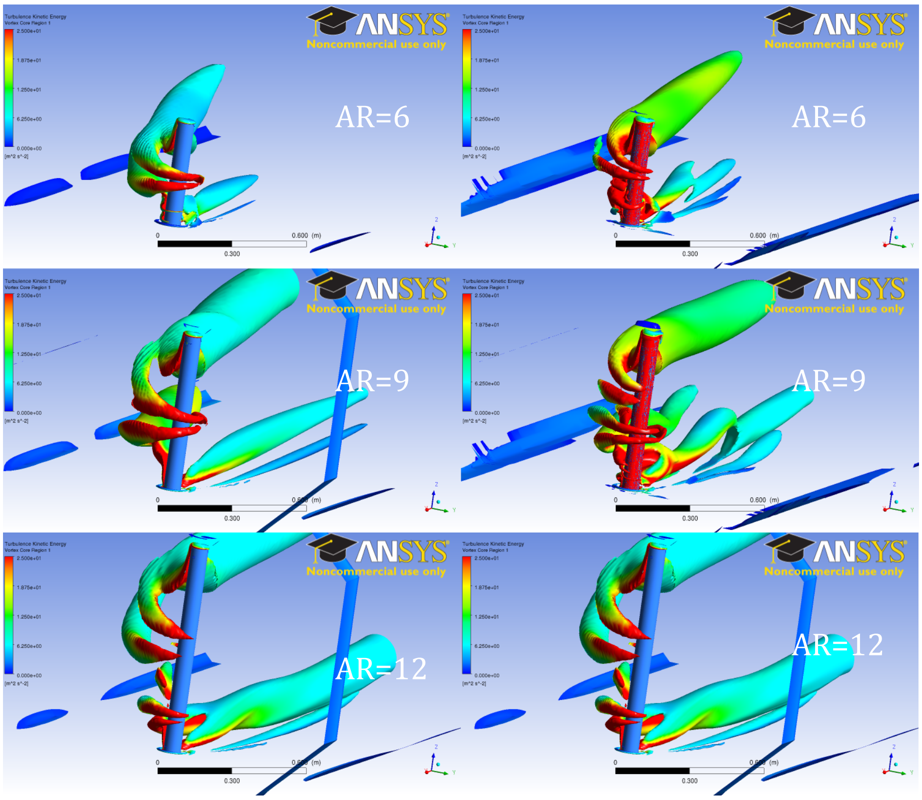

Fig. 7: Vortex behind the Flettner rotor for different AR(The left is the result of ANSYS CFX and the right is the result of ANSYS fluent, for D=70, Re=100,000)

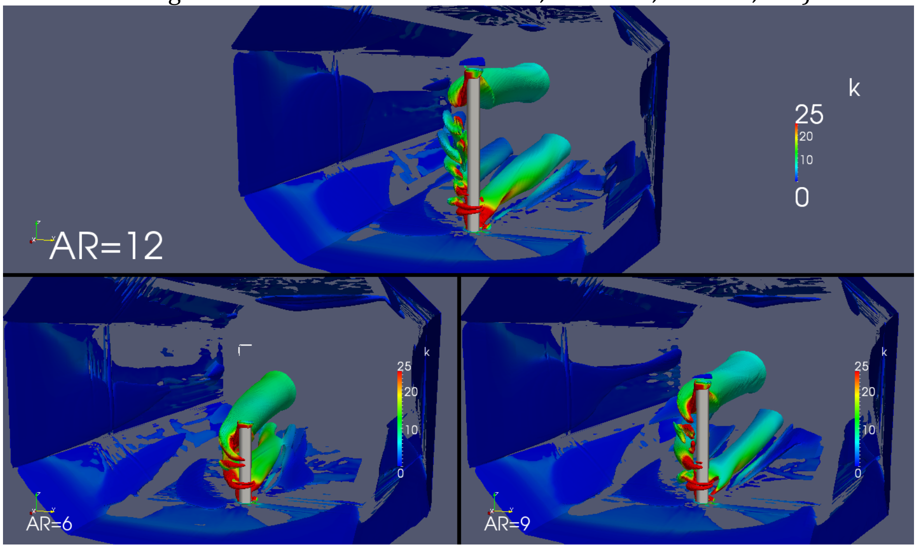

Fig. 8: Vortex behind the Flettner rotor for different AR(result of :OpenFOAM, for D=70, Re=100,000)

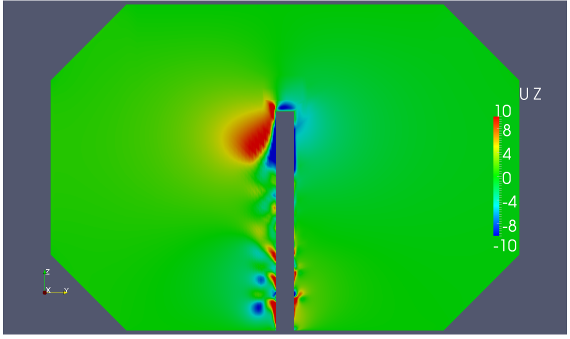

Fig. 9: vortex couples around Flettner rotor

A Verification and Validation Study Based on Resistance Submissions to the Gothenburg 2010 Workshop on Numerical Ship Hydrodynamics

Lu Zou and Lars Larsson
Dept. Shipping and Marine Technology, Chalmers University of Technology, Sweden
lu.zou@chalmers.se

1 INTRODUCTION

In the ship hydrodynamics community, the series of international Workshops on Numerical Ship Hydrodynamics (1980, 1990, 1994, 2000, 2005 and 2010) is well known for its consistent motivation of assessing the state of the art of Computational Fluid Dynamics (CFD) computations in ship hydrodynamics. One of its most important focuses lies in the assessment of the level of accuracy in CFD computations. The error and uncertainty estimation for accuracy quantification by the verification and validation (V&V) was first introduced and reported at the workshop in Gothenburg since 2000[1]. And then it was requested at the subsequent workshops, in 2005[2] and 2010[3]. At the lately held 2010 workshop in Gothenburg, the entries of both participant and test case were greatly expanded: the number of V&V test cases was set to 9, 33 research groups attended and 16 of them submitted the V&V results. To evaluate the CFD computed results, and furthermore to help understand the accuracy in computations, it is worthwhile to make use of the database at this workshop and dig more deeply into numerical solutions and the accuracy evaluation by means of comprehensive V&V study and statistical analysis, on which this paper will report.

2 VERIFICATION AND VALIDATION

Currently, verification and validation (V&V) tend to be useful to quantify the numerical and modeling errors in CFD computations. Several constructive V&V processes based on Richardson Extrapolation (RE) have been put forward in the past decade. In general, verification consists of code verification and solution verification. The former determines that a CFD code solves the mathematical equations correctly, and it can be controlled from the error evaluation in the light of a known benchmark solution (e.g. manufactured solution). The latter estimates the numerical error and uncertainty in the computation for a particular problem, in which the solution to such a problem is unknown. Prior to a practical application of the CFD code, it is normally assumed that the code has been developed correctly and the code verification has been adequately tested and achieved, so that the interest in a verification process is very often concentrated on the solution verification. In practical cases, solution verification estimates the numerical error and uncertainty, in which the most important issue is the determination of the iterative and discretization error and uncertainty. Although there are several techniques available (Roache [4]), a so-called convergence study is the normal type of investigation. Preceded by verification, validation is a process controlling the numerical solution against the appropriate experimental data, so as to reveal the error and uncertainty from both numerical and modeling deficiency in dealing with the real physical problem through mathematical modeling.

2.1 Verification Processes

This section introduces two verification processes to be applied to estimate the numerical uncertainty U_{SN}. Here we consider only a steady state computation. Assuming that the round-off error is negligible, the contribution to the numerical error comes from the iteration and grid discretization, and the numerical uncertainty is given as: $U_{SN} = \sqrt{U_I^2 + U_G^2}$. U_I is the iterative uncertainty due to the lack of convergence in the iteration process, and U_G is the grid discretization uncertainty caused by the limited grid resolution. For a well converged computation, the contribution from the former uncertainty should approach a negligible level, such that: $U_{SN}=U_G$. One of the verification processes is the Factors of Safety (FS) method by Xing et al (updated version in 2010[5]); and the other one is denoted as the LSR method in this paper due to the fact that it is on the basis of the Least Squares

Root approach. The LSR method was developed by Eça et al (revised version in 2010[6]). Both methods formulate the determination of numerical error and uncertainty based on systematic grid refinement computations.

2.1.1 FS method

This method presupposes that the iterative convergence has been achieved. In the grid convergence study, three systematic similar grids (to be used as a triplet) are created and computed. The uniform refinement ratio is defined as: $r = \frac{h_2}{h_1} = \frac{h_3}{h_2}$, where h_3, h_2, h_1 denote the grid spacing of the coarse, medium and fine grid respectively. The corresponding computed solutions are represented by S_3, S_2, S_1, and the solution changes of two successive grids are defined as: $\varepsilon_{12}=S_2-S_1$, $\varepsilon_{23}=S_3-S_2$. The convergence ratio R has the form: $R=\varepsilon_{12}/\varepsilon_{23}$.

Based on the R value, the state of discretization convergence can be decided as:

1). Monotonic convergence: $0<R<1$
2). Oscillatory convergence: $R<0$, $|R|<1$
3). Monotonic divergence: $R>1$
4). Oscillatory divergence: $R<0$, $|R|>1$

Only for the monotonic convergence $0<R<1$, the generalized RE can be used to express the numerical solution with a form of power series, which gives (e.g., considering the leading term only):

$$S_i = S_0 + \alpha h_i^p \tag{1}$$

where S_i is the solution on the i th grid (i=1, 2, 3), S_0 is the extrapolated solution to zero step size, α is a constant, and p is the order of accuracy. From eq. (1) the order of accuracy p and the error δ_{RE} in numerical solutions of systematically refined grids can be derived as:

$$p = \frac{\ln(\varepsilon_{23}/\varepsilon_{12})}{\ln(r)}, \quad \delta_{RE} = S_1 - S_0 = \frac{\varepsilon_{12}}{r^{p_{RE}} - 1} \tag{2}$$

Theoretically, the converged solutions should be within the asymptotic range where the attained order of accuracy equals the theoretical one designated in the numerical method, such that, $p=p_{th}$. However, in practical applications, solutions are often out of the asymptotic range ($p > p_{th}$ or $p < p_{th}$), then p is referred to as the 'observed order of accuracy'. In FS method, a distance metric P is used to define the distance of solutions from the asymptotic range, where: $P= p/p_{th}$. Then the error estimate is defined as: $\delta=P\delta_{RE}$.

To estimate the numerical uncertainty U_{SN}, the FS method adopts the general form proposed by Roache [4]: $U_{SN} = FS|\delta_{RE}|$ (FS is the factor of safety in general), but specifies three FS quantities according to the P value: FS_0 (P=0), FS_1 (P=1), FS_2 (P=2). The uncertainty estimate is formulated as below:

$$U_{SN}^{FS} = FS(P)\,|\delta_{RE}| = \begin{cases} [FS_1 \cdot P + FS_0 \cdot (1-P)]\,|\delta_{RE}| \\ [FS_1 \cdot P + FS_2 \cdot (P-1)]\,|\delta_{RE}| \end{cases} = \begin{cases} (2.45 - 0.85P)\,|\delta_{RE}|, & 0 < P \le 1 \\ (16.4P - 14.8)\,|\delta_{RE}|, & P > 1 \end{cases} \tag{3}$$

where FS_0=2.45, FS_1=1.6, FS_2=14.8, decided from statistical analysis [5].

2.1.2 LSR method

The LSR method is characterized by including more than three grid densities, considering the scatter in numerical solutions, and using a curve fit by the Least Squares Root approach to determine the order of accuracy and the numerical uncertainty. It is designed for computations with a theoretical second order of accuracy. The procedure is on the basis of RE and Grid Convergence Index (GCI). The discretization error is denoted by ε, following the general form from RE:

$$\varepsilon \simeq {}_{RE} \quad S_i - S_0 = \alpha h_i^p \tag{4}$$

where i=1, 2…n_g, n_g: available number of grids, $n_g>3$.

To determine three unknowns (S_0, α, p) in the equation above, at least three solutions are needed. For more than three solutions, the observed order of accuracy p can be estimated through the curve fit of the Least Squares Root approach. The convergence condition is then decided, following the rules below:

1. Monotonic divergence: $p<0$
2. Monotonic convergence: $p>0$
3. Oscillatory convergence: $n_{ch} \geq \mathrm{INT}(n_g/3)$, where n_{ch} is the number of triplets with $(S_{i+1} - S_i)(S_i - S_{i-1})<0$
4. Otherwise, anomalous behavior

Considering that the determination of p depends considerably on the scatter in the solutions, the estimation of the numerical error ε in this method is not only from δ_{RE}. Instead, three alternative error estimators are introduced (the first two estimators are obtained from curve fit as well) [6]:

$$\delta_{RE}^{02} = S_i - S_0 = \alpha_{02} h^2 \tag{5}$$

$$\delta_{RE}^{12} = S_i - S_0 = \alpha_{11} h + \alpha_{12} h^2 \tag{6}$$

$$\delta_{\Delta_M} = \frac{\Delta_M}{\left(h_{n_g}/h_1\right) - 1}, \text{ where } \Delta_M \text{ is the data range, } \Delta_M = \max\left(|S_i - S_j|\right) \quad 1 \leq i, j \leq n_g \tag{7}$$

The numerical uncertainty then is formulated as follows:
1. Monotonic convergence:
a. $0.95 \leq p \leq 2.05$: $U_{SN} = 1.25\delta_{RE} + U_{SD}$ (8)
b. $p \leq 0.95$: $U_{SN} = \min\left(1.25\delta_{RE} + U_{SD},\ 3\delta_{RE}^{12} + U_{SD}^{12}\right)$ (9)
c. $p \geq 2.05$: $U_{SN} = \max\left(1.25\delta_{RE} + U_{SD},\ 3\delta_{RE}^{02} + U_{SD}^{02}\right)$ (10)
2. Oscillatory convergence: $U_{SN} = 3\delta_{\Delta M}$ (11)
3. Anomalous behavior: $U_{SN} = \min\left(3\delta_{\Delta_M},\ 3\delta_{RE}^{12} + U_{SD}^{12}\right)$ (12)

where $U_{SD}, U_{SD}^{02}, U_{SD}^{12}$ are standard deviations of the curve fit for equations (4) (5) (6), e.g:

$$U_{SD} = \sqrt{\frac{\sum_{i=1}^{n_g}\left(S_i - \left(S_0 + \alpha h_i^p\right)\right)^2}{n_g - 3}} \tag{13}$$

2.2 Validation Procedure

Unlike the specific control of numerical accuracy at the verification stage, validation evaluates the error or uncertainty for a CFD computation in a more fundamental and extensive sense. It determines the level of accuracy to which a numerical model describes the real physical problem, in combination with the comparison with experimental data. The validation procedure adopted here is a simplified version of the ASME V&V 20-2009 Standard [7], which was used at the 3rd Lisbon Workshop on CFD Uncertainty Analysis (2008) [8] as well. Two parameters are specified: the validation comparison error, denoted as $E=S-D$ and the validation uncertainty (at 95% confidence level) defined as $U_{val}^2 = U_{SN}^2 + U_{input}^2 + U_D^2$. Here S and D represent the simulated solution and experimental data respectively, U_{SN} is the numerical uncertainty, U_{input} is the input parameter uncertainty (for a strong model concept, $U_{input}=0$) and U_D is the data uncertainty in the experiment. Hence U_{val} is approximated as: $U_{val}^2 = U_{SN}^2 + U_D^2$. If $|E| >> U_{val}$, it indicates that the sign and magnitude of E could be used to improve the modeling (reduce the comparison error or modeling error); but if $|E| \leq U_{val}$, the modeling error is within the 'noise level' of U_{val} caused by numerical, (input parameter) and experimental data uncertainties, and thus not much information can be used to improve the modeling error.

3 V&V SUBMISSIONS AT 2010 WORKSHOP

At 2010 Workshop the nine V&V test cases include the V&V of CFD predictions for three benchmark hull forms (KVLCC2: Case1; KCS: Case2; DTMB 5415: Case3) in different conditions, such as low or high speeds, zero/fixed dynamic/free sinkage and trim, self-propulsion. In the present V&V study, only total resistance predictions are considered. For detailed case descriptions the reference is made to [3]. Totally 43 submissions from 16 research groups contributed to the test cases. 13 of 43 submissions used more than 3 grids. These entries can apply both FS (3 grids) and LSR (>3 grids) method. For FS method, the solutions are split into several triplets with certain refinement ratio. From the two methods, several essential factors/variables in V&V are estimated: type of convergence; observed order of accuracy (denoted by P); numerical uncertainty U_{SN}; validation uncertainty U_{val}; comparison error $|E|$.

4 DISCUSSIONS OF THE V&V STUDY

4.1 V&V Credibility

Accuracy assessment through the comparison between numerical solutions and experimental data has a long tradition, while the concept of V&V and its application have not attracted enough attention, especially for complex turbulent flows, like in ship hydrodynamics. The reason often points to the doubt mentioned frequently about how helpful and reliable V&V really is. Considering this, the two most well-known verification processes, FS and LSR, are presented in this paper and both are used to estimate the numerical error and uncertainty. If it can be demonstrated that these two produce similar results, it would strengthen the credibility of both. Such a comparison will now be made. We take the 12 entries for which both methods can be applied, that is, 12 finest triplets (3-2-1) for the FS method and 12 sets (>3 solutions) for the LSR method from the same submissions in the test cases. The results are summarized in Fig. 1.

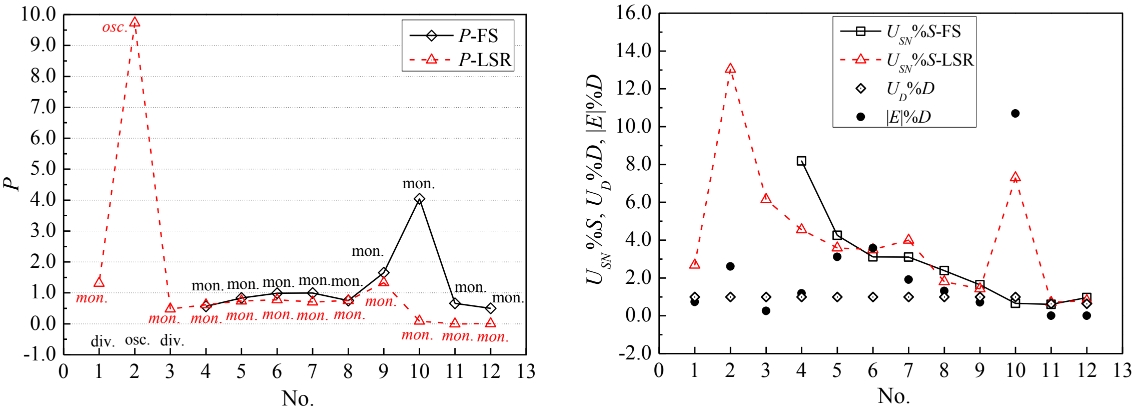

Fig. 1 V&V results from FS and LSR method for 12 entries

First considering the convergence state (mon.: monotonic convergence, osc.: oscillatory convergence, div.: divergence; results from the LSR method are denoted by italic fonts), it is seen that the same type is obtained in 10 out of the 12 entries. The difference is items No.1 and No.3, for which the LSR method produces monotonic convergence while the FS method shows divergence. The difference is likely to be due to scatter in the solutions, which is smoothed out in the LSR method but may create divergence in the FS method. Turning next to the observed order of accuracy P, a comparison between the two methods is shown in Fig. 1. Note that P can only be estimated for the 9 monotonically convergent cases in the FS method. Out of these 9 cases only one (No.10) exhibits completely different P values in the two methods. The reason for this discrepancy is the large scatter in the solutions for this case. This scatter is smoothed out in the LSR method but not in the FS method. For No. 4 to No.9 the correspondence is very good, but for No.11 ~ 12 the LSR method produces a lower P. The most interesting quantity is the numerical uncertainty, U_{SN}. Comparing the solid and dashed curves of Fig. 1 a rather good correspondence is noted. The exception is No.10, for which the P value is quite different. As for validation, finally, the two methods give the same result, $|E|<U_{val}$ in all cases, except No.6, where however U_{val} is very close to $|E|$ in both methods.

Considering the fact that the two methods used here were developed based on entirely different benchmark data, the achieved correspondence between the results is surprising and lends significant credibility to both methods. This is so particularly when the solutions are close to the asymptotic range. Far away from this range the differences become larger, which is not surprising, since the formulas used are based on data close to the range. (In the FS method P=2 is stated as the upper limit of validity). It should be stressed, however, that the number of cases which this study has used is very limited. Since in most verification methods U_{SN} is quantified on the basis of experience or statistical analysis to ensure a 95% level of confidence, more practical or complicated applications are necessary to test the V&V methods.

4.2 Verification Investigation

With respect to verification, the questions of significance during a grid convergence study are always the selection of grid type, grid size, grid refinement ratio, and then the determination of the observed convergence type, the convergence rate (order of accuracy), the applied discretization error/uncertainty estimator, and the relevant consequences.

4.2.1 Convergence type and observed order of accuracy

In principle, the general convergence conditions are classified as (monotonic or oscillatory) convergence and (monotonic or oscillatory) divergence, and the ideal situation is that the solutions converge monotonically. Note that solutions with large U_I should be omitted, because it will pollute the determination of U_G. Finally all the solutions submitted by the participants give *71 triplets* in the FS method and *11 sets* in the LSR method. As shown in Fig. 2, overall 64% P values from the LSR method are in the vicinity ($0.5<P\le1.5$) of the theoretical one, which is comparable with the 55% in the FS method. The proportion of those having low accuracy within $0<P\le0.5$ (27%) is larger than in the FS method (7%), however. The scatter in numerical solutions is a possible explanation for the too high or low level of accuracy (P), as suggested by the developers of the LSR method. The Least Squares Root curve fit works well in smoothing the scatter out. However, since the number of entries that can be used in the LSR method here is very limited, it is difficult to draw more reliable statistical conclusions.

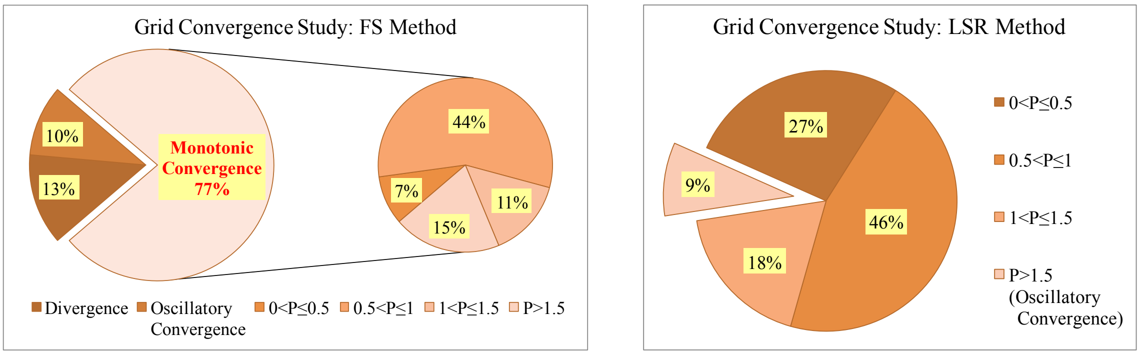

Fig. 2 Convergence type and P value in the FS method and the LSR method

4.2.2 Convergence state versus grid type

In the grid convergence study, the level of accuracy is always associated with the form of grid discretization, e.g., the adopted grid type, the grid sizes and the refinement ratio used to create the systematic similar grids. First and foremost is the grid type. Classifying it as structured or unstructured, in the FS method 63 triplets used structured grids, among which 53 achieve monotonic convergence (84%); the other 8 triplets used unstructured grids and 2 of them achieved monotonic convergence (25%). However, in the LSR method, among the 11 sets of submissions, only 1 used an unstructured grid and it attained monotonic convergence. 9 of the other 10 sets with a structured grid attained monotonic convergence and the remaining one had oscillatory convergence. These observations imply that the structured grids clearly are more widely applied and achieve monotonic convergence more easily than the unstructured grids in the context of error estimation based on Richardson extrapolation. Still, since the number of entries with unstructured grids are only 8 it is hard to draw statistical conclusions.

4.2.3 Numerical uncertainty versus order of accuracy and grid size

The estimated numerical uncertainties U_{SN} from the FS and LSR methods against the obtained order of accuracy P are presented in Fig. 3, where the relevant uncertainty bars are plotted. Open symbols represent the finest solutions in the triplets (FS), and solid symbols represent the finest solutions in sets (LSR). In the figure, results are grouped by three grid sizes: small size (≤3 million grid points), medium size (between 3 and 8 million) and large size (>8 million), and then split for low-speed (Fr<0.2) and high-speed (Fr>0.2) computations.

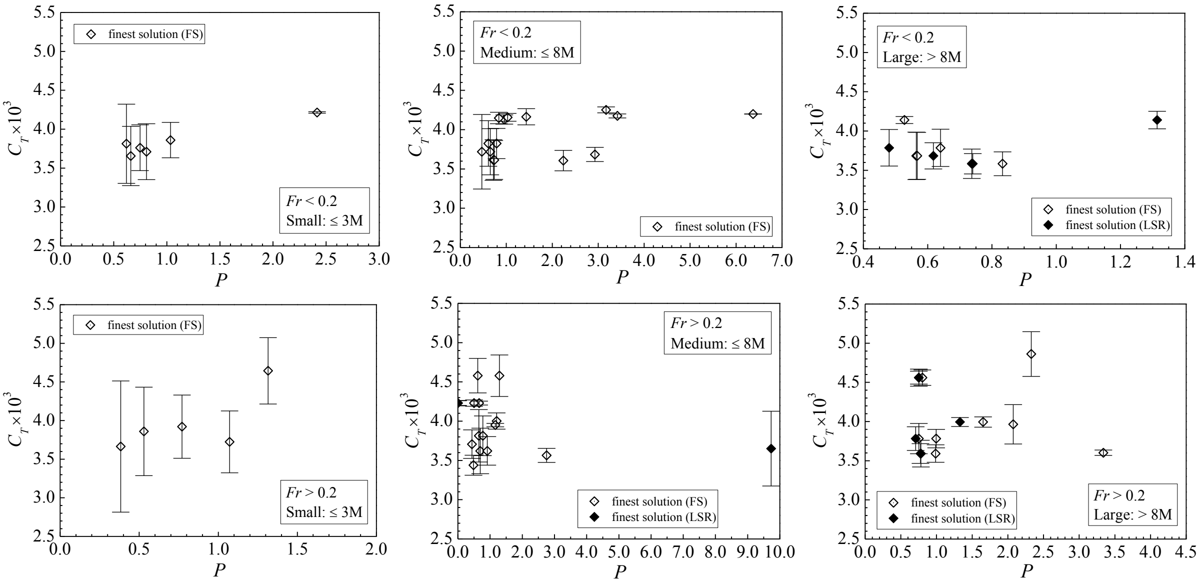

Fig. 3 Numerical uncertainties versus grid size and P value for Fr <0.2 and Fr >0.2

Fig.3 indicates the medium size is widely used in the low-speed computations, while in the high-speed computations the medium and large sizes are more frequent. In both low- and high-speed computations, the less used small grid sizes always produce larger numerical uncertainty. And if we compare the global U_{SN} at Fr<0.2 and Fr>0.2, it is seen that the magnitudes in the high-speed computations are larger than those in the low-speed computations, especially with small grid sizes. Furthermore, for medium and large grid size in low- and high-speed computations, the relation between U_{SN} and P indicates that when the solutions are far from the asymptotic range, the estimated uncertainties from the FS method are either very large or very small, revealing the difficulties in quantifying the error or uncertainty in such situations.

4.3 Validation: U_{val} versus $|E|$

For validation experimental data are always necessary. Following the suggestion of the V&V 20 standard [7], the present work is focused on the quantitative assessment of the validation (within $E \pm U_{val}$) instead of making any judgment of success or failure.

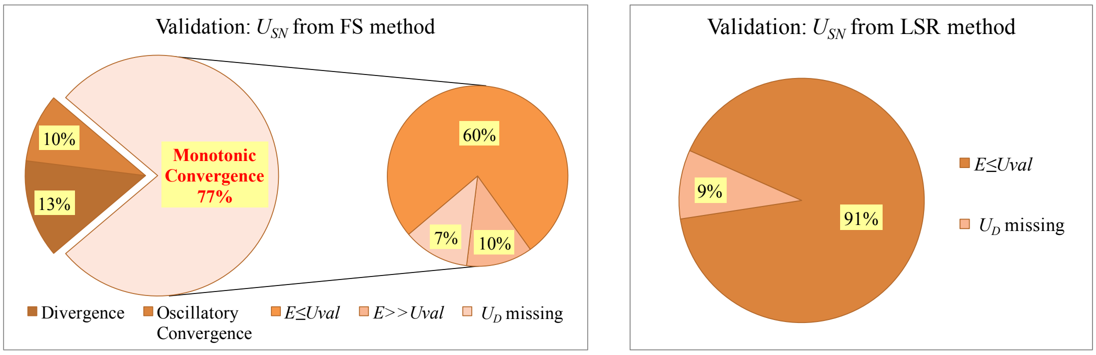

Fig. 4 Validation results (based on U_{SN} from the FS method and the LSR method)

Results are summarized in Fig. 4. The validation study by the FS method can only be made for the 77% monotonically converged solutions. And the classification of the results is: 60% $E \le U_{val}$, 10% $E >> U_{val}$. For 7% U_D are missing (the self-propulsion cases) so that no comparison can be made. From the LSR method, except for one submission with the missing U_D in the self-propulsion case, all the others (91%) yield $E \le U_{val}$, indicating a relatively small comparison error and thus unclear deficiency in the numerical computations. Note that only an overview of the summarized results from the FS and LSR methods is presented in Fig. 4. The correspondence between the two methods for the same submissions is illustrated by Fig. 1.

5 CONCLUDING REMARKS

This paper presents a part of the observations from an extensive survey of V&V applications in practical complex turbulent flow. Although the present investigations are limited to the available submissions, several general conclusions can be drawn:

1) V&V appears to be able to give a relatively reliable error and uncertainty estimation, as implied by the corresponding results from the V&V study by the two different methods, FS and LSR. However, this is only applicable for the solutions in the vicinity of the asymptotic range.

2) The grid convergence study is complicated by several aspects: grid type, grid size, grid refinement ratio, convergence state, convergence rate (order of accuracy), etc., to which the grid discretization error is always related. From present investigations, the following observations can be obtained:

  a. Grid type: the unstructured grids in general imply more difficulty in achieving monotonic convergence than the structured grids.

  b. Convergence state and observed order of accuracy: in the vicinity of the asymptotic range ($0.5<P<1.5$), results from the FS and LSR methods present promising correspondence. However, the observations for solutions far away from the asymptotic range are very different between the two methods, indicating the complexity of determining the grid convergence and numerical error for that case. Another typical issue in the grid convergence study is the scatter in solutions, which complicates the study and has been shown to affect the determination of the grid convergence and the order of accuracy significantly. Although the LSR method takes the scatter into consideration, more investigations are needed to further improve the determination of grid convergence for solutions with the scatter.

3) Most resistance solutions are estimated to have a lower comparison error than validation error, i.e. $|E|<U_{val}$ so that the modeling error is buried in the numerical and experimental noise. For the fewer cases with $|E|>U_{val}$ on the other hand modeling errors are significant, and reducing the E value is regarded as a target of the model improvement. The potential sources of modeling error should be further investigated.

6 REFERENCES

[1] Larsson, L., Stern, F., and Bertram, V., ‘Gothenburg 2000-A Workshop on Numerical Hydrodynamics’, Department of Naval Architecture and Ocean Engineering, Chalmers University of Technology, Gothenburg, Sweden, 2002

[2] Hino, T., Proceedings of CFD Workshop Tokyo 2005, Tokyo, Japan, 2005

[3] Larsson, L., Stern, F., and Visonneau, M., ‘Proceedings of a Workshop on Numerical Hydrodynamics’, Gothenburg, Sweden, 2010

[4] Roache, P. J., ‘Verification and Validation in Computational Science and Engineering’, Hermosa Publishers, Albuquerque, 1998

[5] Xing, T., and Stern, F., ‘Factors of Safety for Richardson Extrapolation’, Journal of Fluids Engineering 132(6): 061403-13

[6] Eça, L., Vaz, G., Hoekstra, M., ‘A Verification and Validation Exercise for the Flow Over a Backward Facing Step’, V European Conference on Computational Fluid Dynamics, ECCOMAS CFD 2010, Eds. Pereira J.C.F., Sequeira A., Lisbon, June 2010

[7] ASME V&V 20-2009, Standard for Verification and Validation in Computational Fluid Dynamics and Heat Transfer, issued on November 30, 2009

[8] http://maretec.ist.utl.pt/html_files/CFD_workshops/Workshop_2008.htm. 3rd Workshop on CFD Uncertainty Analysis, Lisbon, 2008

CALL FOR PAPERS

15th Numerical Towing Tank Symposium (NuTTS'12)

Cortona, Italy, 7-9th October 2012

Topics:

- Nonlinear flows around marine structures (LES, RANSE, Euler with or w/o free surface)
- Free-surface flows around marine structures (3-d ship seakeeping, free-surface viscous flows)
- Related topics (validation experiments, numerical techniques, grid generation, etc)

Deadlines:		
	Early feedback (optional):	15 April 2012
	Extended Abstracts received:	15 July 2012
	Payment received:	15 August 2012

You are invited to participate in the above event. The objective of the event is to provide a forum for informal discussions among experts in the field and to disseminate latest results. Younger workers and Ph.D. students are especially encouraged to participate. The event will be held at the Oasi Neumann hotel in lovely Cortona (Tuscany). All participants stay and have meals together to maximize interaction and discussion.

The extended abstracts of the proposed talk will be directly reproduced in pdf proceedings. Work in progress, encountered problems, etc. should be discussed in an open, informal atmosphere (no ties!) among colleagues. The first page of the extended abstract should be headed with the title and authors' names, affiliation and email address in a compact form to economize on space. Academic titles and page numbers shall be omitted. The extended abstract shall neither contain an abstract of the abstract, nor keywords, nor further headers. Font size shall not be less than 10pt Times New Roman. Extended abstracts should be limited to 6 pages in A4 format with 2.5 cm margin. An early reply will help us in organizing the event better. For the early feedback, a tentative title or topic will suffice.

Following the tradition of previous NuTTS events, the fees will be kept low to allow a maximum number of scientists to attend. The fees including accommodation (2 nights) and all meals during the symposium will be:

300 Euro PhD candidates and students
400 Euro authors
450 Euro other participants

Contact: Volker Bertram
volker.bertram@GL-group.com

Sponsors: CD-adapco, INSEAN, further sponsors to be announced